REFERENCE

Fabrication and characterisation of high efficiency inverted P3HT:PCBM polymer solar cells

Vikas Kumar

A thesis submitted in partial fulfilment of the requirements of
Sheffield Hallam University
for the degree of Doctor of Philosophy

April 2014

Abstract

Among many photovoltaic (PV) technologies polymer-fullerene based inverted bulk heterojunction (BHJ) solar cells have drawn lot attention in recent years due to low cost fabrication over a large area by using simple solution-processed methods. This thesis presents a study of inverted organic solar cells (OSCs) on indium tin oxide (ITO) coated glasses and metal substrates using spin coating technique. Zinc oxide (ZnO) and poly(3,4-ethylenedioxythiophene): poly(styrenesulfonate) (PEDOT:PSS) were used as the electron transport layer (ETL) and hole transport layer (HTL) respectively. Poly(3-hexylthiophene):[6,6]-phenyl C61-butyric acid methylester (P3HT:PCBM) was used as an active layer. The ZnO layers deposited using nanoparticles (NPs) and sol-gel route at a temperature of 150 °C. The poor wettability of aqueous PEDOT:PSS on the hydrophobic P3HT:PCBM layer was improved with the addition of surfactant Triton X-100. The P3HT:PCBM photoactive layer was optimised in terms of solvents, concentrations and layer thickness. However, the thickness of the active layer in BHJ devices need to be very thin (~ 200 nm) which causes poor light absorption and low carrier mobilities. Therefore, it is important to introduce new approaches to enhance the photon absorption efficiency of the active layer under the film thickness limitation. Among all the approaches plasmonic nanostructures have recently emerged as an expanding area to enhance light absorption in organic photovoltaic (OPV) devices.

A low vacuum Plasma assisted physical vapour deposition (PAPVD) method was used to deposit Gold (Au) NPs thin film onto the PEDOT:PSS layer in the inverted P3HT:PCBM OSC devices. The Au NPs incorporated into the PEDOT:PSS layer and reaching the active P3HT:PCBM layer can provide a significant plasmonic broadband light absorption enhancement to the active layer. An improvement in the short circuit current density of 50-90% has been achieved compared with those OSC devices without the plasmonic light absorption enhancement. The enhanced current density is directly related to the enhancement of light absorption in the active P3HT:PCBM layer due to the creation of localized surface plasmonic resonance (LSPR) by Au NPs or nanometer-sized Au clusters. OSC devices were fabricated with various thicknesses of Au NPs films; the OSC device with ~5.0 nm Au NPs film exhibited an efficiency of ~ 5.01% with a fill factor of ~66.61%. The obtained improvement in power conversion efficiency (PCE) is mainly assigned to the noticeable increase of photocurrent and the improvement in the fill factor.

Top illuminated inverted OSC devices were fabricated on metal substrates, namely: polished stainless steel (SS), titanium coated steel (Ti-S), chromium coated aluminium (Cr-Al) and polished aluminium (Al). OSC devices on metals had the simple structure of (Metal substrate/sol-gel ZnO/P3HT:PCBM/PEDOT:PSS/hcPEDOT:PSS). Good performance OSC devices were achieved on both the SS and Cr-Al substrates with an efficiency of ~3.10% while no effective devices were produced on Ti-S and Al substrate. Electrical impedance spectroscopy experiments showed that the native oxide layer on top of different metal substrates causes significantly different performance in PCE for the inverted OSC devices.

Acknowledgement

I would like to take this opportunity to express my sincere gratitude to my supervisor Dr. Heming Wang for his invaluable guidance, immense interest and continuous assistance with moral support for the completion of the present work. It is my pleasure to work with him who always put me on the right track in handling many problems from the chemistry point of view. The patient and understanding that he exhibited towards me was very much needed.

I gratefully thank to the heads of the Institute (during last three years) Prof. Robert Akid and Prof. Alan Smith for providing the facilities in the Institute.

Thanks to all the admin staff of the Institute for making the paper work easy. Special thanks to Mr. Vinay Patel, Ms. Deeba Zahoor, Mr. Stuart Creassey, Mr. Robert Burton and Mr. Gary Robinson for their help in different measurements.

I deeply appreciate Dr. Oliver Lewis for reviewing my RF2 report. I sincerely thank him for his great support during discussion and helpful suggestions. I also thank to Prof. Doug Cleaver for the generic skills training.

I greatly appraise the company given by the colleagues and good friends in MERI. My heart-felt thanks to their friendship.

I extend special thanks to Dr. Cornelia Rodenburg and Dr. Andrew Pearson to carry out the LVSEM images and the electrical measurement in their laboratory at Sheffield University.

I gratefully acknowledge to Dr. Chris Lowe and Mr. Sonny Ngo from Becker Industrial Coating Ltd. for their full financial support on facilities, raw materials and the wonderful vegetarian lunch they bought for me during the meetings in Liverpool. I am also thankful to

Dr. Chris Lowe and Mr. Sonny Ngo for their technical support and valuable discussions at several stages of my experiments.

My final words of thanks go to my parents and my family for their constant supports and encouragements. Especially, I want to thank my wife Deepika Chaudhary for her intense support to my decisions and for the addition of my little angel Advika Chaudhary to our life.

Last but not the least, An enormous thanks to the Divinity for giving me the direction, patience and strength to complete this PhD work.

Publications

[1] Vikas Kumar, Heming Wang, Plasmonic Au nanoparticles for enhanced broadband light absorption in inverted organic photovoltaic devices by plasma assisted physical vapour deposition, Organic Electronics. 14 (2013) 560-568

[2] Vikas Kumar, Heming Wang, Selection of metal substrates for completely solution-processed inverted organic photovoltaic devices, Solar Energy Materials & Solar Cells. 113 (2013) 179-185

[3] Yaqub Rahaq, Heming Wang, Vikas Kumar, Fabricating the solution-processable inverted photovoltaic devices by the dip-coating method, Organic Electronics, 15 (2014) 984-990 (Not included in this thesis)

[4] Vikas Kumar, Heming Wang, High-efficiency inverted polymer solar cells via dual effects of introducing the high boiling point solvent and the high conductive PEDOT:PSS layer, Organic Electronics, 15 (2014) 2059-2067.

Conference presentations:

[1] Vikas Kumar, Heming Wang, Completely solution-processed inverted organic photovoltaic devices on metal substrates with a conducting polymer anode, UK semiconductor 2013, Sheffield, UK

[2] Vikas Kumar, Heming Wang, Plasmon-enhanced light absorption in inverted polymer solar cells by incorporating Au nanoparticles in a buffer layer, EUPVSEC 2013, Paris, France

Contents

List of Figures

Chapter 1

Chapter 2

Chapter 3

Chapter 4

Chapter 6

Chapter 7

List of Tables

Chapter 6

Chapter 7

List of Abbreviations

A: Acceptor

ACF: Auto-correlation Functions

AFM: Atomic force microscope

Ag: Silver

Al: Aluminium

APTS: Aminopropyl triethoxysilane

ATR-FTIR: Attenuated total reflectance-Fourier transform infrared spectroscopy

Au: Gold

θ: Angel

ω: Angular frequency

BHJ: Bulk hetero-junction

C: Capacitance

CB: Chlorobenzene

CO_2: Carbon dioxide

CPE: Constant phase element

Cr-Al: Chromium coated aluminium

CSP: Commercial concentrated power

Cu: Copper

D: Donor

DD: 1,8-diiodooctane

EIS: Electrical impedance spectroscopy

EQE: External quantum efficiency

ETL: Electron transport layer

eV: Electron volt

FF: Fill factor

fs: Femtosecond

FWHM: Full width at half maximum

GO: Graphene oxide

GPS: Glycidoxy-propyl-trimethoxy-silane

hcPEDOT:PSS: Highly conducting poly (3,4-ethylenedioxythiophene): poly (styrenesulfonate)

HOMO: Highest Occupied Molecular Orbital

HTL: Hole transport layer

Hz: Hertz

IPCE: Incident photon to charge carrier efficiency

IR: Infrared

ITO: Indium tin oxide

J_{sc}: Short circuit current density

J-V: Current density-voltage

LSPR: Localised surface plasmon resonance

LUMO: Lowest Unoccupied Molecular Orbital

LVSEM: Low voltage scanning electron microscopy

γ_{lv}: Liquid-vapor interfacial tensions

µl: Microliter

mm: Milimeter

µm: Micrometer

MPTS: Methylpropyl tryethoxy silane

NDs : Nanodots

nm: Nanometer

nN: nanonewton

NPs: Nanoparticles

NRs: Nanorods

ns: Nanosecond

NSs: Nanospheres

NWs: Nanowires

Ω: Ohm

ODCB: Oortho-dichlorobenzene

OPV: Organic photovoltaic

OSCs: organic solar cells

P3HT: Poly (3-hexylthiophene)

PAPVD: Plasma assisted physical vapour deposition

PCBM: [6,6]-phenyl C61-butyric acid methylester

PCE: Power conversion efficiency

PEDOT:PSS: Poly (3,4-ethylenedioxythiophene): poly(styrenesulfonate)

PRs: Plasmonic resonances

PEO: Polyethylene oxide

PET: Polyethylene tere-phthalate

P_{light}: Intensity of light

PVs: Photovoltaics

R: Resistance

rpm: Round per minute

R_s: Series resistance

R_{sh}: Shunt resistance

SEM: Scanning electron microscope

Si: Silicon

SPPs: Surface plasmon polaritons

SPR: Surface plasmon resonance

SS: Stainless steel

γ_{sl}: Solid-liquid interfacial tensions

γ_{sv}: Solid-vapor interfacial tensions

Ti-S: Titanium coated steel

2D: Two dimensional

UV: Ultraviolet

V: Volt

V_{oc}: Open circuit voltage

λ: Wavelength

XRD: X-ray diffraction

ZnO: Zinc oxide

1.1 Combustion of fossil fuels

The global energy demand is increasing dramatically at an alarming rate. Fossil fuels are our society's main sources for energy, accounting for 87% of world energy consumption in 2012. It is foreseeable that these resources are limited and cannot provide enough energy to meet the increasing needs by the world in the future [1-3]. Nuclear energy can play an important role on supplying the power; however, it has its limitations on the supply of raw materials and the long-term safety for storage of waste materials. The waste materials generated by the nuclear power plant are radioactive and has a lifespan of more than ten times the half-life of the used materials [4]. Currently, the carbon dioxide (CO_2) emission has reached to 34.5 billion tonnes per in 2012 [5] mainly due to the burning of fossil fuels based energy sources including petroleum and coal. As a result, the CO_2 concentration in the atmosphere continues to mount and has reached to approximately 393.31 ppm by volume in September 2013 [6]. This massive amount of CO_2 and other greenhouse gases create harmful effects on the delicate balance of nature. The rising of sea level and global surface mean temperature have already increased the frequency and severity of natural disasters [7]. It is likely to have more devastating effects on human beings and other life forms in the future time. Therefore, renewable energy sources are urgently required to play a prominent role in coping with this challenge.

1.2 Energy requirement issues

According to International Energy Agency (2012), it is very difficult to limit the global warming within 2°C and becomes more expensive with each year that passes [8]. All

the permissible CO_2 emissions would be locked-in by the existing energy infrastructure, if there is no action before 2017 [9]. The world energy demand has increased about 26% from 2000 to 2010 and a further growth of 47% has been predicted up to 2020. From 1973 to 2010 the annual growth was 3.4% and it is estimated to grow 89% from 2010 to 2035 [10]. In 2010 the global consumption was 18,443Terawatt-hour (TWh) and predicted to grow to 35,000 TWh in 2035. United Nations has predicted that the world population grow from 6.6 billion in 2007 to 8.7 billion by 2035 [11,12] and the demand for energy also increases substantially over this period. Energy is a basic need underlying all aspects of the global economy. Currently some two billion people have no access to electricity and in future time it is a high priority to address this issue.

As outlined above, the growth in population associated with the increased living standard pattern in most developing countries will lead to a big increase in energy consumption. The increased share in the global energy demand can reach up to 70% for the developing countries, led by India and China [13]. Security concerns are also driving the pursuit of renewable energy sources. A large portion of oil based fossil fuels have been found to exist in regions where are politically instable and sometime create disturbances in regular supplies. Such disturbances can be serious issues for one individual country securing its energy supply. Furthermore, the security concerns are not limited to supplies only, but also associated with the electric power blackout; examples are the "August 2003" blackout in North America and the "July 2012" blackout in India that affected over 620 million peoples, caused enormous economic losses and presented serious national security concerns. According to the World Energy Outlook 2012 new policies scenario, the global energy demand will increase rapidly due to increased urbanisation and the limited supply of carbon based fossil fuels, which has motivated the world to pursue for new energy sources [14].

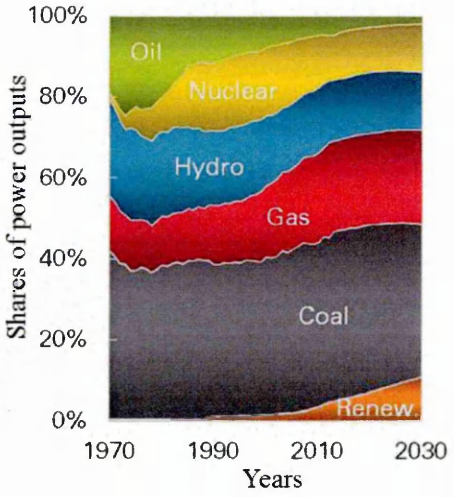

Figure 1.1.Shares of different sectors in the final production. (Source: BP Energy Outlook 2013)

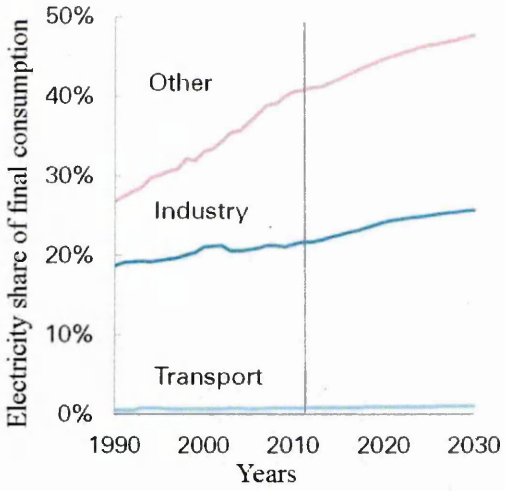

Figure 1.2.Shares of different sectors in the final consumption. (Source: BP Energy Outlook 2013)

1.3 Solar energy

A solution to the twin problems of getting exhausted conventional fossil fuels and their environmental impacts is to explore the renewable energy sources. The Sun is the main energy source on earth and direct conversion of solar energy into electricity is a very appealing way to satisfy the future energy needs in the modern world creating the minimal impact on the ecosystem. The Sun can deliver enough energy to meet the global energy demand. The total solar flux intercepted by the earth is called "solar constant" that is equal to 1.37 kilowatt/square meter (kW/m^2). The time-and-space-averaged solar flux striking the outer atmosphere of the earth is one quarter of this, ie. 342.5 W/m^2. Out of it, nearly about 19% of this flux is absorbed by the atmosphere including clouds while 30% of this flux is scattered (Wallace 1977, pp. 320-321). Therefore, the average striking flux towards the earth's surface is 174.7 W/m^2. The total theoretical potential of solar power (integral of this average flux over the earth's surface area) is 89,300 TW. This theoretical potential could be used to generate 15 TW of solar

power from the 10% power conversion efficiency solar-conversion systems covering only 0.17% of the earth's surface area (15 TW / 89,300 TW) / (0.1)= ~.0017) that is 858,792 km^2. This is roughly equal to the land area of Namibia (825,418 km^2) or Venezuela (882,050 km^2) [15].

The solar power can be exploited in several different ways. Firstly, solar power can be used directly for buildings heating. There are massive efforts being taken place to integrate the passive solar energy captures into the building architecture. Secondly, the energy associated with solar radiation can also be used to heat water for household or domestic use. This water heating technology has been adopted in many regions of the world like Israel where nearly 90% of the household utilize solar power for water heating [16]. Thirdly, solar power can also be used directly to generate electricity.

There are two primary methods for generating electricity through solar power. One is the solar thermal way and another is the direct conversion of solar power into electricity using the photovoltaic effect. Total global operating capacity of solar PV has reached the 100 gigawatt (GW) milestones [17]. The most of the installed capacity is in Europe with significant additions in Asia in the latest year. As prices are going down, solar power is expanding to new markets, from Africa and the MENA region to Asia and to Latin America.

Interests in the community-owned and self-generation systems continued to grow in 2012, while the number and scale of large solar power projects also increased. The first commercial concentrated solar power plants were developed in the 1980s. The Mojave (located at California, United States) 354 megawatt (MW) SEGS commercial concentrated power (CSP) installation is currently the largest solar power plant in the world [19]. The Solnova solar power station (150 MW) and the Andasol solar power station (150 MW), both in Spain are other CSP based power plants. The 250+ MW

Agua caliente Solar Project in the United States and the 221 MW Charanka Solar Park in Gujarat, India, are the world's largest photovoltaic power stations [19].

Table 1.1 Electricity generation from solar power [18]

Year	Energy (TWh)	(%) of Total
2005	3.7	0.02%
2006	5.0	0.03%
2007	6.7	0.03%
2008	11.2	0.06%
2009	19.1	0.09%
2010	30.4	0.14%
2011	58.7	0.27%
2012	93.0	0.41%
2013	124.8	0.54%

In 2013, solar power supplied a very small portion of the world's energy and about 0.54% (Table 1) of the total energy and the total non-hydro- renewable energy share was 5.2% [17]. This small market share is due to the high manufacturing and installing cost of photovoltaics (PVs), but it has been predicted that in future decade fossil fuels based power conversion will lose their shares and renewable energy starts to penetrate at large scale. Reductions in the production costs and governmental subsidies are necessary if PVs are to compete with the fossil fuels.

1.4 Motivation behind the thesis

Extensive research in photovoltaic (PV) technologies has been carried out since discovery of the PV effect in silicon (Si) diodes in 1954 [20]. In recent decades, among many PV technologies, considerable efforts have been focused on the study of organic photovoltaic (OPV) devices due to their advantages of relative ease low temperature fabrication, with a good mechanical flexibility, and potential cost-effective production rate compared to crystalline Si and various inorganic thin film solar cells [21-24].

The efficiency and lifetime of organic solar cells are lower as compared to Silicon and various inorganic (CdTe, CIGS) thin film solar cells. Thus, investigation of new materials which could fulfil the multiple parameters for OPVs and the simple cost efficient production process must be carried out in order to lead to the commercialised organic solar cells in the near future. The research demonstrated in this thesis is to investigate different device architectures for enhancement of the power conversion efficiency (PCE). In this thesis, two kinds of approaches have been studied to increase the solar cell PCE and to understand fundamental principles why the PCE has been improved.

The first approach is to study the devices with inverted PV structures on ITO coated glasses. Enhancement in optical absorption and device efficiency of poly (3-hexylthiophene) (P3HT) and [6,6]-phenyl C61-butyric acid methylester (PCBM) based inverted organic solar cells has been achieved through the incorporation of Au nanoparticles (NPs) in the hole transport layer and the modification of active layer using the high boiling point material additive. Different noble metallic NPs and their positions with different concentrations, shapes and sizes have been reviewed [25-27]. It is usually recognized that metallic NPs embedded inside the active layer cannot improve the device performance due to the loss mechanism including non-irradiative decay and

charge carrier recombination that can lead to a decrease of charge carriers [28]. Although deposition of noble metallic NPs on ITO electrodes or poly (3,4-ethylenedioxythiophene): poly(styrenesulfonate) (PEDOT:PSS) HTL layers has been widely studied and some good enhancement in efficiency and fill factor has been achieved [27, 29], Compared with the incorporation of periodic nanostructures in the devices that leads to a narrow spectral enhancement, physical mechanism that received much attention is the randomly distributed NPs with varying shapes and sizes owing to that broadband light absorption enhancement can be realised [30]. The second approach is to study the inverted organic solar cells on flexible metal substrates using high conducting organic as the top anode.

Currently most of the reported inverted OPV devices have been fabricated on either glasses or transparent plastic substrates coated with ITO. Glasses are rigid, which is not compatible with roll-to-roll processing unlike highly flexible plastic substrates. However, the sheet resistance of ITO films obtained on flexible plastic substrates is relatively high, which decreases short circuit current and fill factor of the OPV devices. Therefore, metal substrate is a potential alternative of producing flexible OPV devices via the inverted structures [31, 32]. The opposite charge collection mechanism of the inverted configuration also allows the use of the high work function metal as the substrate and highly stable transparent materials as the hole collecting electrode, which can increase the overall stability of the devices.

Furthermore, compared to the plastics, metal has high conductivity and has the advantages of cost-effective, excellent mechanical flexibility and thermal stability in the industrial fabrication processes at the required elevated temperature. Several different techniques are used to characterise electrical, optical, structural and morphological properties of the devices. Multiple techniques allow for independent confirmation of the

results, and provide further understanding to optimise the devices and to achieve high PCE.

1.5 Thesis objectives

The overall aim of this study is to fabricate high-efficiency (~5.0%) inverted top illuminated organic solar cells on ITO coated glass and metal substrates using all solution processed techniques by the spin coating method. The fabricated thin films and devices will be characterised by various techniques. The optical properties of the deposited layers and devices will be studied by the UV-VIS/NIR spectrophotometer and the ellipsometry, respectively. X-ray diffraction and electrical impedance spectroscopy will be used to investigate the structural and the interlayer resistance of the deposited thin films, respectively. Morphologies of the thin films will be observed by the scanning electron microscope (SEM) and the atomic force microscope (AFM) to understand the mechanism for achieving high-efficiency devices. Current–voltage characteristics and external quantum efficiency of the produced devices will be studied to determine their photovoltaic properties.

The point wise objectives are described as follows:

1. To study the dispersion of zinc oxide nanoparticles in different solvents and the deposition of the sol-gel derived zinc oxide thin films below 200 °C on glass and metal substrates to obtain an optimised electron transport layer.

2. To study the deposition of the active layer based on the blend of the P3HT as a donor and the PCBM as an accepter and to optimise the parameters of the active layer for the best performance.

3. To study the incorporation of Au nanoparticles in the hole transport layers to enhance light absorption of the active layer through the plasmonic effect in organic solar cells.

4. To study the performance of organic photovoltaic devices based on the ITO coated glasses.

5. To study the fabrication methods and the performance of the top illuminated inverted organic solar cells on different flexible metal substrates using the high conducting organic material as the top anode.

1.6 References:

[1] C. J. Campbell and J. H. Laherrere, The end of cheap oil, Scientific American March, 60 (1998).

[2] C. B. Hatfield, Oil back on the global agenda. Permanent decline in global oil is virtually certain to begin within 20 years, Nature, 387 (1997) 121.

[3] T. Busch, V. H. Hoffmann, Emerging carbon constraints for corporate risk management, Ecological Economics, 62 (2007) 518.

[4] http://www.greens.org/s-r/11/11-08.html

[5] J. G. J. Olivier, G. J. Maenhout, M. Muntean, J. A. H. W. Peters,Trends in global CO2 emissions: 2013 Report.

[6] http://weatherdem.wordpress.com/2013/10/10/september-2013-co2-concentrations-393-31ppm/

[7] K. Oberrecht, The Effects of Rising Sea Levels, http://www.oregon.gov /dsl/SSNERR/docs/EFS/EFS39risesea.pdf

[8] G. P. Peters, R. M. Andrew, T. Boden, J. G. Canadell, P. Ciais, C. L. Quéré, G. Marland, M. R. Raupach, C. Wilson, The challenge to keep global warming below 2 °C, Nature Climate Change 3, (2013) 4-6.

[9] World Energy Outlook 2012-Executive Summary, http://www.worldenergyout look.org

[10] World Energy Needs and Nuclear Power - World Nuclear Association, www. world-nucler.org.

[11] "World Population Prospects: The 2012 Revision". Population Division of the Department of Economic and Social Affairs of the United Nations Secretariat. June 2013. Retrieved August 7, 2013.

[12] "World Population – Total Midyear Population for the World: 1950–2050". Census.gov., June 2012. Retrieved August 12, 2013.

[13] International Energy outlook 2013, Website: www.eia.gov

[14] World Energy Outlook 2013, Website: http://www.worldenergyoutlook.org

[15] From CIA 2005, http://www.mongabay.com/igapo/world statistics by area.

[16] http://en.wikipedia.org/wiki/Solar power.

[17] Renewables 2013, Global status report, Website: www.ren21.net

[18] Historical data workbook (2013 calender year).

[19] http://www.ghodawatenergy.com/Solar.

[20] D. M. Chapin, C. S. Fuller, G. L. Pearson, A new silicon p–n junction photocell for converting solar radiation into electrical power. J. Appl. Phys., 1954, 25, 676.

[21] C. J. Brabec, N. S. Sariciftci, J. C. Hummelen, Plastic solar cells. Adv. Funct. Mater., 11(2001) 15.

[22] K. M. Coakley, M. D. McGehee, Conjugated polymer photovoltaic cells. Chem. Mater., 16 (2004) 4533.

[23] S. K. Hau, H. L. Yip, A. K. Y. Jen, A review on the development of the inverted polymer solar cell architecture, Polym. Rev., 50 (4) (2010) 474.

[24] F. Zhang, X. Xu, W. Tang, J. Zhang, Z. Zhuo, J. Wang, J. Wang, Z. Xu, Y. Wang, Recent development of the inverted configuration organic solar cells, Sol. Energ. Mat. Sol. Cells, 95 (2011) 1785.

[25] D. Kozanoglu, D. H. Apaydin, A. Cirpan, E. N. Esenturk, Power conversion efficiency enhancement of organic solar cells by addition of gold nanostars, nanorods and nanospheres, Org. Electron., 14 (2013) 1720-1727.

[26] J. Pei, J. Tao, Y. Zhou, Q. Dong, Z. Liu, Z. Li, F. Chen, J. Zhang, W. Xu, W. Tian, Efficiency enhancement of polymer solar cells by incorporating a self-assembled layer of silver nanodisks, Sol. Energ. Mat. Sol. Cells, 95 (2011) 3281-3286.

[27] B. Gholamkhass, S. Holdcroft, Enhancing the durability of polymer solar cells using gold nano-dots, Sol. Energ. Mat. Sol. Cells, 95 (2011) 3106-3113.

[28] M. Xue, L. Li, B. J. T. de Villers, H. Shen, J. Zhu, Z. Yu, A. Z. Stieg, Q. Pei, B. J. Schwartz, K. L. Wang, Charge-carrier dynamics in hybrid plasmonic organic solar cells with Ag nanoparticles, Appl. Phys. Lett., 98 (2011) 253302.

[29] X. Chen, L. Zuo, W. Fu, Q. Yan, C.Fan, H.Chen, Insight into the efficiency enhancement of polymer solar cells by incorporating gold nanoparticles, Sol. Energ. Mat. Sol. Cells, 111 (2013) 1-8.

[30] H. A. Atwater, A. Polman, Plasmonics for improved photovoltaic devices, Nature Mater., 9 (2010) 205-213.

[31] V. Kumar, H. Wang, Selection of metal substrates for completely solution-processed invertedorganic photovoltaic devices, Sol. Energ. Mat. Sol. Cells, 113 (2013) 179-185.

[32] F. C. Chen, J. L. Wu, C. L. Lee, W. C. Huang, H. M. P. Chen, W. C. Chen, Flexible Polymer Photovoltaic Devices Prepared With Inverted Structures on Metal Foils, IEEE Electron Device Lett., 30 (2009) 727-729.

2.1 Introduction

The discovery of the PV effect can be traced back to 1839 when a French physicist A. E. Becquerel performed his pioneering studies in liquid electrolytes [1]. Smith and Adams made their first report on photoconductivity of selenium in 1873 and 1876, respectively [2,3]. After that, Albert Einstein explained the photoelectric effect in 1905 and received the Physics Nobel prize for it in 1921. Studies on electrical conducting organics started when Pochettino in 1906 [4] and Volmer in 1913 [5] observed photoconductivity in Anthracene. The potential use of organic materials as photoreceptors in imaging systems was recognized in the late 1950s and 1960s [6]. In 1954, the discovery of high electrical conductivity in perylene bromine attracted much scientific interests in organic semiconductors [7]. In the early 1960s it was discovered that many common dyes, such as methylene blue, had semiconducting properties [8]. In the later days these organic materials exhibited the PV effect.

The research on organic solar cells had started since Terenin et al. discovered the photovoltaic behaviour of chlorophyll in 1959 [9]. A maturity on studies of organic solar cells came when Tang et al. and Morel et al. demonstrated the first organic light emitting diode (OLED) and a photovoltaic device based on the Schottky junction of aluminium and a merocyanine dye that showed an overall power conversion efficiency of 1% in 1987 and 1978, respectively [10,11].

In the last decades organic based solar cells have attracted significantly scientific and industrial attention so that a massive research has been undertaken by many researchers all over the world [12-16]. Solar cell manufacturing companies like Heliatek has also invested heavily in this area for development of OSCs. Progress in organic solar cells

has been made tremendously in very recent years [17]. For P3HT:PCBM solar cells G. Li et al. in 2005 studied the growth conditions of the active layer with different annealing temperatures and reported an efficiency of 4.4% for the slowly dried active layer.

The performance of OSCs was further improved by the interfacial modification with a fullerene self-assembled monolayer that improved the coupling of the organic /inorganic interface through the process of the photo induced charge transfer. The PCE has increased more than 20% higher compared to the unmodified devices, giving the highest PCE of 4.9%. Kim et al. studied the efficient use of the thicker absorbing layers and reported a tremendous gain in the overall performance with the external power efficiency exceeding 6%. In 2010 Zhao et al. reported a 6.5 % efficient OSC with the indene-C_{60} bisadduct (ICBA) as an acceptor material. The obtained V_{oc} was 0.84 V because the LUMO energy level of ICBA is - 3.74 eV which is 0.17 eV higher than that of PCBM. In 2011 Price et al. reported a new organic incorporating benzo-dithiophene (BnDT) as the donor and either benzotriazole (HTAZ) or its fluorinated analog (FTAZ) as the acceptor. Both organics show an optical gap of 2.0 eV, which is even slightly bigger than that of P3HT (1.9 eV). The obtained efficiency with the 250 nm thick PBnDT-FTAZ active layer was 7.1 %. However, the 1 μm thick active layers are also able to achieve an efficiency of 6%.

Small et al. in 2012 demonstrated that the inverted organic solar cells based on a low-band gap organic with an alternating dithienogermole–thienopyrrolodione (PDTG–TPD) repeat unit received the certified power conversion efficiency of 7.4%. Recently, He et al. reported the inverted organic solar cells with a power conversion efficiency of 9.2 % where the active layer was sandwiched between the Al, Ag and PFN-modified ITO electrodes [18]. Currently, Heliatek, Dresden, Germany, reported that it has pushed

the conversion efficiency of its standard size tandem organic solar cells to 12%. According to Heliatek, the unique behaviour of organic solar cells at high temperatures and low light conditions makes it one of the most potentially promising candidates for satisfying the future energy needs [19].

In the organic photovoltaics, the bulk hetero-junction device configuration is achieved by a facile method of blending the n-type and p-type materials. The blending processing increases the number of interfaces between the donor and the acceptor, which provides more exciton dissociation/charge separation sites for the generation of more charge carriers. The separated charges then need to travel to the respective electrodes, i.e. holes to the anode and electrons to the cathode, to provide voltage and to be available for injection into the external circuit. The solar cell devices in the current thin film technologies are very expensive and high embedded energy, that gives a high energy payback period and hence results in the high capital cost [20]. Amongst various thin film techniques, the solution processed organic solar cells have one of the highest potentials for becoming a true low-cost technology since their production demands only the solution based deposition methods at low processing temperature [21-26]. The advantage of all solution processed routes makes it possible to produce PV structures continuously on plastics or the metal sheets by the roll-to-roll process and thus greatly to minimize the fabrication cost in the future [27-32].

2.2 Fundamental of organic photovoltaics

2.2.1 Organic semiconductor

The study of organic semiconductors is not new. In the early 20th century, the dark and photoconductivity of anthracene crystals have been studied [4,5]. The electroluminescence of organic semiconductors was discovered in 1960s [33]. The

successful synthesis of conjugated organics in 1970s [10] is an important milestone for organic semiconductors which was honoured with the Chemistry Nobel prize in 2000. Organic semiconductors are alternating single and double bond carbon based materials that present electrical semiconducting characteristics. Atoms inside an organic semiconductor molecule have the conjugated π-bond system with different bonding configurations as shown in Figure 2.1. The molecules of organic semiconductors are bonded by a weak van der Waals force that is opposite to the covalent structure of inorganic semiconductor materials. Macroscopically, the band structures of organic and inorganic semiconductors are relatively similar. The Highest Occupied Molecular Orbital (HOMO) and the Lowest Unoccupied Molecular Orbital (LUMO) in organic semiconductors are the corresponding valence band and the conduction band in inorganic semiconductors, respectively.

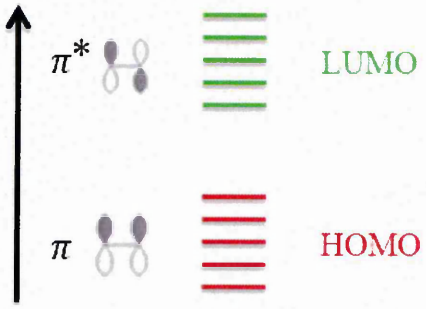

Figure 2.1 Bonding and antibonding interaction between HOMO and LUMO of an organic semiconductor [34].

The π-conjugated system of organic molecules is formed by the P_z-orbitals of sp2 hybridized carbon atom. The π-bonding is relatively weaker than that of the σ-bonding with the neighbour atoms [35]. The different energy levels of an organic semiconductor

correspond to the different hybridisation states of π-bonds (i.e. π and π*). The energy difference between HOMO and LUMO is known as the energy band gap (E_g).

When an electron is excited from HOMO to the LUMO of an organic semiconductor, the molecule itself is excited into the higher energy state, while in inorganic semiconductor the free electron will excite from the valence band to the conduction band. The charge transportation mechanisms of organic semiconductors are also different from inorganic semiconductors. The formation of photo excited excitons (bound electron-hole pairs) in molecular materials, rather than free electrons and holes, is a fundamental difference between solar cells based on organic semiconductors and the corresponding inorganic counterparts. The photo excited exciton separation and the charge transportation all occur within organic semiconductors [36], which leads to low mobility of organic semiconductors when compared with their inorganic counterparts.

The electron and hole mobility of small molecule organic semiconductors has reached to ~1 x 10^{-5} m^2 V^{-1} s^{-1} and ~ 1.5 x 10^{-3} m^2 V^{-1} s^{-1} [37-40], while silicon has much higher electron and hole mobility of up to ~0.1 x 10^{-2} m^2 V^{-1} s^{-1} and ~4.5 x 10^{-2} m^2 V^{-1} s^{-1}[41], respectively. The electron and hole mobility of the commonly studied P3HT:PCBM blend films is of the order of ~10^{-7}-10^{-8} m^2 V^{-1} s^{-1} [42]. As compared to inorganic semiconductors, the low electron and hole mobility of organic semiconductors is a major challenge and focused studies are needed towards new materials development in order to overcome these issues.

2.2.2 Polarons and polarons excitons

A polaron is a quasi-particle and considered as a "charge". Charge means an electron or a hole plus a distortion of the charge's surroundings. In 1933, Lev Landau first proposed the concept of polaron that is used to understand the electron interaction with

atoms in a solid material [43]. The associated charge creates lattice polarisations that decrease the electron mobility and increase the effective mass of electrons [44]. The polaron formation decreases the mobility of electrons in semiconductors. Organic materials are very sensitive to polaronic effects because of the conjugated system in organic semiconductors that exhibits massive electron- lattice coupling effects compared to the inorganic semiconductor. The strong electron-lattice coupling is responsible for the existence of the quasi-particles such as polarons and polaron excitons in the conjugated organic systems.

2.2.3 Operation of organic solar cells

Performance of organic solar cells can be characterised by considering the below four steps:

2.2.3.1 Exciton generation

In an organic semiconductor, an electron is excited from HOMO to the LUMO after the absorption of incident photon. The generated electron-hole pairs are bounded by the Coulomb force because of the lower dielectric constant of organic semiconductors [45]. The bound electron-hole pair is known as an exciton with a binding energy of 0.1-1.4 eV [46]. The photon absorption depends on the product of the absorption coefficient and the film thickness. However, it has been studied that the absorption coefficient of organic materials is high at $\sim 10^5$ cm^{-1} [47] and the thickness of the active layer are limited by the electrical conduction. Therefore, few hundred nanometers (mainly 100-200 nm) thick active layer should be enough to absorb the required incident light. The most studied material for organic solar cells is P3HT that has a band gap of ~1.9 eV while most of the semi-conducting organics have band gaps of ~2.0 eV [47]. The large

band gap is the main concern for organic solar cells, which limits the maximum absorption of incident photon to less than 30%.

2.2.3.2 Exciton diffusion and dissociation

The generated photo excited excitons need to be separated into free charges to generate electricity. For an efficient dissociation, Tang et al. demonstrated heterojunction structures in the form of bilayer solar cells [48] where two different organic materials make heterojunction as shown in Figure 2.2. The heterojunction has become a basis of organic photovoltaic devices. Out of these two different materials, one is called donor (D) and the second is acceptor (A). When an exciton is generated in the donor material, it drifts towards heterojunction. When the potential difference between the HOMO of donor material and the LUMO of the acceptor material is lower than the potential difference of the bound electron-hole pair, the exciton dissociates efficiently.

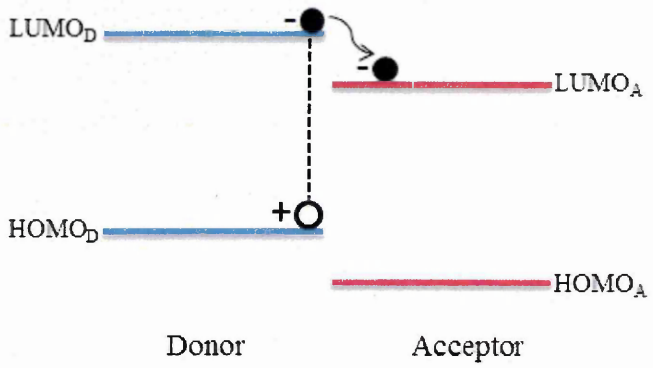

Figure 2.2 Donor and acceptor band alignment of a heterojunction

To achieve an efficient dissociation, the active layer thickness should be of the order of the exciton diffusion length (keeping the surface for absorption), because radiative recombination occurs at a time scale of ~ 1.0 ns [49]. Because the exciton diffusion

length is in the range of few tens of nanometers [50] in organic semiconductors, the phase separation between the donor and acceptor needs to be within the exciton diffusion length for the efficient charge dissociation. This process can be realised in the bulk heterojuuction organic solar cells.

2.2.3.3 Carrier Transport

The dissociated excitons generate electrons and holes, however, they still form charge pairs called "geminate pairs" that bound via the Coulomb force and need an internal electric field to separate them. The difference of the work function between the cathode and the anode can create a built-in electric field for their separation inside the solar cells. When carriers diffuse away from the heterojunction, a current is generated called "diffusion current". Due to applied external field across the semiconductor material, the charge carriers attain a certain drift velocity and this movement of the charge carriers constitutes a current known as "drift current".

After separation, the drift current and diffusion current motivate separated charges to transport towards respective electrodes [51]. Under the external bias, there is a change in the internal electric field that changes the drift current. The change in drift current encourages charges to move towards respective electrodes for collection. The concentration of electrons and holes is high nearby the heterojunction. This is also another mechanism to support charge transport. Both of the currents are dominants in different regimes. When the internal electric field is large, drift will dominate while diffusion dominates in the case of the zero internal electric field (with the external bias). The charge transport in organic solar cells is also limited by the low intrinsic mobility of organic materials, impurities (e.g. oxygen), and defects.

2.2.3.4 Charge collection at electrodes

To achieve maximum charge collection efficiency at the electrode, it is required that the transit time of charges drifting through the inter-electrode distance under the influence of an electric field is shorter than the life time of a charge carrier [52]. When the HOMO of donor and the LUMO of acceptor nearly match the corresponding electrodes' work function, the contacts are ohmic in nature and the difference between the donor HOMO and the acceptor LUMO represents the open circuit voltage (V_{oc}). For inverted organic solar cells on glasses, the indium tin oxide (ITO) thin film is the common material for cathode while high work function metals (e.g. Au) are used as anode. The interlayers (e.g. ZnO, TiOx, PEDOT:PSS, and MoOx) between the active layer and the electrodes can enhance the charge collection efficiency through a better alignment of the electrode work function with HOMO of the donor and LUMO of the acceptor [53-56]. The increased roughness of the interfacial area by changing the work function of electrodes creates a bigger area for more efficient charge collection.

2.2.4 Loss mechanism

Two key loss mechanisms of organic solar cells are geminate pair losses and bimolecular recombination losses [57]. After the exciton dissociation at heterojunction interface, the dissociated electron-hole pairs still remain bound at the interface due to the electron-hole Coulombic attraction called "geminate pair". In order to reach to the respective electrodes, the bound pair must therefore overcome this bound energy barrier. When the geminate pair does not dissociate completely they will recombine with other geminate pairs. After the complete dissociation of geminate pairs into free charges, there is also a probability of electron and hole collision and recombination before collected at their respective electrode, which is called bimolecular recombination loss.

Other loss mechanisms are due to low motility of electrons and holes in organic semiconductors and mobility mismatch that also limits the collection efficiency by the space charge recombination.

2.3 Types of organic solar cells

2.3.1 Single layer solar cells

Single layer organic solar cells are the simplest structure of organic solar cells. These types of solar cells are fabricated by sandwiching a layer of the conjugated organic between two metallic (or conducting) electrodes. The basic structure of the device is shown in Figure 2.3. The device consists of an organic active layer sandwiched between a high-work-function indium tin oxide (ITO) electrode and a low-work-function aluminium (Al) electrode. The main drawback for this type of structure is its small thickness of the active layer at approximately ~10-20 nm, therefore only a small portion of the visible light is absorbed by the solar cell for the power conversion. Furthermore, the electric field generated between two electrodes is insufficient to dissociate the excitons. Photo induced electrons and holes will recombine before reaching the electrodes. The reported power conversion efficiency was in the range of only 10^{-3} to 10^{-2} % [58-59].

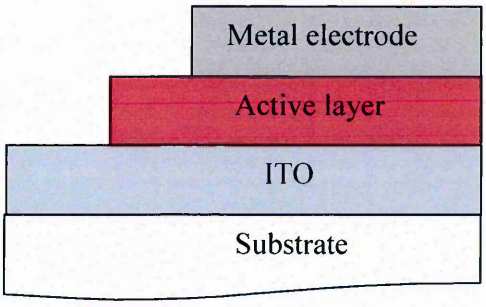

Figure 2.3 Schematic diagram of a single layer organic solar cells

2.3.2 Bi-layer solar cells

A bilayer solar cell includes two different organic layers sandwiched between the electron collecting layer and the hole collecting layer followed by the conducting electrodes. Figure 2.4 shows the basic structure of the device. This type of solar cell is also called as the planar-donor-acceptor-hetero junction solar cell. The donor and acceptor planar interface acts the location for the exciton dissociation. The electron collecting layer and the hole collecting layer modify the work function of the respective electrodes to form the ohmic contacts. Acceptors have higher electron affinity and ionisation potentials than the donors. Incident light is absorbed by the donor layer and electrons in the donor material are excited from HOMO level to LUMO level, forming excitons. If an acceptor molecule is in proximity of this exciton, the exciton can transfer to the LUMO of the acceptor and then be dissociated at the interface.

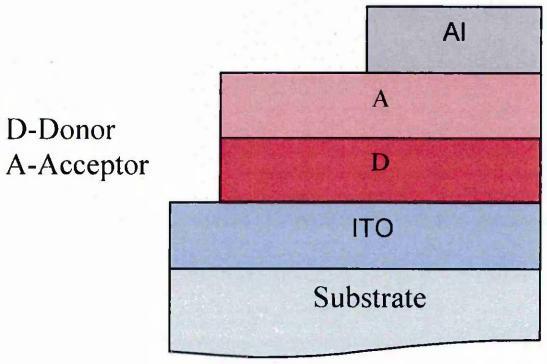

Figure 2.4 Schematic diagram of Bi- layer organic solar cells

The main advantage of the bi-layer structure is in minimisation of the recombination losses. The disadvantage of the bi-layer structure is the short exciton diffusion length that limits the thickness of the donor and acceptor layers and provides small interfacial area for excitons dissociation. In 1986, Tang reported a power conversion efficiency of ~1% for a bi-layer structure device [48].

2.3.3 Bulk hetero-junction (BHJ) solar cells

In this type of photovoltaic structures, the donor and acceptor materials are mixed together to form an organic blend. A facile method of blending the donor and acceptor materials achieves the bulk hetero-junction device configuration. The blending processing increases the number of interfaces between the donor and the acceptor, which provides more exciton dissociation/charge separation sites for the generation of more charge carriers. The main challenge in fabrication of such type of solar cells is to obtain the interpenetrating and bi-continuous network between the acceptor and the donor phases.

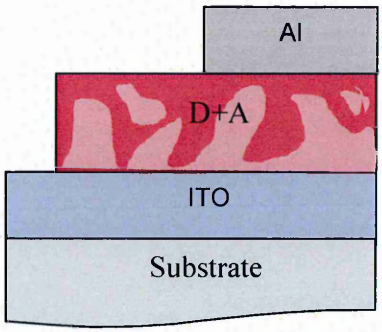

Figure 2.5 Schematic of bulk heterojunction organic solar cells

If the phase separation within the film is the same as the diffusion length of excitons (~10-20 nm), most of the generated excitons can reach the donor and acceptor interface and a nearly unity internal quantum efficiency can be realised [60]. Figure 2.5 shows a basic structure of this type of PV device. Electrodes have to be chosen so that the work function of one electrode is close to the LUMO level of the acceptor and the other electrode forms good contact with the HOMO level of the donor material. The maximum voltage obtained for this type of device is the energy difference of LUMO of the acceptor and HOMO of the donor. Various combinations of the donor and the

acceptor materials have been used as a sandwiched layer in the bulk heterojunction solar cells. One of the most significant combinations of this structural device is based on P3HT as a donor and PCBM as an acceptor. The achieved maximum PCE for the P3HT: PCBM based organic solar cells has been reached over 5.0% [61].

2.3.4 Tandem solar cells

To overcome the limit of weak absorption and narrow absorption range of organic solar cells from the active layer, the well-known concept of tandem solar cells has been proposed for the first time in 1990 [62]. The tandem structure is a series stacking of solar cells that absorb light over a wide range and produce higher V_{oc} than other types of solar cells. The tandem organic solar cell structure comprised of two different devices stacked on top of each other (Figure 2.6) and the active layer of each stack is based on a blend of the donor-acceptor materials.

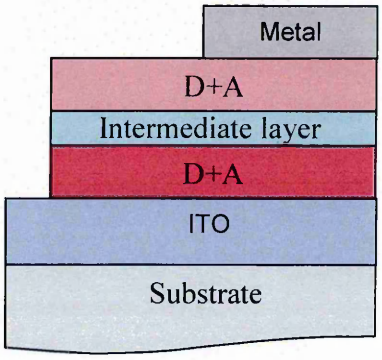

Figure 2.6 Schematic of tandem organic solar cells

The top and the bottom cell can be connected in either series (2-terminal structure) or parallel (3-terminal structure) [63,64]. Light that is not absorbed in the bottom cell can be further absorbed by the top solar cell. In tandem devices the use of different band gap materials reduces the thermal losses. Out of all these advantages, the tandem organic solar cells suffer difficulty in matching their sub cells. Current matching between the

top and bottom has to be achieved to overcome the charge accumulation on subs cells and extra care is needed in fabrication to prevent the damage of successive layers. Recently, the power conversion efficiency of standard tandem organic solar cells has been reached up to 12.0% as reported by Heliatek [19].

2.4 Inverted organic BHJ solar cells

2.4.1 Device structures

The solution processed OSCs have one of the highest potentials due to the possibility of low cost fabrication over large areas at low processing temperature. The majority of organic solar cells are fabricated in the conventional configuration; i.e. substrate/transparent anode/hole collector/active layer/electron collector/cathode shown in Figure 2.7a. The transparent ITO thin film is used as the hole collecting electrode that is able to let sunlight pass through. The conducting organic of PEDOT:PSS is then deposited onto the ITO thin film to smooth its surface and works as a hole transport layer. The photo active layer of organic solar cells is situated between the hole-transporting layer (PEDOT:PSS) and the electron transport layer (ETL). The ETL is used to collect electrons and is connected to the low-work-function metal electrode (cathode) [65]. Metals with the low work function are not very stable as the top electrodes due to their sensitivity to oxygen and moisture in air. In order to protect the top electrode, bi-layered metals have been used as the composite top electrode [66]. However, the top metal electrode usually requires to be deposited at high vacuum instrument in the conventional configuration for fabrication of solar cells, which increases the manufacturing cost.

Compared with the conventional one, the inverted type of solar cell where the nature of charge collection is reversed was proposed as a good device alternative [67]; i.e.

substrate (glasses, plastics or Metals)/cathode contact/electron collector/active layer/hole collector/anode contact shown in Figure 2.7b and c. This type of device configuration has recently gained considerable attention due to its advantages of better device stability and potential low-cost processing compared to the conventional configuration. The inverted configuration can be further classified as bottom illuminated in Figure 2.7b or top illuminated in Figure 2.7c according to the direction of the incoming light illumination to the device. The top illuminated configuration utilizes a reflective buried bottom electrode and a transparent top electrode whereas the bottom-illuminated-type inverted architecture configuration uses a reflective and high-work-function electrode as the top hole-collecting contact and a transparent conducting electrode at the bottom for the collection of electrons.

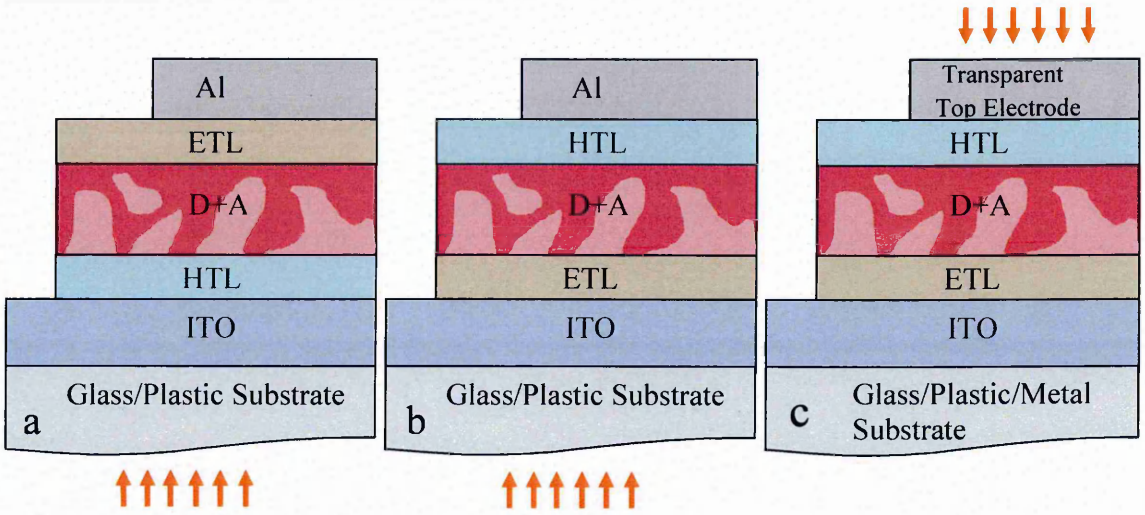

Figure 2.7 Schematic of the bulk hetero-junction device structures; (a) conventional (b) inverted bottom illuminated (c) inverted top illuminated

demonstrated in literatures, there have been far fewer studies focused on the top-illuminated-type inverted solar cells where the requirements are that the top electrode needs to be transparent or semi-transparent so that light can reach the active layer. However, it is always a big challenge in finding a suitable transparent conducting

material as the top electrode for the top illuminated devices. As mentioned previously, the top-illuminated inverted configuration of organic solar cells has the advantage of stable devices because the low work function metal (e.g. aluminium) as the cathode and the high work function metal (ITO, Ag, Au and modified PEDOT:PSS) as the anode can effectively avoid the device degradation that is induced by the environment and contamination of the metal cathode. Furthermore, the performance of OSCs is closely affected by the blends of n-type and p-type materials (e.g. P3HT:PCBM). In normal configuration OSCs, the blends of P3HT:PCBM are usually inhomogeneously distributed due to the vertical phase separation [68] that is attributed to the surface energy difference between the donor and acceptor components and their interactions with the substrates. This inhomogeneous distribution of the donor and acceptor components significantly affects normal configuration OSCs performance and makes the inverted configuration OSCs as a promising choice.

Hence, the inverted configurations OSCs have a chance to be one of the best candidates in the development of novel organic photovoltaics to meet the requirements for applications including high efficiency, stability, low-cost, and high-speed production. Very recently, the inverted device configuration has also been investigated as a suitable configuration tailoring for the solution processing, which allows various cell layers to be deposited onto the flexible substrates and shows very promising for the scale-up production via industrial roll-to-roll fabrication [69,70].

2.4.2 Selection of substrates

The advantage of all solution processed routes makes it possible to produce PV structures continuously on different substrates and thus greatly to minimize the fabrication cost in the future. As discussed above, the inverted structure has many

advantages over the conventional structures. The top illuminated inverted organic solar cells structure can be produced on a flexible substrate; e.g. metal foils and plastics. According to the literatures, up to now only a few researchers have used the metal substrate for the fabrication of organic solar cells and demonstrated some promising results with different substrate structures [27-32]. The top illuminated inverted configuration was also manufactured onto a flexible polymer substrate [71,72]. For the fabrication of top illuminated inverted organic solar cell structures, most of the researchers used the metal grid as the top contact layer. Jianyong el al. presented a laminated organic light emitting diode (OLED) using the glass as the substrate and ITO coated polyethylene tere-phthalate (PET) as a laminated electrode [73]. In this thesis, ITO coated glasses and different metal substrates namely: stainless steel (SS), titanium coated steel (Ti-S), chromium coated aluminium (Cr-Al) and aluminium (Al) have been chosen as the substrates for inverted solar cell devices.

2.4.3 Working principle of BHJ solar cells

In organic solar cells, absorption of photon leads to the creation of bound electron and hole pairs (excitons) rather than free-photo induced charge carriers. These excitons dissociated at the donor-acceptor interface under the influence of a strong electric field. The separated charges then need to travel to the respective electrodes, holes to the anode and electron to the cathode, to provide voltage and be available for injection into an external circuit. In summary, the overall operation of a good organic solar cell follows the below four steps as also illustrated in Figure 2.8.

(1) Photo induced exciton generation

(2) Exciton diffusion at the donor-acceptor interface

(3) Exciton dissociation and the formation of geminate pairs

(4) Charge carrier transport and collection

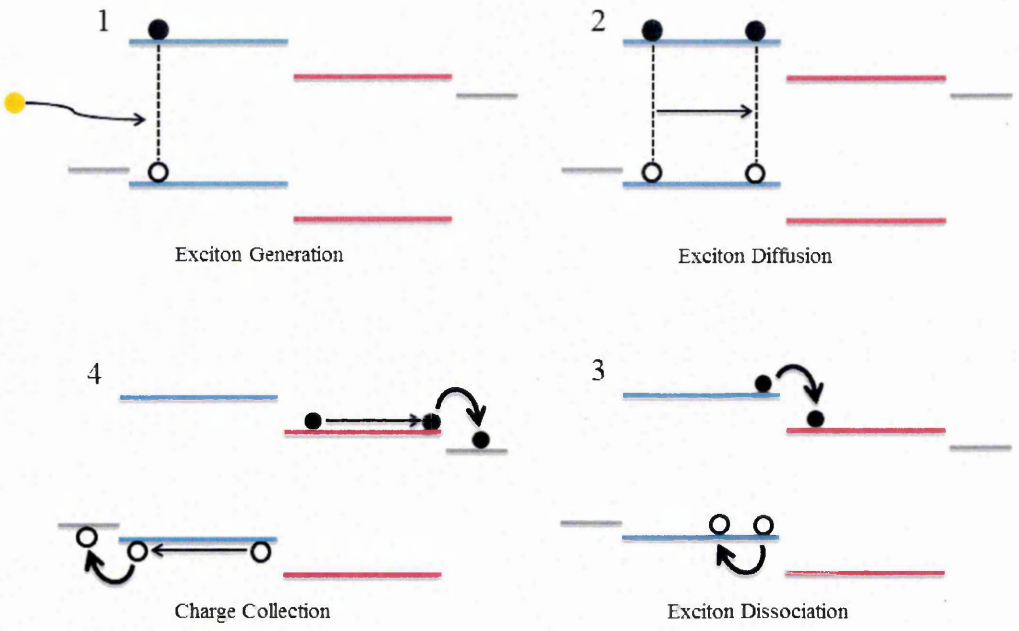

Figure 2.8 Schematic of working principle of organic solar cells [34]

2.4.4 Current-voltage characterisation

Current-voltage (I-V) measurement of organic solar cells are usually carried out under AM 1.5 solar spectrum with an intensity of 100 mW/cm^2. The magnitude of current flow depends on the biasing voltage. When the applied bias voltage (i) is less than zero, the device is operated in the reverse bias, which enhances the internal electric field or built-in electric field. This operation enhances the exciton dissociation efficiency and the separated charge carriers drift towards the respective electrodes those results in a large photo current. For the zero bias (ii), the built-in electric field due to the work function difference between the electrodes drifts the separated charges towards the electrodes. The current flow in the device under zero bias condition is called the short circuit current (I_{sc}). When the bias voltage increases in the positive direction, the built in electric field opposes by the positive bias voltage that can reduce the magnitude of the output current. In this case, a point came where (iii) the applied field is equal to the built

in electric field and the applied voltage is called "open circuit voltage" (V_{oc}). At this point, the dominated current is due to the diffusion current. When the external bias is higher (iv) than V_{oc} (forward bias), the applied field is higher than that of the built in field. The excess value of the applied field reverses the potential gradient and tunnelling is the mechanism for the large positive current.

2.4.5 Primary challenges limiting device efficiency

The performance of organic photovoltaic is limited by materials and fabrication challenges. The first key issue is the low power conversion efficiency between light absorption and exciton diffusion. The efficiency of photon absorption is not uniform across the solar spectrum because the active layers do not efficiently harness the red and infrared region photons of the solar spectrum. Except intrinsic properties of materials, the limited thickness of the active layer is also a barrier to overcome these issues. As we have discussed above, the diffusion length of excitons within organic materials is only few tens of nanometers and the timescale of the charge transfer process is much shorter, being of the order of ~45 fs [52].

If the active layer thickness increased, photo induced excitons need to travel further to get dissociated that increases the possibility of radiative recombination of excitons, occurs at a timescale ~1 ns [49]. The second issue is that the V_{oc} of organic solar cells is relatively low and is one of the reasons for high efficiency loss. The reason for low Voc is due to the recombination of separated charges at the donor-acceptor interface [74]. The exciton dissociation followed the formation of geminate pairs and the efficient separation of geminate pairs is required for high V_{oc} organic photovoltaic device. The third factor is the fill factors (FF) of the organic photovoltaic devices that need to be increased comparable to their inorganic counterparts. Typically, organic solar cells have

lower FF compared with the conventional p-n junctions. This is due to high series resistance and lower mobility of charge carriers in organic thin films that increase the recombination rate [75,76].

2.4.6 Potential routes to enhance the device performance

The large band gap of organic semiconductors is commonly the key concern for small absorption range which limits the light absorption efficiency of longer wavelength photon. It has been reported that ~77% of solar light will be absorbed by a HOMO-LUMO difference of 1.1 eV [50]. There are also many other concerns as described in section 2.4.5 for the commercial use of OSCs. Therefore, potential routes that are considered for enhancing the performance of OSCs can be as follows:

(1) to improve the light harvesting;

(2) to improve the charge carrier generation;

(3) to improve the charge transport;

(4) to improve the stability of devices;

In the past decade much attention has been paid to the conducting polymer and PCBM based devices. One of the most studied materials is P3HT with a band gap of ~1.9 eV [47]. For P3HT active materials, a large portion of energy cannot be utilised due to lack of light absorption in the long wavelength region (>700 nm). Therefore (1) broad absorption bands and appropriate energy level are the first requirement. In order to utilize more sunlight, the absorption edge of the conducting organic should be extended to the near-infrared region of the optical spectrum. Therefore, the tuning of the band gap for organic photovoltaic materials is a way for enhancement of the absorption efficiency. Since the band gap and the molecular energy levels of a conjugated organic are closely related to the molecular weight, molecular configuration and conformation,

intermolecular interaction, effective conjugation length, and so on. Therefore, synthesis of low band gap polymer materials needs to be designed on these parameters.

As well known, the thin active layer limits the light absorption efficiency, and thereby the power conversion efficiency of the OSCs. Therefore, the use of light trapping techniques such as folded configuration [77], diffraction grating [78], photonic crystal [79], and surface plasmon resonance (SPR) [80] are another way to improve the absorption efficiency (1) and charge carrier generation (2). The morphologies of the active layer also affect the generation and the transportation (3) of the charge carriers. Different approaches including annealing temperatures [81], post annealing [82], various growth processes (slow or fast) [75,83], solvent annealing [84], additives in the active blend [85] are further routes to improve the generation and the transportation of charge carriers.

The improvement in the mobility (3) of organic semiconductors is another route to enhance charge transportation. The organic semiconductors have much lower mobility than inorganic semiconductors because in organic semiconductors charges are localized due to their low dielectric constant. For the efficient charge transportation, both inter- and intra-molecular charge transfer properties of organic semiconductor are important. In organic semiconductors, molecules are stacked together by weak forces, like van der Waals force, and the charges transported through the hopping mode, so the enhanced intermolecular stacking (compact stacking) might be an effective way to facilitate the inter-molecular charge transport. Therefore, how to improve the hole and electron mobility is one of the critical objectives that needs to be resolved. Besides (4) the absorption band, molecular energy levels (HOMO and LUMO), mobility, other issues like solubility in different solvents and chemical stability, should also be considered in

the molecular design for development of an ideal photovoltaic material with the better stability.

In addition to the above mentioned, the use of fullerene derivative acceptors including Indene-fullerene Monoadduct (ICMA), Indene-fullerene Bisadduct (ICBA), PC84BM and endohedral fullerenes other than $PC_{60}BM$ is also a way to enhance the performance of the OSC devices [86-89]. LUMO levels of ICMA and ICBA are -3.86 and -3.74 eV respectively [86], which is higher than that of PCBM. Therefore, ICMA:P3HT and ICBA:P3HT based devices showed higher V_{oc} than that of P3HT:PCBM based devices [86]. ICMA has the poor solubility in CB or DCB, which limits the photovoltaic performance of the devices; ICBA can be easily dissolved into CB or DCB, and its LUMO level was higher than that of ICMA and PCBM and a V_{oc} of 0.84 V can be obtained without changing other parameters like J_{sc} and FF.

2.4.7 Physics of plasmonic effects

The typical thickness of the active layer limits its absorption efficiency and hence the power conversion efficiency of the devices. The tunable resonance plus unique near field concentration of plasmon makes it enabling technique for light manipulation and management for enhancement of optical absorption in the active layer [80,90]. Among the metals that can support plasmonic resonances (PRs) modes, noble metals (Au, Ag and Cu) present resonances in the visible or near infrared (IR) region of the electromagnetic spectrum. For the excited plasmons, the surface plasmon resonance (SPR) and localised plasmon resonance (LPR) are denoted for planer surfaces and nanometer sized metallic structures, respectively [91,92]. These novel plasmonic nanostructures significantly improve the absorption efficiency of the active layer and have emerged as an expanding area to increase the performance of OSC devices. There

are three principles to enhance the performance of thin film solar cells by altering plasmonic nano structures. The first way is to create the surface plasmon resonance by metallic gratings fabricated on the top or bottom of the active layer [93-95]. The second approach is to generate the local plasmon resonance by metallic nanostructures incorporated into or near to the active layer [96-101] and the third method is to achieve the scattering from metal nanoparticles at the surface of the solar cells where multiple and high-angle scattering increases the effective optical path length in the cell [102-104]. Figure 2.9 shows the schematic diagram of these mechanisms.

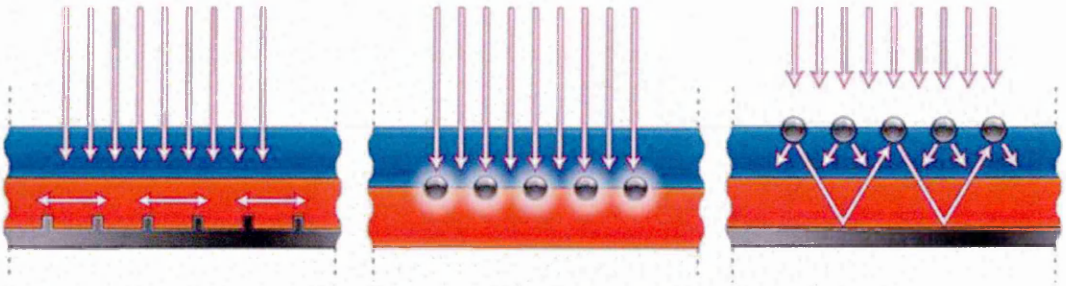

Figure 2.9 Different plasmonic light trapping techniques, (a) Surface plasmon resonance by metallic gratings and propagation of photonic modes will be in the plane of the semiconductor, (b) localised surface plasmon resonance by metallic nanostructures incorporated into or near to the active layer, (c) scattering of light by metallic nanostructures [80].

The incorporation of plasmonic nanostructures allows us to enhance light absorption by scattering of incident light into waveguide mode in the active layer while the effect of the localised surface plasmon resonance (LSPR) is achieved by mixing the plasmonic nano-particles with different layers of OSC devices. The plasmonic nanoparticles then act as an effective 'antenna' for the incident sunlight that stores the incident energy in a localized surface plasmon mode (Figure 2.10). The surface plasmon resonance (SPR) of

metallic nano-structured electrodes is another effective way to enhance optical absorption of the active layer by increasing the field near to the dielectric/metal interface. The incorporation of metallic nanostructures into the active layer, the hole transport layer, and the electron transport layer has their potential to improve the absorption and hence the efficiency of the organic solar cells. Incorporation of metallic

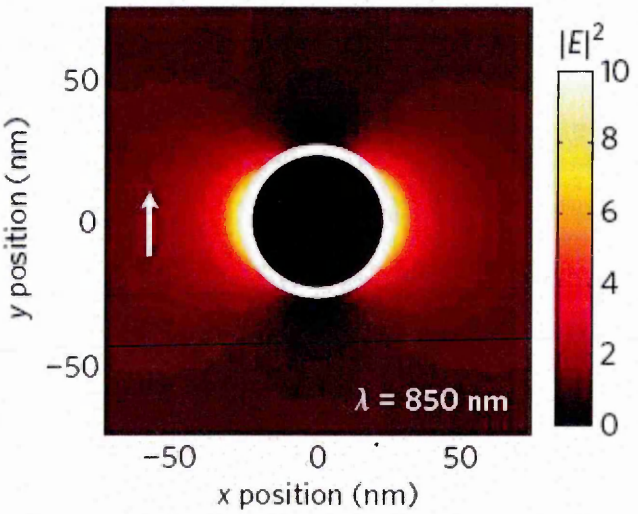

Figure 2.10 Intensity enhancement around a 25-nm-diameter Au particle embedded in a medium with index n = 1.5 (plasmon resonance peak at 500 nm). Light with a wavelength λ = 850 nm is incident with a polarization indicated by the vertical arrow [105].

nanostructures into the PEDOT:PSS hole transport layer is the simple approach of taking advantage of plasmonic effects. In this case, light-trapping can be achieved by scattering incident light at wide angles into the active layer. It is also possible for this scattered light to excite surface plasmon polaritons (SPPs) and other photonic modes into the active layer. However, the degree of contribution of LSPR effects is still unclear.

2.4.7.1 Incorporation of plasmonic nanostructures into PEDOT:PSS HTLs

It has shown that the incorporation of ~18 nm Au NPs into the PEDOT:PSS layer of the P3HT:PCBM based OSC leads to an efficiency enhancement of 13% [106]. Improvements originate from the increase in FF and J_{sc} from 58.0% to 62.0% and 8.50 to 9.40 mA/cm^2, respectively. Furthermore, the simultaneous incorporation of Au NPs into the PEDPT:PSS layer and the active layers, respectively, leading to an improvement of PCE by ~22% compared to the control device [107]. Figure 2.11 shows the absorption spectra of the active layers where device A has no NP doping, while devices B, C, and D have NPs doped into the PEDOT:PSS, the P3HT:PCBM, and both of the layers, respectively. The incorporation of NPs into the active layer and both the PEDOT:PSS and active layers shows an enhanced absorption.

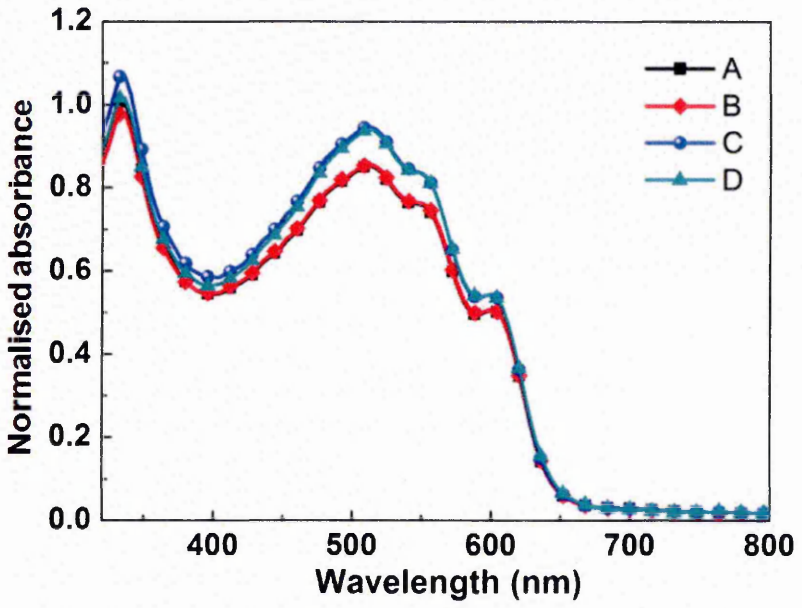

Figure 2.11 Absorbance of the active layer for different NP doping structures, (A) no NPs, (B) NPs in PEDOT:PSS only, (C) NPs in P3HT:PCBM only, (D) NPs in both P3HT:PCBM and PEDOT:PSS [107].

This is good agreement with our reported result [101] where we incorporated the Au NPs into the PEDOT:PSS layer using the plasma assisted physical vapour deposition method and claimed that the NPs can also reach the surface of the P3HT:PCBM active layer or maybe be slightly embedded into the active layer because the thickness of the nanocavities formed in the PEDOT:PSS layer is within the range of several nanometers. As the NPs reaches the active layer, the strong near field around the embedded Au NPs due to the localized surface plasmon resonance (LSPR) distributes laterally along the P3HT:PCBM active layer. There are many plasmonic nanostructures embedded in the PEDOT:PSS HTL of OSCs that have been reported [108]. Another study reported a mono-dispersed octahedral 45 nm Au NPs were blended into the PEDOT:PPS layer [109]. In this study, an efficiency enhancement of 19% was observed due to the LSPR absorption enhancement and the LSPR induced reduction of the exciton lifetime that facilitated the charge transfer processes.

The size effect of chemically synthesized Au nanospheres (NSs) embedded in PEDOT:PSS layer has also been investigated [110]. It was found that the efficiency enhancement strongly depended on the sizes of NPs. Furthermore, Au nanostructures of various sizes and shapes (nanospheres (NSs) and nanorods (NRs)) were mixed with the PEDOT:PSS buffer layer [111] for investigation. Since NSs and NRs exhibited different absorption bands, the presence of a combination of NSs and NRs enhanced absorption as a result of LSPR and scattering effects, leading to the increased efficiency by 24.0% compared to that of the reference devices.

J. Yang et. al. reported that Au NPs were successfully incorporated into the PEDOT:PSS film, [112] which was used as the interconnecting layer for connecting two sub-cells in an inverted tandem OSC device. The addition of Au NPs improved both the top and bottom sub cells' efficiency simultaneously via the LSPR enhancement to their

optical absorption. An efficiency enhancement of 20% was achieved. Plasmonic effects of the size-controlled silver nanoparticles (Ag NPs, diameter: 10-100 nm) that were incorporated into the PEDOT:PSS layer has also been studied [113]. Because electrical conductivity of the PEDOT:PSS film was unchanged after the incorporation of Ag NPs, the enhanced performance was only due to the optical effect. The PCE increased from 6.4% to 7.6% in poly[N-9-hepta-decanyl-2,7-carbazolealt- 5,5-(4,7-di-2-thienyl-2,1,3-benzothiadiazole)] (PCDTBT):[6,6]-phenyl C71-butyric acid methyl ester (PC70BM) based-OSCs and from 7.9% to 8.6% in polythieno [3,4-b] thiophene/ benzodithiophene (PTB7):PC70BM based-OSCs respectively upon embedding the Ag NPs into the PEDOT:PSS layer.

Mahmoud et al. studied the performance of the P3HT:PCBM solar cells after the incorporation of Au nanorods (Au NRs) into the PEDOTPSS layer [114]. The resulting devices showed a significant enhancement of 21.3% in the power conversion efficiency and a 13.0% enlargement in J_{sc}. This enhancement was attributed to the localized transverse and longitudinal plasmon resonance modes in the metallic nanostructures that increased the light absorption to the active layer. Incorporation of metallic nanostructures also induced morphological and/or chemical changes in the PEDOT:PSS layer [115]. Such morphological and/or chemical effects may contribute to the overall performance of OSCs when incorporating NPs into or in contact with the PEDOT:PSS layer.

2.4.7.2 Incorporation of plasmonic nanostructures into photoactive layers

Dispersion of metallic NPs into the photoactive layers of OSC devices can also enhance the optical absorption due to the excitation of LSPR modes when less than 10 nm NPs are used. Kim and Carroll et al. reported the addition of small amounts of Au and Ag

NPs into the photoactive layer [116]. NPs with a diameter of 5–6 nm were stabilised with a ligand shell of dodecylamine and reported the enhancement of more than 70% in PCE that was mainly attributed to the introduction of the dopant states in the active layer. The enhancement of light absorption due to the scattering was reported to be a minor effect. Because the presence of the surfactant decreased the plasmonic improvement effect due to non-radiative energy transfer between the NPs and the active layer. M. Xue et. al. revealed that the dispersion of chemically synthesized Ag NPs in the active layer enhanced the local absorption and also increased the carrier mobility [117]. However, the overall PCE was not improved owing to the increased carrier recombination at Ag NPs that acted as traps.

The effect of poly (ethylene glycol) and dodecylamine capped Au NPs have also been investigated by M. Xue and K. Topp et al. It has been shown that the LSPR introduced by the metallic NPs enhanced the light absorption in the active layer. However, the inferior electrical properties of NPs-based blends compared to the NPs-free ones gave rise to the reduced overall performance [118]. In order to prevent NPs acting as traps, the insulating material capped NPs were recommended [119]. Nevertheless, the plasmonic efficiency and thus absorption enhancement declined with the increased thickness of the insulating coating [120].

Thus, the use of bare, uncoated NPs can be a solution to mitigate the proposed adverse effect of the capped NPs [121]. For this purpose, surfactant and passivation free NPs have been used as additives in the active layer of the OSC devices. G. Spyropoulos et al. studied the incorporation of surfactant-free Au NPs in the active layer that significantly enhanced the device performance by 40% (Figure 2.12 a) due to LSPR and the scattering effects of Au NPs in the active layer [121]. The enhancement in incident photon to charge carrier efficiency (IPCE) in Figure 2.12 (b) was also found to comply

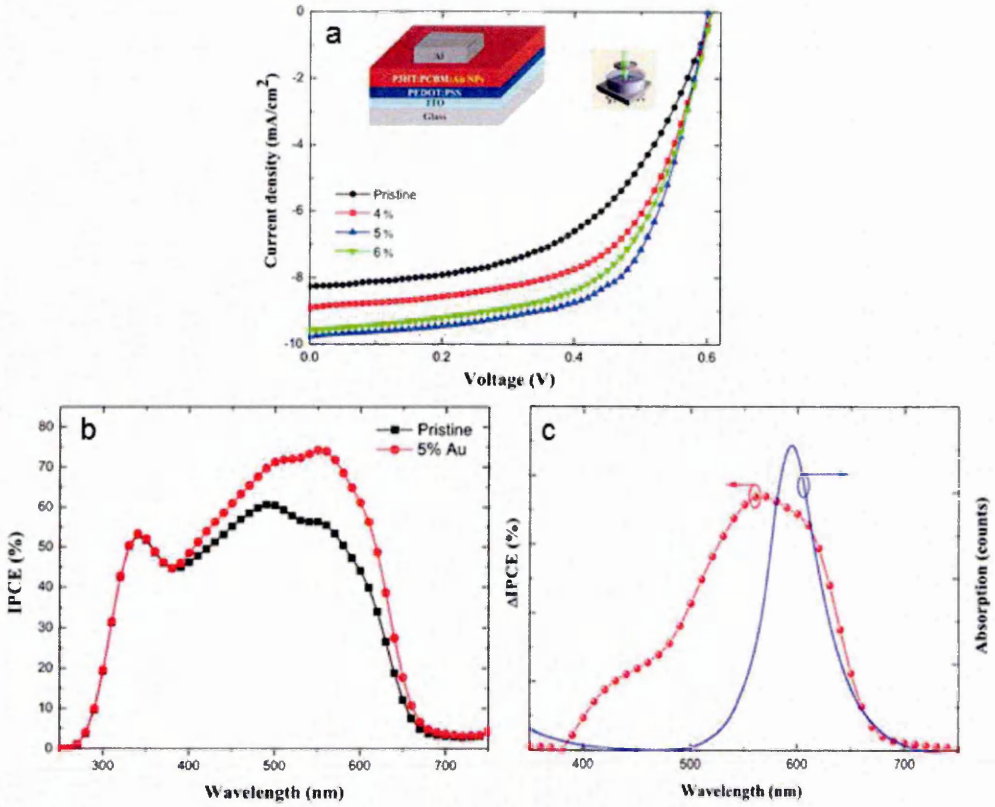

Figure 2.12 (a) J–V characteristics of the OSC devices with Au NPs embedded in the photoactive layer. (b) Corresponding IPCE curves of these OSC devices. (c) Comparison between the curve of the increase in IPCE (ΔIPCE) after incorporating Au NPs and the calculated extinction spectrum of the Au NPs in the P3HT:PCBM medium [121].

with the theoretically predicted extinction spectra of Au NPs (Figure 2.12 c), suggesting that LSPR effects were primarily responsible for the efficiency enhancement. Therefore, the incorporation of surfactant free NPs seems to be an effective way to enhance the optical absorption and the exciton dissociation to the organic active layers. The incorporation of 70 nm octahedral Au NPs and 40 nm Ag NPs clusters in the P3HT:PC70BM and PCDTBT:PC70BM photoactive layer has also been studied by Wang et al. For the Au NPs-incorporated P3HT/PC70BM devices, the PCE increased

from 3.54% to 4.36% [122], while for Ag NPs-based PCDTBT/PC70BM devices the enhancement was 6.30% to 7.11% [123], respectively. In case of Au NPs, the efficiency enhancement was attributed to the improved light absorption due to scattering from NPs LSPR modes. In a different way, the efficiency enhancement of Ag NPs based devices was due to the improved charge transport within the active layer. The shapes of the NPs also influence the performance of plasmonic OSC devices. A comparison study between the Ag NPs and NWs was performed by C. H. Kim et al. Compared to the reference device (3.31%), the efficiency of Ag NPs based OSC device was 3.56%, while the OSC device composed of Ag NWs exhibited a PCE of 3.91%. The enhancement of metallic NWs was higher than that of NPs due to the improved electron transport that was exhibited by the respective devices [124].

D. H. Wang et.al compared Ag NPs with Ag nano plates as additives in the P3HT-$PC_{71}BM$ OSC devices. Results showed an efficiency enhancement of 3.2 to 4.0% for NPs and 3.2 to 4.4% for nano plates, respectively. These results attributed to the fact that the shape of a metal NP is an important factor in maximising the light trapping [125]. Li et al. compared the incorporation of Ag NPs with nano prism into the P3HT:PCBM active layer [126]. The incorporation different shaped nano structures that exhibited the varied LSPR and scattering region into the active layer resulted in the broadband absorption enhancement. The enhancement in the photocurrent for Ag nano particles, Ag nano prisms, and the blended Ag NPs plus Ag nano prisms was approximately 9.0%, 10.1%, and 17.91%, respectively, compared to the optimised control OSC sample. Therefore, OSC devices with the Ag NPs showed a high PCE of 4.3%. The reported results anticipated that the mixing of nanostructures in OSCs can attribute to the broadband light absorption enhancement due to the simultaneous excitation of versatile plasmonic resonances of different nanostructures.

2.4.7.3 Incorporation of plasmonic nanostructures at the interfaces

Metal NPs are also incorporated in the interfaces between the blend and ITO or the PEDOT:PSS layer in the OSC devices. In this way, it is possible to excite both LSPRs at their vicinity and SPPs along the intervening planar surfaces. Therefore, the incorporation of metallic NPs at the interfaces enhances the performance in two ways; the first route is to enhance light absorption of the active layer and the second is to improve the efficient charge collection at the corresponding interface.

The first report came in 1995 when Stenzel et al. studied the incorporation of Ag, Au and Cu nano clusters at the ITO-CuPc (copper phthalocyanine) interface. The incorporation of metal nano clusters at the ITO-CuPc interface led to a significant enhancement in photocurrent which was a factor of 1.3 for Ag clusters, 2.2 for Au clusters, and 2.7 for Cu clusters separately [127]. The enhancements were assigned to both local plasmon excitation and inter band transitions in the metal clusters. However, Westphalen et al. reported the incorporation of Ag nanocluster at the ITO-ZnPc (zinc phthalocyanine) interface for a ZnPc based OSC devices. They argued that a plasmon enhanced excitation of an electron took place inside the metal cluster. The electron was transferred to the ITO electrode while it was replaced by an electron from the valence band of the ZnPc. This charge separation process was driven by the static electric field of the depletion layer [128].

In 2004, Rand et al. reported a break through by the incorporation of Ag nano clusters as the intermediate layer in the tandem OSCs [129] with a two-fold efficiency enhancement. The enhancement was attributed to both LSPR and scattering supported by clusters. Kulkarni et al. demonstrated that charge carrier generation could be enhanced more than three times if a thin film of Ag nano prisms was introduced under the photoactive layer [130] and the excitation enhancement could in principle be used to

enhance the photocurrent of OSCs. Such nano structures might be particularly attractive for the low-band gap organics that have red and near-IR absorption with the low absorption coefficient [131]. More recently, Kymakis et al. explored the effect of surfactant-free Au-NPs-induced surface plasmons on the performance of the P3HT:PCBM photovoltaic devices, utilizing single-walled carbon-nanotube (SWNT) films as the transparent electrode, instead of ITO [132]. The NP incorporation led to a 70% enhancement in PCE due to an enhanced exciton generation rate of the photoactive layer caused by localized surface-plasmon resonances of the conduction electrons within the NPs.

One more approach was the incorporation of irregular NPs structures at various interfaces of OSCs by different vacuum deposition techniques. In this respect, Chen at el. reported the thermal assisted deposition of a discontinuous thin Au layer between the P3HT:PCBM/LiF interface [133]. The OSC device with the P3HT:PCBM/Au/LiF configuration showed a 20%-30% improved both the short-circuit current density and the PCE compared with the devices without the Au layer. The photocurrent enhancement was ascribed to the plasmon enhanced absorption due to the presence of a nano textured Au layer.

Kim et al. followed the work with the placement of pulse-current electrodeposited uniform sized Ag NPs between the ITO electrode and the PEDOT:PSS HTL [134] and observed a PCE enhancement of 20%. Another interrelated work reported by Kalfagiannis et al. where they studied a direct comparison of the P3HT:PCBM OSC device performance with the electron beam evaporated Ag NPs. The NPs were incorporated either between the ITO electrode and the PEDOT:PSS buffer layer or between the P3HT:PCBM and the Al electrode [135] in the conventional structural devices. NPs on top of the ITO led to the improved performance with an efficiency

enhancement of 2.41(reference device) to 2.82%, being equal to an increment of 17%. Both light scattering and LSPR effects contributed to the improvement of the device performance. When the NPs were placed on top of the P3HT:PCBM active layer, the devices exhibited an efficiency enhancement of 2.41-2.65%, i.e. an increase of ~10%. They attributed this enhancement to the improved performance of the PEDOT:PSS layer due to a significant reduction in series resistance.

Lee et al. studied the effect of Au nano dots (Au NDs) between the ITO and the PEDOT:PSS layer. Initially, Au nano structures were deposited through the layer-by-layer deposition onto the ITO substrates and then transformed into Au NDs through a thermally induced shape transition method [136]. The efficiency increased from 3.04% to 3.65% which was mainly due to the presence of the plasmon field in the vicinity of the Au NDs that enhanced the overall absorption to the P3HT:PCBM photoactive layer. More recently, solution processed ultrafine Au NWs have also been successfully exploited as the plasmonic antennae in organic photovoltaic devices [137]. The reduction of the spacer layer thickness enhanced the far-field scattering and the localized plasmon excitation field to the P3HT:PCBM photoactive layer. Both mechanisms led to the absorption enhancement in the P3HT:PCBM photoactive layer, resulting in the increased photocurrent of 7.87 to 9.02 mA/cm^2. The power conversion efficiency has increased from 2.44 to 2.72%.

2.4.7.4 Incorporation of dual plasmonic nanostructures at different layers

Combination of the distinct nanostructures in two different layers of OSC devices has recently been explored to successfully extend the wavelength region of enhanced light absorption. In this study, dual plasmonic nanostructures composed of Au NPs embedded in the active layer and an Ag nano grating electrode as the back reflector in

inverted OSC devices has been fabricated [138]. A PCE increase from 7.59% to 8.79% attributed to broadband absorption enhancement due to simultaneous excitation of hybridized LSPRs from the Ag nano grating and Au NPs, respectively. It also demonstrated that Au-Cu alloy NPs were able to be incorporated between the ITO and the PEDOT:PSS layer of the OSC devices. A polystyrene- block -poly (2-vinylpyridine) (PS-b-P2VP) copolymer template was used to make arrays of metal nano particles [139]. It was found that, due to LSPR effects in bimetallic NPs, light absorption of the organic thin layer was enhanced, resulting in the improved efficiency of 3.35% compared to the conventional OSC devices with the PCE of 2.90%.

Moreover, Fan et al. reported the incorporation of the solution processed Au NPs and graphene oxide (GO) into the PEDOT:PSS layer [140]. The incorporation of the GO template is helpful to avoid the aggregation of the blended Au NPs during the formation of the PEDOT:PSS layer and to promote the plasmonic effect without dramatically sacrificing the electrical properties. The efficiency of the optimised devices increased to 3.55% from a value of 3.27% for the reference device without the Au-GOs addition. The enhancement is mainly ascribed to the increase of light absorption and exciton generation rate in the active layer caused by the plasmonic near-field effect.

2.4.8 Stability issues of OSCs (conventional and inverted)

The power conversion efficiency of organic solar cell devices has been increased from 1 % in 1999 to 9.2 % in 2013 [18,48]. However, it is still far away to commercialise OSCs. The reason for this is that OSC devices have to satisfy many requirements in terms of cost, efficiency, and operation stability. The low production cost and easy fabrication process on glass, plastic, and metal substrates provide a strong impact on pursuing this technology. However, one of the commercial unviable factors is the

environmental degradation or the short life of the OSC devices. Although studies on stability and degradation of OSCs can be found in the early 1990s [141], this issue has not been paid much attention during the early development stage. Recently enormous studies have been carried out towards the device stability and some improvements have been achieved. Cumpston and Neugebauer et al. studied the photo-oxidation behaviour of OSCs and found that the organic molecules reacted with oxygen and water, forming new compounds with inferior optical and electrical properties [142,143]. Some organics can degrade slowly whereas others degrade quickly. For example, P3HT is comparatively stable than MEH-PPV and MDMO-PPV.

Krebs and Norrman have reported a lifetime of up to 10,000 hours for poly(3-carboxydithiophene (P3CT) and C60 based heterojunction devices [144]. After that Hauch et al. reported an outdoor life time of more than one year for the P3HT:PCBM based OSCs in 2008 [145]. For degradation studies, the devices were packed with transparent barrier films with the water vapour transmission rate of 0.03 g/(m^2 day) at 38 °C/100% relative humidity, which was estimated to be roughly equivalent to one-year outdoor exposure as the accelerated lifetime testing. Therefore, compared with inorganic counterparts, instability of OSC devices is still a key issue for future applications. The factors affecting the device stability are mainly due to oxygen, water, and reaction of the electrode material with the photoactive layer [145-150]. It is well known that low work function metals (Ca, Mg and Al) are used as a cathode [151-154] in the conventional device structures. The strong oxidation nature of these metals is a route for diffusion of oxygen and water into the photoactive layer, which leads to the chemical degradation.

Aluminium has very high tendency of electrochemical reaction with oxygen and water to form an insulating metal oxide layer between the active layer and the electrode

material. The forming metal oxide layer degrades the performance of the OSC devices [32, 146]. De Bettignies et al. carried out the temperature dependence lifetime measurements on the optimised P3HT:PCBM solar cells [155]. A significant difference was noted in the degradation with the Ca/Ag and LiF/Al electrodes. For the initial 25 h, the degradation was independent on the nature of the cathode, but after, the LiF/Al cathode led to a faster degradation of the devices in performance (Figure 2.13). The ITO thin film is used as the anode material in most conventional OSC devices and the PEDOT:PSS is utilised as the commonly used anode buffer layer between the ITO and the photoactive layer. The use of the PEDOT:PSS as an anode buffer layer for hole collecting is to prevent oxygen penetration, to manage the work function of the ITO film, and to prevent the indium diffusion into the active layer.

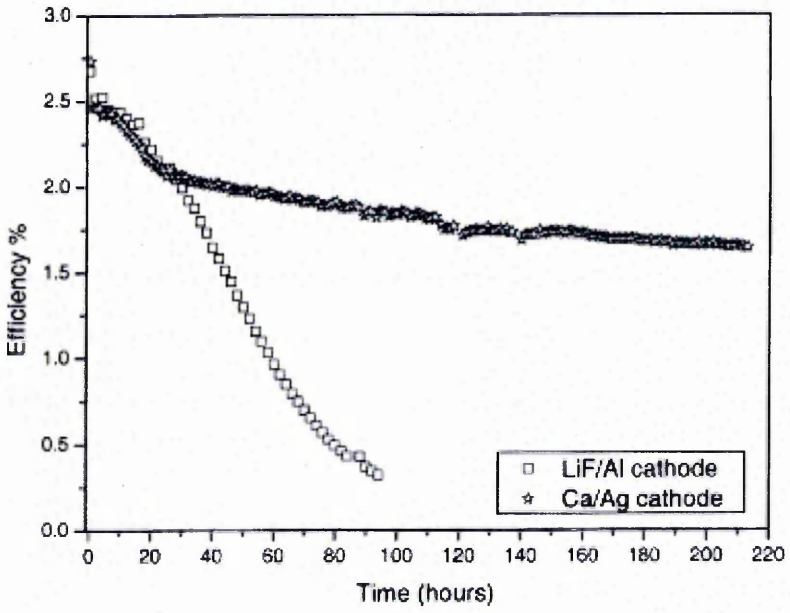

Figure 2.13 Efficiency degradation data up to 100 h ageing for the P3HT:PCBM solar cells with two types of cathodes LiF/AI (square) and Ca/Ag (stars) under a 100 mW/cm^2, AM 1.5 illumination at 60 °C [155].

It has been reported that the PEDOT:PSS itself creates the interface instability because of its strong acidic property of the PEDOT:PSS solution [156]. Study disclosed that in the preparation of glass/ITO/PEDOT:PSS samples, the concentration of indium in the PEDOT:PSS film was 0.02 at. % due to etching of the ITO film in the spin-coating process of the PEDOT:PSS film. Annealing in nitrogen at 100 °C for 2500 h increased the indium concentration to 0.2 at. %. Much faster degradation happened when exposed to air. The amount of indium reached a saturation concentration of 1.2 at. % after several days kept in air. That means the interface between the active layer and the ITO electrode is a major cause for degradation in the P3HT:PCBM based conventional OSC devices is also reported by Reese at al. [157]. Hence, replacement of the PEDOT:PSS film by choosing other interface materials such as transition metal oxides (e.g. MoO_3, V_2O_5 and WO_3) has been widely explored for potential promising alternatives in order to improve the interface stability of the conventional OSC devices [158-161].

In this concern, inverted organic solar cell devices have been suggested as a feasible approach to increase the stability of OSC devices. In the inverted configuration, the ITO electrode works as the electron collecting electrode (cathode) and the high work function metals as the hole collecting electrode (anode). Work function of ITO thin films is modified to work as the electron collecting cathode. Metal oxide layers such as ZnO, TiO_2 and some alkali metal compounds like Cs_2CO_3 have been studied to modify the work function of the ITO film as the electron collecting layer [162-167]. Among all these selections, the ZnO film has been found to be one of the most promising ways that can be easily used in the roll to roll processing. Hau et al. reported the environmental stability of the inverted devices based on the ZnO nanoparticles as the electron transport layer and the PEDOT:PSS/Ag as the hole transport layer and top anode, respectively [162].

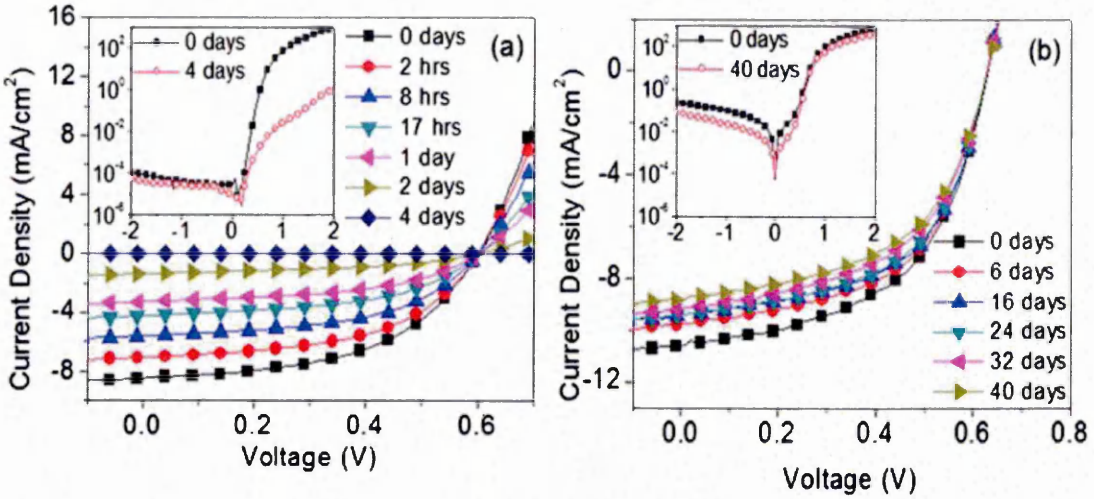

Figure 2.14 (a) J-V characteristics of unencapsulated conventional P3HT:PCBM OSCs over a period of four days in air under ambient conditions. (b) J-V characteristics of un-encapsulated inverted P3HT:PCBM OSCs (ZnO NPs on ITO-coated plastic substrate) over a period of 40 days in air under ambient conditions. (Inset shows unencapsulated dark current device characteristics at 0 and 40 days in air under ambient conditions) [162].

Compared to the conventional structures, inverted structures retained over 80% of its original efficiency after 40 days (Figure 2.14). The conventional OSC device using LiF/Al as the electrode was extremely unstable as its PCE was reduced to less than half of its original value after one day of storage and totally degraded after 4 days. The V_{oc}, J_{sc} and FF decrease dramatically after one day of air exposure due to the interface instability of the electrode from oxidation of the aluminium. The key parameters (PCE, J_{sc}, V_{oc} and FF) dependence on the storage time is shown in Figure 2.15. The improved stability was attributed to both the PEDOT:PSS layer and Ag electrode. The Ag electrode in air can form a layer of silver oxide which increases its effective work

function to -5.0 eV. This matches well with the PEDOT:PSS HOMO of 5.25 eV and hence improves its electrical coherence at the interface [168]. In addition, the PEDOT:PSS film acts as a barrier for oxygen penetration into the active layer. Another study has reported the increased stability in the inverted OSC devices by using TiO_2 as the ETL and sulfonated poly(diphenylamine) (SPDPA) as the HTL [164].

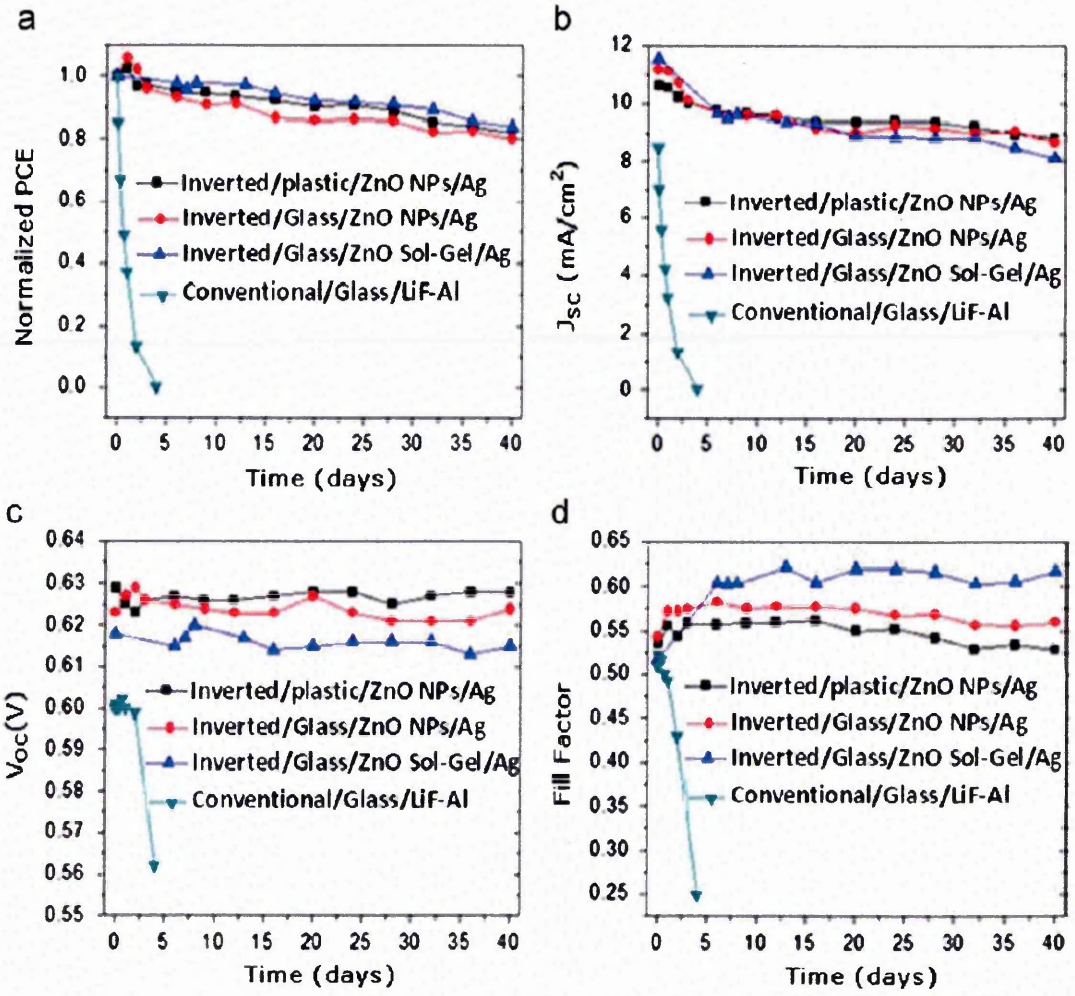

Figure 2.15 Device performance of un-encapsulated conventional and inverted solar cells stored 40 days in air under ambient conditions, (a) Normalized PCE, (b) J_{sc}, (c) V_{oc}, (d) FF [162]

The PCE of the inverted devices was 3.91%, which was the same as that for the conventional devices with an ITO/PEDOT:PSS/ P3HT:PCBM /Ca/Al structure. Inverted OSC devices maintained a PCE of 2.82% after 400 h of air-storage (Figure 2.16), while the conventional devices rapidly declined due to the oxidization of Ca and its poor protection to the active layer. The enhanced stability of inverted OSC devices attributed to both TiO_2 and SPDPA layers, where the TiO2 layer provided an appropriate work function to form an ideal contact with the active layer and a smooth

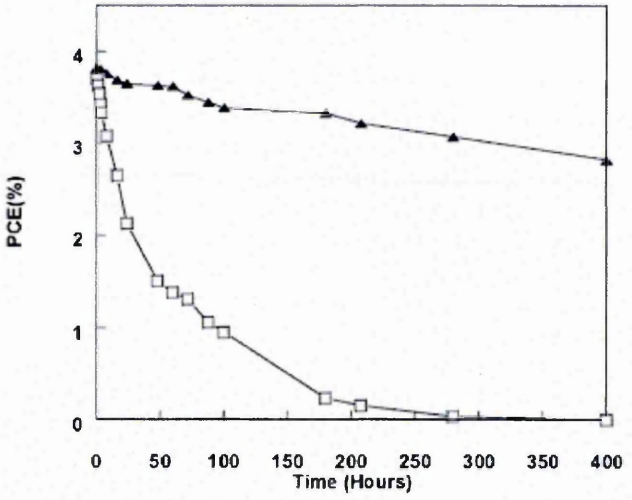

Figure 2.16 PCE parameters as a function of storage time for a conventional device (□) and an inverted device (▲) [164]

surface over the ITO film, avoiding pinholes and the SPDPA film improved the interfacial dipole effect between the metal and the photoactive layer. In the inverted structures, the PCE has also been significantly improved by the use of the PEDOT:PSS and/or other transition metal oxides (e.g. MoO_3, V_2O_5 and WO_3) as the hole transport layer between the active layer and the high work function anode. Jang et al. reported the stability of the inverted (ITO/Cs_2CO_3 /P3HT:PCBM/MoO_3 /Al) and conventional

(ITO/PEDOT:PSS/P3HT:PCBM/LiF/Al) OSCs in air for 40 days [169]. The inverted OSCs showed better stability than the conventional OSCs in ambient air at 295 K for 40 days. The PCE of the inverted OSCs dropped to about 93.5% of the initial value, while the efficiency of the conventional OSCs decreased to 87.7% (Figure 2.17).

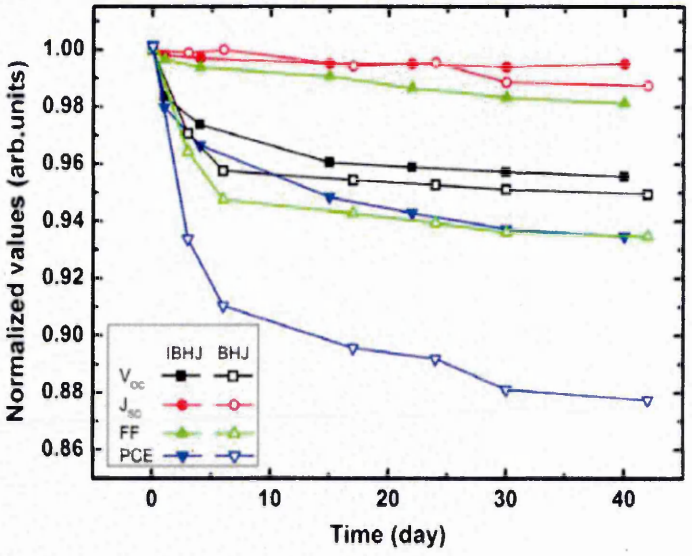

Figure 2.17 PCE parameters as a function of storage time in ambient air, Solid symbols represent the parameters of inverted OSCs and open symbols represent that of conventional OSCs (the parameters are normalized to initial values) [169].

This may be due to reduced effect or damage to the ITO film by the acidic property of the PEDOT:PSS in the inverted configuration OSCs because there is no process of depositing the PEDOT:PSS film and replacement of a thin MoO_3 film has improved the carrier extraction. In addition to investigating the ambient device stability, Zhang et al. reported thermal studies of organic-based solar cells. [170] The phase separated morphologies of the blends are not very thermodynamically stable, which means that the blend still has a certain degree of freedom to diffuse or segregate into larger phases,

leading to reduction in the number of interfaces and thus causing degradation in the device performance. In the study, they used amorphous fullerene derivatives as the electron accepting material in the P3HT:fullerene based inverted OSCs. The amorphous fullerenes were based on modification to the PCBM by replacing the planar phenylene ring with a bulky triphenylamine (TPA) or 9,9-dimethylfluorene (MF).

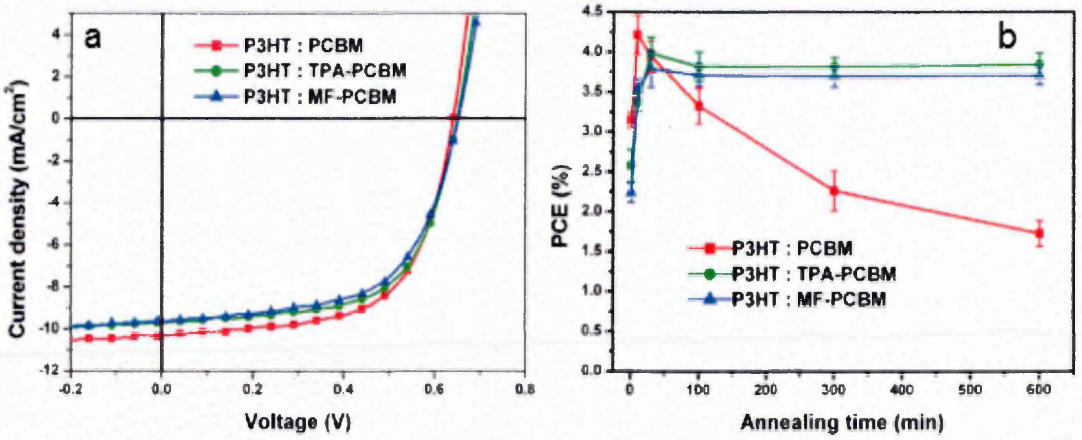

Figure 2.18 (a) J-V characteristic of PCBM-,TPA-PCBM-,and MF-PCBM- based OSC devices, (b) Plot of PCE vs annealing time of PCBM-, TPA-PCBM-, and MF-PCBM-based devices annealed at 150° C [170]

The modified amorphous fullerenes suppress the crystallisation-induced morphological changes that cause the device degradation. The PCE of the OSCs fabricated with the TPA-PCBM and MF-PCBM were 4.0% and 3.8%, respectively, which is comparable to those fabricated with the PCBM as the electron acceptor (4.2%). Slight differences in PCE attributed to the lower mobility of the two amorphous fullerenes as compared to the PCBM. The thermal stability of these OSCs has examined by a typical post-treatment temperature of 150° C for a time period of 10 min to 10 hours. Figure 2.18 shows the J-V curve and dependence of the PCE on the annealing time of the three

different OSC devices. The PCE of the PCBM based device was 4.2% after 10 min of annealing and gradually decreased to 1.8% after annealing for 10 hours. However, both the TPA-PCBM and MF-PCBM showed a significantly higher thermal stability, presenting negligible PCE loss even after 10 hours of annealing. Comparatively less stability of the PCBM based devices was due to severe aggregation and micro crystallites in the P3HT:PCBM films after annealed for 10 hours whereas both the TPA-PCBM and MF-PCBM films showed no signs of severe phase segregation even after 10 hours of annealing. Therefore, the use of amorphous fullerene acceptors might be a promising way for improving the long-term thermal and morphological stability of the inverted OSCs.

2.5 Development of OSCs

In the last decade, OSCs have attracted a significant amount of academic and industrial attentions due to their advantages of being less expensive and using the solution processable fabrication method. C. Tang demonstrated a 1% efficient organic solar cell with the use of perylene pigment combined with CuPc in 1986 [48]. Meissner et al. produced more than 1 % efficient organic solar cell structures in mid 1990s with the C-60 doped ZnPc layer [171]. Heterojunction based devices were found to be more efficient and the first heterojunction based device was fabricated with MEH-PPV and C-60 conjugated polymers [172-175].

Furthermore, the P3HT:PCBM blend was found to be the most deliberate active material for fabrication of the photoactive layers. Schilinnsky generated the highest short circuit current of 8.7 mA/cm^2 using the P3HT:PCBM blend [176] in 2002. Padinger et al. illustrated a 3.5 % efficient device by a postproduction treatment in 2003 [177]. Afterward, P3HT:PCBM came under the intense investigation by many groups

all over the world. The mobility and the crystallisation of the P3HT thin film were continually improved by different growth conditions and annealing treatments. The improved regioregularity also increased the performance of OSCs and obtained a PCE of 4.4%, even without optimisation of electrodes [178]. The enhanced performance was attributed to enhanced optical absorption and improved carrier transport due to better organisation of the P3HT chains via the better stacking in their structures [22]. The ratio of P3HT and PCBM in the blend has been studied and the best performance of PCE up to 3.85% was achieved for the device with the 1:1 ratio of P3HT and PCBM due to better absorption and carrier transport in the active layer [179]. For the conventional structures Yang et al. has reported an efficiency of ~4.4% using the solvent annealing approach to change the P3HT:PCBM morphology [75,180]. Different additives in the HTL have also been studied including glycerol, graphene oxide and fluoro surfactant. The reported PCEs were 4.32%, 3.80% and 3.10%, respectively [181-183].

The buffer layers are important in OSCs. Kim et al. introduced an optical spacer layer of titanium oxide (TiO_x), inserted between the organic active layer and the metal cathode as the ETL in 2006 [184]. Under AM1.5 illumination, an efficiency enhancement of 2.3% to 5.0% has been demonstrated with the application of TiO_x as an optical spacer. W. Ma et al. studied the different post-production annealing of the photoactive layer and the PCE reached to 5.0 % [61]. However, the stability and life time of these devices were very poor due to the etching of the acidic PEDOT:PSS to the ITO film and the high oxidation nature of top low work function metal electrode. Therefore, a novel OSCs structure with the high work function metal or metal oxide as the top electrode and low work function metal as the bottom anode has proposed and named as the inverted OSCs. For inverted organic solar cells, ZnO and TiO_x thin films are the most commonly used ETLs on top of the ITO film while the PEDOT:PSS film is the most

studied HTL. The reported efficiency for the ZnO and TiOx films as the ETL and the PEDOT:PSS as the HTL are 3.78% and 3.81%, respectively [162,185]. Some other HTLs (e.g. MoO_3, V_2O_5 and graphene oxide films) with the ZnO film as the ETL have also been studied and showed promising results with PCEs of 4.18%, 3.90% and 3.61% respectively [186-188]. Afterward, S. K. Hau and Hsieh et al. demonstrated the interfacial modification of the ETL using self-assembled monolayer (SAM) and cross-linked-[6,6]-phenyl-C_{61}-butyric styryl dendron ester (C-PCBSD). The modified OSC devices showed higher PCE of 4.90 % and 4.4 %, respectively as compared to unmodified devices [189, 56].

Recently, T. Kuwabara et. al. studied the effect of UV light on the ZnO ETL and the reported PCE was 3.0% [190]. The addition of a high boiling point solvent like 1,8-diiodooctane and 1,8-octanedithiol has also been studied for optimisation of the morphology of the active layer. Y. Kim et. al. and H. Kim et. al. reported an electro-spray coated and spin coated P3HT:PCBM OSCs with the 1,8-diiodooctane and 1,8-octanedithiol additives [191-192]. The obtained PCE was 3.08 % and 3.46 % respectively. X. Han et. al. published their inverted OSCs with an fluorinated acceptor-doped P3HT:PCBM layer and reported the PCE of 4.22% [193]. 1,8-diiodooctane additives were also used in other types of OSCs. Recently, J. Huang et. al. has published a solution-processed diketopyrrolopyrrole (DPP) based small molecule OSCs with 5.29 % efficiency by the addition of 1,8-diiodooctane into the active layer [194]. Many different solvent additives including 1,8-octanedithiol (ODT) [195], 1-chloronaphthalene (CN) [196], 1,8-diiodooctane (DD) [197], 2,3,5,6-tetrafluoro-7,7,8,8-tetracyanoquinodimethane (F4-TCNQ) [198] and nitrobenzene (NB) [199] have also been investigated. Due to the thin active layer and the narrow absorption range of the P3HT, the device efficiency is still very low compared to that of other types of PV

devices. Therefore, the incorporation of random and periodic plasmonic metallic nanostructures into ETLs, active layers and HTLs has also been widely studied, which demonstrated the improved performance in terms of the enhancement of optical absorption, fill factor and current density in the devices without changing the thickness of the active layer [80,101,182]. Section 2.4.7 has described the detailed discussions on the incorporation of different metallic nanostructures into ETLs, active layers and HTLs. Additionally; the effects of different metallic nanostructures on the properties of OSCs are listed in Table 2.1 [200].

Table 2.1 Device characterisation data of OSCs with NPs embedded in different layers

Geometry	**Photoactive layer**	**η (%)**	**± (%)**	**Mechanism**	**Ref.**
NPs dispersed into the active layer					
20 nm Ag NPs	P3HT:PCBM	2.06	96	LSPR + morphology	[201]
110 nm Ag NWs	P3HT:PCBM	3.91	18	LSPR + scattering	[124]
Ag NPs	P3HT/$PC_{71}BM$	4.0	25	Scattering	[125]
1.5–20 nm Au NPs	P3HT:PCBM	3.71	41	LSPR + scattering + morphology	[121]
3.7 nm Au NPs	P3HT:PCBM	1.5	−67	Exciton quenching	[120]
40 nm Ag clusters	PCDTBT:$PC_{70}BM$ P3HT/$PC_{70}BM$	6.45 4.36	16 23	Charge transport	[122]
70 nm Au NPs	PCDTBT:$PC_{70}BM$	7.1	13	Scattering	[202]
4.8–7.4 nm Au NPs	P3OT-C_{60}	1.9	73	Electrical	[116]
NPs dispersed into the					

HTL (PEDOT:PSS)					
15 nm Au NSs	MEH-PPV:PCBM	2.36	19	LSPR	[110]
30–40 nm Au NPs	P3HT:PCBM	4.19	20	LSPR	[182]
45 nm Au NPs	P3HT:PCBM	4.24	19	LSPR	[203]
18 nm Au NPs	P3HT:PCBM	3.51	13	LSPR, charge transport	[106]
15 nm Au NPs	P3HT:PCBM	4.05	90	LSPR, electrical	[101]
Au 55 nm NSs + 12 nm NRs	P3HT:PCBM	4.28	24	LSPR	[127]
60 nm Ag NPs	P3HT:PCBM	2.75	64	LSPR	
70–80 nm Au NPs in PEDOT intermediate layer	Tandem P3HT:IPCA–PSBTBT:$PC_{70}BM$	6.24	19	Strong local near-field	[204]
NPs dispersed into the ETLs					
Cs_2CO_3 +45 nm Au NPs	P3HT:PCBM	3.54	13	LSPR	[205]
TiO_2+ (40±5) nm Au NPs TiO_2+ (50±5) nm Ag NPs	PTB7:$PC_{71}BM$	7.02 7.52	12 20	LSPR	[206]
ZnO+24 nm Au NPs+16 nm ZnO	P3HT:PCBM	2.35	4	Charge transport	[207]
NPs dispersed between interfacing layers					
13 nm Ag NPs at the ITO/PEDOT:PSS interface	P3HT:PCBM	3.61	20	LSPR	[134]
1 nm thick Ag NPs film at the ITO/PEDOT:PSS interface	P3HT:PCBM	2.2	69	Plasmon	[208]
30 nm Au nanodots at the ITO/PEDOT:PSS interface	P3HT:PCBM	3.65	20	Plasmon	[136]
12.5 nm Ag NPs between ITO/PEDOT:PSS interface	P3HT:PCBM	2.82	17	Scattering	[135]

110 nm Au NPYs (nanopyramids) at the ITO/PEDOT:PSS/interface	P3HT:PCBM	1.1	200	Near field plasmonic	[209]
5–10 nm Au NPs at the PEDOT:PSS/active layer interface	P3HT:PCBM	3.36	−8	Recombination	[210]
7–9 nm Au NWs (nanowires) at the ITO/PEDOT:PSS/interface	P3HT:PCBM	2.72	12	Far field scattering	[137]
40 nm Ag NTs (nanotriangles) at the ITO/PEDOT:PSS/interface	PCDTBT:$PC_{61}BM$	4.52	7	LSPR + scattering	[211]
NPs combinations					
18 nm Au NPs in PEDOT and 35 nm Au NPs in active layer	P3HT:PCBM	3.85	22	LSPR	[107]
50 nm Au NPs into the active layer and Ag back grating with 750 nm period	PBDTTT-C-T:PC70 BM	8.79	16	LSPR + SPP	[138]
40–50 nm Au and Ag NPs into the PEDOT:PSS layer	PTB7:PC70BM	8.67	20	LSPR	[212]
25 nm Au–Cu NPs alloy between the ITO and PEDOT:PSS layers	P3HT:PCBM	3.35	14	LSPR	[139]
10 nm Au-GO into PEDOT:PSS layer	P3HT:PCBM	3.55	10	LSPR	[140]
2D arrays of NPs					
Periodic Ag nanotriangle array on ITO	PCDTBT:PCBM	4.52	7	LSPR	[211]
Periodic Au nanopyramids on ITO	(P3):PCBM	1.1	205	LSPR	[213]

Studies about fabrication of the OSC devices on metals have also been published based on the mostly popular active blend of P3HT:PCBM [27-32]. Y. Galagan et al. and Y.M. Chang et al. reported their inverted OSC devices on the stainless steel substrate [27, 28]. the reported PCE was 1.30% and 0.97%, respectively. B. Zimmermann et al. investigated the top illuminated inverted OSC devices directly on the vacuum deposited and stored Ti/Al/Ti or Cr/Al/Cr coated glass substrates, obtaining the PCE at 3.1% [29]. T.S. Kim et al. presented the inverted OSC devices on the copper sheets with PCE at ~ 2.5% [30]. D. Angmo et al. reported the R2R processed large area OSC devices with Ag coatings as back electrodes with the best PCE at 1.61 % [31]. PCE of the OSC devices on metals is related to many factors; e.g. surface properties of metals including roughness, the passive layer, work function and the transparency of top electrode, etc. [214]. Y. Zhou et al. presented PCE of 2.4% for the bottom illuminated OSC devices with the conducting organic top transparent anode [215].

Generally, the obtained PCE for the devices using the P3HT:PCBM based photoactive layer remains limited (~5%). However, significant strides have been made in the last few years by the development of low band gap organics that can harvest energy in the long wavelength region. Liang et al. demonstrated 7% and lately above 8% PCE of the OSC devices with the PTB7:$PC_{71}BM$ photoactive layer in 2010 [216]. Two NREL certified devices have been reported to break the 8% PCE mark [217, 218]. The Solarmer Company (2009) has achieved a device that exhibits 8.13% PCE [217] and Konarka's demonstrated a world-record breaking efficiency of 8.3%. Both were certified by NREL [218]. Konarka Company also developed the encapsulated device with a roof top life span of more than two years. Heliatek GmbH and the Institute of Applied Photophysics at Dresden University have reported a standard 1.1 cm^2 organic solar cell with an efficiency of 8.3% [219]. The claimed efficiency was measured by

Heliatek and independently confirmed by the Fraunhofer ISE CalLab. For the tandem OSC devices, Yang's group has announced PCE of 8.6% [220].

Afterward, J. You et al. reported the efficiency of 10.60% using the P3HT:ICBA/PDTP-DFBT (poly[2,6-(4,4-bis-(2-ethylhexyl)-4H-cyclopenta[2,1-b;3,4-b']-dithiophene)-alt-4,7-(2,1,3-difluoroben-zothiadiazole):PC61BM based tandem OSCs [16]. Recently, an efficiency of 12.0 % has also been reported by Heliatek and they expect to reach the 15% efficiency by 2016 [19].

Conclusions are made; i.e. the incorporation of metallic NPs can enhance the optical absorption without increasing the thickness of the active layer. By controlling the shape, the size, the concentration and the place of incorporation of the NPs, it is possible to enhance the overall PCE in these so-called "plasmonic devices". The top illuminated OPV decices on flexible metal substrates is also a potential alternative of producing flexible OPV devices via the inverted structures with a transparent top anode.

In this context, it is still quite a long way to go for realising the real commercial products in terms of the PCE and device stability for OSCs when compared with inorganic PV devices.

2.6 References:

[1] E. Becquerel, Mémoire sur les effets électriques produits sous l'influence des rayons solaires. Comt. Rend. Acad. Sci., 9 (1839) 561-567.

[2] W. Smith, Effect of Light on Selenium During the Passage of An Electric Current, Nature, 7 (1873) 303-303.

[3] W. G. Adams, R.E. Day, The Action of Light on Selenium, Proc. R. Soc. London, 25 (1876) 113-117.

[4] A. Pochettino, SuI comportamento foto-elettrico dell' antracene, Acad. Lincei Rend., 15 (1906) 355.

[5] M. Volmer, The different photoelectric phenomena in anthracene, their relationships to each other, for fluorescence and Dianthracenbildung, Ann. Physik, 40 (1913) 775-796.

[6] P. M. Borsenberger, D. S. Weiss, Organic Photoreceptors For Imaging Systems, Marcel Dekker,New York, (1993).

[7] H. Akamatu, H. Inokuchi, Y. Matsunaga, Electrical conductivity of the perylene bromine complex, Nature, 173 (4395) (1954) 168-169.

[8] R. H. Bube, Photoconductivity of Solids, Wiley, New York, (1960)

[9] A. Terenin, E. Putzeiko, I. Akimov, Energy transfer in systems of connected organic molecules, Discuss. Faraday Soc., 27(1959) 83-93.

[10] C. W. Tang, S. A. VanSlyke, Organic electroluminescent diodes. Appl. phys. lett., 51 (1987) 913.

[11] D. L. Morel, A. K. Ghosh, T. Feng, E. L. Stogryn, P. E. Purwin, R. F. Shaw, C. Fishman, High-efficiency organic solar cells Appl. Phys. Lett., 32 (1978) 495 .

[12] X. Yang, J. Loos, S. C. Veenstra, W. J. Verhees, M. M. Wienk, J. M. Kroon, M. A. Michels, R. A. Janssen, Nanoscale morphology of high-performance polymer solar cells, Nano Lett., 5 (2005) 2005 579-83.

[13] G. J. Zhao, Y. J. He, Y. F. Li, 6.5% Effi ciency of Polymer Solar Cells Based on poly(3 hexylthiophene) and Indene-C 60 Bisadduct by Device Optimization, Adv. Mater., 22 (2010) 4355-4358

[14] S. C. Price, A. C. Stuart, L. Yang, H. Zhou, W. You, Fluorine Substituted Conjugated Polymer of Medium Band Gap Yields 7% Efficiency in Polymer-Fullerene Solar Cells, J. Am. Chem. Soc., 2011, 133, 4625–4631

[15] C. E. Small, S. Chen, J. Subbiah, C. M. Amb, S. W.Tsang, T. H. Lai, J. R. Reynolds, F. So, High-efficiency inverted dithienogermole–thienopyrrolodione-based polymer solar cells, Nat. Photon., 6 (2012) 115-120.

[16] J. You, L. Dou, K. Yoshimura, T. Kato, K. Ohya, T. Moriarty, K. Emery, C. C. Chen, J. Gao, G. Li, Y. Yang, A polymer tandem solar cell with 10.6% power conversion efficiency, Nat. Commun., 4 (2013) 1446.

[17] J. Siegel, C. Nelder, N. Hodge, Investing in Renewable Energy: Making Money on Green Chip Stocks, John Wiley & sons Inc., Hoboken New Jersey 2008.

[18] Z. He, C. Zhong, S. Su, M. Xu, H. Wu, Y. Cao, Enhanced power conversion efficiency in polymer solar cells using an inverted device structure, Nat. Photon., V 6 (2012) 591-595.

[19] http://www.heliatek.com

[20] H. Schaefer, G. Hagerdorn, Hidden Energy and Correlated Environmental Characteristics of PV Power Generation, Renewable Energy, 2 (1992) 159-166.

[21] C. J. Brabec, J. A. Hauch, P. Schilinsky, and C. Waldauf, Production Aspects of Organic Photovoltaics and Their Impact on the Commercialization of Devices, MRS Bull., 30 (2005) 50-52.

[22] Y. Kim, S. Cook, S. M. Tuladhar, S. A. Choulis, J. Nelson, J. R. Durrant, D. D. C. Bradley, M. Giles, I. McCulloch, C. S. Ha, and M. Ree, A strong regioregularity effect in self-organizing conjugated polymer films and high-efficiency polythiophene:fullerene solar cells, Nat. Mater., 5 (2006) 197-203.

[23] R. R. Søndergaard, M. H¨osel, F. C. Krebs, Roll-to-Roll fabrication of large area functional organic materials, Journal of Polymer Science Part B: Polymer Physics, 51 (2013)16-34.

[24] F. C. Krebs, T. Tromholt, M. Jørgensen, Upscaling of polymer solar cell fabrication using full roll-to-roll processing, Nanoscale, 2 (2010) 873-886.

[25] J. S. Yu, I. Kim, J. S. Kim, J. Jo, T. T. Larsen-Olsen, R. R. Søndergaard, M. H¨osel, D. Angmo, M. Jørgensen, F. C. Krebs, Silver front electrode grids for ITO-free all printed polymer solar cells with embedded and raised topographies, prepared by thermal imprint, flexographic and inkjet roll-to-roll processes, Nanoscale, 4 (2012) 6032-6040.

[26] P. Schilinsky, C. Waldauf, C.J. Brabec, Performance analysis of printed bulk heterojunction solar cells, Adv. Funct. Mater., 16 (2006) 1669-1672.

[27] Y. Galagan, D. J. D. Moet, D. C. Hermes, P. W. M. Blom, R. Andriessen, Large area ITO free organic solar cells on steel substrate, Org. Electron., 13 (2012) 3310-3314.

[28] Y. M. Chang, C. P. Chen, J. M. Ding, C. Y. Leu, M. J. Lee, R. D. Chen, Top-illuminated organic solar cells fabricated by vacuum-free and all-solution processes, Sol. Energ. Mat. Sol. Cells, 109 (2013) 91-96.

[29] B. Zimmermann, U. Wurfel, M. Niggemann, Long term stability of efficient inverted P3HT:PCBM solar cell, Sol. Energ. Mat. Sol. Cells, 93 (2009) 491-496.

[30] T. S. Kim, S. I. Na, S. H. Oh, R. Kang, B. K. Yu, J. S. Yeo, J. Lee, D. Y. Kim, All-solution processed ITO-free polymer solar cells fabricated on copper sheets, Sol. Energ. Mat. Sol. Cells, 98 (2012) 168-171.

[31] D. Angmo, M. H¨osel, F. C. Krebs, All solution processing of ITO-free organic solar cell modules directly on barrier foil, Sol. Energ. Mat. Sol. Cells, 107 (2012) 329-336.

[32] V. Kumar, H. Wang, Selection of metal substrates for completely solution-processed inverted organic photovoltaic devices, Org. Electron., 113 (2013) 179-185.

[33] M. Pope, H. Kallman, P. Magnante, Electroluminescence in Organic Crystals, J. Chem. Phys., 38 (1963) 2042.

[34] W. C. H. Choy, Organic solar cells: Material and device physics, Springer-Verlag London 2013.

[35] I. kymissis, Organic Field Effect Transistors Theory, Fabrication and Characterization, Springer Science and Business Media, LLC 2009.

[36] D. Hu, J. Yu, G. Padmanaban, S. Ramkrishnan, P. F. Barbara, Spatial confinement of exciton transfer and the role of conformational order in organic nanoparticles, Nano Lett., 2 (2002) 1121-1124.

[37] V. C. Sunder, J. Zaumseil, V. Podzorov, E. Menard, R. L. Willett, T. Someya, M. E. Gershenson, J. A. Rojers, Elastomeric Transistor Stamps: Reversible Probing of Charge Transport in Organic Crystals, Sceince, 303 (2004) 1644-1646.

[38] T. Kietzke, Recent Advances in Organic Solar Cells, Advances in Opto Electronics, (2007) Article ID 40285, 15 pages.

[39] T. D. Anthopoulosa, B. Singh, N. Marjanovic, N. S. Sariciftci, A. M. Ramil, H. Sitter, M. Cölle, D. M. de Leeuw, High performance n-channel organic field-effect transistors and ring oscillators based on C60 fullerene films, Appl. Phys. Lett., 89 (21) (2006) 213504.

[40] D. J. Gundlach, K. P. Pernstich, G. Wilckens, M. Grüter, S. Haas, B. Batlogg, High mobility n-channel organic thin-film transistors and complementary inverters, J. Appl. Phys., 98 (6) (2005) 064502.

[41] I. McCulloch, M. Heeney, C. Bailey, K. Genevicius, I. MacDonald, M. Shkunov, D. Sparrowe, S. Tierney, R. Wagner, W. Zhang, M. L. Chabinyc, R. J. Kline, M. D. McGehee, M. F. Toney, Liquid-crystalline semiconducting polymers with high charge-carrier mobility, Nat Mater., 5 (4) (2006) 328-333.

[42] L. J. A. Koster, V. D. Mihailetchi, P. W. M. Blom, Ultimate efficiency of polymer-fullerene bulk heterojunction solar cells, Appl. Phys. Lett., 88(9) (2006) 093511.

[43] L. D. Landau, On the motion of the electrons in the crystal lattice, Phys. Z. Sowjetunion., 3 (1933) 644-645.

[44] J. M. Guo, H. Ohkita, H. Benten, S. Ito, Charge generation and recombination dynamics in Poly(3-hexylthiophene)/Fullerene blend films with different regioregularities and morphologies. J. Am. Chem. Soc., 132 (2010) 6154-6164.

[45] B. A. Gregg, M. C. Hanna, Comparing organic to inorganic photovoltaic cells: Theory, experiment, and simulation, J. appl. Phys. 93(6) (2003) 3605-3614.

[46] A. C. Mayer, S. R. Scully, B. E. Hardin, M. W. Rowell, M. D. McGehee, Polymer-based solar cells, Mater. Today., 10 (2007) 28-33.

[47] H. Hoppe, N. S. Sariciftci, Organic solar cells: An overview, J. Mater. Res., 19 (2004) 1924-1945.

[48] C. W. Tang, Two-layer organic photovoltaic cell, Appl. Phys. Lett., 48 (2) (1986) 183.

[49] C. J Brabec, G. Zerza, G. Cerullo, S. D. Silvestri, S. Luzzati, J. C. Hummelen, S. Sariciftci, Tracing photoinduced electron transfer process in conjugated polymer/fullerene bulk heterojunctions in real time, Chem. Phys. Lett., 340 (3-4) (2001) 232-236.

[50] J. M. Nunzi, Organic photovoltaic materials and devices, C. R. Phys., 3 (4) (2002) 523–542.

[51] L. J. A. Koster, E. C. P. Smits, V. D. Mihailetchi, P. W. M. Blom, Device model for the operation of polymer/fullerene bulk heterojunction solar cells, Phys. Rev. B., 72 (8) (2005) 85205.

[52] S. Günes, H. Neugebauer, N. S. Sariciftci, Conjugated Polymer-Based Organic Solar Cells, Chem. Rev., 107 (4) (2007)1324-1338.

[53] A. Hayakawa, O. Yoshikawa, T. Fujieda, K. Uehara S. Yoshikawa, High performance polythiophene/fullerene bulk-heterojunction solar cell with a TiOx hole blocking layer, Appl. Phys. Lett., 90 (16) 2007 163517.

[54] Y. Kim, A. M. Ballantyne, J. Nelson, D. D. C. Bradley, Effects of thickness and thermal annealing of the PEDOT:PSS layer on the performance of polymer solar cells, Org. Electron., 10 (2009) 205-209.

[55] J. J. Jasieniak, J. Seifter, J. Jo, T. Mates, A. J. Heeger, A Solution-Processed MoOx Anode Interlayer for Use within Organic Photovoltaic Devices, Adv. Funct. Mater., 22 (2012) 2594-2605.

[56] C. H. Hsieh, Y. J. Cheng, P. J. Li, C. H. Chen, M. Dubosc, R. M. Liang, C. S. Hsu, Highly efficient and stable inverted polymer solar cells integrated with a cross-linked fullerene material as an interlayer, J. Am. Chem. Soc., 132 (2010) 4887-4893.

[57] J. D. Servaites, M. A. Ratner, T. J. Marks, Organic solar cells: A new look at traditional models, Energy Environ. Sci., 4 (2011) 4410-4422.

[58] A. K. Ghosh, D. L. Morel, T. Feng, R. F. Shaw, C. A. Rowe, Photovoltaic and rectification properties of Al/Mg phthalocyanine/Ag Schottky-barrier cells, J. Appl. Phys., 45 (1974) 230.

[59] C. W. Tang, A. C. Albrecht, The Electrodeposition of Films of Chlorophyll-a Microcrystals and Their Spectroscopic Properties, Mol. Cryst. Liq. Acta., 25 (1974) 53-62.

[60] S. H. Park, A. Roy, S. Beaupre, S. Cho, N. Coates, J. S. Moon, D. Moses, M. Leclerc, K. Lee, A. J. Heeger, Bulk heterojunction solar cells with internal quantum efficiency approaching 100%, Nat. Photon., 3 (5) (2009) 297–302.

[61] W. L. Ma, C. Y. Yang, X. Gong, K. Lee, A. J. Heeger, Thermally Stable, Efficient Polymer Solar Cells with Nanoscale Control of the Interpenetrating Network Morphology, Adv. Funct. Mater., 15 (2005) 1617-1622.

[62] M. Hiramoto, M. Suezaki and M. Yokoyama, Effect of Thin Gold Interstitial-layer on the Photovoltaic Properties ofTandem Organic Solar Cell, Chem. Lett., 119 (1990) 327-330.

[63] A. G. F. Janssen, T. Riedl, S. Hamwi, H. H. Johannes, W. Kowalsky, Highly efficient organic tandem solar cells using an improved connecting architecture, Appl. Phys. Lett., 91 (2007) 073519.

[64] S. Sista, Z. Hong, M. H. Park, Z. Xu, Y. Yang, High-Efficiency Polymer Tandem Solar Cells with Three-Terminal Structure, Adv. Mater., 22 (2010) E77-E80.

[65] K. W. Wong, H. L. Yip, Y. Luo, K. Y. Wong, W. M. Lau, K. H. Low, H. F. Chow, Z. Q. Gao, W. L. Yeung, and C. C. Chang, Blocking reactions between

indium-tin oxide and poly (3,4-ethylene dioxythiophene):poly(styrene sulphonate) with a self-assembly monolayer, Appl. Phys. Lett., 80 (2002) 2788-2790.

[66] M. O. Reese, M. S. White, G. Rumbles, D. S. Ginley, S. E. Shaheen, Optimal negative electrodes for poly(3-hexylthiophene): [6,6]-phenyl C61-butyric acid methyl ester bulk heterojunction photovoltaic devices. Appl. Phys. Lett., 92 (2008) 053307.

[67] M. Glatthaar, M. Niggemann, B. Zimmermann, P. Lewer, M. Riede, A. Hinsch, and J. Luther, Organic solar cells using inverted layer sequence, Thin Solid Films., 491 (2005) 298-300.

[68] Z. Xu, L. M. Chen, G. W. Yang, C. H. Huang, J. H. Hou, Y. Wu, G. Li, C. S. Hsu, Y. Yang, Vertical Phase Separation in Poly(3-hexylthiophene): Fullerene Derivative Blends and its Advantage for Inverted Structure Solar Cells, Adv. Funct. Mater., 19 (2009) 1227-1234.

[69] M. A. Green, K. Emery, Y. Hishikawa and W. Warta, Solar cell efficiency tables (version 37), Prog. Photovolt: Res. Appl., 19 (2011) 84-92.

[70] F. Zhang, X. Xu, W. Tang, J. Zhang, Z. Zhuo, J. Wang, J. Wanga, Z. Xu, Y. Wanga, Recent development of the inverted configuration organic solar cells, Sol. Energ. Mat. Sol. Cells., 95 (2011) 1785-1799.

[71] D. Angmo, F. C. Krebs, Flexible ITO-free polymer solar cells, J. Appl. Polym. Sci., 129 (2013) 1-14.

[72] H. W. Lin, S. W. Chiu, L. Y. Lin, Z. Y. Hung, Y. H. Chen, F. Lin, K. T. Wong, Device Engineering for Highly Efficient Top-Illuminated Organic Solar Cells with Microcavity Structures, Adv. Mater., 24 (2012) 2269-2272.

[73] J. Ouyang, Y. Yany, Conducting Polymer as Transparent Electric Glue, Adv. Mater., 18 (2006) 2141-2144.

[74] K. Vandewal, A. Gadisa, W. D. Oosterbaan, S. Bertho, F. Banishoeib, The Relation Between Open-Circuit Voltage and the Onset of Photocurrent Generation by Charge-Transfer Absorption in Polymer : Fullerene Bulk Heterojunction Solar Cells, Adv. Funct. Mater., 18 (2008) 2064-2070.

[75] G. Li, V. Shrotriya, J. Huang, Y. Yao, T. Moriarty, K. Emery, Y. Yang, High-efficiency solution processable polymer photovoltaic cells by self-organization of polymer blends, Nat. Mater., 4 (2005) 864-868.

[76] B. Qi, J. Wang, Fill factor in organic solar cells, Phys. Chem. Chem. Phys., 15 (2013) 8972-8982.

[77] A. Gadisa, W. D. Oosterbaan, K. Vandewal, J. C. Bolsée, S. Bertho, J. D'Haen, L. Lutsen, D. Vanderzande, J. V. Manca, Effect of Alkyl Side-Chain Length on Photovoltaic Properties of Poly(3-alkylthiophene)/PCBM Bulk Heterojunctions, Adv. Funct. Mater., 19 (2009) 3300-3306.

[78] S. B. Rim, S. Zhao, S. R. Scully, M. D. McGehee, P. Peumans, An effective light trapping configuration for thin-film solar cellsAppl. Phys. Lett., 91 (2007) 243501.

[79] C. Cocoyer, L. Rocha, L. Sicot, B. Geffroy, R. de Bettignies, C. Sentein, C. Fiorini-Debuisschert, P. Raimond, Implementation of submicrometric periodic surface structures toward improvement of organic-solar-cell performances, Appl. Phys. Lett., 88 (2006) 133108.

[80] D. H. Ko, J. R. Tumbleston, L. Zhang, S. Williams, J. M. DeSimone, R. Lopez, E. T. Samulski, Photonic Crystal Geometry for Organic Solar Cells, Nano Lett., 9 (2009) 2742.

[81] H. A. Atwater, A. Polman, Plasmonics for improved photovoltaic devices, Nature Mater., 9 (2010) 205-213.

[82] A. Ng, X. Liu, C. H. To, A. B. Djurišić, J. A. Zapien, W. K. Chan, Annealing of P3HT:PCBM Blend Film-The Effect on Its Optical Properties, ACS Appl. Mater. Interfaces., 5 (2013) 4247-4259.

[83] A. J. Moulé, K. Meerholz, Controlling Morphology in Polymer-Fullerene Mixtures, Adv. Mater., 20 (2008) 240-245.

[84] J. H. Chang, Y. H. Chen, H. W. Lin, Y. T. Lin, H. F. Meng, E. C. Chen, Highly efficient inverted rapid-drying blade-coated organic solar cells, Org. Electron., 13 (2012) 705-709.

[85] G. Li, Y. Yao, H. Yang, V. Shrotriya, G. Yang, Y. Yang, Solvent Annealing" Effect in Polymer Solar Cells Based on Poly(3-hexylthiophene) and Methanofullerenes, Adv. Funct. Mater., 17 (2007) 1636-1644.

[86] Y. J. He, H. Y. Chen, J. H. Hou, Y. F. Li, Indene-C60 bisadduct: a new acceptor for high performance polymer solar cells, J. Am. Chem. Soc., 132 (2010)1377-1382.

[87] Y. J. He, G. J. Zhao, B. Peng, Y. F. Li, High-yield synthesis and electrochemical and photovoltaic properties of indene-C70 bisadduct, Adv. Funct. Mater., 20 (2010) 3383-3389.

[88] F. B. Kooistra, V. D. Mihailetchi, L. M. Popescu, D. Kronholm, P. W. M. Blom, J. C. Hummelen, New C84 derivative and its application in a bulk heterojunction Solar Cell, Chem. Mater., 18 (2006) 3068-3073.

[89] S. Stevenson, G. Rice, T. Glass, K. Harich, F. Cromer, M. R. Jordan, J. Craft, E. Hadju, R. Bible, M. M. Olmstead, K. Maitra, A. J. Fisher, A. Balch, H. C. Dorn, Small-bandgap endohedral metallofullerenes in high yield and purity, Nature, 401 (1999) 55-57.

[90] J. A. Schuller, E. S. Barnard, W. Cai, Y. C. Jun, J. S. White, M. L. Brongersma, Plasmonics for extreme light concentration and manipulation, Nat. Mater., 9 (2010) 193-204.

[91] S. A. Maier, Plasmonics: Fundamentals and Applications: Fundamentals and Applications. (2007) Springer, New York

[92] S. Zeng, K. T. Yong, I. Roy, X. Q. Dinh, X. Yu, F. Luan, A review on functionalized gold nanoparticles for biosensing applications. Plasmonics., 6 (3) (2011) 491–506.

[93] K. Tvingstedt, N. K. Persson, O. Ingan, A. Rahachou, I. V. Zozoulenko, Surface plasmon increase absorption in polymer photovoltaic cells. Appl. Phys. Lett., 91 (2007) 113514.

[94] M. G. Kang, T. Xu, H. J. Park, X. Luo, L. J. Guo, Efficiency Enhancement of Organic Solar Cells Using Transparent Plasmonic Ag Nanowire Electrodes Adv. Mater., 22 (2010) 4378- 4383.

[95] C. J. Min, J. Li, G. Veronis, J. Y. Lee, S. H. Fan, P. Peumans, Enhancement of optical absorption in thin-film organic solar cells through the excitation of plasmonic modes in metallic gratings. Appl. Phys. Lett., 96 (2010) 133302-1–133302-3.

[96] A. J. Morfa, K. L. Rowlen, T. H. Reilly III, M. J. Romero, J. van de Lagemaat, Plasmon-enhanced solar energy conversion in organic bulk heterojunction photovoltaics, Appl. Phys. Lett., 92 (2008) 013504.

[97] D. Duche, P. Torchio, L. Escoubas, F. Monestier, J.J. Simon, F. Flory, Improving light absorption in organic solar cells by plasmonic contribution, Sol. Energy Mater. Sol. Cells, 93 (2009) 1377-1382.

[98] C. M. Liu, C. M. Chen, Y. W. Su, S. M. Wang, K. H. Wei, The dual localized surface plasmonic effects of gold nano dots and gold nanoparticles enhance the performance of bulk heterojunction polymer solar cells, Org. Electron., 14 (2013) 2476-2483.

[99] S. Y. Chou, W. Ding, Ultrathin, high-efficiency, broad-band, omni acceptance, organic solar cells enhanced by plasmonic cavity with sub wavelength hole array, Optic Express., 21 (2013) A60.

[100] P. P. Cheng, L. Zhou, J. A. Li, Y. Q. Li, S. T. Lee, J. X. Tang, Light trapping enhancement of inverted polymer solar cells with a nanostructured scattering rear electrode, Org, Electron., 14 (2013) 2158-2163.

[101] V. Kumar, H. Wang, Plasmonic Au nanoparticles for enhanced broadband light absorption in inverted organic photovoltaic devices by plasma assisted physical vapour deposition, Org. Electron., 14 (2013) 560-568.

[102] V. E. Ferry, L. A. Sweatlock, D. Pacifici, H. A. Atwater, Plasmonic nanostructure design for efficient light coupling into solar cells. Nano Lett., 8 (2008) 4391-4397.

[103] R. A. Pala, J. White, E. Barnard, J. Liu, M. L. Brongersma, Design of plasmonic thin-film solar cells with broadband absorption enhancements. Adv. Mater., 21 (2009) 3504-3509.

[104] W. E. I. Sha, W. C. H. Choy, Y. P. Chen, W. C. Chew, Optical design of organic solar cell with hybrid plasmonic system, Optics Express, 19 (2011) 15908-15918.

[105] H. A. Atwater, A. Polman, Plasmonics for improved photovoltaic devices. Nat. Mater., 9 (2010) 205-213.

[106] D. D. S. Fung, L. Qiao, W. C. H. Choy, C. Wang, W. E. I. Sha, F. Xie, S. He, Optical and electrical properties of efficiency enhanced polymer solar cells with Au nanoparticles in a PEDOT–PSS layer, J. Mater. Chem., 21 (2011) 16349-16356.

[107] F. X. Xie, W. C. H. Choy, C. C. D. Wang, W. E. I. Sha, D. D. S. Fung, Improving the efficiency of polymer solar cells by incorporating gold nanoparticles into all polymer layers, Appl. Phys. Lett., 99 (2011) 153304.

[108] E. Stratakis, E. Kymakis, Nanoparticle-based plasmonic organic photovoltaic devices, Mater. Today., 16 (2013) 133-146.

[109] C. C. Chang, H. L. Wu, C. H. Kuo, M. H. Huang, Hydrothermal synthesis of monodispersed octahedral gold nanocrystals with five different size ranges and their self-assembled structures, Chem. Mater., 20 (2008) 7570-7574.

[110] L. Qiao, D. Wang, L. Zuo, Y. Ye, J. Qian, H. Chen, A. She, Localized surface plasmon resonance enhanced organic solar cell with gold nanospheres, Appl. Energy, 88 (2011) 848-852.

[111] Y. S. Hsiao, S. Charan, F. Y. Wu, F. C. Chien, C. W. Chu, P. L. Chen, F. C. Chen, Improving the light trapping efficiency of plasmonic polymer solar cells through photon management, J. Phys. Chem., C 116 (2012) 20731-20737.

[112] J. Yang, J. B. You, C. C. Chen, W. C. Hsu, H. R. Tan, X. W. Zhang, Z. R. Hong, Y. Yang, Plasmonic polymer tandem solar cell, ACS Nano, 5 (2011) 6210-6217.

[113] S. W. Baek, J. Noh, C. H. Lee, B. Kim, M. K. Seo, J. Y. Lee, Plasmonic Forward Scattering Effect in Organic Solar Cells: A Powerful Optical Engineering Method, Sci. Rep., 3 (2013) 1726.

[114] A. Y. Mahmouda, J. Zhang, D. Ma, R. Izquierdo, V. V. Truong, Optically-enhanced performance of polymer solar cells with low concentration of gold nanorods in the anodic buffer layer, Org. Electron., 13 (2012) 3102-3107.

[115] M. Stavytska-Barba, M. Salvador, A. Kulkarni, D. S. Ginger, A. M. Kelley, Plasmonic enhancement of raman scattering from the organic solar cell material p3ht/pcbm by triangular silver nanoprisms, J. Phys. Chem., C 115 (2011) 20788-20794.

[116] K. Kim, D. L. Carroll, Roles of Au and Ag nanoparticles in efficiency enhance- ment of poly(3-octylthiophene)/C60 bulk heterojunction photovoltaic devices, Appl. Phys. Lett., 87 (2005) 203113-1–203113-3.

[117] M. Xue, L. Li, B. J. T. de Villers, H. Shen, J. Zhu, Z. Yu, A. Z. Stieg, Q. Pei, B. J. Schwartz, K. L. Wang, Charge-carrier dynamics in hybrid plasmonic organic solar cells with Ag nanoparticles, Appl. Phys. Lett., 98 (2011) 253302.

[118] K. Topp, H. Borchert, F. Johnen, A. V. Tunc, M. Knipper, E. von Hauff, J. Parisi, K. Al-Shamery, Impact of the Incorporation of Au Nanoparticles into Polymer/Fullerene Solar Cells, J. Phys. Chem., A 114 (2010) 3981-3989

[119] M. D. Brown, T. Suteewong, R. S. S. Kumar, V. D'Innocenzo, A. Petrozza, M. M. Lee, U. Wiesner, H. J. Snaith, Plasmonic dye-sensitized solar cells using core–shell metal–insulator nanoparticles, Nano Lett., 11 (2010) 438-445.

[120] H. Shen, P. Bienstaman, B. Maes, Plasmonic absorption enhancement in organic solar cells with thin active layers, J. Appl. Phys., 106 (2009) 073109-1/073109-5

[121] G. D. Spyropoulos, M. M. Stylianakis, E. Stratakis, E. Kymakis, Organic bulk heterojunction photovoltaic devices with surfactant-free Au nanoparticles embedded in the active layer, Appl. Phys. Lett., 100 (2012) 213904-213915.

[122] D. H. Wang, D. Y. Kim, K. W. Choi, J. H. Seo, S. H. Im, J. H. Park, O. O. Park, A. J. Heeger, Enhancement of Donor–Acceptor Polymer Bulk Heterojunction Solar Cell Power Conversion Efficiencies by Addition of Au Nanoparticles, Angew. Chem., 50 (2011) 5519-5523.

[123] D. H. Wang, K. H. Park, J. H. Seo, J. Seifter, J. H. Jeon, J. K. Kim, J. H. Park, O. O. Park, A. J. Heeger, Enhanced power conversion efficiency in PCDTBT:$PC_{70}BM$ bulk heterojunction photovoltaic devices with embedded silver nanoparticle clusters, Adv. Energy Mater., 1 (2011) 766-770.

[124] C. H. Kim, S. H. Cha, S. C. Kim, M. Song, J. Lee, W. S. Shin, S. J. Moon, J. H. Bahng, N. A. Kotov, S. H. Jin, Silver nanowire embedded in P3HT:PCBM for high-efficiency hybrid photovoltaic device applications, ACS Nano, 5 (2011) 3319-3325.

[125] D. H. Wang, J. K. Kim, G. H. Lim, K. H. Park, O. O. Park, B. Lim, J. H. Park, Enhanced light harvesting in bulk heterojunction photovoltaic devices with shape-controlled Ag nanomaterials: Ag nanoparticles versus Ag nanoplates, RSC Adv., 2 (2012) 7268-7272.

[126] X. Li, W. C. H. Choy, H. Lu, W. E. I. Sha, A. H. P. Ho, Efficiency Enhancement of Organic Solar Cells by Using Shape-Dependent Broadband Plasmonic Absorption in Metallic Nanoparticles, Adv. Funct. Mater., 23 (2013) 2728-2735.

[127] O. Stenzel, A. Stendal, K. Voigtsberger, C. von Borczyskowski, Enhancement of the photovoltaic conversion efficiency of copper phthalocyanine thin film devices by incorporation of metal clusters, Sol. Energy Mater. Sol. Cells, 37 (1995) 337-348

[128] M. Westphalen, U. Kreibig, J. Rostalski, H. LuKth, D. Meissner, Metal cluster enhanced organic solar cells, Sol. Energy Mater. Sol. Cells, 61 (2000) 97-105.

[129] B. P. Rand, P. Peumans, S. R. Forrest, Long-range absorption enhancement in organic tandem thin-film solar cells containing silver nanoclusters, J. Appl. Phys., 96(2004) 7519-7526.

[130] A. P. Kulkarni, K. M. Noone, K. Munechika, S. R. Guyer, D. S. Ginger, Plasmon-enhanced charge carrier generation in organic photovoltaic films using silver nanoprisms, Nano Lett., 10(2010) 1501-1505.

[131] O. Inganas, F. Zhang, M. R. Andersson, Alternating Polyfluorenes Collect Solar Light in Polymer Photovoltaics, Acc. Chem. Res., 42 (2009) 1731-1739.

[132] E. Kymakis, E. Stratakis, E. Koudoumas, C. Fotakis, Plasmonic Organic Photovoltaic Devices on Transparent Carbon Nanotube Films, IEEE Trans. Electron Dev., 58 (2011) 860-864.

[133] X. Chen, C. Zhao, L. Rothberg, M. K. Ng, Plasmon enhancement of bulk heterojunction organic photovoltaic devices by electrode modification, Appl. Phys. Lett., 93 (2008) 123302.

[134] S. S. Kim, S. I. Na, J. Jo, D. Y. Kim, Y. C. Nah, Plasmon enhanced performance of organic solar cells using electrodeposited Ag nanoparticles, Appl. Phys. Lett., 93 (2008) 073307.

[135] N. Kalfagiannis, P. Karagiannidis, C. Pitsalidis, N. T. Panagiotopoulos, C. Gravalidis, S. Kassavetis, P. Patsalas, S. Logothetidis, Plasmonic silver nanoparticles for improved organic solar cells, Sol. Energy Mater. Sol. Cells, 104 (2012) 165-174.

[136] J. H. Lee, J. H. Park, J. S. Kima, D. Y. Lee, K. Cho, High efficiency polymer solar cells with wet deposited plasmonic gold nanodots, Org. Electron. 10 (2009) 416-420.

[137] T. Z. Oo, N. Mathews, G. Xing, B. Wu, B. Xing, L.H. Wong, T. C. Sum, S. G. Mhaisalkar, Ultrafine Gold Nanowire Networks as Plasmonic Antennae in Organic Photovoltaics, J. Phys. Chem., C 116 (2012) 6453-6458.

[138] X. Li, W. Choy, L. Huo, F. Xie, W. Sha, B. Ding, X. Guo, Y. Li, J. Hou, J. You, Y. Yang, Dual plasmonic nanostructures for high performance inverted organic solar cells. Adv. Mater., 24 (2012) 3046-3052.

[139] M. Heo, H. Cho, J. W. Jung, J. R. Jeong, S. Park, J. Y. Kim, High-Performance Organic Optoelectronic Devices Enhanced by Surface Plasmon Resonance, Adv. Mater., 23 (2011) 5689-5693.

[140] G. Q. Fan, Q. Q. Zhuo, J. J. Zhu, Z. Q. Xu, P. P. Cheng, Y. Q. Li, X. H. Sun, S. T. Lee, J. X. Tang, Plasmonic-enhanced polymer solar cells incorporating solution-processable Au nanoparticle-adhered graphene oxide, J. Mater. Chem., 22 (2012) 15614-15619.

[141] Q. L. Song, F. Y. Li, H. Yang, H. R. Wu, X. Z. Wang, W. Zhou W, J. M. Zhao, X. M. Ding, C. H. Huang, X. Y. Hou, Small molecule organic solar cells with improved stability, Chem. Phys. Lett., 416 (2005) 42-46.

[142] B. H. Cumpston, K. F. Jensen, Photooxidative stability of substituted poly(phenylene vinylene) (PPV) and poly(phenylene acetylene) (PPA). Journal of Applied Polymer Science, 69 (1998) 2451-2558.

[143] H. Neugebauer, C. J. Brabec, J. C. Hummelen, N. S. Sariciftci, Stability and photodegradation mechanisms of conjugated polymer/fullerene plastic solar cells. Sol. Energy Mater. Sol. Cells, 61 (2000) 35-42.

[144] F. C. Krebs, K. Norrman, Analysis of the failure mechanism for a stable organic photovoltaic during 10 000 h of testing, Prog. Photovolt.: Res. Appl., 15 (2007) 697-712.

[145] J. A. Hauch, P. Schilinsky, S. A. Choulis, R. Childers, M. Biele, C. J. Brabec. Flexible organic p3ht:pcbm bulk-heterojunction modules with more than 1 year outdoor lifetime, Sol. Energy Mater. Sol. Cells, 92(7) (2008) 727-731.

[146] M. Glattharr, M. Riede, N. Keegan, K. Sylvester-Hvid, B. Zimmermann, M. Niggemann, A. Hinsch, A. Gombert. Efficiency limiting factors of organic bulk heterojunction solar cells identied by electrical impedance spectroscopy. Sol. Energy Mater. Sol. Cells, 91 (2007) 390-393.

[147] M. Jørgensen, K. Norrman, F. C. Krebs, Stability/degradation of polymer solar cells. Sol. Energy Mater. Sol. Cells, 92 (2008)686-714.

[148] K. Norrman, N. B. Larsen, F.C. Krebs, Lifetimes of organic photovoltaics: Combining chemical and physical characterisation techniques to study degradation mechanisms. Sol. Energy Mater. Sol. Cells, 90 (2006) 2793-2814.

[149] M. Jørgensen, K. Norrman, S. A. Gevorgyan, T. Tromholt, B. Andreasen, F. C. Krebs, Stability of Polymer Solar Cells, Adv. Mater., 24 (2012) 580-612.

[150] H. Choi, J. S. Park, E. Jeong, G. H. Kim, B. R. Lee, S. O. Kim, M. H. Song, H. Y. Woo, J. Y. Kim, Combination of Titanium Oxide and a Conjugated Polyelectrolyte for High-Performance Inverted-Type Organic Optoelectronic Devices, Adv. Mater., 23 (2011) 2759-2763.

[151] T. S. van der Poll, J. A. Love, T. Q. Nguyen, G. C. Bazan, Non-Basic High-Performance Molecules for Solution-Processed Organic Solar Cells, Adv. Mater., 24 (2012) 3646-3649.

[152] J. Zhou, X. Wan, Y. Liu, Y. Zuo, Z. Li, G. He, G. Long, W. Ni, C. Li, X. Su, Y. Chen, Small Molecules Based on Benzo[1,2-b:4,5-b']dithiophene Unit for High-Performance Solution-Processed Organic Solar Cells, J. Am. Chem. Soc., 134 (2012) 16345-16351.

[153] Y. Sun, G. C. Welch, W. L. Leong, C. J. Takacs, G. C. Bazan, A. J. Heeger, Solution-processed small-molecule solar cells with 6.7% efficiency, Nat. Mater., 11 (2011) 44-48.

[154] S. L. Shen, P. Jiang, C. He, J. Zhang, P. Shen, Y. Zhang, Y. P. Yi, Z. J. Zhang, Z. B. Li, Y. F. Li, Solution-Processable Organic Molecule Photovoltaic Materials with Bithienyl-benzodithiophene Central Unit and Indenedione End Groups, Chem. Mater., 25 (2013) 2274-2281.

[155] R. De Bettignies, J. Leroy, M. Firon, C. Sentein, Accelerated lifetime measurements of P3HT:PCBM solar cells. Synth. Met., 156 (2006) 510-513.

[156] M. P. de Jong, L. J. van Ijzendoorn, M. J. A. de Voigt, Stability of the interface between indium-tin-oxide and poly(3,4-ethylenedioxythiophene)/poly(styrenesulfonate) in polymer light-emitting diodes, Appl. Phys. Lett., 77 (2000) 2255-2257.

[157] M. O. Reese, A. J. Morfa, M. S. White, N. Kopidakis, S. E. Shaheen, G. Rumbles, D. S. Ginley, Pathways for the degradation of organic photovoltaic p3ht:pcbm based devices, Sol. Energy Mater. Sol. Cells., 92 (2008) 746-752.

[158] V. Shrotriya, G. Li, Y. Yao, C. W. Chu, Y. Yang, Transition metal oxides as the buffer layer for polymer photovoltaic cells, Appl. Phys. Lett., 88 (2006) 073508-1-3.

[159] Y. Sun, C. J. Takacs, S. R. Cowan, J. H. Seo, X. Gong, A. Roy, A. J. Heeger, Efficient, air stable bulk heterojunction polymer solar cells using MoOx as the anode interfacial layer, Adv. Mater., 23 (2011) 2226-2230.

[160] S. Han, W. S. Shin, M. Seo, D. Gupta, S. J. Moon, S. Yoo, Improving performance of organic solar cells using amorphous tungsten oxides as an interfacial buffer layer on transparent anodes, Org. Electron.,10 (2009) 791-797.

[161] H. Pana, L. Zuoa, W. Fua, C. Fana, B. Andreasenc, X. Jiang, K. Norrmanc, F. C. Krebs, H. Chen, MoO3–Au composite interfacial layer for high efficiency and air-stable organic solar cells. Org. Electron., 14 (2013) 797-803.

[162] S. K. Hau, H. L Yip, N. S. Baek, J. Zhou, K. O'Malley, A. K. Y. Jen, Air-stable inverted flexible polymer solar cells using zinc oxide nanoparticles as an electron selective layer, Appl. Phys. Lett., 92 (2008) 253301-1-3.

[163] A. K. K. Kyaw, X. W. Sun, C. Y. Jiang, G. Q. Lo, D. W. Zhao, D. L. Kwong, An inverted organic solar cell employing a sol–gel derived ZnO electron selective layer and thermal evaporated MoO_3 hole selective layer, Appl. Phys. Lett., 93 (2008) 221107.

[164] C. Y. Li, T. C. Wen, T. H. Lee, T. F. Guo, J. C. A. Huang, Y. C. Lin, Y. J. Hsu, An inverted polymer photovoltaic cell with increased air stability obtained by employing novel hole/electron collecting layers, J. Mater. Chem., 19 (2009) 1643-1647.

[165] S. K. Hau, H. L. Yip, O. Acton, N. S. Baek, H. Ma, A. K. Y. Jen, Interfacial modification to improve inverted polymer solar cells, J. Mater. Chem., 18 (2008) 5113-5119.

[166] G. Li, C. W. Chu,V. Shrotriya, J. Huang, Y. Yang, Efficient inverted polymer solar cells. Appl. Phys. Lett., 88 (2006) 253503.

[167] H. H. Liao, L. M. Chen, Z. Xu, G. Li, Y. Yang, Highly efficient inverted polymer solar cell by low temperature annealing of Cs_2CO_3interlayer, Appl. Phys. Lett., 92 (2008) 173303.

[168] F. J. Zhang, A. Vollmer, J. Zhang, Z. Xu, J. P. Rabe, N. Koch, Energy level alignment and morphology of interfaces between molecular and polymeric organic semiconductors, Org. Electron., 8 (2007) 606-614.

[169] Y. Lee, J. H. Youn, M. S. Ryu, J. Kim, H. T. Moon, J. Jang, Highly efficient inverted poly(3-hexylthiophene): methano-fullerene [6,6]-phenyl C71-butyric acid methyl ester bulk heterojunction solar cell with Cs_2CO_3 and MoO_3, Org. Electron., 12 (2011) 353-357.

[170] Y. Zhang, H. L. Yip, O. Acton, S. K. Hau, F. Huang, A. K. Y. Jen, A simple and effective way of achieving highly efficient and thermally stable bulk-heterojunction polymer solar cells using amorphous fullerene derivatives as electron acceptor, Chem. Mater., 21 (2009) 2598-2600.

[171] J. Rostalski, D. Meissner, Monochromatic versus solar efficiencies of organic solar cells, Sol. Energy Mater. Sol. Cells., 61 (2000) 87-95.

[172] N. S. Sariciftci, L. Smilowitz, D. Braun, G. Srdanov, V. Srdanov, F. Wudl, A. J. Heeger, Observation of a photoinduced electron transfer from a conducting polymer (MEHPPV) onto C60, Synth. Met., 56 (1993) 3125-3130.

[173] N. S. Sariciftci, D. Braun, C. Zhang, V. Srdanov, A. J. Heeger, G. Stucky, F. Wudl, Semiconducting polymer-buckminsterfullerene heterojunctions: Diodes, photodiodes, and photovoltaic cells, Appl. Phys. Lett., 62 91993) 585-587.

[174] N. S. Sariciftci, A. J. Heeger, Reversible, Metastable, Ultrafast Photoinduced Electron Transfer from Semiconducting Polymers to Buckminsterfullerene and in

the Corresponding Donor/acceptor Heterojunctions, Int. J. Mol. Phys., B8 (1994) 237-274.

[175] N. S. Sariciftci, Role of Buckminsterfullerene, C60, in organic photoelectric devices, Prog. Quant. Elec., 19 (1995) 131-159.

[176] P. Schilinsky, P. Waldauf, C. J. Brabec, Recombination and loss analysis in polythiophene based bulk heterojunction photodetectors, J. Appl. Phys. Lett., 81 (2002) 3885.

[177] F. Padinger, R. S. Rittberger, N. S. Sariciftci, Effects of post production treatment on plastic solar cells. Adv. Funct. Mater., 13 (2003) 85–88.

[178] Y. Kim, S. Cook, S. M. Tuladhar, S. A. Choulis, J. Nelson, J.R. Durrant, D. D. C. Bradley, M. Giles, I. Mcculloch, C. Ha, M. Ree, A strong regioregularity effect in self-organizing conjugated polymer films and high-efficiency polythiophene: fullerene solar cells, Nat. Mater., 5 (2006) 197-203.

[179] V. Shrotriya, J. Ouyang, R. J. Tseng, G. Li, Y. Yang, Absorption spectra modification in poly(3-hexylthiophene):methanofullerene blend thin films, Chem. Phys. Lett., 411 (2005) 138-143.

[180] G. Li, V. Shrotriya, Y. Yao, J. Huanga, Y,Yang, Manipulating regioregular poly(3-hexylthiophene) : [6,6]-phenyl-C61- butyric acid methyl ester blends-route towards high efficiency polymer solar cells, J. Mater. Chem., 17 (2007) 3126-3140.

[181] T. S. Huang, C. Y. Huang, Y. K. Su, J. S. Fang, M. V. M. Rao, T. F. Guo, T. C. Wen, High-Efficiency Polymer Photovoltaic Devices With Glycerol-Modified Buffer Layer, IEEE Photonics Technol. Lett., 20 (2008) 1935.

[182] F. C. Chen, J. L. Wu, C. L. Lee, Y. Hong, C. H. Kuo, M. H. Huang, Plasmonic-enhanced polymer photovoltaic devices incorporating solution-processable metal nanoparticles, Appl. Phys. Lett., 95 (2009) 013305.

[183] B. Yin, Q. Liu, L. Y. Yang, X. M. Wu, Z. F. Liu, Y. L. Hua, S. G. Yin, Y. S. Chen, J. Nanosci. Buffer Layer of PEDOT:PSS/Graphene Composite for Polymer Solar Cells, Nanotechnology, 10 (2010) 1934-1938.

[184] J. Y. Kim, S. H. Kim, H. H. Lee, K. Lee, W. Ma, X. Gong, A. J. Heeger, New Architecture for High-Efficiency Polymer Photovoltaic Cells Using Solution-Based Titanium Oxide as an Optical Spacer, Adv. Mater., 18 (2006) 572–576.

[185] T. Kuwabara, H. Sugiyama, M. Kuzuba, T. Yamaguchi, K. Takahashi, Inverted bulk-heterojunction organic solar cell using chemical bath deposited titanium oxide as electron collection layer, Org. Electron., 11 (2010) 1136-1140.

[186] Y. Gao, H. L. Yip, S. K. Hau, K. M. O'Malley, N. C. Cho, H. Chen, A. K. Y. Jen, Anode modification of inverted polymer solar cells using graphene oxide, Appl. Phys. Lett., 97 (2010) 203306.

[187] K. Takanezawa, K. Tajima, K. Hashimoto, Efficiency enhancement of polymer photovoltaic devices hybridized with ZnO nanorod arrays by the introduction of a vanadium oxide buffer layer, Appl. Phys. Lett., 93 (2008) 063308.

[188] J. C. Wang, W. T. Weng, M. Y. Tsai, M. K. Lee, S. F. Horng, T. P. Perng, C. C. Kei, C. C. Yu, H. F. Meng, Highly efficient flexible inverted organic solar cells using atomic layer deposited ZnO as electron selective layer, J. Mater. Chem., 20 (2010) 862-866.

[189] S. K. Hau, H. L. Yip, H. Ma, A. K. Y. Jen, High performance ambient processed inverted polymer solar cells through interfacial modification with a fullerene self-assembled monolayer, Appl. Phys. Lett., 93 (2008) 233304.

[190] T. Kuwabara, C. Tamai, Y. Omura, T. Yamaguchi, T. Taima, K. Takahashi, Effect of UV light irradiation on photovoltaic characteristics of inverted polymer

solar cells containing sol–gel zinc oxide electron collection layer, Org. Electron., 14 (2013) 649–656.

[191] Y. Kim, G. Kim, J. Lee, K. Lee, Morphology controlled bulk-heterojunction layers of fully electro-spray coated organic solar cells, Sol. Energy Mater. Sol. Cells, 105 (2012) 272–279

[192] H. Kim, S. Ok, H. Chae, Y. Choe, Performance characteristics of polymer photovoltaic solar cells with an additive-incorporated active layer. Nanoscale Res Lett., 7 (2012) 56.

[193] X. Han, Z. Wu, B. Sun, Enhanced performance of inverted organic solar cell by a solution-based fluorinated acceptor doped P3HT:PCBM layer, Org. Electron., 14 (2013) 1116-1121.

[194] J. Huang, C. Zhan, X. Zhang, Y. Zhao, Z. Lu, H. Jia, B. Jiang, J. Ye, S. Zhang, A. Tang, Y. Liu, Q. Pei, J. Yao, Solution-Processed DPP-Based Small Molecule that Gives High Photovoltaic Efficiency with Judicious Device Optimization, ACS Appl. Mater. Interfaces, 5 (2013) 2033-2039.

[195] J. K. Lee, N. E. Coates, S. Cho, N. S. Cho, D. Moses, G. C. Bazan, K. Lee, A. J. Heeger, Efficacy of TiOx optical spacer in bulk-heterojunction solar cells processed with 1,8-octanedithiol, Appl. Phys. Lett., 92 (2008) 243308/1-3.

[196] F. C. Chen, H. C. Tseng, C. J. Ko, Solvent mixtures for improving device efficiency of polymer photovoltaic devices, Appl. Phys. Lett., 92 (2008) 103316-/1-3.

[197] J. K. Lee, W. L. Ma, C. J. Brabec, J. Yuen, J. S. Moos, J. Y. Kim, K. Lee, G. C. Bazan, A. J. Heeger, Processing Additives for Improved Efficiency from Bulk Heterojunction Solar Cells, J. Am. Chem. Soc.,130 (2008) 3619–3623.

[198] X. Han, Z. Wu, B. Sun, Enhanced performance of inverted organic solar cell by a solution-based fluorinated acceptor doped P3HT:PCBM layer, Org. Electron., 14 (2013) 1116-1121.

[199] A. J. Moule, K. Meerholz, Controlling Morphology in Polymer- Fullerene Mixtures, Adv. Mater., 20 (2008) 240–245.

[200] E. Stratakis, E. Kymakis, Nanoparticle-based plasmonic organic photovoltaic devices, Mater. Today, 16 (2013) 133-146.

[201] B. Paci, G. D. Spyropoulos, A. Generosi, D. Bailo, V. R. Albertini, E. Stratakis, E. Kymakis, Enhanced Structural Stability and Performance Durability of Bulk Heterojunction Photovoltaic Devices Incorporating Metallic Nanoparticles, Adv. Funct. Mater., 21 (2011) 3573-3582.

[202] D. H. Wang, Y. Kim, K. W. Choi, J. H. Seo, S. H. Im, J. H. Park, O. O. Park, A. J. Heeger, Enhancement of donor-acceptor polymer bulk heterojunction solar cell power conversion efficiencies by addition of Au nanoparticles, Angew. Chem. Int. Ed., 50 (2011) 5519-5523.

[203] J. L. Wu, F. C. Chen, Y. S. Hsiao, F. C. Chien, P. L. Chen, C. H. Kuo, M. H. Huang, C. S. Hsu, Surface plasmonic effects of metallic nanoparticles on the performance of polymer bulk heterojunction solar cells, ACS Nano,5 (2011) 959-967.

[204] R. S. Kim, J. F. Zhu, J. H. Park, L. Li, Z. B. Yu, H. J. Shen, M. Xue, K. L. Wang, G. Park, T. J. Anderson, Q. B. Pei, E-beam deposited Ag-nanoparticles plasmonic organic solar cell and its absorption enhancement analysis using FDTD-based cylindrical nano-particle optical model, Opt. Express, 20 (2012) 12649-12657.

[205] C. S. Kao, F. C. Chen, C. W. Liao, M. H. Huang, C. S. Hsu, Plasmonic-enhanced performance for polymer solar cells prepared with inverted structures, Appl. Phys. Lett., 101 (2012) 193902–193904.

[206] M. F. Xu, X. Z. Zhu, X. B. Shi, J. Liang, Y. Jin, Z. K. Wang, L. S. Liao, Plasmon resonance enhanced optical absorption in inverted polymer/fullerene solar cells with metal nanoparticle-doped solution-processable TiO_2 layer, ACS Appl. Mater. Interfaces, 5 (2013) 2935-2942.

[207] J. Wang, Y. J. Lee, A. S. Chadha, J. Yi, M. L. Jespersen, J. J. Kelley, H. M. Nguyen, M. Nimmo, A. V. Malko, R. A. Vaia, W. Zhou, J. W. P. Hsu, Effect of plasmonic Au nanoparticles on inverted organic solar cell performance, J. Phys. Chem. C, 117 (2013) 85-91.

[208] A. J. Morfa, K. L. Rowlen, T. H. Reilly III, M. J. Romero, J. V. D. Lagemaatb, Plasmon-enhanced solar energy conversion in organic bulk heterojunction photovoltaics, Appl. Phys. Lett., 92 (2008) 013504.

[209] D. M. O'Carroll, J. Fakonas, D. M. Callahan, M. Schierhorn and H. A. Atwater, Metal–Polymer–Metal Split-Dipole Nanoantennas, Adv. Mater., 24 (2012) OP136–OP142.

[210] H. Liu, W. P. Goh, M. Y. Leung, Y. Li, T. B. Norsten, Effect of nanoparticle stabilizing ligands and ligand-capped gold nanoparticles in polymer solar cells, Sol. Energy Mater. Sol. Cells, 96 (2012), 302-306.

[211] B. Wu, X. Liu, X. Li, X. Liu, X. Wu, E. K. L. Yeow, H. J. Fan, N. Mathews, T. C. Sum, Efficiency Enhancement in Bulk-Heterojunction Solar Cells Integrated with Large-Area Ag Nano triangle Arrays, J. Phys. Chem. C, 116 (2012) 14820-14825.

[212] L. Lu, Z. Luo, T. Xu, L. Yu, Cooperative Plasmonic Effect of Ag and Au Nanoparticles on Enhancing Performance of Polymer Solar Cells, Nano Lett., 13 (2013) 59-64.

[213] A. Kirkeminde, M. Retsch, Q. Wang, G. Xu, R. Hui, J. Wu and S. Ren, Surface passivated plasmonic nano-pyramids for bulk heterojunction solar cell photocurrent enhancement, Nanoscale, 4 (2012) 4421-4425.

[214] B. Zimmermann, M. Glatthaar, M. Niggemann, K. M. Riede, A. Ziegler, T. Gombert, Organic solar cells with inverted layer sequence incorporating optical spacers-simulation and experiment, SPIE-Organic Optoelectronics and Photonics, 6197 (2006).

[215] Y. Zhou, H. Cheun, S. Choi, C. F. Hernandez, B. Kippelen, Optimization of a polymer top electrode for inverted semitransparent organic solar cells, Org. Electron., 12 (2011) 827-831.

[216] Y. Liang, Z. Xu, J. Xia, S. Tsai, Y. Wu, G. Li, C. Ray, L. Yu, For the bright future-bulk heterojunction polymer solar cells with power conversion efficiency of 7.4%. Adv. Mater., 22 (2010) E135–E138.

[217] Solarmer Energy, Inc. Website:http://www.solarmer.com

[218] Konarka Company, website:http://www.konarka.com.

[219] Heliatek GmbH, Website:http://www.heliatek.com.

[220] L. Dou, J. You, J. Yang, C. Chen, Y. He, S. Murase, T. Moriarty, K. Emery, G. Li, Y. Yang, Tandem polymer solar cells featuring a spectrally matched low-bandgap polymer, Nat. Photon., 6 (2012) 180-185.

3.1 Materials selection

3.1.1 Active layer materials

Bulk heterojunction organic solar cells consist of an organic photovoltaic active layer sandwiched between two electrodes. The active layer material is a blend of the donor and the acceptor semiconductors. The donor is a conjugated organic and the acceptor is a small molecular material. The donor and acceptor blend is a key factor and has a great importance for the fabrication of high performance organic solar cell devices. A number of donor and acceptor materials have been developed in the last decades. The blend of P3HT and PCBM is one of the most studied photoactive materials [1] for application in OSCs, organic light emitting diodes (OLEDs), [2,3] and field effect transistors (FETs) [4-6].

The performance of the PV device depends on degree of crystallinity and the regioregularity of the donor organic material [7,8]. P3HT is a conjugated organic with a thiophene backbone that is coupled between the 2- and 5-positions (2-position is known as head, and the 5-position is known as tail). The presence of the alkyl-group enhances the solubility of P3HT that causes the high potential of crystallinity [9]. P3HT usually has a regioregularity of more than 90% and higher regioregularity provides higher crystallinity. In this study, the blend of the active materials is based on the P3HT and PCBM. The P3HT for our PV devices is from Merck (Lisicon SP001) and has a regioregularity of more than 94% and the PCBM is from Solenne BV with a purity of 99.5%. The PCBM is n-type fullerene based materials and contains a buckyball (C60) with a solubility enhanced methyl-ester group. Fullerene and its derivatives are widely used as the electron acceptor materials in the organic PV technology. Hummelen and

Wudl et al., reported synthesis of most successful fullerene derivatives with excellent photovoltaic properties as the electron acceptor in 1995 [10]. The HOMO and LUMO energy level of the P3HT:PCBM blend are shown in Figure 3.1.

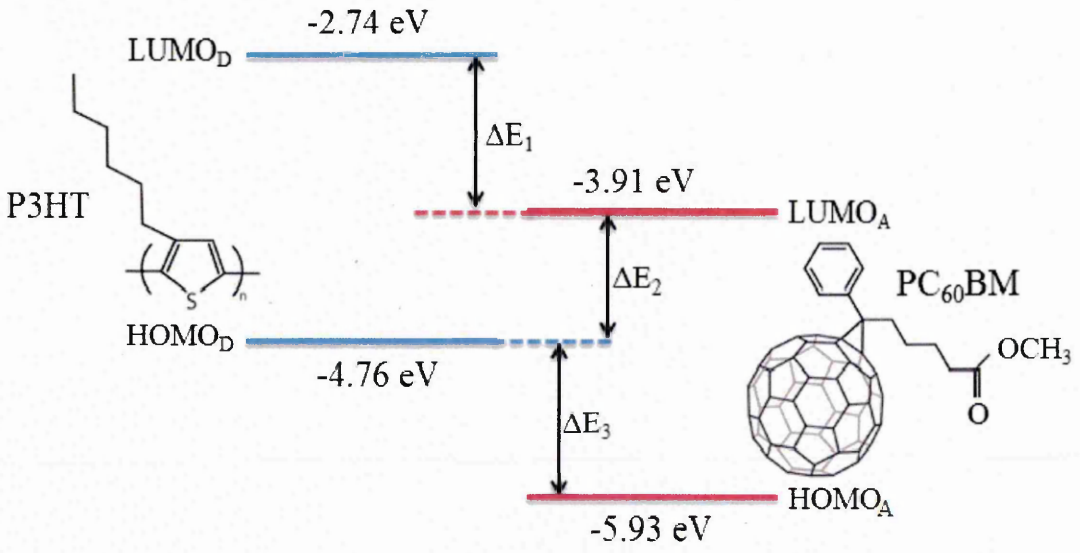

Figure 3.1 Molecular structures and the HOMO and LUMO energy level of the P3HT:PCBM blend systems [11]

This P3HT:PCBM based photoactive layer absorbs incident light and generates excitons. The excitons then diffuse at the donor-acceptor interface and dissociate into electrons and holes. The dissociated electrons and holes move towards the respective electrodes by the influence of the built-in electric field and then are collected by the electrodes. The P3HT:PCBM absorbs light in the range of 380-670 nm, which means that excitons generated by the absorption of photons have the bandgap energies between 2.0 to 3.3 eV. The energy difference between the LUMO and HOMO of the donor and acceptor separate the excitons into free electrons and holes. The electrons and holes will transport towards respective electrodes through the LUMO of PCBM and the HOMO of P3HT,

respectively. When the HOMO and LUMO of the donor material is higher (0.2–0.3 eV) than that of the acceptor material, the charge separation is efficient (Figure 3.1). However, when photons have energies greater than 2.0 eV, it can only be absorbed by the P3HT:PCBM means a more than 70% energy loss taking place during the photoelectric conversion. Therefore, it is required to tune the HOMO and LUMO levels of the donors and the acceptors in order to minimise this loss.

3.1.2 Electron transport layer (ETL)

The work function of the electron collecting electrode affects the photovoltaic performance of the organic solar cells devices and the maximum performance can be achieved when the work function of the electron collecting electrode is aligned ohmically with the LUMO level of the acceptor. The role of the electron transport layer is to improve the electron collection efficiency by providing an ohmic contact between electron collecting electrode and the acceptor material. The electron affinity needs to be high enough to block the positive charge carriers. An efficient electron transport layer needs to be stable and should not increase the device series resistance. High transparency is also an important parameter for the inverted device configuration.

To be used in organic solar cells, the devices need to be processed under low temperature using the simple method, maintaining flexibility and retaining a thin form factor. These requirements can be easily fulfilled by the inverted device architecture with the low temperature solution-processed n-type metal oxide layer with high electron mobility for transportation of electrons. In the inverted organic solar cell configuration, ZnO and TiO_x are the most studied electron transport layers. The high electron mobility of ZnO compared to titanium oxide makes it the ideal electron selective contact layer in organic solar cells [12]. The solution-processed ZnO electron transport layer or zinc

oxide nanoparticles (ZnO NPs) layer has been shown to be produced via a spin-coating technique at room temperature [13]. The ZnO NPs derived layer exhibits good electron mobility (~0.066 cm^2 /V s) without the need of an additional post-thermal treatment [14].

Additionally, the zinc oxide layer has many other properties; e.g. low-cost, non-toxicity, good substrate adherence, and excellent chemical and thermal stability [15]. A wide variety of techniques for the fabrication of high quality ZnO thin films have been reported so far, including mist pyrolysis chemical vapor deposition (MPCVD) [16], pulsed laser deposition (PLD) [17], sol–gel method (18), plasma sputtering [19], and electrochemical deposition [20]. The sol gel technique is one of the simple low-temperature methods for the deposition of ZnO thin films on flexible substrates. When a ZnO buffer layer is inserted between the organic active layer and the electron collecting electrode in organic solar cells, efficient electron transfer at the PCBM/ZnO interface is achievable [21] because the energy level of the conduction band of ZnO is very close to that of the LUMO of PCBM and is well suited to the work function of ITO electrode.

Hence, a low temperature solution-processed thin layer of ZnO has been chosen as the electron transport layer in this study to fabricate an environmentally stable inverted organic solar cell on ITO coated glass or metal substrates. The solution-processed ZnO electron transport layer effectively blocks holes and collects electrons from the PCBM. It requires no vacuum processing and is fabricated from inexpensive materials. Furthermore, the device performance can be improved because the ZnO layer provides the advantages of high quality surface of thin films, good wettability, and adhesion with the photoactive layer.

3.1.3 Hole transport layer (HTL)

The direct deposition of high work function metal electrode on top of the photoactive layer can reduce the photovoltaic performance due to the poor charge selectivity. For an efficient hole transport layer, the work function need to be large enough so that the Fermi levels of the interlayer match the HOMO levels of the active layer. The best hole transport layer material must provide an ohmic contact with the donor material for an efficient hole transport and have a strong electron blocking potential. The ideal hole transport layer needs to be stable and should not increase the device series resistance (R_S).

For top illuminated inverted organic solar cells devices on glasses or metal substrates, the hole transport layer needs to be optically transparent. There are several high work function materials including MoO_3 [22], WO_3 [23,24], V_2O_5 [25] and PEDOT:PSS [26,27] that have been utilized as a hole transport layers. In the literature, comparatively PEDOT:PSS is the widely used hole transport layer because of its easy fabrication with all the known solution processed techniques. The PEDOT:PSS is the mixture of two ionomers. One is the PEDOT which is a conjugated polymer and carries positive charges and the second is polystyrene sulfonate (PSS) that carries negative charges. The PEDOT:PSS is an aqueous dispersion and is difficult to form a thin film on top of the P3HT:PCBM active layer because of the hydrophobic property of the photoactive layer. The addition of co-solvent [26] and surfactant [28,29] is used to overcome this problem to obtain the interfacial compatibility. In this study, the Heraeus-Clevios PEDOT:PSS (HTL Solar) with a solid content percentage of 1.0-1.2 was chosen as the HTL layer material. The work function of the PEDOT:PSS is ~5.1eV that makes it form an ohmic contact between the photoactive organic and the high work function metal electrode.

3.1.4 Electrodes

Electrodes are the layers that deliver the photo-generated charges to the external circuit. The stability and the high conductivity are the key properties for the electrodes. In organic solar cells devices, one electrode must be optically transparent so that the solar radiation can reach to the photoactive layer. In most organic solar cells, the ITO thin film is used as the transparent conductive electrode while the conductive metal layer (Al, Au and Ag) is utilised as the rear electrode. The choice of the best electrode materials depends on the configuration and the energy band diagram corresponding to the active layer of the devices. Conventional and inverted configuration of organic solar cells needs different electrode materials for an efficient charge collection.

As compared to the conventional structure, the inverted structure uses a reflective and high-work-function electrode as the top hole-collecting contact and a transparent conducting electrode at the bottom for the collection of electrons. In this study, ITO coated glass substrates have been used electron collecting electrodes and the vacuum-deposited high work function metal (Au) is used as hole collecting electrodes. For an inverted device that is fabricated on non-transparent substrates (metal or glass/metal) substrates, finding the high work function optically transparent electrode with good properties is a challenge. In this study, the PEDOT:PSS in its high conductivity form has been selected as the hole collecting electrode for inverted organic solar cells that are fabricated on metal substrates [30,31]. Heraeus-Clevios high conducting PEDOT:PSS known as PH1000 is obtained from Ossila Limited UK.

3.2 Preparations

3.2.1 Solution preparation

10 wt% zinc oxide dispersion was obtained by mixing ~35 nm zinc oxide nanoparticles

(Sigma Aldrich) in a mixture (10:0.7) of methanol and dichloromethane (Sigma Aldrich). The ZnO colloid for the deposition of the electron collecting layer was prepared using the ball mill technique. For the sol gel based zinc oxide electron transport layer, 0.1M-0.4 M zinc acetate dihydrate (Sigma Aldrich) was dissolved in a mixture of 2-methoxyethanol and then ethanolamine was added as the stabilising agent. For the active layer deposition, different concentration e.g. 20 mg/ml, 30 mg/ml, 35 mg/ml and 40 mg/ml of P3HT (MERCK-Lisicon SP001) and PCBM (Solenne b.v.) were dissolved in different solvents such as chlorobenzene and dichlorobenzene. The as received dispersion of PEDOT:PSS from Heraeus-Clevios was used for deposition of the hole collecting layer. Triton X-100 (Sigma Aldrich) was added (~0.05%) to the PEDOT:PSS dispersion to increase the wettability on the active layer. Thin films were deposited using the spin coating technique.

3.2.2 Cleaning the substrates

Prior to the deposition of the thin films, rigorous cleaning of the substrate is essential for removing detrimental organic and inorganic impurities from the substrate. All metals and glass substrates were first cleaned with a liquid soap solution and then washed thoroughly with deionised water. The substrates were finally degreased ultrasonically in acetone and then isopropyl alcohol for 10 min at room temperature. Finally, the substrates were dried with either heating on hot plate or nitrogen-blowing.

3.2.3 Deposition of the thin films via spin coating

The spin coating method was used for the thin film deposition in this study. The spin coating equipment is the Sheen filmfuge-1110N spin coater. A coating process involves dropping a small amount of a solution (100 µl) at the centre of the 2 cm x 2 cm substrate

and then spinning the substrate at a given speed to get the required thickness. Centrifugal acceleration will cause the solution to spread first and then eventually off through the edge of the substrate leaving a thin film of solution on the substrate surface. Figure 3.2 shows the different steps involved in the spin coating process. Film properties and thicknesses depend on the nature of the solution (Viscosity, drying rate, solid content, surface tension, etc.) and the parameters of the spin process (rpm and spinning time).

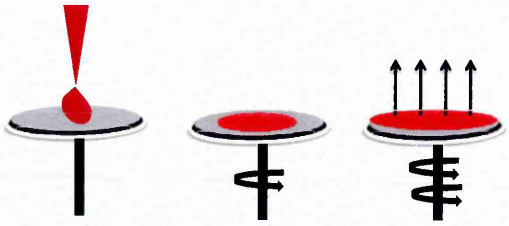

Figure 3.2 Different stages involved in spin coating, deposition of the solution, spin up, spin off and evaporation of the solvent

Factors of the spinning speed, acceleration, and the solvent evaporation rate contribute to how the properties of the formed film are defined. One of the most important factors in the spin coating is its reproducibility. Slight variation in the spin process parameters can result in the drastic variation in the formed thin film. Spin coating technique has been widely used in many aspects as mentioned below [32]:

- Organic thin films for solar cells, light emitting diode, flat panel displays and sensors.
- Photo-resist for defining patterns in microcircuit fabrication.
- Dielectric/insulating layers for micro electric fabrication.

- Flat screen display coating-antireflection coating, conductive oxide etc.

3.2.4 Deposition of the vacuum-technology-based electrodes

The top metal electrode is normally deposited by the vacuum method. One of the most common methods is thermal evaporation where the substrate is placed inside a vacuum chamber with the source material. The source material is heated to a point where it gets evaporated and condensed on the substrate to form a film. In this study, we used the plasma assisted physical vapour deposition method (PAPVD) to produce our electrodes. An important advantage of PAPVD is that the high melting point materials (Au, Pt and Ag) can simply be produced. The gold electrode was deposited onto the hole transport layer by the PAPVD instrument. The 99.99% pure gold target was used for Au deposition. The deposition chamber is equipped with a rotated sample holder to obtain the uniform film at a base pressure of $1x10^{-2}$ mbar.

The deposition method includes the strong electric and magnetic field close to the surface of the target. The intensity of the electric field can be adjusted by changing the deposition current that controls the deposition rate. The carrier gas is Argon with a flow rate of 18 psi. Under the electric field, the gas atoms became positively charged due to the escape of outer shell free electrons. These gas ions accelerate towards the negatively charged gold target and excite the gold target to inject the neutral particles. These particles travel towards the substrate to form the thin film of gold as the hole collecting electrode.

3.3 Characterisation techniques

3.3.1 UV-VIS-NIR spectrophotometer

A double beam Varian Inc. - Cary 50 UV-VIS spectrophotometer was used to measure the optical properties of the organic and other oxide thin films. The operating range of the spectrophotometer is from 190 nm to 1100 nm. A schematic diagram showing the principle of the UV-VIS spectrophotometer is given in Figure 3.3. The light source in this instrument is the xenon lamp and the resolution of the instrument is 1.5 nm in the UV-VIS region. In this instrument, light emitted from the source passes through a grating monochromator (for creating the monochromatic beam) and the beam passes

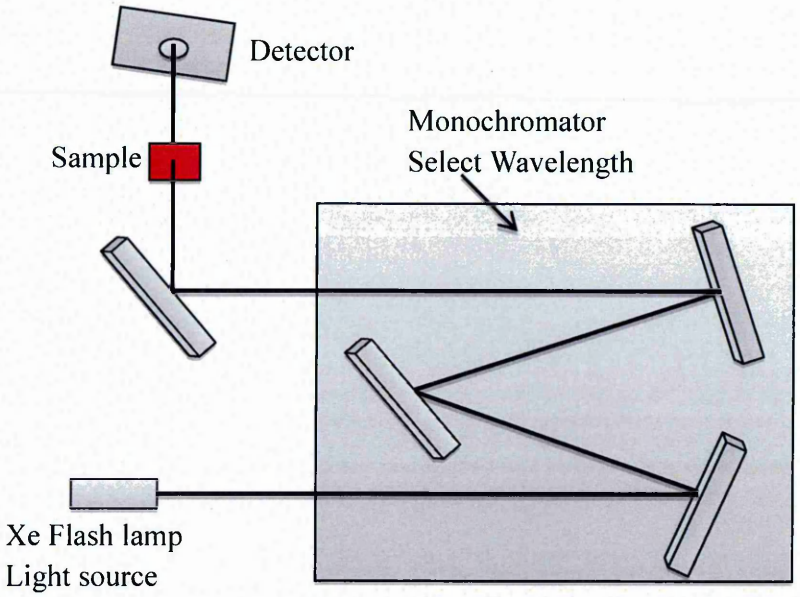

Figure 3.3 Experimental setup of UV-VIS Spectrophotometer

through the sample substrate. After passing through the sample compartment, the monochromatic beam gets converged and is converted into the electrical signal by the silicon diode detector. The electrical signal is then amplified and converted into the digital signal to obtain the optical spectra. Thin films of photoactive layers, ETLs and

HTLs on 2cm x 2cm glass substrate used for the characterisation of optical properties in the range of 300-800 nm. Baseline correction made with bare glass substrates.

3.3.2 Attenuated total reflectance- Fourier transform infrared spectroscopy (ATR-FTIR)

Attenuated total reflection spectroscopy (ATR-FTIR) is also referred as internal reflection spectroscopy (IRS). The principle of attenuated total reflection spectroscopy

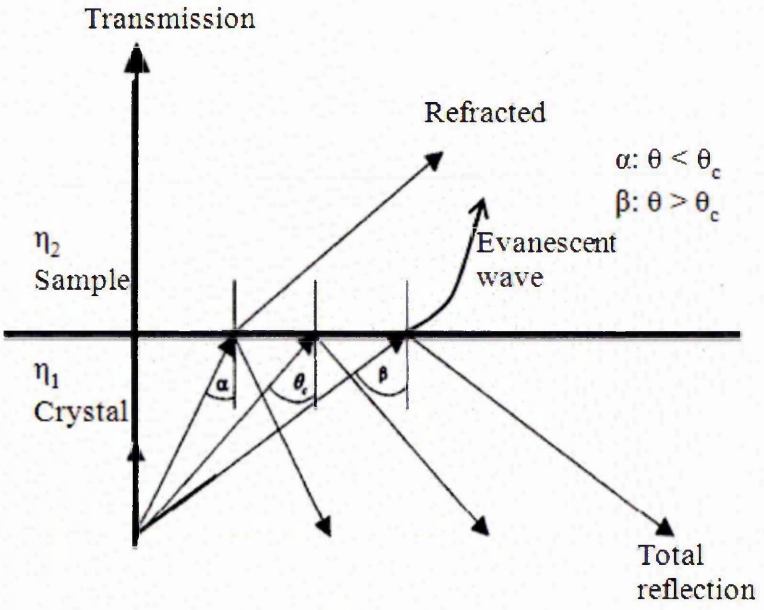

Figure 3.4 Schematic diagram of the behaviour of electromagnetic waves at the interface of two phases [33].

or internal reflection spectroscopy is that when a propagating wave of radiation incidents from an optically denser medium to an optically rarer medium, both of which are in contact, and then this vane undergoes the total internal reflection. The schematic diagram of the phenomenon internal reflection spectroscopy is shown in Figure 3.4.

When light propagates through the denser medium of the refractive index (η_1) to a rarer medium of the refractive index (η_2), the total internal reflection occurs at the interface of the denser and the rarer medium if the angle of incidence (θ) is greater than the critical wave angle (θ_c). Evanescent wave that arises at the interface of the denser and the rarer medium penetrates into the rarer medium (sample). The evanescent field generated by this wave decays exponentially into the rarer medium and has a component in all special directions. In case of ATR, the information obtained from a sample sitting on the top of ATR crystal is only up to 10 microns as the penetration depth of the evanescent wave is assumed to be about 8-10 microns. High reflective index materials (diamond, zinc selenide, silicon and germanium) are usually used to make the ATR crystal. A single reflection temperature controlled diamond ATR cell (Graseby Specac, UK) that is coupled to a Thermo Nicolet NEXUS FTIR spectrometer is used for this study.

The setup has a trade name as "Golden Gate" as shown in Figure 3.5. The headings 1 to 5 on the Figure show various parts of the golden gate. The samples are placed on the ATR crystal area and are fixed by a limiter torque head screw for the intimate contact between the sample and the ATR crystal. The clamp bridge is used to tight the torque head screw over the right place. The lens barrel is used to focus the IR beam over the entire ATR crystal face. The mirrors reflect the infrared radiation (IR) coming in from the IR source. After the internal reflection from the ATR crystal, the beam incident on the mirror and the reflected beam goes into the detector to get an interferogram, which is converted into a spectrum. Dry powder obtained by removing the film from the glass substrates used for the investigation of the FTIR.

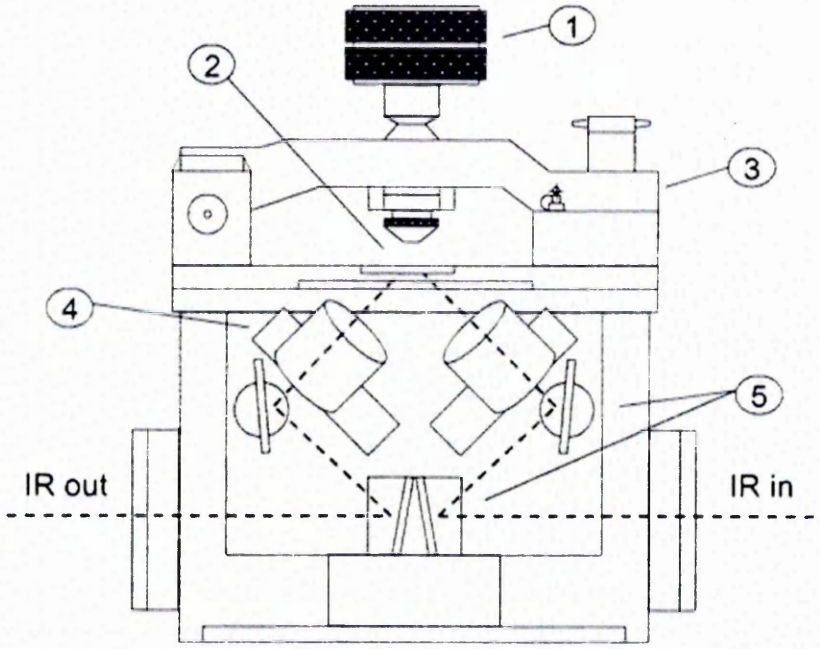

Figure 3.5 Schematic diagram of side view of the "Golden Gate":(1) torque head screw with limiter screw; (2) ATR crystal area; (3) clamp bridge; (4) lens barrel; (5) mirrors [33].

3.3.3 Electrical impedance spectroscopy (EIS)

Princeton Applied Research PARSTAT 2273 Advanced Electrochemical System was used to perform the electrical impedance spectroscopy (EIS) measurement of the OPV devices. The term impedance is the opposition to the flow of alternating current (AC) within the system. This technique is used to measure the frequency dependence of resistances, capacitances or constant phase elements and inductances that may be acting within the device. In the organic photovoltaic devices, the use of EIS is to measure the interface resistance between the photoactive layer and the electrodes. The experiment carried out by applying an AC test signal to the device with the direct current (DC) bias voltage under the dark condition. The value of the testing signal and the DC bias voltage are 100 mV and 0.6 V respectively with a frequency range of 1.0 Hz to 1.0 MHz.

The typical EIS data, as the so-called Nyquist plots, are analysed by the ZSimp 3.10 fitting software with an equivalent circuit to fit the experimental data. Each equivalent circuit is a parallel combination of resistance (R) and capacitance (C) as shown in Figure 3.6. In the equivalent circuit, R_s represents series resistance that arose due to the connection leads, metallic contact, etc and ω is the angular frequency which decreases from left to right.

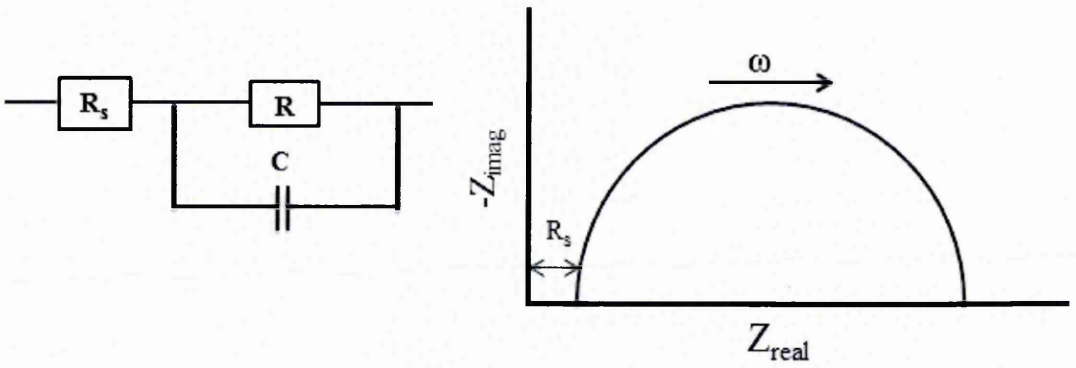

Figure 3.6 Example of equivalent circuit to fit the experimental data and the corresponding Nyquist plots

3.3.4 Scanning electron microscopy (SEM)

The scanning electron microscope (SEM) uses electrons rather than light to form an image of the surface. The combination of higher magnification, larger depth of focus and greater resolution makes the SEM one of the most widely used instruments. In a typical SEM, an electron gun produces an electron beam where electrons are accelerated with the potential of 5-20 kV and magnification can go up to more than 300,000 times. A fully computerised FEI Nova Nano 200 SEM is used for studying the morphological properties of the thin films. The electron beam produced by the electron gun is focussed by the lens mechanism onto a fine spot (diameter ~1 nm) on the specimen surface.

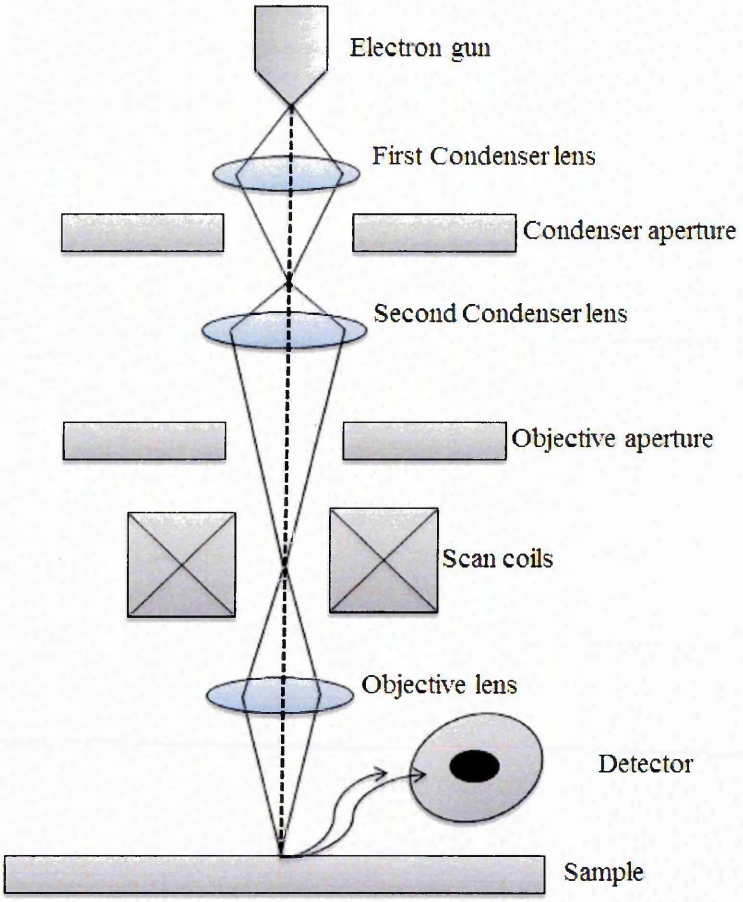

Figure 3.7 Schematic diagram of the imaging component of SEM

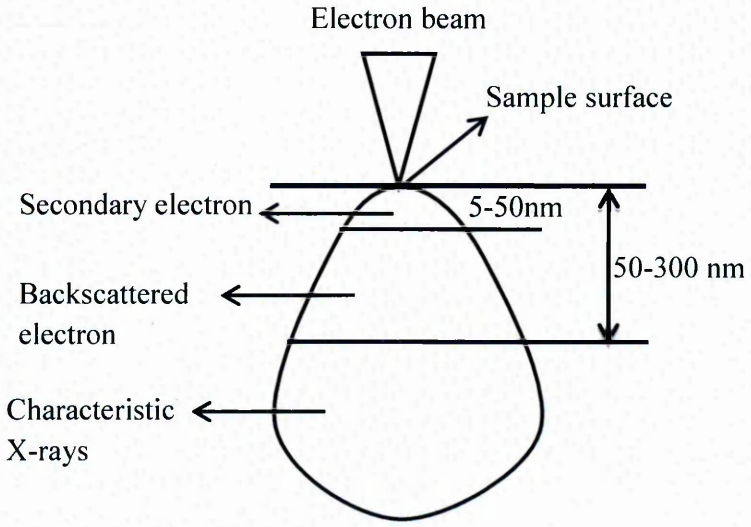

Figure 3.8 The interaction zone of electrons and sample atoms below a sample surface [34]

The schematic diagram showing the principle of SEM is given in Figure 3.7. Some electrons accelerate beyond the anode down the evacuated column towards the sample. The electron beam is then collimated by the condenser lens and is focused by the objective lens on the sample. The scan coils are energized by varying the voltage produced by the scan generator for creating a magnetic field, which deflects the electron beam back and forth in a controlled manner. The electron beam hits the sample, producing a wide variety of emissions as illustrated in Figure 3.8.

The secondary electrons from the sample are collected by a secondary electron detector or a backscatter electron detector. The secondary electron detector produces a voltage signal which gives the output at the PC after amplification provides the standard topographic image. The backscattered electrons that produced by the elastic interactions with the nuclei of the sample atoms provide information about the chemical composition of the materials. For SEM characterisation ~5mm x 5 mm sample stick to the metal disc by double sided tape. A very thin film of gold was deposited using Quorum gold coater to avoid the charging problem for nonconductive thin films and then Silver paste used to connect the top gold surface to the metal disc. We tested the surface morphologies of ETLs, active layer and metal substrates using SEM.

3.3.5 Atomic force microscopy (AFM)

Atomic force microscope (AFM) is a very high resolution type of instrument. An AFM has a very sharp tip, a few atoms wide at the end, attached to a micro-cantilever arm (Figure 3.9) that has the length at the order of 100-250 microns. A fully computerised digital instrument Nanoscope IIIa Atomic Force Microscope is used for studying the sample surface.

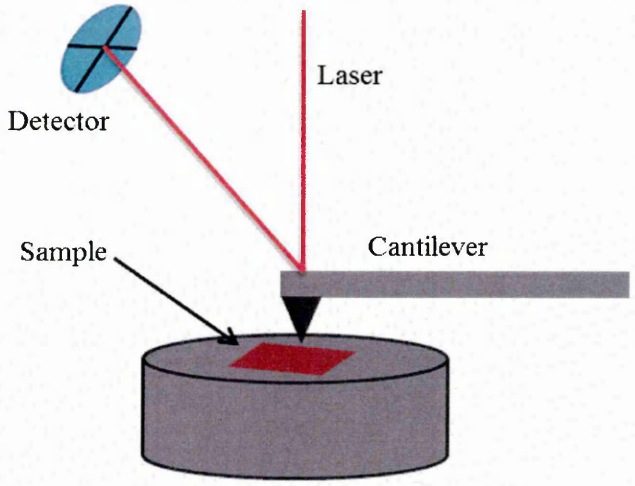

Figure 3.9 Schematic diagram of the operation of AFM

The basic objective of the operation of AFM is to measure forces (at the atomic level) between the sharp tip and the sample surface. The images are taken by scanning the sample relative to the probing tip and measuring the deflection of the cantilever as a function of lateral position. The typical force between the sample and the tip ranges from 0.5 to 1 nN. Among the various operating modes of AFM, the tapping mode was used for experiments because the tapping mode provides high resolution without inducing the destructive frictional force [34]. For AFM characterisation ~5mm x 5 mm sample stick to the metal disc by double sided tape. The metal disc placed on the magnetic substrate holder of AFM for morphological characterisation. We tested the surface morphologies of ETLs, HTLs and active layers using AFM.

3.3.6 X-ray diffraction (XRD) measurement

It is a non-destructive characterisation technique based on the elastic scattering of X-rays at a lattice and is used to study the structural properties of materials including

powders and thin films. The schematic diagram showing the principle of the glancing angle diffractometer (GAXRD) is given in Figure 3.10.

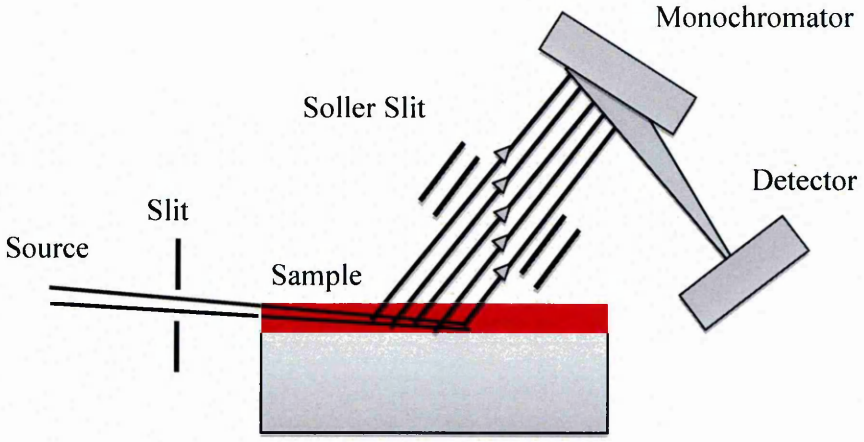

Figure 3.10 Schematic diagram of the Glancing angle X-ray diffraction

X-rays are generated when a high energy electron beam bombards on a copper target, emitting 8 keV X-rays, corresponding to a wavelength of 0.154 nm. Choosing a fixed, low angle of incidence (Glancing angle geometry) for the X-ray beam makes the analysis more sensitive to the maximum sample area and helps minimise the contribution from the substrate. In glancing angle X-ray diffraction geometry, the incident angle α is fixed and 2θ arm will rotate on the goniometer circle. If we consider the parallel lattice planes spaced d apart, the constructive interference of the radiation from the successive planes occurs when the path difference is an integral number 'n' of X-ray wavelength λ, so that $2d_{hkl}\ Sin(\theta) = n\lambda$, where $2d_{hkl}\ Sin(\theta)$ is the path difference for X-rays reflected from the adjacent plane as illustrated in Figure 3.11. In this study, Philips X'Pert XRD is used to study the thin film samples. The characteristics of X-rays generated from the X-ray source are narrowed by a vertical divergence slit and then made incident on samples at a fixed glancing angle. The diffracted X-rays from the sample are allowed to pass through the parallel soller slit assembly.

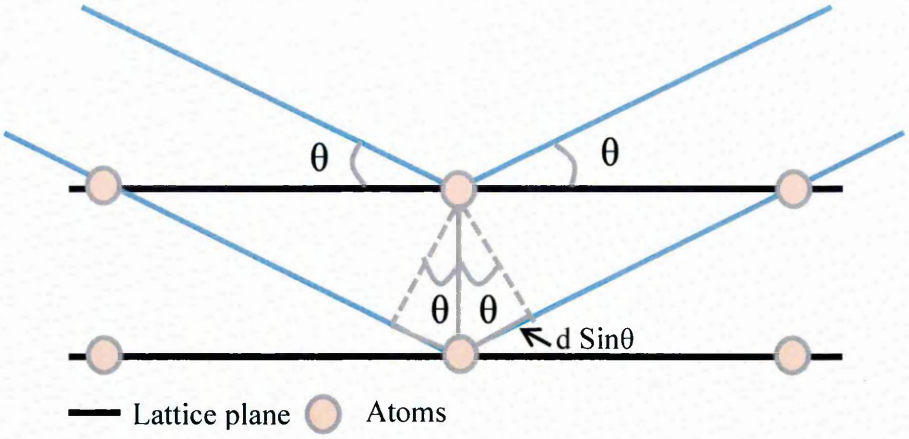

Figure 3.11 Schematic representation of X-ray diffraction in a crystalline lattice

The parallel beam of X-rays is further reflected by a monochromator to allow only Cu K_α radiation to reach the detector and diffraction pattern is then obtained that is directly related to the atomic spacing. The electronic signal from the detector is connected to the personal computer which provides the data output [34]. We studied the structural characterisation of P3HT:PCBM photoactive layer on glasses in the 2θ range of 4 to 14° with a step size of 0.017°.

3.3.7 Contact angle measurement

Contact angle measurement studies usually involve the measurement of contact angles when a solid and liquid comes into interaction. If the contact angle is small (<<90°) means wettability will be high, while for large contact angles (>>90°) wettability will be low. The intersection of the liquid-solid and the liquid-vapor interfaces is defined as the contact angle. The contact angle is determined by a combination of surface tension and external forces (usually gravity). The shape of the droplet depends on the contact angle which is measured by Young's relation [35].

$$\gamma_{lv} \cos \theta = \gamma_{sv} - \gamma_{sl}$$

Where γ_{lv}, γ_{sv}, and γ_{sl} represent the liquid-vapor, solid-vapor, and solid-liquid interfacial tensions, respectively, and θ is the contact angle.

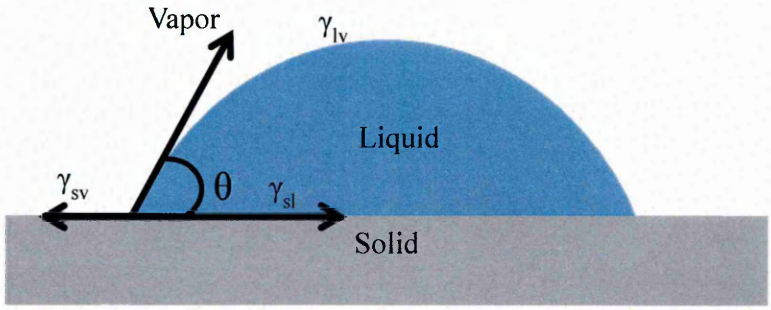

Figure 3.12 Schematic representation of the contact angle measurement method

In this method we used dataphysics OCA 15EC contact angle measurement where horizontal camera capture the image of the droplet and θ will be calculated by the slope of the droplet tangent as illustrated in Figure 3.12. For this experiment we measured the contact angle of PEDOT:PSS on top of P3HT:PCBM photoactive layer.

3.3.8 Current voltage characteristics

Current-voltage (I-V) characteristics reveal how solar cells would operate under solar illumination as shown in Figure 3.13. I-V characterisation setup has a sample stage, a source meter and a calibrated light source which provides an illumination intensity of 100 mW/cm^2. The source meter provides the bias voltage and records the corresponding current when the device is illuminated by the calibrated light source. Solar cells output the power when the applied bias and current are opposite in directions and the detailed analysis has already explained in 2.4.4.

The most important parameter of OSCs is the power conversion efficiency, which is determined as

$$PCE\ (\eta) = \frac{V_{oc} \times J_{sc} \times FF}{P_{light}}$$

V_{oc} - Open circuit voltage, J_{sc} - Short circuit current density, FF- Fill factor and P_{light} - Intensity of light. FF is calculated by the following equation.

$$Fill\ factor\ (FF) = \frac{V_{max} \times J_{max}}{V_{oc} \times J_{sc}}$$

Where V_{max} and J_{max} are the value of voltage and current density at maximum power.

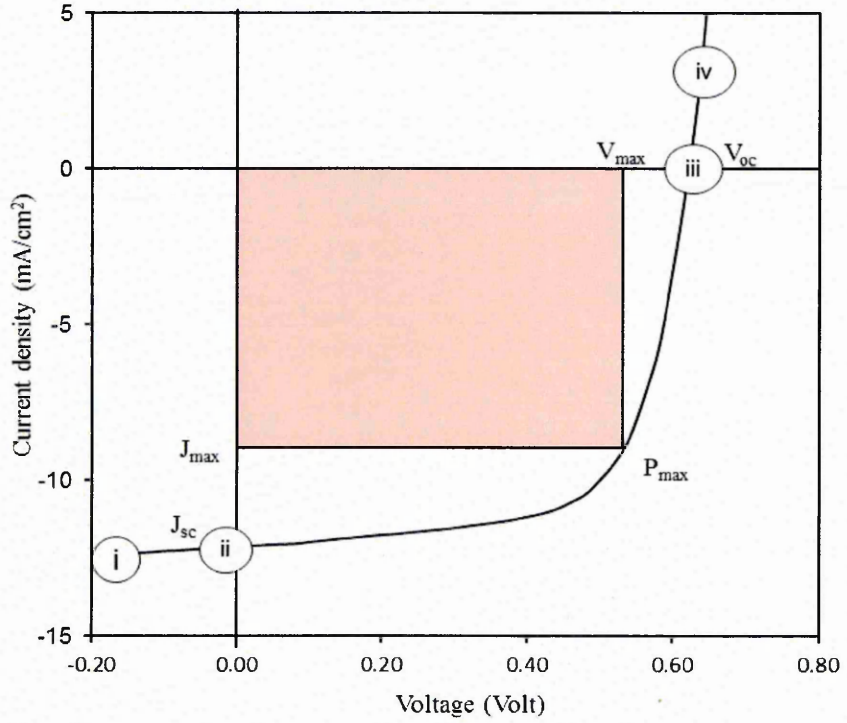

Figure 3.13 Schematic representation of I-V curve under illumination

The J-V characteristic of the inverted OSC devices was recorded with Keithley source meter and Bentham solar simulator. For bottom illuminated inverted OSC devices on ITO coated glass substrates, incident light reached to the P3HT:PCBM photoactive layer through glass side. Whereas for top illuminated inverted OSC devices on metals,

light reaches to the P3HT:PCBM photoactive layer through hcPEDOT:PSS side, which is working as the hole collecting anode. The tested active area of the OSC devices decided with help of metal shadow mask.

3.3.9 External quantum efficiency

External quantum efficiency (EQE) is the ratio of the number of charge carriers collected by the solar cell to the number of photons of a given energy incident on the solar cells. Therefore, EQE depends on both the absorption of light and the collection of charges. Once the photo-induced electron-hole pairs have been generated, these charges must be separated and then collected at the respective electrodes without recombination. Charge recombination is the main cause to decrease the EQE.

The external quantum efficiency (η_{EQE}) of organic solar cells is given by

$$\eta_{EQE} = \eta_A \times \eta_{Diff} \times \eta_{Diss} \times \eta_C$$

Where η_A- efficiency of incident photon absorption

η_{Diff} - efficiency of the photo-induced exciton diffusion at heterojunction

η_{Diss} -efficiency of the exciton dissociation at heterojunction to form geminate pairs

η_C -efficiency of the carrier transport and the carrier collection at electrodes

The internal quantum efficiency (η_{IQE}) can be written as

$$\eta_{IQE} = \frac{\eta_{EQE}}{\eta_A} = \eta_{Diff} \times \eta_{Diss} \times \eta_C$$

3.4 References:

[1] M. T. Dang, L. Hirsch, G. Wantz, P3HT:PCBM, Best Seller in Polymer Photovoltaic Research, Adv. Mater., 23 (2011) 3597-3602.

[2] I. F. Perepichka, D. F. Perepichka, H. Meng, F. Wudl, Light-Emitting Polythiophenes, Adv. Mater., 17 (2005) 2281-2305.

[3] Y. N. Li, G. Vamvounis, S. Holdcroft, Tuning Optical Properties and Enhancing Solid-State Emission of Poly(thiophene)s by Molecular Control: A Postfunctionalization Approach, Macromolecules., 35 (2002) 6900-6906.

[4] A. Zen, J. Pflaum, S. Hirschmann, W. Zhuang, F. Jaiser, U. Asawapirom, J. P. Rabe, U. Scherf, D. Neher, Effect of Molecular Weight and Annealing of Poly(3-hexylthiophene)s on the Performance of Organic Field-Effect Transistors, Adv. Funct. Mater., 14 (2004) 757-764.

[5] H. C. Yang, T. J. Shin, L. Yang, K. Cho, C. Y. Ryu and Z. N. Bao, Effect of Mesoscale Crystalline Structure on Field-Effect Mobility of Regioregular Poly(3-hexyl thiophene) in Thin Film Transistors, Adv. Funct. Mater., 15 (2005) 671–676.

[6] S. Yang, N. Zhao, L. Zhang, H. Zhong, R. Liu, B. Zou, Field-effect transistor-based solution-processed colloidal quantum dot photo detector with broad bandwidth into near-infrared region, Nanotechnology., 23 (2012) 255203.

[7] Y. Kim, S. Cook, S. M. Tuladhar, S. A. Choulis, J. Nelson, J. R. Durrant, D. D. C. Bradley, M. Giles, I. McCulloch, C. S. Ha, M. Ree, A strong regioregularity effect in self-organizing conjugated polymer films and high-efficiency polythiophene:fullerene solar cells, Nat. Materials., 5 (2006) 197 - 203.

[8] G. Li, V. Shrotriya, Y. Yao, J. Huanga Y. Yang, Manipulating regioregular poly(3-hexylthiophene) : [6,6]-phenyl-C61- butyric acid methyl ester blends—route towards high efficiency polymer solar cells, J. Mater. Chem., 17 (2007) 3126–3140.

[9] W. Y. Huang, C. C. Lee, S. G. Wang, Y. K. Han, M. Y. Chang, Side Chain Effects of Poly(3-alkylthiophene) on the Morphology and Performance of Polymer Solar Cells, J. Electrochem. Soc., 157 (2010) B1336-B1342.

[10] J. C. Hummelen, B. W. Knight, F. LePeq, Fred Wudl, Preparation and characterization of fulleroid and methanofullerene derivatives, J. Org.Chern., 60 (1995) 532-538.

[11] W. C. H. Choy, Organic solar cells: Material and device physics, Springer-Verlag London 2013.

[12] H. Li, J. Wang, H. Liu, H. Zhang, and X. Li, Zinc oxide films prepared by sol–gel method, Growth, 275 (2005) 943.

[13] S. K. Hau, H. L. Yip, N. S. Baek, J. Y. Zou, K. O'Malley, A. K. Y. Jen, High performance ambient processed inverted polymer solar cells through interfacial modification with a fullerene self-assembled monolayer, Appl. Phys. Lett., 2008, 92, 253301.

[14] A. L. Roest, J. J. Kelly, D. Vanmaekelbergh, E. A. Meulenkamp, Staircase in the Electron Mobility of a ZnO Quantum Dot Assembly due to Shell Filling Phys. Rev. Lett. 89 (2002) 036801.

[15] J. Boucle, P. Ravirajan, J. Nelson, Hybrid polymer–metal oxide thin films for photovoltaic applications, J. Mater. Chem., 17 (2007) 3141-3153.

[16] K. S. Shin, H. J. Park, B. Kumar, K. K. Kim, S. G. Ihn, S. W. Kim, Low-temperature growth and characterization of ZnO thin films for flexible inverted organic solar cells, J. Mater. Chem., 21 (2011) 12274-12279.

[17] J. A. Sans, A. Segura, M. Mollar, B. Mari, Optical properties of thin films of ZnO prepared by pulsed laser deposition, Thin Solid Films, 453 (2004) 251-255.

[18] B. S. Ong, C. S. Li, Y. N. Li, Y. L. Wu, R. Loutfy, Stable, Solution-Processed, High-Mobility ZnO Thin-Film Transistors, J. Am. Chem. Soc., 129 (2007) 2750-2751.

[19] J. Gilot, I. Barbu, M. M. Wienk, R. A. J. Janssen, The Use of ZnO as Optical Spacer in Polymer Solar Cells: Theoretical and Experimental Study, Appl. Phys. Lett., 91, (2007) 113520.

[20] R. E. Marotti, D. N. Guerra, C. Bello, G. Machado, E. A. Dalchiele, Bandgap energy tuning of electrochemically grown ZnO thin films by thickness and electrodeposition potential, Sol. Energy Mater. Sol. Cells., 82 (2004) 85-103.

[21] M. S. White, D. C. Olson, S. E. Shaheen, N. Kopidakis, D. S. Ginley, Inverted Bulk-Heterojunction Organic Photovoltaic Device Using A Solution-derived ZnO Under layer, Appl. Phys. Lett., 89 (2006) 143517.

[22] C. Tao, S. P. Ruan, X. D. Zhang, G. H. Xie, L. Shen, X. Z. Kong, W. Dong, C. X. Liu, W. Y. Chen, Performance improvement of inverted polymer solar cells with different top electrodes by introducing a MoO3 buffer layer. Appl. Phys. Lett., 93 (2008) 193307-1993307.

[23] C. Tao, S. P. Ruan, G. H. Xie, X. Z. Kong, L. Shen, F. X. Meng, C. X. Liu, X. D. Zhang, W. Dong, W. Y. Chen, Role of tungsten oxide in inverted polymer solar cells. Appl. Phys. Lett., 94 (2009) 043311-043313.

[24] M. Y. Chan, C. S. Lee, S. L. Lai, M. K. Fund, F. L. Wong, H. Y. Sun, K. M. Lau, S. T. Lee, Efficient organic photovoltaic devices using a combination of exciton blocking layer and anodic buffer layer. J. Appl. Phys., 100 (2006) 094506-094504.

[25] J. S. Huang, C. Y. Chou, M. Y. Liu, K. H. Tsai, W. H. Lin, C. F. Lin, Solution-processed vanadium oxide as an anode interlayer for inverted polymer solar cells hybridized with ZnO nanorods. Org. Electron., 10 (2009) 1060-1065.

[26] C. Waldauf, M. Morana, P. Denk, P. Schilinsky, K. Coakley, S. A. Choulis, C. J. Brabec, Highly efficient inverted organic photovoltaics using solution based titanium oxide as electron selective contact. Appl. Phys. Lett., 89 (2006) 3-233517.

[27] Y. J. Cheng, C. H. Hsieh, Y. He, C. S. Hsu, Y. Li, Combination of indene-c60 bis-adduct and cross-linked fullerene interlayer leading to highly efficient inverted polymer solar cells. J. Am. Chem. Soc., 132 (2010) 17381-17383.

[28] W. R. Wei, M. L. Tsai, S. T. Ho, S. H. Tai, C. R. Ho, S. H. Tsai, C. W. Liu, R. J. Chung, J. H. He, Above-11%-Efficiency Organic–Inorganic Hybrid Solar Cells with Omnidirectional Harvesting Characteristics by Employing Hierarchical Photon-Trapping Structures, Nano Lett., 13 (2013) 3658-3663.

[29] F. J. Lim, K. Ananthanarayanan, J. Luther, G.W. Ho, Influence of a novel fluorosurfactant modified PEDOT:PSS hole transport layer on the performance of inverted organic solar cells, J. Mater. Chem., 22 (2012) 25057-25064.

[30] Y. F. Lim, S. Lee S, D. J. Herman, M. T. Lloyd, J. E. Anthony, G. G. Malliaras, Spray-deposited poly(3,4-ethylenedioxythiophene):poly(styrenesulfonate) top electrode for organic solar cells. Appl. Phys. Lett., 93 (2008) 193301-193303.

[31] Y. Zhou, H. Cheun, S. Choi, J. W. J. Potscavage, C. F.Hernandez, B. Kippelen, Indium tin oxide-free and metal-free semitransparent organic solar cells. Appl. Phys. Lett., 97 (2010) 3-153304.

[32] W. Ki, Synthesis, characterization, and film fabrication of inorganic and hybrid semiconductor materials for optoelectronic applications, Rutgers The State University of New Jersey - New Brunswick. Graduate School - New Brunswick.

[33] A. Tuchbreiter, J. Marquardt, J. Zimmermann, P. Walter, R. Mülhaupt, High Throughput Evaluation of Olefin Copolymer Composition by Means of Attenuated Total Reflection Fourier Tranform Infrared Spectroscopy, J. Comb. Chem., 3 (2001) 598-603.

[34] Y. Leng, Material Characterization-Introduction to microscopic and Spectroscopic Methods, John Wiley & Sons (Asia) Pte Ltd (2008).

[35] T. Young, An essay on the cohesion of fluids, Philos. Trans. R. Soc. Lond., 95 (1805) 65-87.

4.1 Introduction

This chapter describes the preparation and optimisation of different layers: i.e. ETLs, P3HT:PCBM active layers, HTLs and their applications in the bulk heterojunction OSCs. OSCs compose of the active layer (P3HT:PCBM) that is sandwiched between the transparent metal oxide (ITO) electrode and the metal thin film electrode. In the inverted OSC devices, the ITO electrical conducting film works as electron collecting electrode (cathode) and the metal thin film works as hole collecting electrode (anode).

In principle, ITO can collect either electrons or holes because its work function lies between the typical HOMOs and LUMOs of the common OSC materials. However, the polarity of ITO needs to be modified for an efficient collection of electrons. In the inverted OSC devices, the low work function ETL is deposited on top of the ITO film to modify the ITO interface for the efficient electron collection. ZnO thin film has been one of the most commonly utilised ETL materials in the inverted OSCs. Different approaches have been studied to optimise the ZnO ETL. In general, there are two ways to deposit the ZnO layer via the solution-based process. The straight way is to use the ZnO NPs dispersion in either the water-based or organic solvent based solution. The NPs based ZnO dispersion is very unstable if without an appropriate additive. However, adding the additives in the solution may affect the electrical property of the ZnO film when the formed ZnO thin film is only cured at low temperature. Hence, the sol-gel processed ZnO ETL was further studied and deposited at low temperature of ~150°C. The devices fabricated from the sol-gel based ZnO ETL on the ITO coated glass showed a PCE of 1.8% that is nearly the same as that obtained from the ZnO NPs based ETL on the ITO coated glass with an efficiency of 1.85%.

In order to achieve high efficiency inverted OSC devices, optimisation of the P3HT:PCBM active layers is very important. The parameters like concentrations, material ratios, solvents used, and film thicknesses play a major influence on the device performance for an efficient OSC. The active layer is deposited inside the glove box using the spin coating method to prevent oxidation. In the inverted configuration, the HTL is deposited on top of the active layer for an efficient hole transportation to the metal electrode. The electrical conducting organic PEDOT:PSS was chosen in our studies. The PEDOT:PSS solution is an aqueous dispersion and very difficult directly to coat the hydrophobic active layer of the P3HT:PCBM thin film that presented very high contact angle. Thus, the PEDOT:PSS solution was modified by adding a small amount of surfactant, which significantly reduced the contact angle. All these work were divided into different sections below according to the fabricated device configuration. Finally, the inverted OSC device after optimisation has reached a PCE of ~2.3%.

4.2 Solution preparation for thin films of the ETLs, active layer and HTLs

4.2.1 Preparation of the NPs and sol gel based solutions for the ZnO layer

In this study, dispersion of the ZnO NPs in the solution is a big challenge because nanoparticles can agglomerate together due to their high surface energy. The alcoholic solvents (e.g. ethanol or methanol) are the widely used dispersion medium for the ZnO NPs because of their high vaporisation rate. Water can also be used as the dispersion medium; however, dispersing the ZnO NPs in water is more difficult than that in the solvent-based solution. It has also been found that agglomeration of ZnO NPs is much faster in water than that in the alcoholic solvents [1]. We studied different solvents for the ZnO NPs (size <35 nm) dispersion as described in Table 4.1.

Table 4.1 Solution details of the ZnO NPs thin films

Solution name	Concentration	Solvents	Properties
ZNP1	10 wt.%	Chlorobenzene	Very poor stability
ZNP2	10 wt.%	Ammonium hydroxide	No dispersion
ZNP3	10 wt.%	Methanol	Poor stability
ZNP4	10 wt.%	Methanol and dichloromethane	Stable for 1-2 days
ZNP5	10 wt.%	Methanol and dichloromethane by the ball mill	Stable for 2 weeks
ZNP6	10 wt.%	Methanol and dichloromethane with a 3% PEO additive	Stable for 2 weeks
ZNP7	10 wt.%	Methanol and dichloromethane with a 3% GPTS additive	Stable for 2 weeks
ZNP8	10 wt.%	Methanol and dichloromethane with a 3% MPTS additive	Stable for 2 weeks
ZNP9	10 wt.%	Methanol and dichloromethane with 3% PEO plus 3% MPTS	Stable for 2 weeks
ZNP10	50 wt.%	Water with APTS	Stable

PEO- polyethylene oxide
GPTS- glycidoxy-propyl-trimethoxy-silane
MPTS- methylpropyl tryethoxy silane
APTS-3-Aminopropyl triethoxysilane

A 10 wt% dispersion of ZnO NPs in chlorobenzene (ZNP1), ammonium hydroxide (ZNP2) and methanol (ZNP3) was obtained respectively by a continuous stirring for 24 hrs. The stability of these dispersions was very poor. Dispersion ZNP4 was achieved by a combination of methanol and dichloromethane (at the ratio of 10:0.7) under a continuous stirring for 24 hrs. ZNP4 was used to make the ZnO NPs thin film by the

spin-coating method on the glass substrates and then annealed at temperature of 150 °C for 10 min on a hot plate. ZNP5 was obtained via further modification to the ZNP4 using the ball mill technique where the ZnO NPs were first dispersed in the solvent medium, stirred, and then ball- milled for 48 hrs. The final dispersion ZNP5 was stable for 2 weeks.

This fabricating procedure was also used to make ZNP6, ZNP7, ZNP8, and ZNP9, separately. A number of stabilising agents like PEO (in ZNP6), GPS (in ZNP7), MPTS (in ZNP8) and their combination (in ZNP9) have been studied to increase the stability of the NPs solution. For a comparative study, the commercially available aqueous dispersion of ZnO NPs supplied by the Sigma Aldrich was also used to deposit the electron transport layer ; i.e. ZNP10 where 3-aminopropyl triethoxysilane was used as the additive. For deposition of the very thin film, the ZNP10 dispersion was further diluted to 20 times by deionised water under the vigorous stirring. The ZnO films were deposited using the spin coating method and then annealed at temperature of 150 °C for 10 min. For the sol gel based ZnO thin film, the initial ZnO sol was made by dissolving zinc acetate dehydrate in 2-methoxyethanol and then ethanolamine was added as the stabilising agent. The molar ratio of zinc acetate to ethanolamine is at 1:1. Different concentrations of zinc acetate dehydrate were used to optimise the ZnO thin films. Details of different ZnO sols are listed in Table 4.2.

Table 4.2 Solution details for the sol gel based ZnO thin films

Sample name	Concentration	Solvents
ZSG1	0.1M	2-methoxyethanol and ethanolamine
ZSG2	0.2M	2-methoxyethanol and ethanolamine

ZSG3	0.3M	2-methoxyethanol and ethanolamine
ZSG4	0.4M	2-methoxyethanol and ethanolamine

4.2.2 Preparation of the P3HT:PCBM blend solution for the active layer

4.2.2.1 Selection of the solvent for the P3HT:PCBM blend

Among several conjugated organics, P3HT and fullerene PCBM are the most studied donor and acceptor materials. The blend of P3HT and PCBM form the active layer of the OSC devices with a common solvent. Most of the OSCs devices consist of a single BHJ active layer. The morphology of the active layer depends mainly on two factors: the first is the molecular organisation between the donor and the acceptor phase; the second is the nano scale phase separation between the donor and acceptor which affects the mobility of charge carriers and influences exciton dissociation and charge transportation.

The impact on morphologies using different solvents including chlorobenzene (CB), trichlorobenzene (TCB), chloroform ($CHCl_3$), toluene (T), ortho-dichlorobenzene (ODCB) and tetrahydronaphthalene (THN) has been widely investigated by researchers [4]. The evaporation rate of the solvent is very important to the morphology of the active layer, which depends on the boiling point of the solvent. A low evaporation rate of the solvent leads to high carrier mobility due to the enhancement of the segregated bi-continuous network of the P3HT and PCBM blend. However, the reported efficiency when using the high boiling point solvents; e.g. THN and TCB is not very high, which is attributed to the difficulty on removing the residual solvent in the active layer that can affect the nano scale interpenetrating networks within the photoactive layer [4]. The commonly used solvents were CB and ODCB in the literatures for the preparation of the active layer blend. Both solvents (CB and ODCB) were studied for the preparation of

active layers. Figure 4.1 (a &b) shows the photos of the deposited films using ODCB and CB as the casting solvent by the spin-coating method. The film deposited by the ODCB casting blend shows a non-uniform surface, while the film made using the CB casting blend is very uniform and smooth. Furthermore, the boiling point of ODCB is higher at 182.0°C than that of CB at ~131.0 °C, which makes it difficult to remove from the active layer. In contrast to in ODCB, the solubility of the P3HT was not as good as in CB. Therefore, CB was chosen as the casting solvent for our studies.

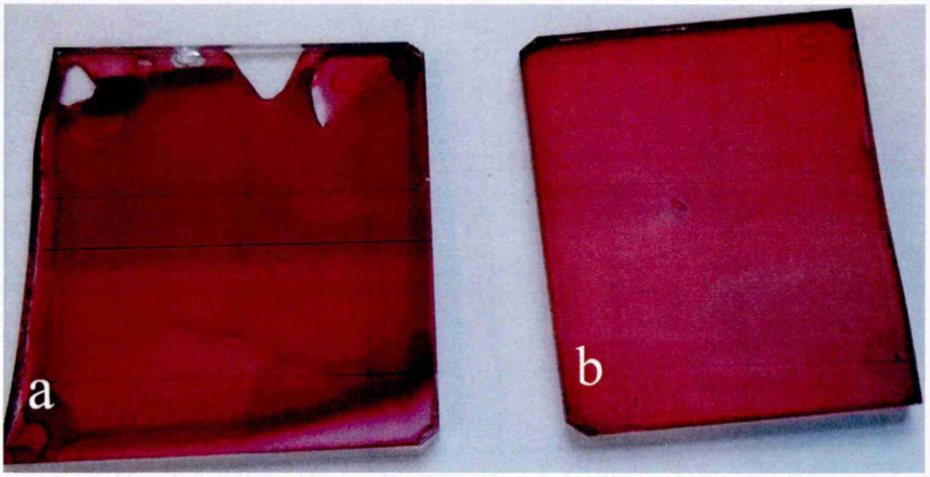

Figure 4.1 Photos of the deposited active layers using different casting solvents; (a) ODCB, (b) CB.

4.2.2.2 Preparation of the CB-based P3HT:PCBM blend solution

The active layer is affected by various parameters like materials, material ratios, drying conditions, and annealing procedures at different temperatures. One of the critical parameters that significantly affect the device performance is the thickness of the active layer. The preparation method and procedure for the P3HT and PCBM also play an important role in affecting the film structure of the P3HT:PCBM blend. In this study, P3HT and PCBM mixture was stirred overnight at temperature of 70 °C using the

magnetic stir bar on the hotplate at the weight ratio of 1:1. [5] The thicknesses of the active layers were optimised by altering the concentrations of the P3HT and PCBM in the solvent. Details of different concentrations of the P3HT:PCBM in CB are listed in Table 4.3.

Table 4.3 Solution details for different P3HT:PCBM thin films

Blend solution name	P3HT:PCBM concentration (mg/ml)	Solvent
CB1	10:10	Chlorobenzene
CB2	15:15	Chlorobenzene
CB3	17.50:17.50	Chlorobenzene
CB4	20:20	Chlorobenzene

4.2.3 Preparation of the PEDOT:PSS solution for the hole transport layer

The co-organic PEDOT:PSS is an electrochemically stable conjugated organic and widely used as HTL in the OSC devices. The oxidised (doped) state of the PEDOT:PSS presents very high electrical conductivity (< 100 Ω/square) and can be used as the hole collecting electrode as well. In the inverted configuration, a thin film of the PEDOT:PSS is deposited on top of the organic active layer as the HTL for improvement of the anode contact. This process eliminates the direct contact between the active layer and the electrode for prevention of the inter-diffusion. However, the commercial PEDOT:PSS formulation (H.C. Starck CLEVIOS) is an aqueous dispersion and exhibits very poor wettability on the hydrophobic organic active layer of the P3HT:PCBM. Thus, the commercial aqueous PEDOT:PSS solution cannot be directly applied on the surface of the P3HT:PCBM by the spin-coating technology. Many methods have been reported to solve this problem, including treatment of the active layer using mild plasma etching,

insertion of an interlayer between the active layer and the PEDOT:PSS layer, and modification of the wettability of the PEDOT:PSS layer by doping surfactants in the solution; e.g. Triton X-100, Zonyl, D-sorbital, isopropanol and n-butyl alcohol [6-12]. Plasma treatment of the P3HT:PCBM layer makes the surface becoming hydrophilic which needs to be carefully controlled without damaging the surface of the P3HT:PCBM film and unsuitable for large scale industrial applications. The insertion of an interlayer increases one more step in the fabrication process and alters the interfacial property between the PEDOT:PSS and the active layer. Doping the surfactant into the solution is the simplest way to change the wettability of the PEDOT:PSS solution to the organic active layer.

Triton X-100 and Zonyl FS 300 does not change the concentration of PEDOT:PSS solution because of very low volume of surfactant addition (~.05%). Triton X-100 was selected and used as the surfactant in our PEDOT:PSS solution. Very small volume of the surfactant (~0.05%) was added in the PEDOT:PSS aqueous solution, which had a negligible effect on the property of the PEDOT:PSS solution. The PEDOT:PSS thin film was deposited by the spin-coating method. Details of different solutions with and without the added surfactants are listed in Table 4.4. Contact angle measurements of the PDS1 and PDS2 on the P3HT:PCBM layer were carried out. Figure 4.2 shows the tested results.

Table 4.4 Solution details for the preparation of HTLs.

Solution name	PEDOT:PSS solid content	Surfactant additive
PDS1	1-1.2%	No additive
PDS2	1-1.2%	~.05%

The contact angle for PDS1 is near to 74.8 ± 4.0° in Figure 4.2 (a), making it very difficult to obtain a uniform film on top of the P3HT:PCBM active layer. The PDS2 shows a significantly lower contact angle at 39.0 ± 3.0° in Figure 4.2 (b). The improved wettability of the PEDOT:PSS solution on top of the hydrophobic P3HT:PCBM active layer can allow the uniform PEDOT:PSS thin film prepared .

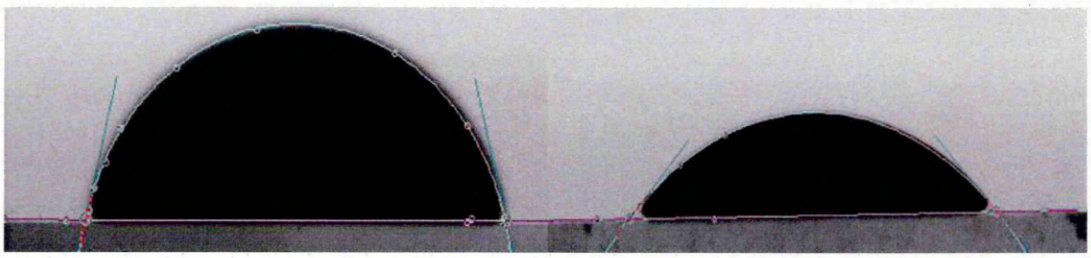

Figure 4.2 Contact angle measurements of a droplet of the PEDOT:PSS solution on the surface of the P3HT:PCBM; (a) by PDS1; (b) by PDS2.

4.3 Results and discussion

4.3.1 Morphologies of the ZnO and P3HT:PCBM thin films

4.3.1.1 Morphologies of the ZnO NPs thin films

Zinc oxide is one of the most widely used electron transport materials in the inverted organic solar cells. The dispersion properties of the ZnO NPs in ZNP1 and ZNP2 were very poor as shown in Figure 4.3 (a) & (b). The ZnO NPs quickly settled down in the bottom and showed a shelf-life of only a few hours. The stability of the dispersion ZNP3 (Figure 4.3 (c)) was slightly better than that of the ZNP1 and ZNP2; however, some ZnO NPs aggregates can be observed in the bottom of the dispersion solution after settlement for a few hours. The combination of methanol and dichloromethane solvents under the vigorous stirring produced the well-dispersed solution ZNP4 as shown in Figure 4.3 (d); however, the stability was still not very good. Figure 4.4 (a) shows the SEM image of the ZNP4-deposited thin film where the ZnO NPs did not form a uniform

distribution, illustrating very high porosity. The non uniform and very porous film may affect the properties of the ZnO thin film by reducing the shunt resistance of the OSC device. Therefore, further modification is required to achieve a stable dispersion for producing a uniform thin film. The high surface energy of the small sized particles needs to be overcome to obtain the stable dispersion of nanoparticles in solutions. Figure 4.4 (b) presents the SEM image of the ZnO NPs thin film deposited by the dispersion ZNP5 as shown in Figure 4.3 (e). The deposited thin film is still porous and shows different sizes and shapes of nanoparticles; however, the ZnO NPs were uniformly distributed in the thin film.

A potential benefit from the porous enhances the charge collection efficiency due to the reduced distance to the electron collecting layer. However, there were some pores showing big sizes around 50-100 nm. Very big sized pores can cause the active layer directly being contacted by the ITO electrode. In this case, it had disadvantages of reducing the hole blocking potential of the ZnO thin film. Therefore, the size of the pores required to be further modified via the dispersion route by adding the stabilizing (or binding) agent into the dispersion medium for obtaining more uniformly distributed, stable NPs dispersion. Figure 4.5 shows the SEM images of the ZnO thin films on the glass substrate with different additives. Figure 4.5 (a) shows the SEM image of the ZnO NPs thin film by the ZNP6 dispersion. The morphology of the formed film is close to that from ZNP5. Very similar morphological results were observed for the ZNP7 and ZNP8 formed thin films as shown in Figure 4.5 (b) and 4.5 (c). In Figure 4.5 (d), a slightly different morphology of the ZNP9 dispersion was presented. In the ZNP9 sample, an equal volume of two different surfactants was added into the dispersion solution. The morphology of the ZNP9 formed thin film is denser than that of other

samples mentioned above. However, some big pores existed in the film, which has detrimental effects for the use of the film as the electron transport layer.

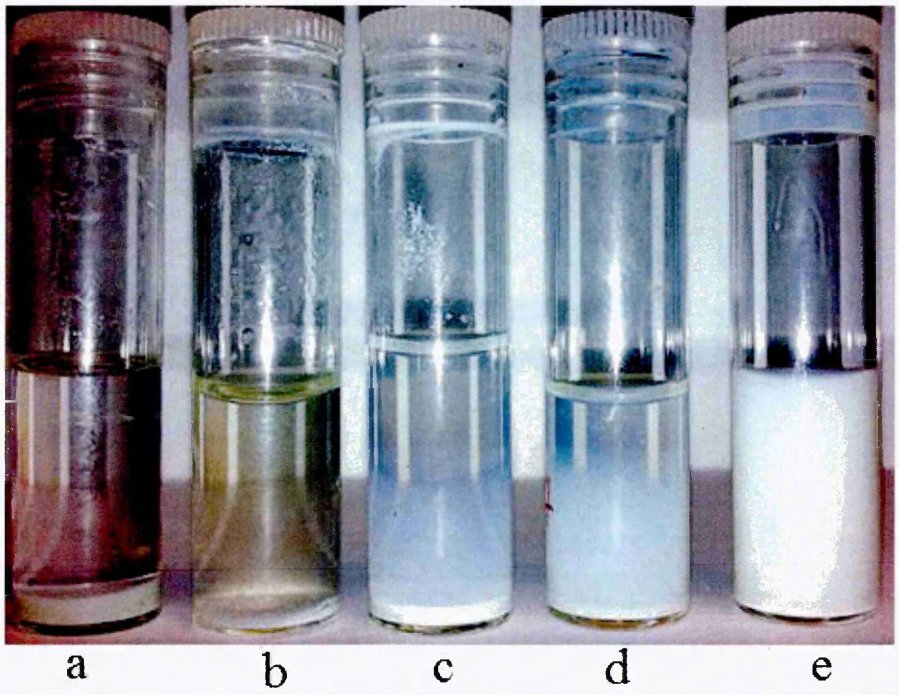

Figure 4.3 ZnO NPs dispersion in different solvents, (a) ZNP1, (b) ZNP2, (c) ZNP3, (d) ZnP4, (e) ZNP5

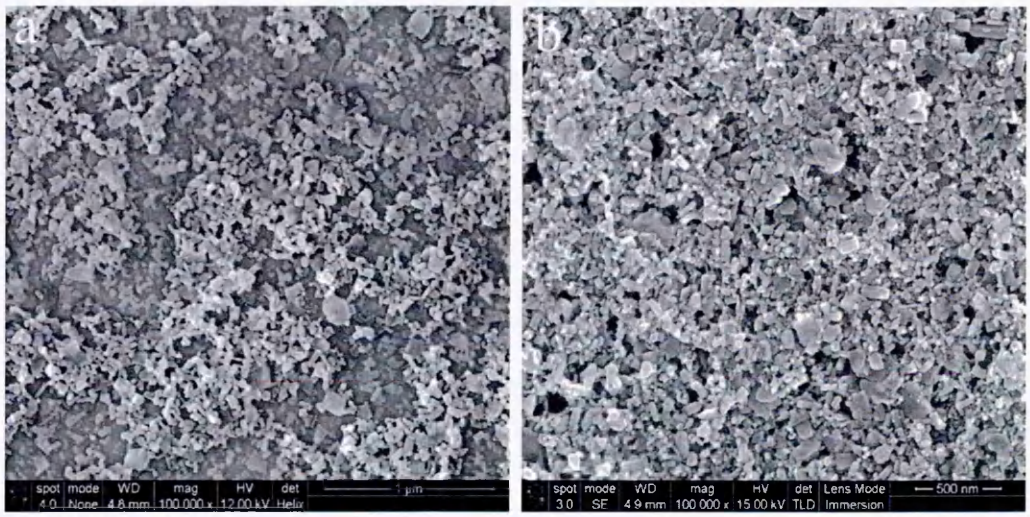

Figure 4.4 SEM images of the ZnO NPs thin film using, (a) ZNP4 dispersion, (b) ZNP5 dispersion

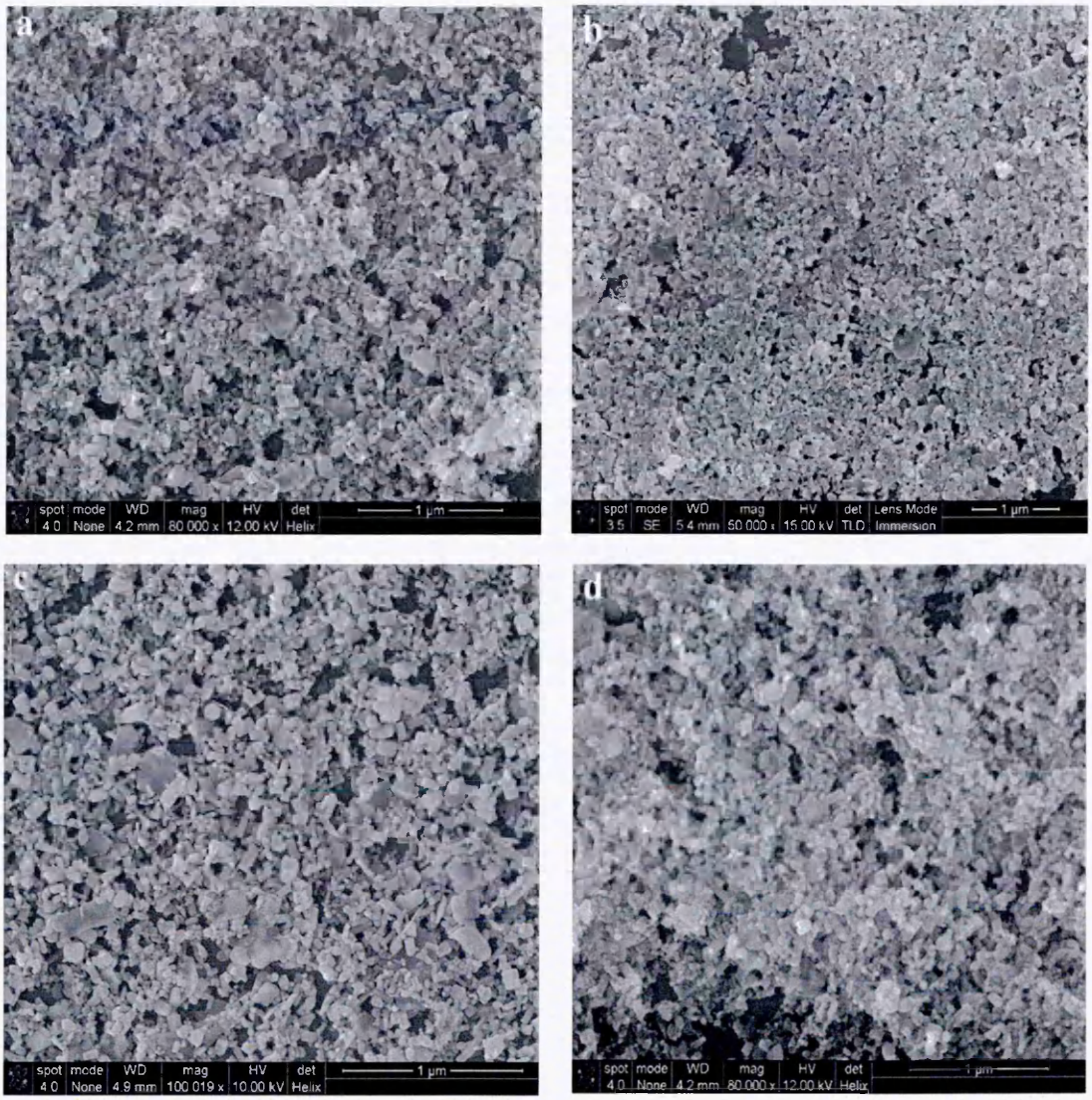

Figure 4.5 SEM images of the ZnO NPs thin films, (a) with ZNP6 dispersion, (b) with ZNP7 dispersion, (c) with ZNP8 dispersion, (d) with ZNP9 dispersion

4.3.1.2 Morphologies of the NPs formed ZnO thin films from the commercial ZNP10

For a comparative study, the ZnO NPs thin film from the commercial dispersion ZNP10 was investigated. Figure 4.6 shows the highly dense SEM morphology of the ZnO NPs film surface with some different shapes of the ZnO NPs. The size, shape, and distribution of particles were also examined by the atomic force microscope. Figure 4.7

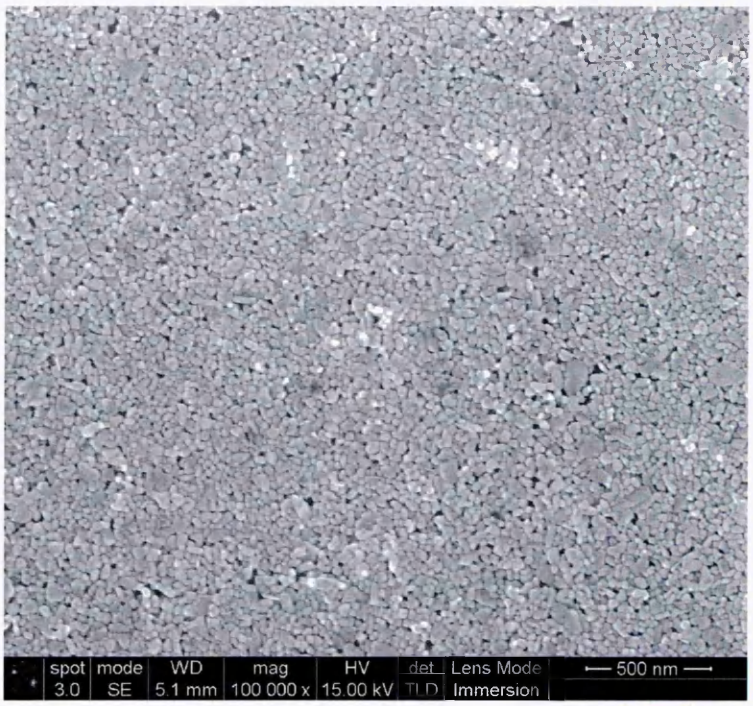

Figure 4.6 SEM image of the ZnO NPs thin film deposited by the ZNP10 dispersion.

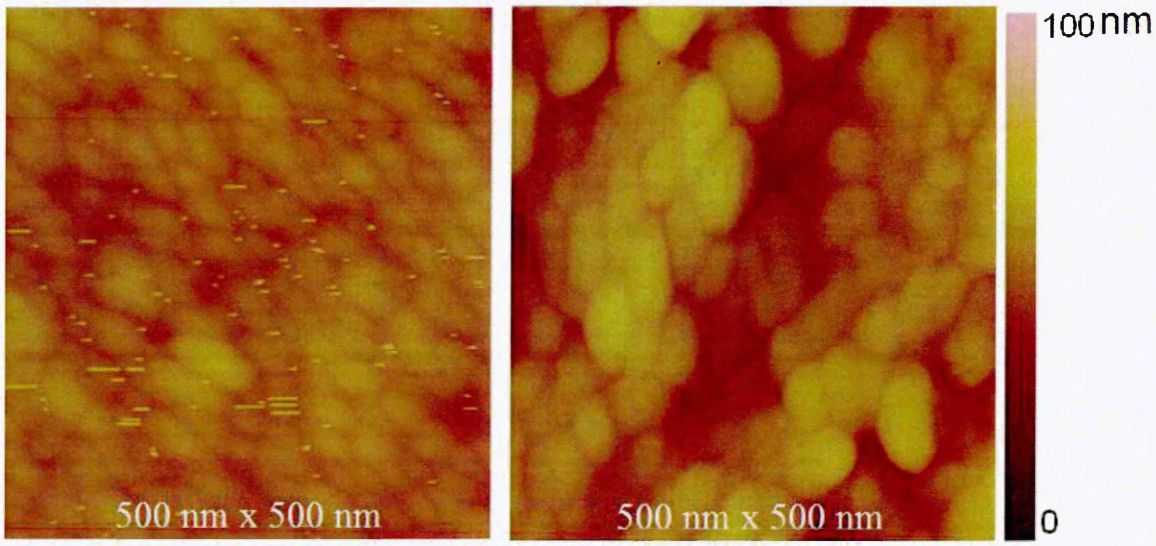

Figure 4.7 AFM surface morphologies of ZnO thin films; (a) by ZNP10 dispersion, (b) by ZNP5 dispersion.

shows the captured real space tapping mode surface morphology of the ZnO NPs thin films on the glass substrate. Figure 4.7 (a) & (b) present the AFM morphologies and roughness of the dense ZnO NPs thin films by the ZNP10 and the porous thin film by the ZNP5, respectively. The surface of the nanoparticles in Figure 4.7 (a) and Figure 4.6 has a root mean square roughness of 4.614 nm while the surface of the nanoparticles in Figure 4.7 (b) and Figure 4.4 (b) shows a root mean square roughness of 11.407 nm.

4.3.1.3 Morphologies of the sol-gel based ZnO ETLs

As discussed previously, dispersion of ZnO nanoparticles in the solution is a difficult process and the use of surfactant additives for enhancement of the colloid solution stability may affect the electrical property of the ZnO film when the formed ZnO thin film is cured at low temperature. Therefore, the inexpensive sol-gel technique is a promising inexpensive route to deposit the ZnO ETLs. The solution processed sol-gel technique is a convenient way for the deposition of ZnO thin films at low processing temperature for low cost and large-scale production. This technique is based on the transformation of the molecular precursors into the oxides by hydrolysis and condensation reactions.

The prepared ZnO sols described in Table 4.2 were used to produce the amorphous ZnO layer which acted as the ETL in OSCs to modify the work function of the ITO electrode. Figure 4.8 shows the SEM images of the sol-gel derived ZnO thin film on glass substrates with different concentrations of zinc acetate dihydrate (Table 4.2). The morphologies of the thin films were different with the changing concentrations of zinc acetate dihydrate. The surface morphology (Figure 4.8a) of the ZnO thin film by the ZSG1 sol presents an amorphous structure with smooth and continuous surfaces. Figure 4.8 (b) shows the morphology of the ZnO film using the ZSG2 sol.

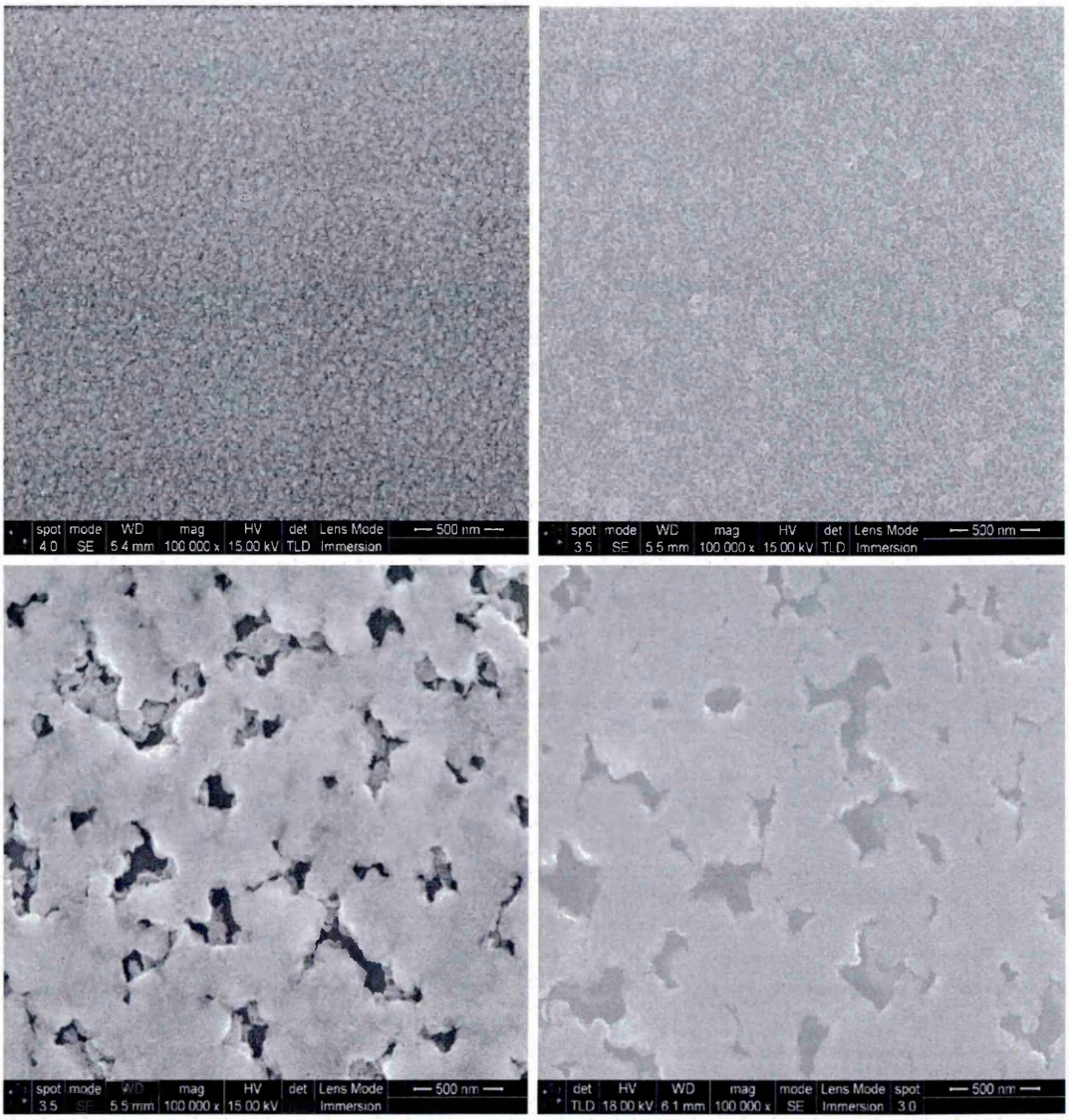

Figure 4.8 SEM images of the sol-gel ZnO thin film; (a) by the ZSG1 sol, (b) by the ZSG2 sol, (c) by the ZSG3 sol, (d) by the ZSG4 sol.

It presented a continuous film but some big sized crystallites on top of the surface. The surface morphologies of the ZnO thin films by the ZSG3 and ZSG4 sols were uniform but illustrating very high porosity (Figure 4.8 c &d). The adhesion of the ZSG2, ZSG3 and ZSG4 based ZnO ETLs with the ITO thin film was very poor. Un-bonded nanoparticles on top of the surface can be observed, which can affect the efficient

electron transport. The AFM image in Figure 4.9 shows the surface morphology of the ZSG1 ZnO thin film also shown in Figure 4.8 (a), disclosing the uniformly covered smooth surface with an average roughness below 5 nm.

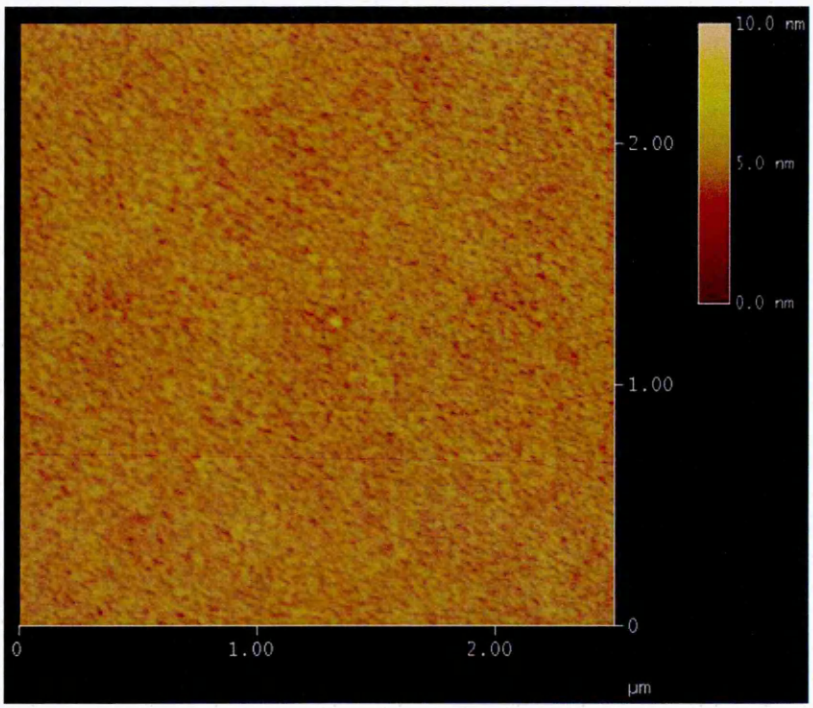

Figure 4.9 AFM image of the sol-gel ZnO thin film by the ZSG1sol

4.3.1.4 Morphologies of the active layers on top of the ZnO NPs thin films

Morphologies of the active layer were affected by the ZnO NPs thin films. Figure 4.10 (a) & (b) show the SEM images of the P3HT:PCBM film on top of the ZnO NPs thin film deposited by the ZNP10 and ZNP5 dispersion respectively. The P3HT:PCBM thin film on top of the ZNP10 ZnO layer is smoother and less feature than that of the P3HT:PCBM thin film on top of the ZNP5 ZnO layer Figure 4.10 (c) &(d) are the AFM images of the P3HT: PCBM films on top of the ZNP10 and ZNP5 ZnO layers deposited on the glass substrates separately. Both show a well interconnected smooth surface with a root mean square roughness of 1.237 nm and 1.984 nm respectively. Morphologies of

the active layers on top of the sol-gel ZnO thin films will be discussed in detail in Chapter 6.

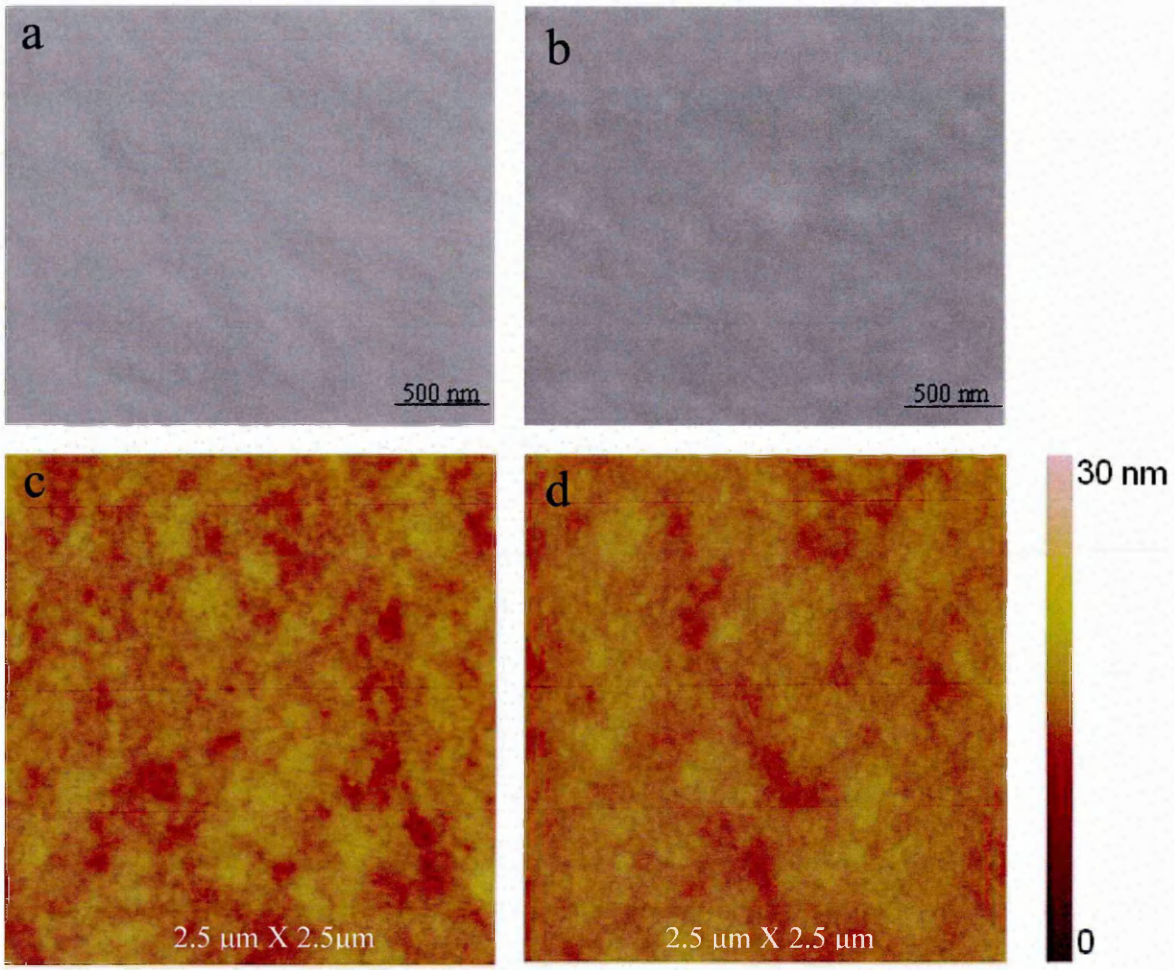

Figure 4.10 (a) SEM image of the P3HT:PCBM film deposited on top of the ZNP10 coated glass substrate; (b) SEM image of the P3HT:PCBM film deposited on top of top of the ZNP5 coated glass substrate; (c) AFM image of the P3HT:PCBM film deposited on top of the ZNP10 coated glass substrate; (d) AFM image of the P3HT:PCBM film deposited on top of the ZNP5 coated glass substrate.

4.3.2 Optical absorption of the P3HT:PCBM active layer on the sol-gel derived ZnO layer

The thin films of the P3HT:PCBM were spin-coated using CB1, CB2, CB3, and CB4 solution at the same spining rate, separately. The absorption spectra of the P3HT:PCBM active layer with the varying concentrations of the P3HT and PCBM in the solvent are plotted in Figure 4.11. It exhibited the well-known absorption band of the P3HT:PCBM blend in the spectral range of 350-650 nm. Optical absorption increased with the increasing concentrations of the P3HT:PCBM (i.e. CB1<CB2<CB3<CB4). When compared with the CB1 active layer, the enhancement of the main absorption peak around 510 nm was ~23.0% for CB2, ~48.0% for CB3, and ~69.0% for CB4 respectively. The enhancement in the absorption peak and the vibronic shoulder at ~610 nm, indicating strong inter chain interactions among the regioregular P3HT chains.

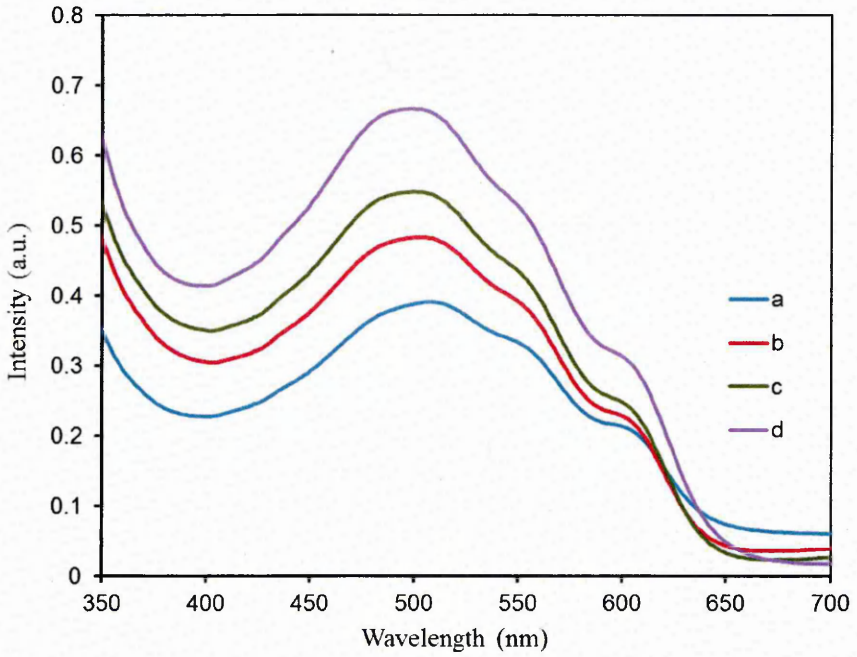

Figure 4.11 Absorption spectra of the active layer with various concentrations of P3HT:PCBM, (a) CB1, (b) CB2, (c) CB3, (d) CB4

4.3.3 Performance of OSC devices

4.3.3.1 Performance of OSC devices by the ZnO NPs ETLs and CB1 P3HT:PCBM active layers

In order to examine the property of the electron transporting ZnO layer, OSC devices were fabricated with and without the ZnO ETLs. Figure 4.12 shows the J-V curve of the OSC devices with and without the ZnO ETL. The results from Figure 4.12 are summarized in Table 4.5. The OSC device without using the ETL shows poor performance due to low V_{oc} at 0.24 V and low fill factor at 0.30. The reason of low V_{oc} was due to non ohmic contact between the active layer and the electron collecting ITO electrode. Compared with the performance of the OSC devices with the ZNP5 electron transport layer, the power conversion efficiency of the OSC devices with the ZNP10 ETL increased to 1.85 % appreciably while the PCE of the OSC devices with the ZNP5 ETL was only at 0.37%. The V_{oc} of the device with the ZNP5 ETL was at 0.28 which is close to the device without using the ETL layer. The reason was due to the big sized pores in the ZNP5 thin film which caused the direct contact of the active layer to the ITO electrode. The performance of OSC devices with the ZNP10 HTL had the significantly increased V_{oc} of 0.56V and fill factor of 0.58.

Table 4.5 Summary of photovoltaic parameters of the champion OSC devices with and without hole transport layers (ETLs)

Device	V_{oc} (Volt)	J_{sc} (mA/cm^2)	FF	η (%)
Without ETL	0.24	5.01	0.30	0.36
With ZNP5 ETL	0.28	3.46	0.38	0.37
With ZNP10 ETL	0.56	5.69	0.58	1.85

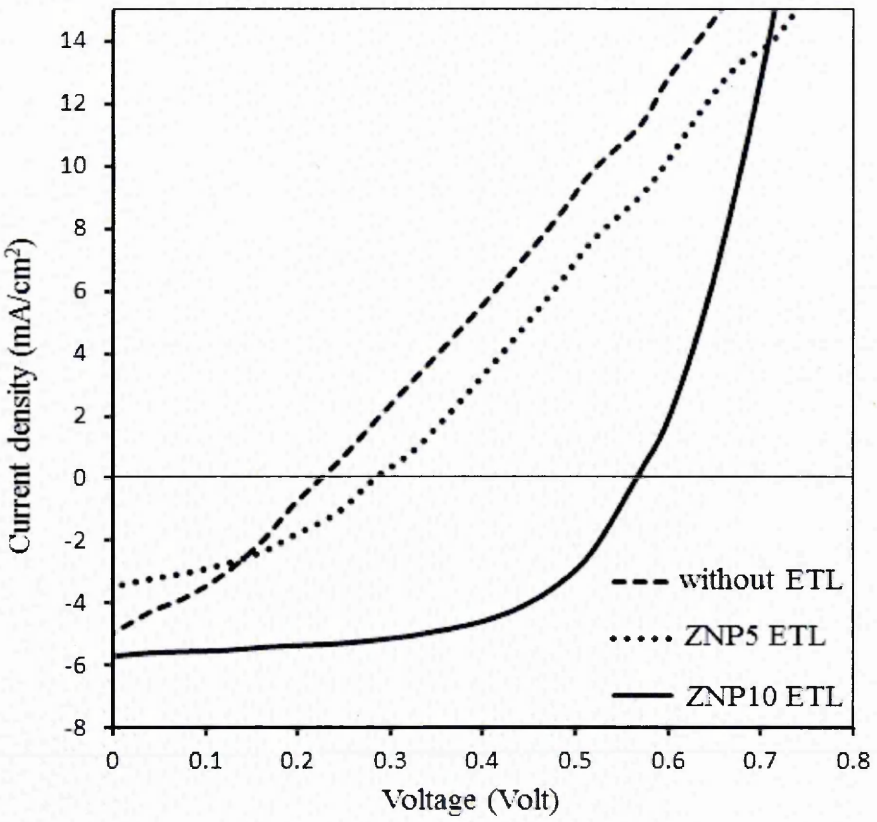

Figure 4.12 J-V characteristics of the OSC devices with and without ETLs

The increased V_{oc} is due to higher shunt resistance in comparison with other two types of devices as can be observed from the J-V curves of the OSC devices. The current density of the OSC device with the ZNP10 ETL is higher than that of the OSC device with the ZNP5 ETL, which also explains that the dense uniform film of the ZNP10 ETL provided the better ohmic contact between the active layer and the electron collecting electrode.

4.3.3.2 Performance of the OSC devices by the sol-gel derived ZnO ETLs and CB1 P3HT:PCBM active layers

For the comparative study, the fabricated devices with the sol-gel based ZnO as ETLs were compared with the OSCs devices with the ZNP10 as the ETLs. Figure 4.13 shows

the J-V characteristics of the OSC devices with the ZNP10 and the ZSG1 ETLs. The PCE of both types of the devices is nearly the same. Table 4.6 summarised the performance of both types of the devices. However, the reference device with the ZNP10 based ETL exhibited an average PCE of 1.85% with V_{oc} at 0.56V, J_{sc} at 5.69 mA/cm^2, and FF at 58%.

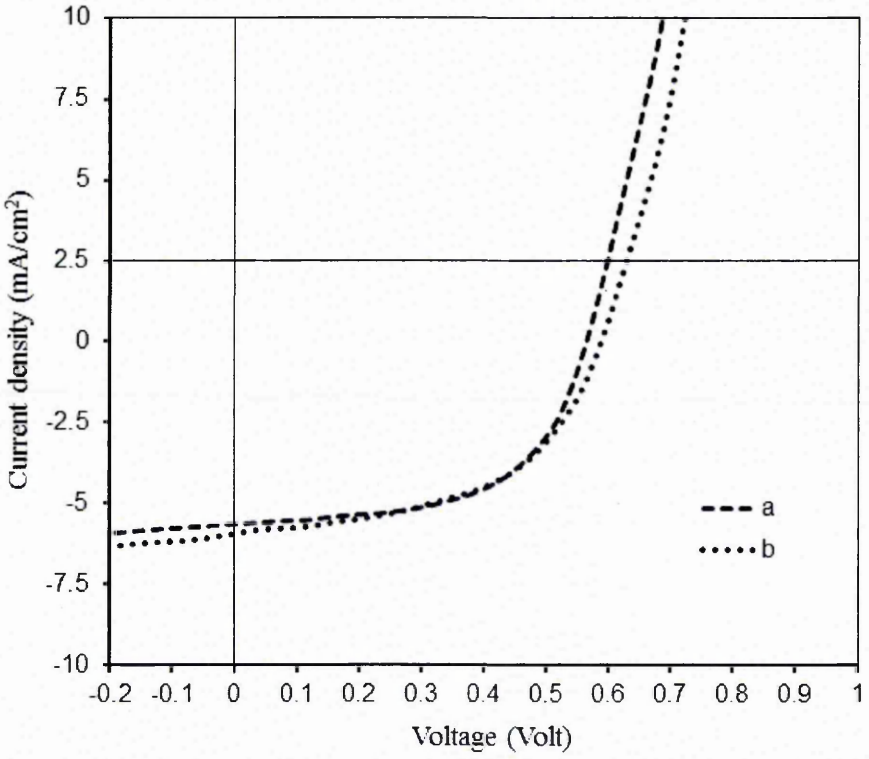

Figure 4.13 J-V characteristics of the inverted OSC devices, (a) with the ZNP10 NPs thin film as ETL, (b) with the ZSG1 ZnO thin film as ETL.

Table 4.6 Summary of photovoltaic parameters of the champion OSC devices with the NPs and sol-gel based ETL layers

Device	V_{oc} (Volt)	J_{sc} (mA/cm^2)	FF	η (%)
With ZNP10 ETL	0.56	5.69	0.58	1.85
With ZSG1 ETL	0.60	6.06	0.50	1.80

The OSCs device using the ZSG1 based ETL presented a PCE 1.80% but a higher V_{oc} at 0.6V, a higher J_{sc} at 6.06 mA/cm^2 and lower FF at 50%. The difference of V_{oc}, J_{sc}, and FF can be assigned to the work function modification of the ITO with different ZnO ETLs. This result demonstrated that the sol-gel ZnO is suitable for use as the ETL for the fabrication of OSC devices in our further studies. Therefore, ZSG1 has been chosen as the ETL for all devices in our further work. The thicknesses of the sol-gel ZnO layer were optimised with the variation of the spinning rate, which was found to be at around 35 to 50 nm.

4.3.3.3 Performance of the OSC devices by different P3HT:PCBM blends

Figure 4.14 shows the J-V characteristics of the OSC devices using different blend solutions of the P3HT:PCBM. The V_{oc} of all the devices presented the same value at 0.60V as listed in Table 4.7. The overall performances of all the devices are summarized in Table 4.7. The OSC device (a) by the CB1 active layer exhibited a PCE of 1.60% with J_{sc} at 5.25 mA/cm^2 and FF near to 51%. The PCE of device (b) using

Table 4.7 Summary of photovoltaic parameters of the champion OSC devices with varying concentration of P3HT:PCBM

Device	V_{oc} (Volt)	J_{sc} (mA/cm^2)	FF (%)	η (%)
a	0.60	5.25	51	1.60
b	0.60	5.40	61	1.98
c	0.60	6.71	58	2.30
d	0.60	5.91	56	1.99

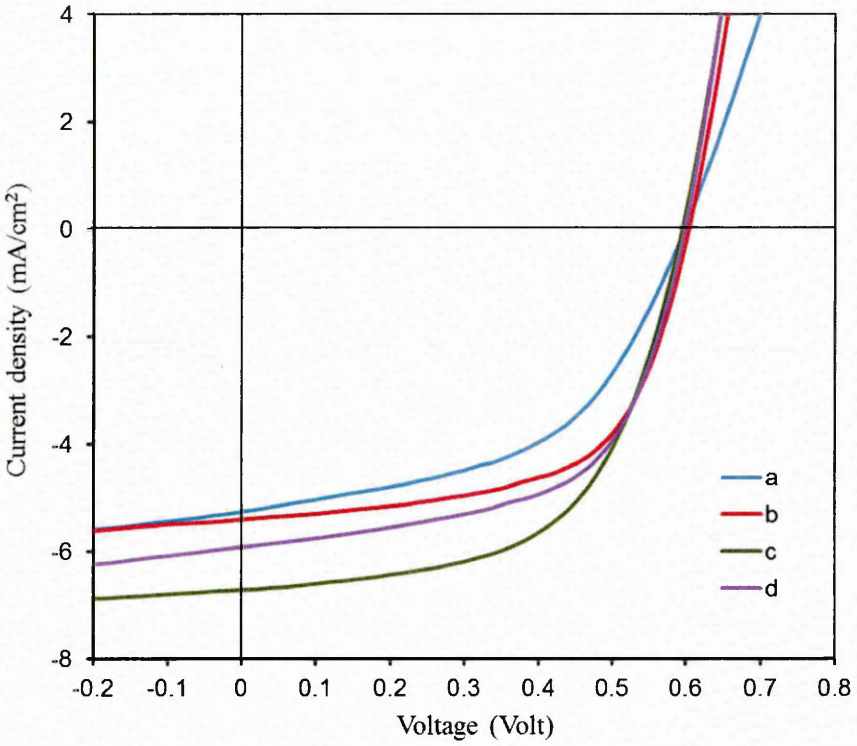

Figure 4.14 J-V characteristics of inverted OSC devices with varying concentrations of P3HT:PCBM active layer: (a) with CB1; (b) with CB2; (c) CB3; (d) with CB4.

the CB2 blend active layer increased to 1.98% with a slightly higher J_{sc} at 5.40 mA/cm^2 and FF at 61%. The PCE of device (c) by the CB3 active layer increased further and revealed the continuing enhancement in PCE, reaching 2.30% with a current density at 6.71 mA/cm^2 and FF at 58%. Although the P3HT:PCBM concentration of the CB4 active layer further increased, the PCE of the device (d) in fact dropped to 1.99% with a current density at 5.91mA/cm^2 and FF at 56%. These results are consistent with the optical absorption properties of the P3HT:PCBM blend as previously shown in Figure 4.11 except the CB4 blend. The thickness of the active layer for device (c) was analysed by surface profiler, presenting the result in the range of 150-180 nm. Since device (d) has higher concentration of the P3HT:PCBM in the solvent, the thickness of the obtained active layer from the CB4 will be greater than 150-180 nm. This can explain

the dropped performance of device (d) compared to device (c). Since the PCE results revealed that device (c) is the best amongst four types of blends listed in Table 4.7, the CB3 blend was chosen as the blend for depositing the active layer for all devices.

4.4 Summary

(1) Various zinc oxide NPs dispersions in different solutions were investigated. The results showed that the ZNP5 has the best stability and the uniform thin films were produced using the spin coating technique from the ZNP5. However, there are still some big sized pores existed in the film deposited from the ZNP5, which limited its use as the efficient ETL layer. As a comparative study, commercial ZNP10 dispersion was also investigated, which formed a moderately dense structure. The OSC devices using the ZNP10 ZnO layer as the ETL performed better than that of the devices using the ZNP5 ZnO layer as the ETL. Hence, sol-gel technology was further used to produce the stable ZnO sol that was used to fabricate the ZnO ETL layer in the devices. The performance of the OSC devices using the sol -gel (SG1) based and ZNP10 based ZnO ETL presented nearly the same results in the PCE; i.e.1.85% and 1.80%, respectively.

(2) The P3HT:PCBM blend was investigated by using two different solvents (i.e. CB and ODCB). Since the blend from the CB can produce more uniform thin film than that from the ODCB, different concentrations of the P3HT:PCBM in CB solvent was further studied. The P3HT:PCBM concentration was optimised to 35 mg/ml (CB3 blend solution) with a weight ratio of 1:1, which presented the best performance in the OSC devices. The power conversion efficiency of the OSC devices from the optimised active layer of CB3 has reached to 2.3%.

(3) The PEDOT:PSS layer was chosen to be as the HTL. However, the aqueous solution of the PEDOT:PSS exhibited poor wettability on the hydrophobic organic active layer of the P3HT:PCBM. The wettability of the PEDOT:PSS solution was improved by adding the surfactant of Triton X-100 into the PEDOT:PSS aqueous solution. After the addition of ~ 0.05% Triton X-100 into the PEDOT:PSS solution, contact angle of the PEDOT:PSS solution on the P3HT:PCBM thin film surface reduced from 74.8 ± 4.0^{o} to 39.0 ± 3.0^{o} which improved the wettability. The uniform PEDOT:PSS thin film was then successfully produce on the hydrophobic surface of the P3HT:PCBM active layer.

4.5 References:

[1]] H. Wang, H. Nakamura, K. Yao, M. Uehara, S. Nishimura, H. Maeda, E. Abe, Effect of Polyelectrolyte Dispersants on the Preparation of Silica-Coated Zinc Oxide Particles in Aqueous Media, J. Am. Ceram. Soc., 85 (2002) 1937-1940.

[2] W. J. E. Beek, M. M. Wienk, M. Kemerink, X. Yang, R. A. J. Janssen, Hybrid Zinc Oxide Conjugated Polymer Bulk Heterojunction Solar Cells, J. Phys. Chem., B 109 (2005) 9505-9516.

[3] S. K. Hau, H. L. Yip, N. S. Baek, J. Zou, K. O'Malley, K. Y. Alex Jen, High performance ambient processed inverted polymer solar cells through interfacial modification with a fullerene,self-assembled monolayer, Appl. Phys. Lett., 93 (2008) 25330.

[4] M. T. Danga, G. Wantz, H. Bejbouji, M. Uriena, O. J. Dautel, L. Vignaua, L. Hirscha, Polymeric solar cells based on P3HT:PCBM: Role of the casting solvent, Sol. Energy Mater. Sol. Cells., 95 (2011) 3408-3418.

[5] F. C. Chen, C. J. Ko, J. L. Wu, W. C. Chen, Morphological study of P3HT:PCBM blend films prepared through solvent annealing for solar cell applications, Sol. Energy Mater. Sol. Cells., 94 (2010) 2426-2430.

[6] M. M. Voigt, R. C. I. Mackenzie, C. P. Yau, P. Atienzar, J. Dane, P. E. Keivandidis, D. D. C. Bradley, J. Nelson, Gravure printing for three subsequent solar cell layers of inverted structures on flexible substrates, Sol. Energy Mater. Sol. Cells., 95 (2011) 731-734.

[7] Q. Dong, Y. Zhou, J. Pei, Z. Liu, Y. Li, S. Yao, J. Zhang, W. Tian, All-spin-coating vacuum-free processed semi-transparent inverted polymer solar cells with PEDOT:PSS anode and PAH-D interfacial layer, Org. Electron., 11 (2010) 1327-1331

[8] W. R. Wei, M. L. Tsai, S.T. Ho, S. H. Tai, C. R. Ho, S. H. Tsai, C. W. Liu, R. J. Chung, J. H. He, Above-11%-Efficiency Organic–Inorganic Hybrid Solar Cells with Omnidirectional Harvesting Characteristics by Employing Hierarchical Photon-Trapping Structures, Nano Lett., 13 (2013) 13 3658-3663.

[9] M. Kaltenbrunner, M. S. White, E. D. Głowacki, T. sekitani, T. someya, N. S. Sariciftci, S. Bauer, Ultrathin and lightweight organic solar cells with high flexibility, Nat. Commun., 3 (2012) 770.

[10] J. S. Huang, G. Li, Y. Yang, A Semi-transparent Plastic Solar Cell Fabricated by a Lamination Process, Adv. Mater., 20 (2008), 415-419.

[11] S. K. Hau, H. L. Yip, J. Zou, A. K. Y. Jen, Indium tin oxide-free semi-transparent inverted polymer solar cells using conducting polymer as both bottom and top electrodes, Org. Electron., 10 (2009)1401-1407.

[12] R. J. Peha, Y. Lua, F. Zhao, C. L. K. Lee, W. L. Kwan, Vacuum-free processed transparent inverted organic solar cells with spray-coated PEDOT:PSS anode, Sol. Energy Mater. Sol. Cells., 95 (2011) 3579-3584.

Chapter 5: Influence of the Plasmonic Gold (Au) Nanoparticles Interfacial Layer on the Device Performance

5.1 Introduction

Organic photovoltaic based on semiconducting organics as the donor and soluble fullerene derivatives as the acceptor has great potential to become a low cost solar cell technology. Among many PV technologies, considerable efforts have been focused on the study of OSCs devices due to their advantages of relative ease fabrication at low temperature, small amount of organic materials required for the cells, good mechanical flexibility, and potential cost-effective devices [1,2]. This is owing to the development of PV devices for conversion of solar energy into electricity that has attracted a great attention in recent years because of the environmental concern and the depletion of fossil fuels. The active layer of such devices typically has to be very thin, which leads to poor light absorption.

Therefore, an efficient light-trapping technique is necessary for improving the light absorption efficiency and effective optical path length. Plasmonic nanostructures have recently emerged as an expanding area to enhance light absorption in OSC devices [3,4] by encapsulating metal NPs in the layers or fabricating gratings on the back contact metal surface. Many studies have been carried out to incorporate Au or Ag NPs into the hole transport layer (HTL), active layer, electrode layer, or all organic layers of single-junction OSCs devices, the interconnecting layer of tandem structures in OSCs devices in order to achieve the plasmonic light enhancement by various methods including high vacuum thermal evaporation, high vacuum electron beam evaporation, or other methods [5-16]. However, enhanced light absorption was usually realised within a relatively narrow wavelength range by using above methods. Currently the broadband light

absorption enhancement published in OSC devices could only be achieved by using complicated dual plasmonic nanostructures [17]. Compared to other inorganic-semiconductor solar cells, OSC devices have very low efficiency which limits their feasibility for their commercial use. Except improving open circuit voltage (V_{oc}), one main limitation of OSC devices is their spectrally narrow absorption of the donor organic material [18,19].

Absorption of OSC devices can be spectrally extended by introducing low band gap materials into the active layer forming the ternary semiconductor blends and/or using tandem structures, where the new components, the second donor, or the new layer with a complementary absorption spectrum is added. Spectrally extended bulk hetero-junction OSC devices have reported a PCE of ~7-8% [20-22]. Since sunlight is a broadband light source, plasmonic nanostructures in OSC devices that can be fabricated to enhance light absorption in a wide spectral range of 350 to 1000 nm could be one of the most potential routes to further increase PCE of OSC devices beyond the 10% threshold for their commercial use.

Among the metals that can support plasmonic resonance (PRs) modes, noble metals (Au, Ag and Cu) present resonances in the visible or near infrared (IR) region of the electromagnetic spectrum. Thus, dual plasmonic nanostructures that are composed of Au NPs embedded in the active layer and an Ag nano grating electrode as the back reflector in inverted OSC devices have recently been explored to successfully extend the wavelength region of enhanced light absorption [17]. However, using dual plasmonic nanostructures needs to precisely and controllably fabricate each nanostructure in different layer of OSC devices to match the theoretically simulated structures without interfering one another. Overall, current techniques for metal plasmonic NPs did not demonstrate a simple processing of obtaining enhanced broadband optical absorption in

OSC devices. PAPVD is a mature and well-established technique [23]. It does not require high vacuum system to produce metal NPs thin films.

This chapter explore the application of a simple one-nanostructure PAPVD coated thin Au NPs film in solution processed single junction P3HT: PCBM inverted OSC devices. This simple Au NPs film was able to provide a significant broadband light absorption enhancement to the OSC devices. We demonstrate that plasmonic resonances from the PAPVD thin Au NPs film have greatly enhanced optical absorption of OSC devices in a wide wavelength range of 350 to 1000 nm. The advantage for this technique is that it can be adopted and easily fit into most OSC device fabrication processes without changing other layers' manufacturing methods, morphologies and properties except providing the functionality of enhancing device broadband light absorption.

5.2 Device structure and experimental methods

The inverted OSC devices are fabricated on pre-patterned ITO coated glass substrates (12-15 ohms/sq. from VisionTek Systems Ltd. UK) that were ultrasonically cleaned in acetone, isopropyl alcohol and deionised water for 10 min, respectively. After drying with nitrogen, the substrates were spin-coated with the SG1 ZnO sol of zinc acetate dihydrate in 2-methoxyethanol and then ethanolamine was added as described in section 4.2.1 of chapter 4. The prepared SG1 ZnO sol produced a ~35 nm thick amorphous ZnO layer and acted as the electron transport layer on the ITO bottom electrode. The deposited ZnO layer was annealed on a hot plate at 150° C for 10 min and then cleaned with deionised water and acetone to remove any residual from the top surface. Then the samples were transferred into a nitrogen-filled glove box. On top of the ZnO layer, a ~150 nm thick active layer was spin-coated from the CB3 chlorobenzene solution of P3HT (Merck):PCBM (Solenne b.v.) and then was annealed at 140°C for 10 min on a

hot plate.Afterwards, the samples were removed out of the glove box, followed a ~25 nm thick PDS2 derived PEDOT: PSS (HTL Solar) layer on top of the active layer as the HTL. The samples were then transferred again into the nitrogen-filled glove box for heat treatment at 110°C for 10 min. Finally, an Au layer was deposited as top electrode by PAPVD at base pressure of $1x10^{-2}$ mbar and was then annealed under the ambient air condition at 110°C for 10 min.

The thickness of the Au layer is at an approximately 40 nm. Two types of sputtered Au thin films were separately produced for OSC devices. One is the ~40 nm thick Au film formed by the Au NPs with an approximately size of 50 nm in diameter (labelled as T1 devices). Another is also the ~40 nm thick Au film composed of the Au NPs with an approximately size of 15 nm in diameter (labelled as T2 devices). The schematic diagram of ITO/ZnO/P3HT:PCBM/PEDOT:PSS/Au device processing structures is shown in Figure 5.1a. Nevertheless, the finally created real structure of OSC devices may be schematically shown in Figure 5.1b and 1c for T1 and T2 devices, respectively. The tested active area of the final OSC devices was 6.0 mm^2.

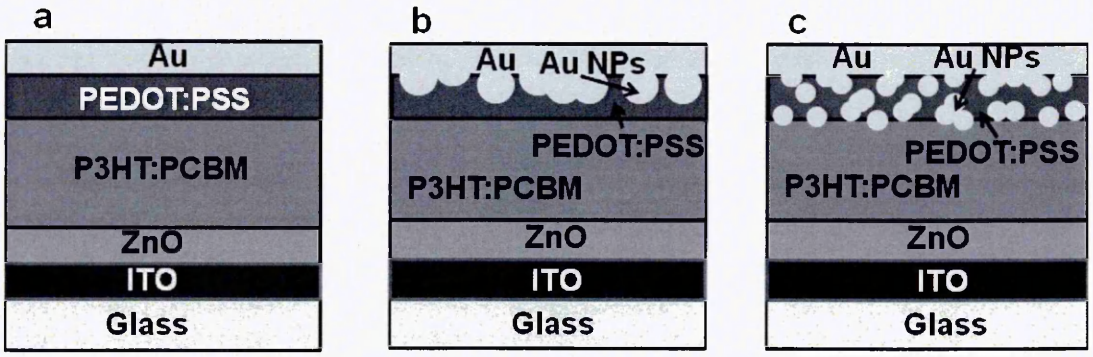

Figure 5.1 Schematic diagram of cross section for inverted OSC devices, (a) the processed structure, (b) the inferred structure for T1 devices where the size of the sputtered Au NPs was 50 nm, (c) the inferred structure for T2 devices where the size of the sputtered Au NPs was 15 nm. (Note: not to scale).

Samples of the SG1 derived ZnO layer and the CB3 based P3HT:PCBM active layer were respectively prepared on glasses for characterisation of morphologies. OSC devices were produced without applying top Au electrode for the investigation of PEDOT:PSS thin film morphologies. OSC T2 devices after applying Au thin films at different thicknesses of approximately 6, 13, 20, and 40 nm were respectively fabricated for their characterisation of morphologies. Sputtered Au thin films (for T2 devices) on glasses at different thicknesses of approximately 5, 11, and 16 nm were separately prepared for characterisation of light absorption. The ~150 nm thick P3HT:PCBM, the ~25 nm thick PEDOT:PSS, and the double-layer (defined as the ~150 nm thick P3HT:PCBM layer plus the ~ 25 nm thick PEDOT:PSS layer) thin films on glasses were separately produced for the analysis of light absorption. For comparative studies, the above three types of thin films on glasses after applying Au thin films at different thicknesses of approximately 5, 11, and 16 nm were also respectively prepared for the testing of light absorption. The films with the plasmonic Au NPs on top were all annealed at 110°C for 10 min.

5.3 Results and discussion

5.3.1 Morphologies of the ETLs, P3HT:PCBM active layer, HTLs and Au NPs thin films

5.3.1.1 Surface morphologies of ZnO and P3HT:PCBM active layers

The sol gel deposition of ZnO thin films is a convenient method for fabrication of the electron transport layer for OSC devices at a lower processing temperature, which guarantees for low cost and large-scale production. Figure 5.2 (a) shows the SEM image

of the sol gel derived ZnO thin film on ITO coated glasses. It shows a smooth and uniform surface.

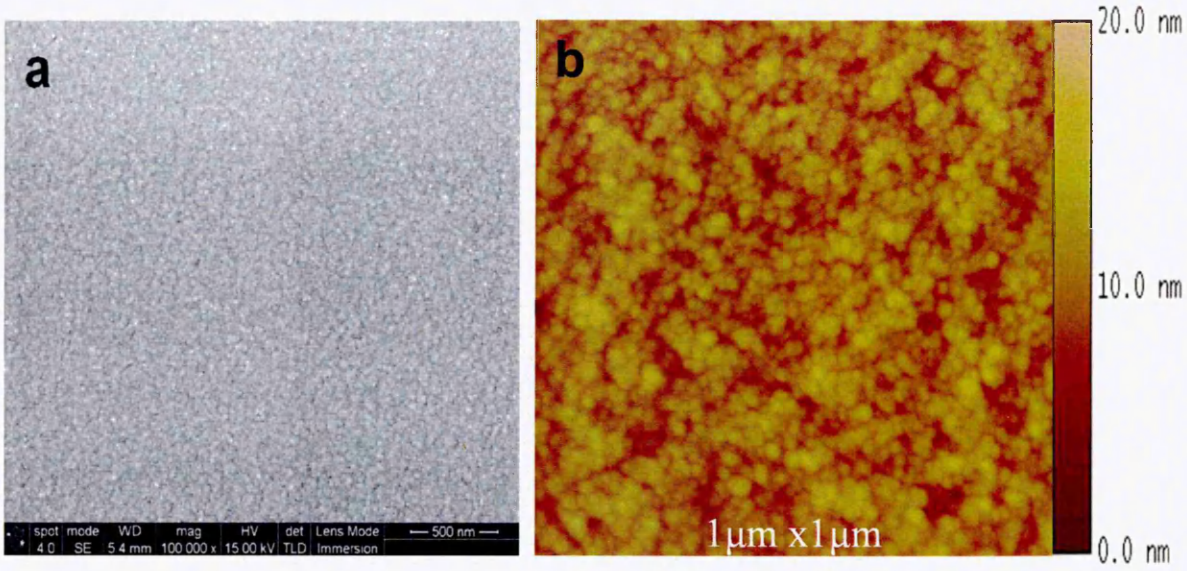

Figure 5.2 Morphologies of sol-gel derived ZnO thin films on ITO coated glasses, (a) SEM image presenting an amorphous structure, (b) AFM image indicating a very smooth surface

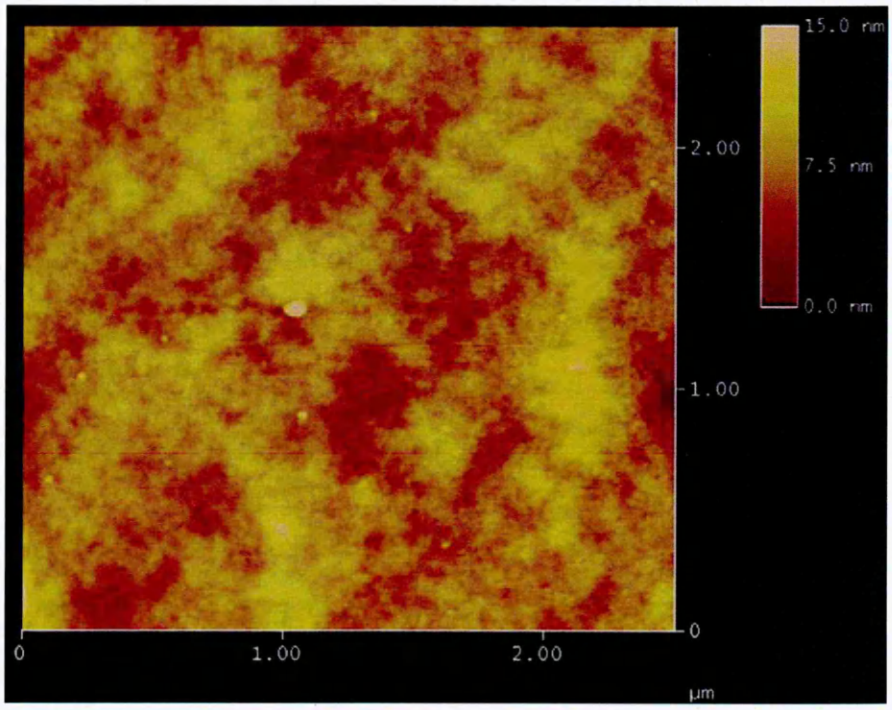

Figure 5.3 AFM morphologies of the P3HT:PCBM thin film

The AFM image in Figure 5.2 (b) shows the uniform coverage over the whole surface of the ITO thin film and disclosed its depth roughness below 5 nm. The AFM morphology of P3HT:PCBM blends is showed in Figure 5.3 and the blend was composed of two contrast phases with an average roughness of 2.4 nm with a maximum of 10.0 nm in depth. It indicated that the blend was reasonably separated with the donor/acceptor interfaces for charges separation and transport.

5.3.1.2 Surface morphologies of the PEDOT:PSS HTLs

Figure 5.4 presents the PEDOT:PSS AFM image. The thin PEDOT:PSS film showed ~5 nm roughness but randomly distributed some ~40 nm sized hole-like nanocavities or nanodents with a ~20 nm low-depth and an average distance of ~250 nm in Figure 5.4 (a), and consisted of ~15 nm featured NPs that interconnected together forming aggregates or clusters with island structures. More details are shown in Figure 5.4 (b). Since the Au NPs had the same size of ~15 nm as the PEDOT:PSS NPs, it can be

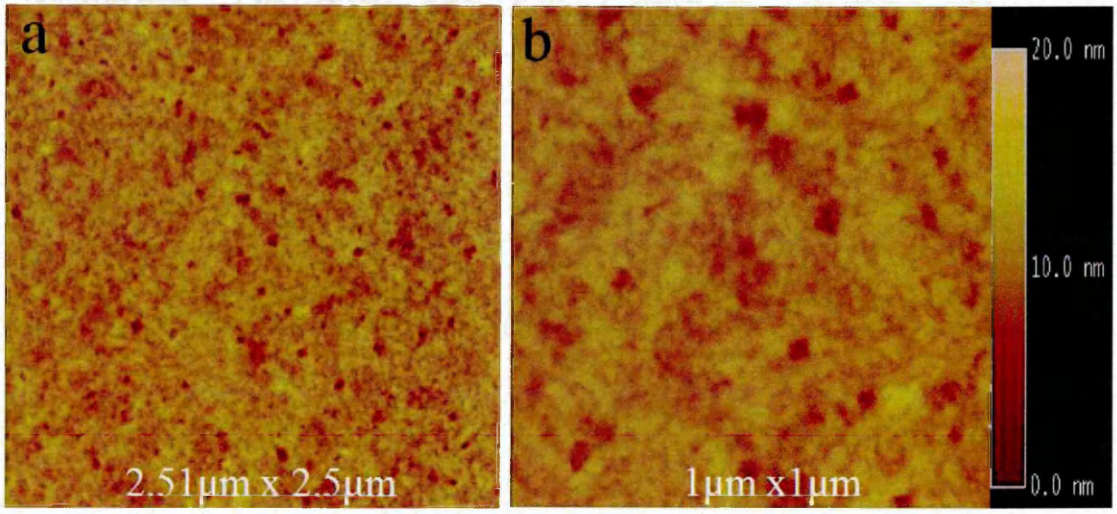

Figure 5.4 AFM images of PEDOT:PSS thin films, (a) morphologies of PEDOT:PSS and (b) magnified morphologies of the PEDOT:PSS film showing ~15 nm NPs.

inferred that Au NPs will easily fit into these low-depth nanocavities or nanodents by the PAPVD method in the initial deposition stage, forming the dispersed Au NPs within the PEDOT:PSS layer. It will also reach the surface of the P3HT:PCBM active layer or perhaps be slightly embedded into the active layer because the thickness of these nanocavities is within the range of several nanometers.

5.3.1.3 Surface morphologies of Au thin films

Morphologies of the PAPVD coated thin Au film are shown in Figure 5.5 where Figure 5.5 (a) is a scanning electron microscope (SEM) image of the PAPVD coated thin Au film with the relatively large size of Au NPs for T1 devices. This Au film presented random round NPs with ~ 50 nm in diameter. However, it demonstrated a limited

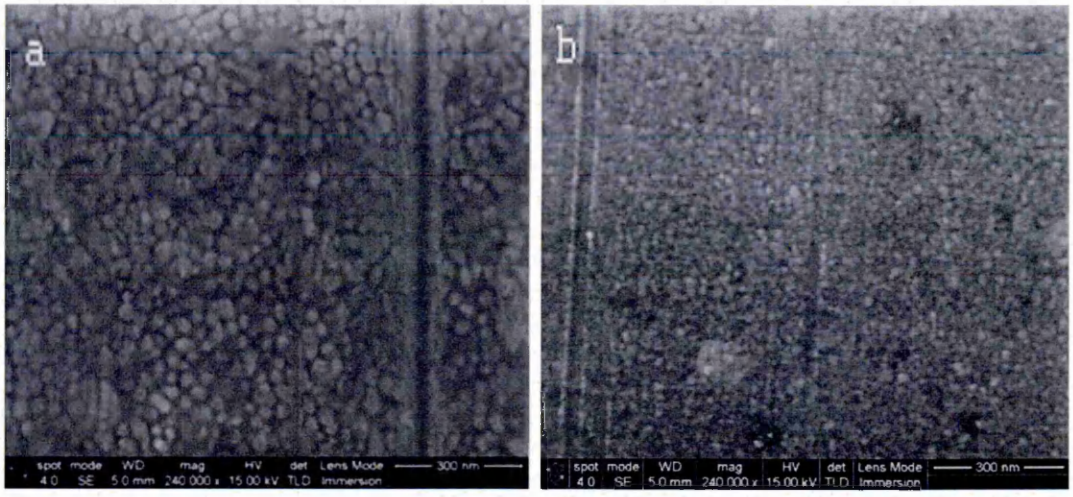

Figure 5.5 SEM morphological images of the PAPVD coated Au thin films, (a) the initial PAPVD Au film presenting ~50 nm nanometer-sized Au NPs for T1 devices and (b) the modified fine structural Au film showing ~15 nm nanometer-sized Au NPs for T2 devices.

enhancement of light absorption by plasmonic resonances in the OSC devices that will be discussed in OSC performance section. To achieve a strong light absorption enhancement, a morphologically modified thin Au film i.e. for T2 devices, was then produced by PAPVD as shown in Figure 5.5 (b). This modified Au film presented much finer nanostructures than the previous Au film in Figure 5.5 (a). The size of Au NPs decreased to be around ~15 nm that can be observed more clearly in the atomic force microscope (AFM) images below. Enhancing light absorption via plasmons to the active P3HT:PCBM layer can be expected here via the way where Au NPs or nanometer sized Au clusters created localized surface plasmonic resonances (LSPRs) [3,4] if they can penetrate the PEDOT:PSS layer and reach to the surface of the P3HT:PCBM layer.

To better understand how the thin Au NPs film formed on the ~25 nm thick PEDOT:PSS layer can provide plasmonic resonances, surface morphologies of T2 devices after being coated by the PEDOT:PSS and/or Au films with different deposition time (5, 10, 15 and 30 s) corresponding to different thicknesses (approximately 6, 13, 20, and 40 nm thick) were analysed by the atomic force microscope separately. Figure 5.6 (a) shows the morphology of the ~6 nm thick Au NPs film on T2 devices. The Au film was in its early processing stage, presenting dispersed or island structures. The island structures expanded after 10 s deposition for the ~13 nm thick Au NPs film and started to touch with each other. This is evident in the AFM image as shown in Figure 5.6 (b). Figure 5.6 (c) presents that the island structures nearly connected together to form a uniform film after 15 s deposition for the ~20 nm thick Au NPs film. The AFM image of the 40 nm thick integrated Au thin film is then shown in Figure 5.6 (d). Thus, we can infer a composite interfacial layer that actually formed between the P3HT:PCBM active layer and the integrated Au top electrode. The interfacial layer contained two types of

NPs; i.e. PEDOT:PSS and Au NPs which were surrounded by each other. Dispersed Au NPs or nanometer- sized Au clusters in the interfacial layer can perform plasmonic resonances. LSPRs created by those Au NPs or nanometer-sized Au clusters that directly contacted with the P3HT:PCBM active layer can be absorbed by this layer, providing enhanced light absorption.

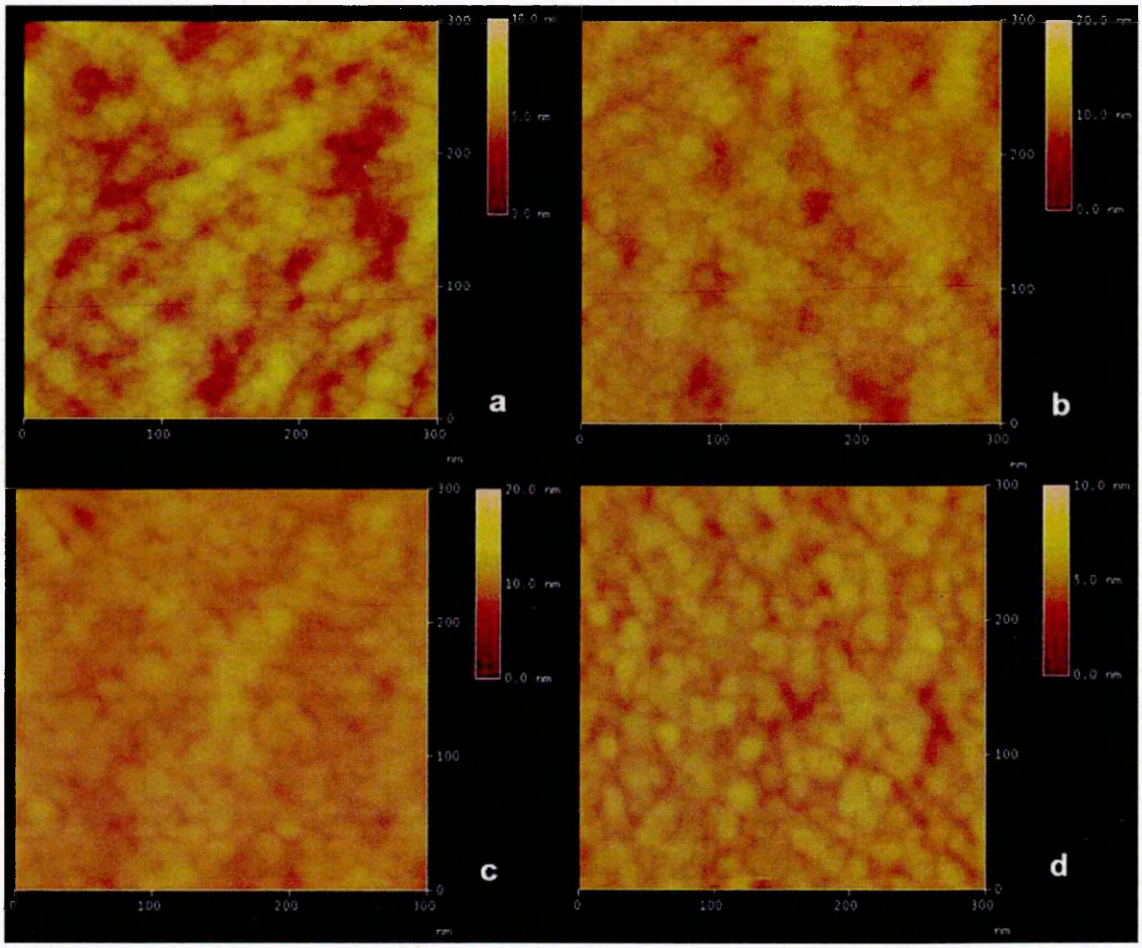

Figure 5.6 AFM morphological images of Au thin films on the PEDOT:PSS layer demonstrating the formation of Au NPs film; (a) ~6 nm thick Au film by 5 s deposition; (b) ~13 nm thick Au film by 10 s deposition; (c) ~20 nm thick Au film by 15 s deposition and (d) ~40 nm thick Au film by 30 s deposition, respectively.

5.3.2 Performance of OSC devices

Performance of two types of OSC devices (T1 and T2 as shown in Figure 5.1b and 5.1c) was investigated, respectively. Typical results of illuminated current-voltage characterisation of OSC devices T1 and T2 are shown in Figure 5.7. The performance parameters of fabricated T1 devices are summarized in Table 5.1. Obtained PCE of the fabricated devices was in average 2.07 % with short circuit current density (J_{sc}) of 6.60 mA/cm^2. The performance parameters of OSC T2 devices are listed in Table 5.2.

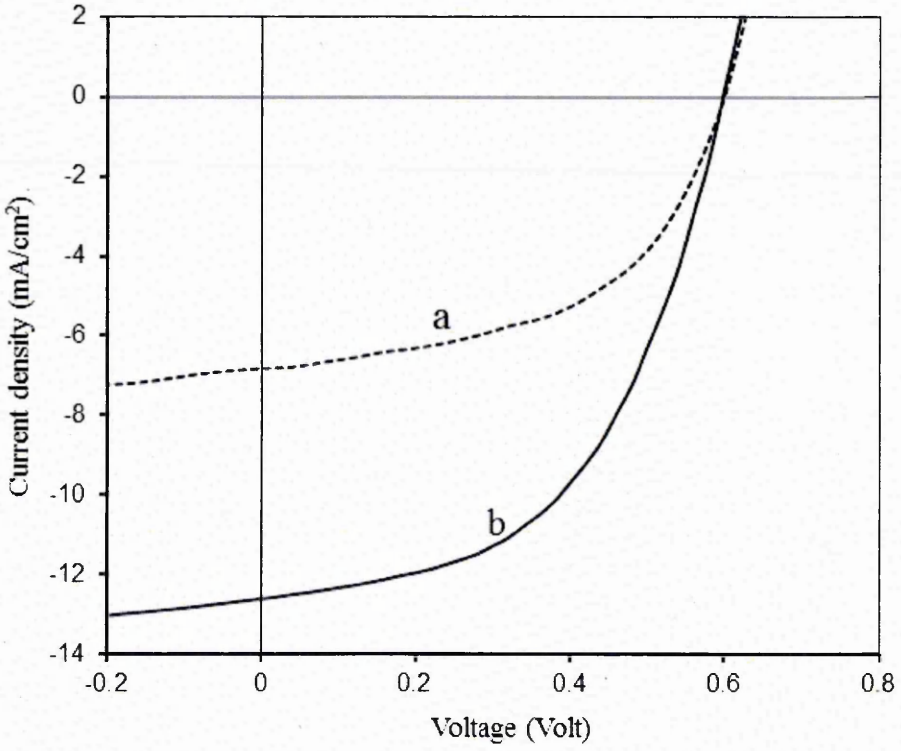

Figure 5.7 J-V characterisation under illumination of inverted OSC devices, (a) T1 devices by the 40 nm thick Au film composed of 50 nm sized Au NPs as top electrode, (b) T2 devices by the 40 nm thick Au film but composed of 15 nm sized Au NPs as top electrode

Table 5.1 Summary of the performances of the T1 devices

Device no.	V_{oc} (Volt)	J_{sc} (mA/cm^2)	PCE (%)	FF	R_s (Ω.cm^2)	R_{sh} (Ω.cm^2)
No.1	0.60	6.80	2.08	0.51	17.02	380.95
No.2	0.60	6.48	2.10	0.54	16.66	320.00
No.3	0.60	6.52	2.02	0.52	17.31	275.86
Average	0.60	6.60	2.07	0.53	17.00	325.60

Table 5.2 Summary of the performances of the T2 devices

Device no.	V_{oc} (Volt)	J_{sc} (mA/cm^2)	PCE (%)	FF	R_s (Ω.cm^2)	R_{sh} (Ω.cm^2)
No.1	0.60	12.69	3.83	0.51	14.05	357.14
No.2	0.60	12.61	3.87	0.53	13.30	370.15
No.3	0.60	12.14	3.91	0.54	13.57	357.68
No.4	0.60	12.26	4.05	0.55	13.24	357.14
No.5	0.60	11.80	4.01	0.57	14.18	416.66
No.6	0.60	11.80	3.98	0.56	14.25	400.00
No.7	0.60	13.40	3.80	0.47	16.30	270.07
Average	0.60	12.38	3.92	0.53	14.13	361.26

Device short circuit current density has reached in average 12.38 mA/cm^2 with a maximum at 13.40 mA/cm^2. PCE on average has obtained the value of 3.92 % with the highest at 4.05%. Series resistance (R_s) and shunt resistance (R_{sh}) calculated from dark and illuminated J-V curves of all devices are also listed in Table 5.1 and 5.2. R_s exhibited a small decrease on average from 17.00 Ω.cm^2 of T1 devices to 14.13 Ω.cm^2 of T2 devices. R_{sh} was within the same range of values for both devices. Thus, a 50 to

90% improvement of OSC T2 devices in current density and PCE compared to that of OSC T1 devices was mainly attributed to plasmon-enhanced optical absorption by smaller Au NPs as seen in Figure 5.7. Some contributions may also be related to a slight decrease of series resistance (R_s) in the T2 devices.

5.3.3 Optical properties of ETL and P3HT:PCBM active layer

5.3.3.1 Transmission spectra of the ZnO ETL

The incident light reaches to the P3HT:PCBM active layer through ZnO ETL. Therefore, Figure 5.8 illustrates the transmission spectra of the sol-gel ZnO thin film on glass substrates. The deposited film shows high transmittances over the entire visible range with more than 95% transmittance at a wavelength of 550 nm.

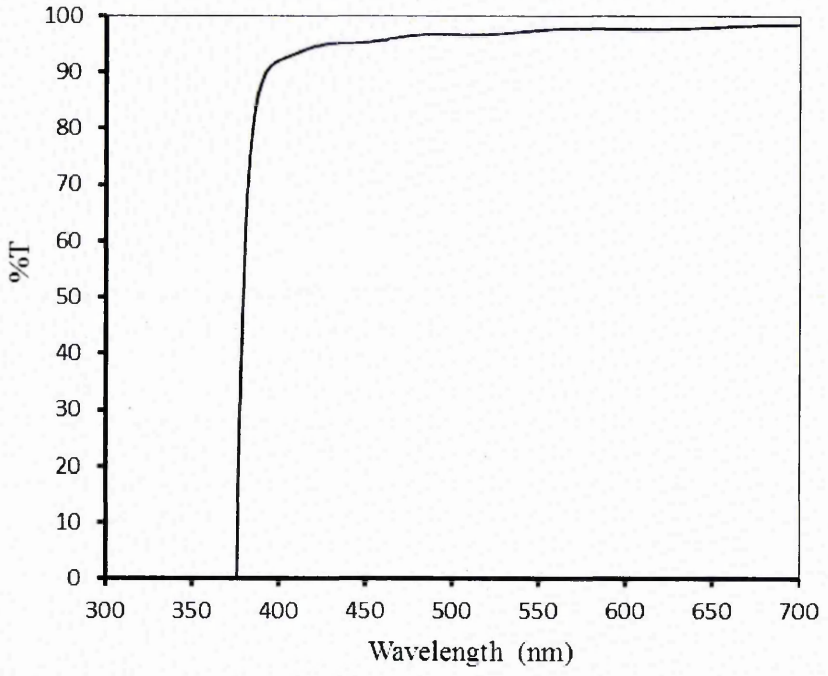

Figure 5.8 Transmission spectrum of the sol gel deposited ZnO electron transport layer

5.3.3.2 Analysis of enhanced light absorption to the P3HT:PCBM active layer

Optical absorption of different samples was analysed to evaluate enhanced light absorption by the Au NPs. In order to explore whether and how much light absorption was actually absorbed by the active P3HT:PCBM layer, the absorbance of various samples as prepared in section 5.2 were studied respectively. Results of optical absorption for the sputtered Au thin films used for T2 devices on glasses at different thicknesses of approximately 5, 11, and 16 nm are presented respectively in Figure 5.9. Plasmonic resonances of Au NPs are very sensitive to the sizes, shapes, and arrangements of NPs as well as the surrounding environment. The localized absorption characteristic of our Au films was found to be the same as those of the sputtered Au films published by Siegel et al. [24]. An absorption minimum around 500 nm was

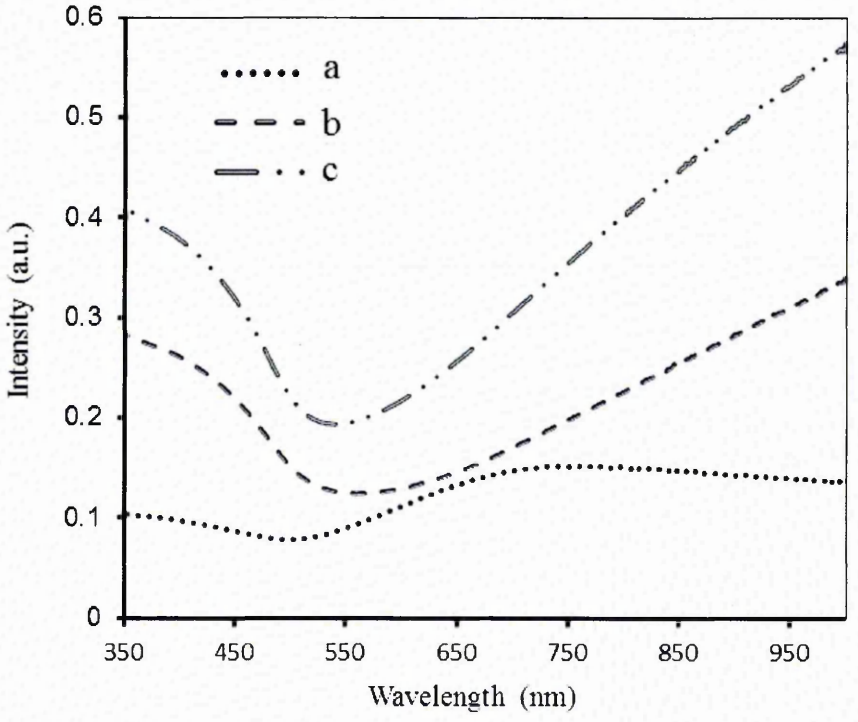

Figure 5.9 Optical absorption spectra of Au thin films on glasses, (a) ~5 nm thick Au film, (b) ~11 nm thick Au film, (c) ~16 nm thick Au film, respectively.

presented in the spectra, which is slightly red-shifted with increasing film thickness. As the thickness becomes greater, the absorption band is broadened due to a wider particle size distribution. The exhibited behaviour of the PAPVD sputtered Au film in the absorbance is due to the surface plasmon [25]. Optical absorption of the single PEDOT:PSS layer after encapsulating the Au NPs was then studied. When obtained optical absorption of the PEDOT:PSS layer with different thicknesses Au layers (shown in Figure 5.10) deducted optical absorption of the sputtered Au thin film at the corresponding thickness (shown in Figure 5.9), the net absorbance of the PEDOT:PSS layer with the incorporated Au plasmonic NPs was obtained as shown in Figure 5.11

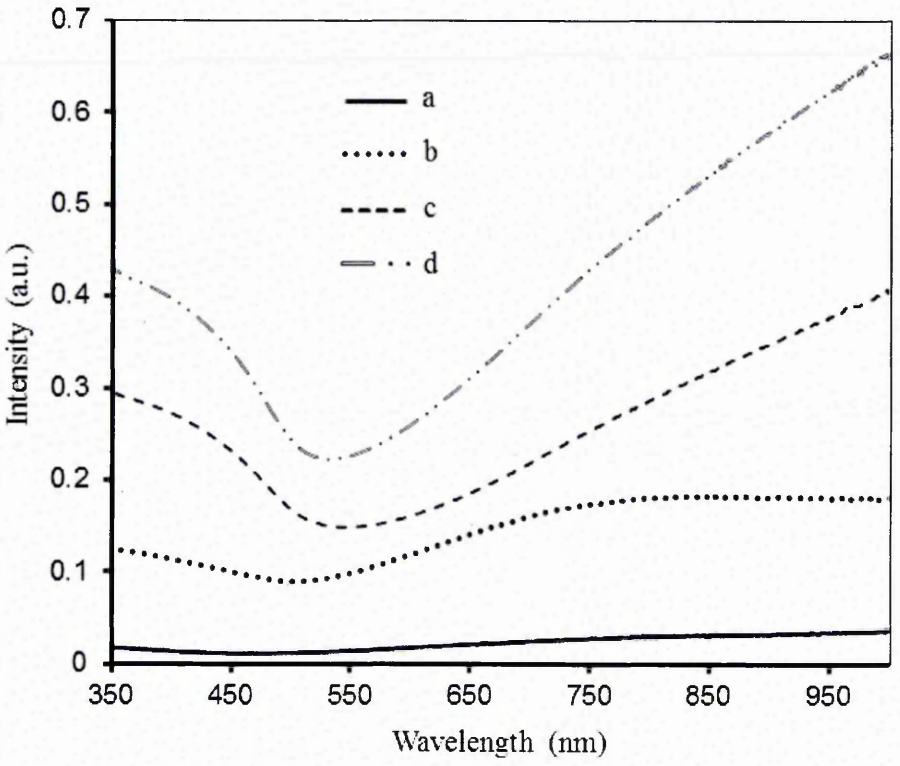

Figure 5.10 Optical absorption spectra of the ~25 nm PEDOT:PSS layer with or without Au NPs films, (a) without Au film, (b) with ~5 nm thick Au film, (c) with ~11 nm thick Au film, (d) with ~16 nm thick Au film.

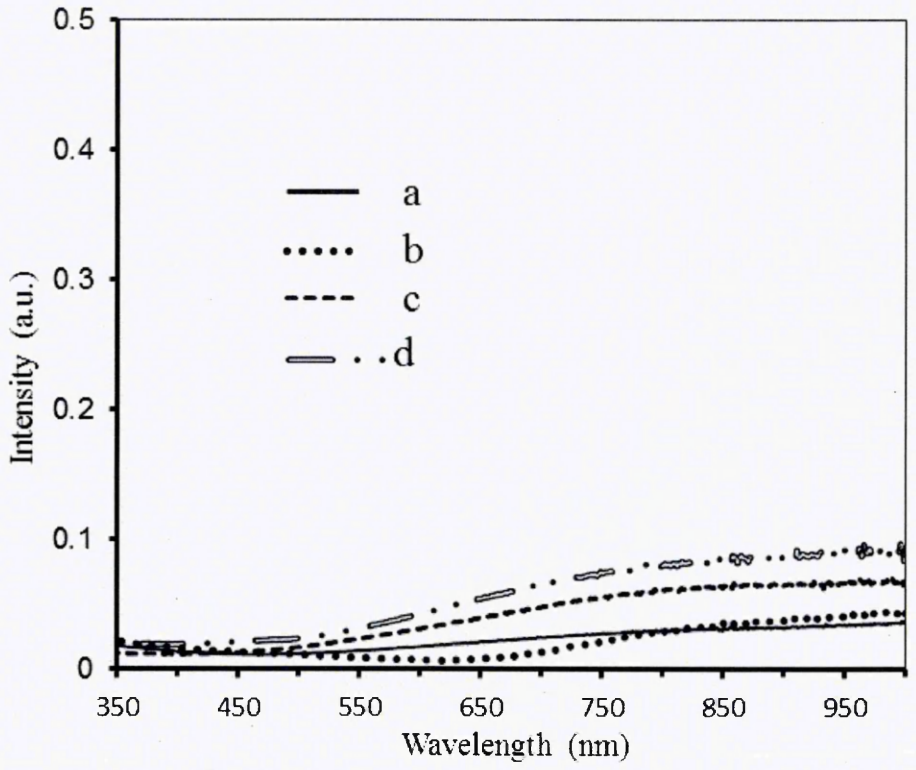

Figure 5.11 Net optical absorption spectra of the ~25 nm thick PEDOT:PSS layer without Au NPs and combined with Au NPs obtained after applying the 5, 11, and 16 nm thick Au NPs films, (a) the PEDOT:PSS film only, (b) the PEDOT:PSS film combined with Au NPs from ~5 nm thick Au film, (c) the PEDOT:PSS film combined with Au NPs from ~11 nm thick Au film, (d) the PEDOT:PSS film combined with Au NPs from ~16 nm thick Au film, respectively.

respectively. No enhanced light absorption was exhibited for the PEDOT:PSS layer after coated by the 5 nm thick Au film while a slight enhancement in the absorbance was observed for the PEDOT:PSS layer coated by the 11 and 16 nm thick Au film respectively in the red and near IR spectral range. Afterwards, optical absorption of the single active P3HT:PCBM layer directly coated by different thicknesses Au NPs films was then analysed respectively. Similarly when optical absorption of the ~150 nm thick

P3HT:PCBM layer with different thicknesses Au NPs films (shows in Figure 5.12) Au NPs was also shown in Figure 5.13. It exhibited its well-known absorption band in the spectral range of 350–650 nm [26]. Unexpectedly, net optical absorption of the active P3HT:PCBM layer with different thicknesses Au NPs films significantly decreased in the wavelength range except a small increase for the active layer coated by the 16 nm thick Au NPs film in the UV spectral range and a slight enhancement for all samples in the near IR spectral range. This result may be assigned to the reason that the morphology of the P3HT:PCBM blend was greatly altered by the directly sputtered Au

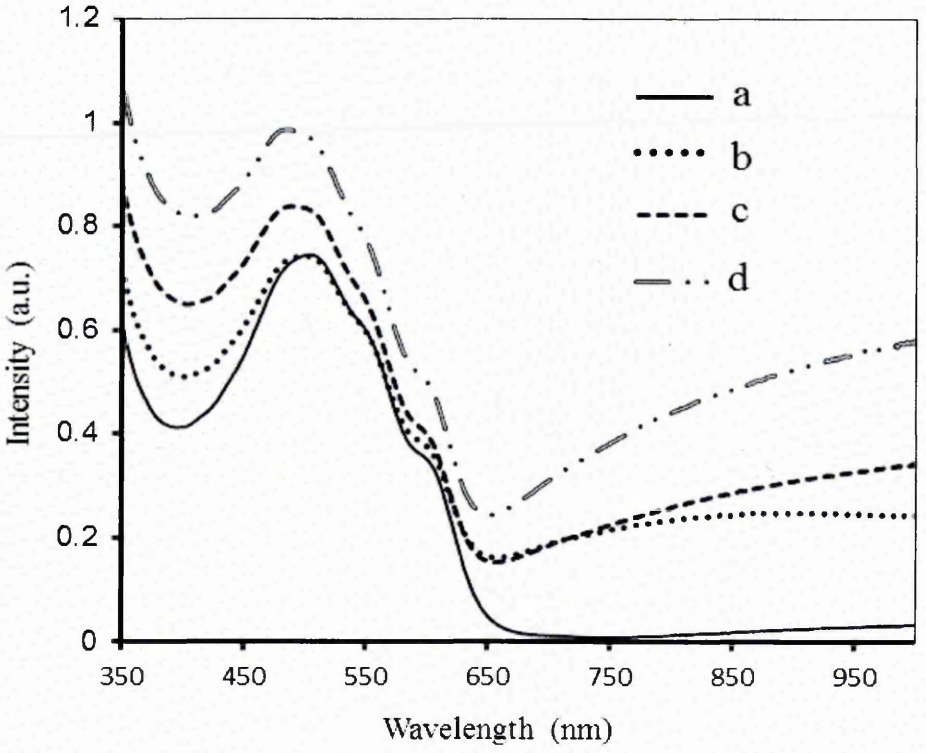

Figure 5.12 Optical absorption spectra of the ~150 nm P3HT:PCBM layer with or without Au NPs films, (a) without Au film, (b) with ~5 nm thick Au film, (c) with ~11 nm thick Au film, d) with ~16 nm thick Au film.

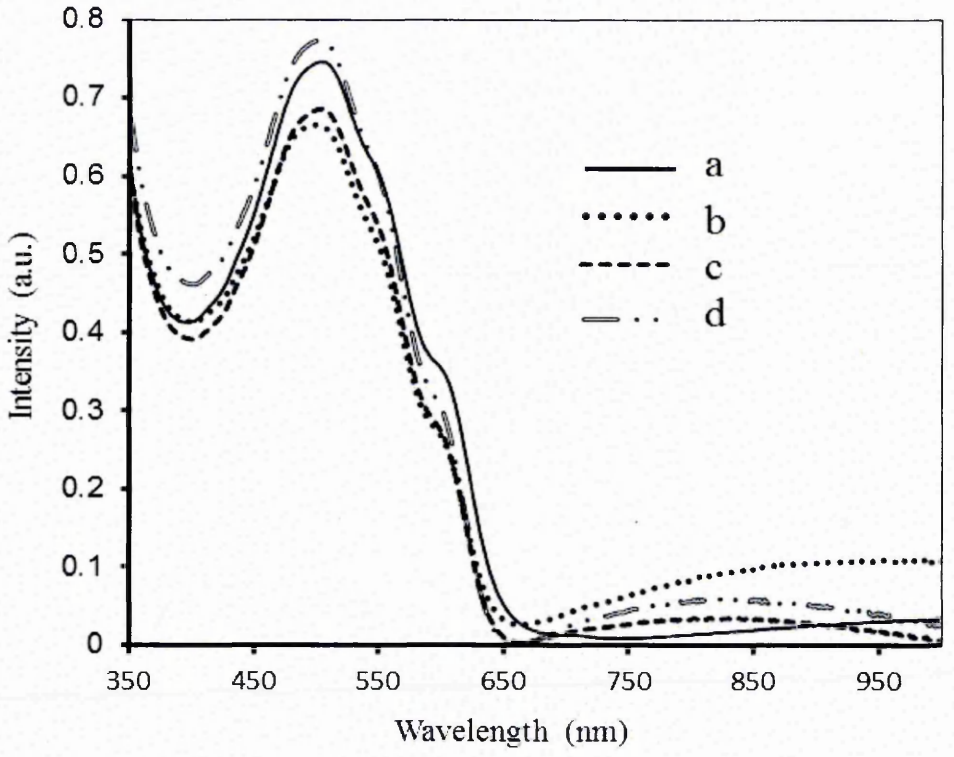

Figure 5.13 Net optical absorption spectra of the ~150 nm thick P3HT:PCBM layer without Au NPs and combined with Au NPs obtained from directly applying the 5, 11, and 16 nm thick Au NPs films, (a) the P3HT:PCBM film only, (b) the P3HT:PCBM film combined with Au NPs from ~5 nm thick Au film, (c) the P3HT:PCBM film combined with Au NPs from ~11 nm thick Au film and (d) the P3HT:PCBM film combined with Au NPs from ~16 nm thick Au film, respectively

NPs. Furthermore, the absorbance of the active P3HT:PCBM layer was investigated after coated by the PEDOT:PSS and then followed the Au NPs films at different thicknesses of 5, 11, and 16 nm, respectively. Net optical absorption was presented in Figure 5.14 when optical absorption of the double-layer film with different thicknesses Au NPs films (Figure 5.15) deducted optical absorption of the PEDOT:PSS film with

the correspondent thickness Au NPs film respectively (as shown in Figure 5.10). For the comparison study, net absorbance of the ~150 nm thick P3HT:PCBM layer without Au NPs was also plotted in Figure 5.14 by deducting optical absorption of the PEDOT:PSS layer from optical absorption of the double layer.

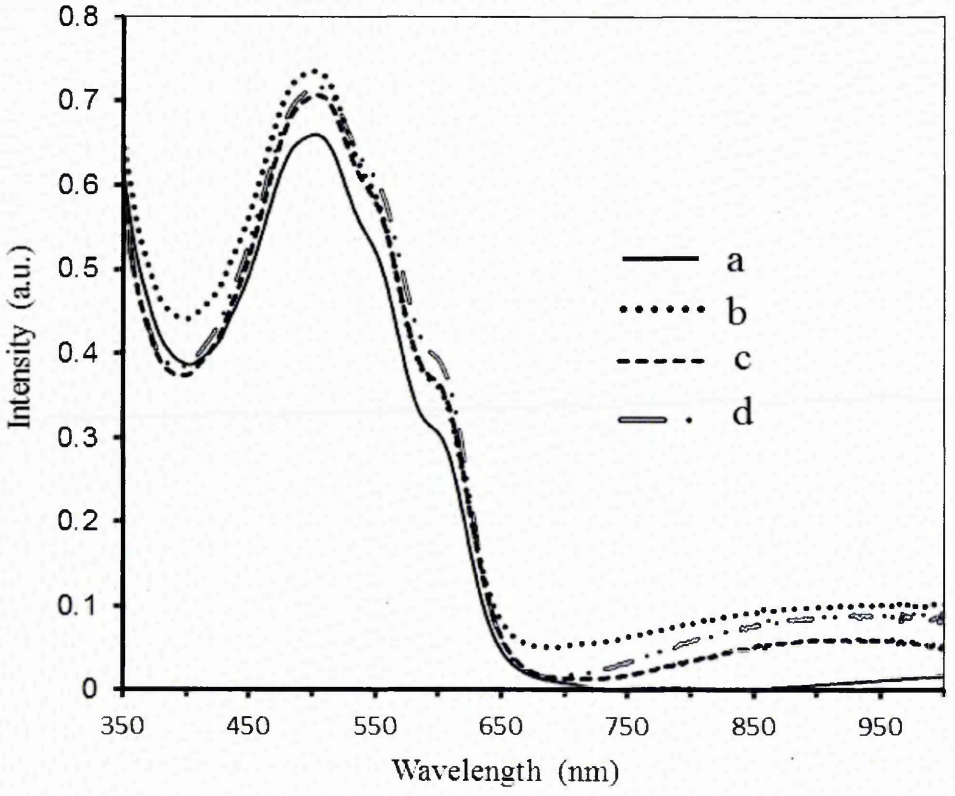

Figure 5.14 Plasmon enhanced net optical absorption spectra of the ~150 nm thick P3HT:PCBM layer obtained from applying the 5, 11, and 16 nm thick Au NPs films on the double-layer film, (a) the P3HT:PCBM film only, (b) the P3HT:PCBM film by the enhancement of Au NPs from the ~5 nm thick Au film, (c) the P3HT:PCBM film by the enhancement of Au NPs from the ~11 nm thick Au film and (d) the P3HT:PCBM film by the enhancement of Au NPs from the ~16 nm thick Au film, respectively.

Enhanced broadband optical absorption for the active layer coated by the 5 nm thick Au NPs film was observed in the whole range spectra of 350–1000 nm. Enhanced light absorption was also maintained for the active layer coated by the 11 and 16 nm thick Au NPs films separately in the spectral range of 450–650 nm and 750–1000 nm. Given the fact that the size of these Au NPs is ~15 nm, this increase was attributed to LSPRs of Au NPs that touched directly with the active blend or probably embedded slightly into the active layer. As described in Section 5.6 about the formation processing of the Au NPs in the PEDOT:PSS layer, the initial deposition stage seems most important to achieve enhanced light absorption in the active layer. Since the best plasmonic light

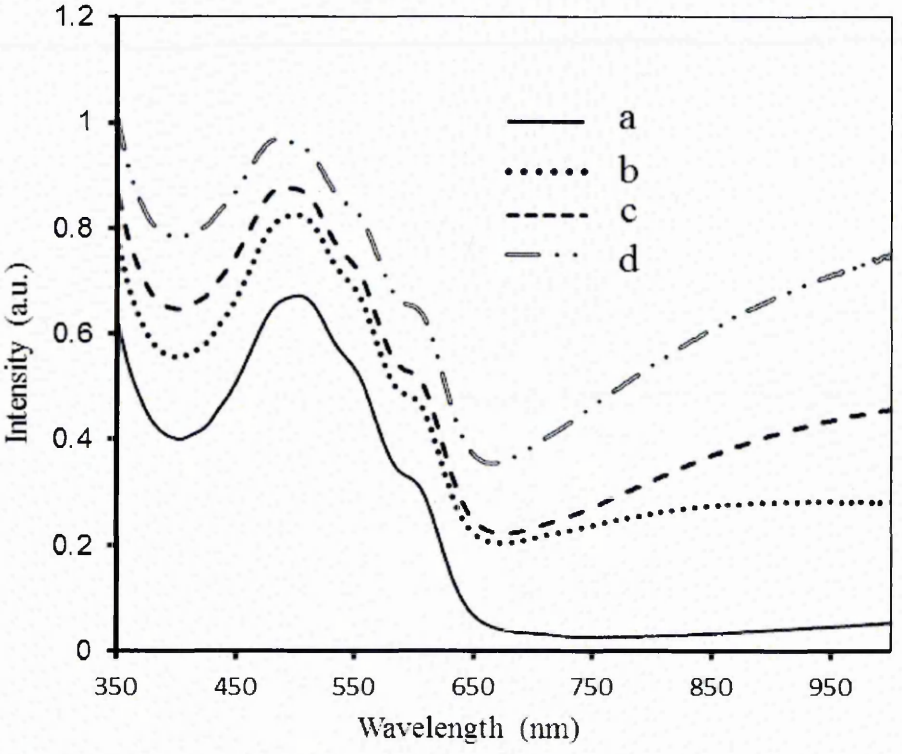

Figure 5.15 Optical absorption spectra of the ~150 nm P3HT:PCBM and ~25 nm PEDOT:PSS layer with or without Au NPs films, (a) without Au film, (b) with ~5 nm thick Au film, (c) with ~11 nm thick Au film, (d) with ~16 nm thick Au film.

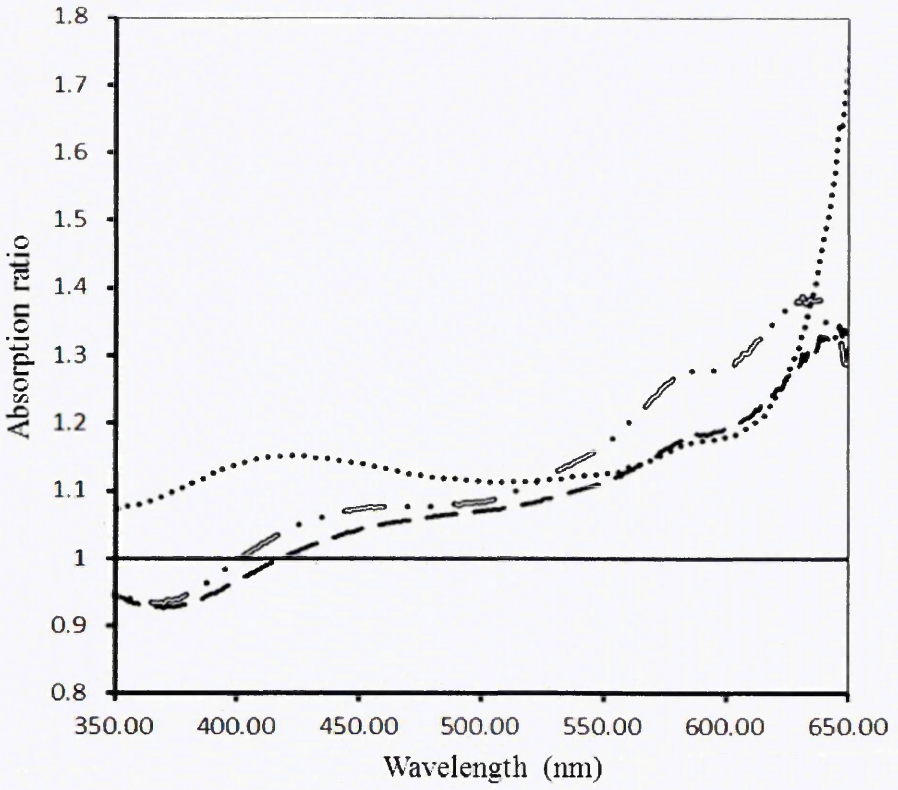

Figure 5.16 Normalised absorption spectra of the P3HT:PCBM layer as shown in (a) relative absorption ratios of the P3HT:PCBM film by the enhancement of Au NPs from the ~5 nm thick Au film, (b) relative absorption ratios of the P3HT:PCBM film by the enhancement of Au NPs from the ~11 nm thick Au film and (c) relative absorption ratios of the P3HT:PCBM film by the enhancement of Au NPs from the ~16 nm thick Au film to that of the P3HT:PCBM film without Au NPs, respectively.

absorption enhancement amongst three different thicknesses samples was obtained by the thinnest Au NPs film, an ideal device structure suggested would be that of ITO/ ZnO/P3HT:PCBM/PEDOT:PSS/thin Au NPs/HTL/other type of electrode for further investigation which will be discussed in later chapter. Figure 5.16 presents the ratios of light absorption of the active layer by the Au NPs enhancement to that of the active layer without Au NPs in the spectral range of 350-650 nm. An ~20% increase on

average of total optical absorption in this spectral range was observed although some small decrease for the active layer with the 11 and 16 nm thick Au NPs films was exhibited in the UV spectral range of 350–400 nm. Enhanced light absorption in the wavelength range of 400–650 nm where the P3HT:PCBM active layer is absorbing was fully contributed to the improvement of PCE of our OSC devices. It is not clear whether enhanced optical absorption in the spectral range of 750–1000 nm was also attributed to the PCE. However, enhanced light absorption in this spectrum is anticipated to be very useful on the improvement of PCE if it is applied on OSC devices fabricated by an active blend with spectrally extended light absorption band to red and near IR [22]. Overall from the above, the sputtered Au NPs were not able to provide either a significant light enhancement to the PEDOT:PSS layer or any light absorption increase to the active P3HT:PCBM layer when the Au NPs film was directly applied on the single layer film. However, enhanced broadband light absorption realised on the active P3HT:PCBM layer when the Au NPs film was coated on the double-layer film. The PEDOT:PSS layer seems playing an important role on providing the bridge as the buffer layer for the sputtered Au NPs reaching the active layer without causing its alteration in the morphology.

5.4 Summary

(1) Surface morphologies of the sol-gel derived ZnO ETL, P3HT:PCBM active layer and PEDOT:PSS HTL were investigated by the SEM and tapping mode AFM. The uniform surface of ZnO film revealed its depth roughness below 5 nm. The AFM morphology of P3HT:PCBM blends composed of two contrast phases with an average roughness of 2.4 nm. The surface morphology of the PEDOT:PSS layer showed less than 5 nm roughness with some ~40 nm sized nanocavities or nanodents, which are

randomly distributed at an average distance of 250 nm. We concluded that the PAPVD deposited Au NPs can be easily fit into these low-depth nanocavities and form the dispersed layer of Au NPs within the PEDOT:PSS layer that enhanced the absorption to the P3HT:PCBM active layer by LSPR and scattering. The morphologies of the Au NPs thin films were also investigated with a featured NPs size using the SEM; i.e. ~50 nm and ~15 nm, respectively. Different thicknesses (approximately 6, 13, 20, and 40 nm) of ~15 nm sized Au NPs thin films on top of ~25 nm thick PEDOT:PSS layer were analysed by the atomic force microscope separately and the morphological result inferred a composite interfacial layer which contained two types of NPs; i.e. PEDOT:PSS and Au NPs surrounded by each other. The interfacial NPs or nano cluster perform plasmonic resonances that can be absorbed by the P3HT:PCBM active layer, providing enhanced light absorption.

(2) The performances of two types of single junction inverted OSC devices (T1 and T2) were investigated, respectively. The devices T2 revealed the average PCE of 3.92% with the highest at 4.05%, whereas, the average PCE of T1 devices was at 2.07%. The significantly improved PCE (~90%) for T2 devices was assigned to the noticeable increase of photocurrent due to plasmon-enhanced optical absorption by smaller (~15 nm)Au NPs embedded into the PEDOT:PSS layer where some contribution may also come from a small decrease of R_s.

(3) We demonstrated that PCE of a single junction inverted P3HT:PCBM OSC device was improved by applying a PAPVD Au NPs film on the thin PEDOT:PSS film after the active layer. Different samples such as P3HT:PCBM/PEDOT:PSS, P3HT:PCBM/Au NPs embedded PEDOT:PSS and Au NPs thin films were analysed to evaluate enhanced light absorption by the Au NPs. The thicknesses of the embedded Au NPs thin films were approximately 5, 11, and 16 nm, respectively. Through the

incorporation of these thicknesses of ~15 nm thick Au NPs into the PEDOT:PSS layer, ~20% increase in the overall absorption to the P3HT:PCBM active layer was observed although some small decrease for the active layer with the 11 and 16 nm thick Au NPs films was exhibited in the UV spectral range of 350–400 nm. The P3HT:PCBM active layer coated by the 5 nm thick Au NPs film was demonstrated enhanced broadband optical absorption in the whole spectral range of 350–1000 nm. The enhanced light absorption in the wavelength range of 400–650 nm where the P3HT:PCBM active layer is absorbing was fully contributed to the improvement of PCE of the OSC devices. In contrast, no enhanced light absorption was realised when the PAPVD Au NPs film was directly applied on the P3HT:PCBM active layer. This result may be assigned to the reason that the morphology of the P3HT:PCBM blend was greatly altered by the directly sputtered Au NPs.

5.5 References:

[1] C. J. Brabec, N. S. Sariciftci, J. C. Hummelen, Plastic solar cells. Adv. Funct. Mater., 11 (2001) 15-26.

[2] K. M. Coakley, M. D. McGehee, Conjugated polymer photovoltaic cells. Chem. Mater., 16 (2004) 4533-4542.

[3] H. A. Atwater, A. Polman, Plasmonics for improved photovoltaic devices. Nature Mater., 9 (2010) 205-213.

[4] H. Shen, B. Maes, Combined plasmonic gratings in organic solar cells. Opt. Express, 19 (2011) A1202-A1210.

[5] A. J. Morfa, K. L. Rowlen, Plasmon-enhanced solar energy conversion in organic bulk heterojunction photovoltaics. Appl. Phys. Lett., 92 (2008) 013504.

[6] X. Chen, C. Zhao, L. Rothberg, M.K. Ng, Plasmon enhancement of bulk heterojuction organic photovoltaic devices by electrode modification. Appl. Phys. Lett., 93 (2008) 0123303.

[7] G. D. Spyropoulos, M. Stylianakis, E. Stratakis, E. Kymakis, Plasmonic organic photovoltaics doped with metal nanoparticles. Phot. Nano. Fund. Appl., 9 (2011) 184-189.

[8] D. D. S. Fung, L. F. Qiao, W. C. H. Choy, C. D. Wang, W. E. I. Sha, F. X. Xie, S. L. He, Optical and electrical properties of efficiency enhanced polymer solar cells with Au in a nanoparticles PEDOT–PSS layer. J. Mater. Chem., 21 (2011) 16349-16356.

[9] D. H. Wang, K. H. Park, J. H. Seo, J. Seifter, J. H. Jeon, J. K. Kim, J. H. Park, O. O. Park, A. J. Heege, Enhanced power conversion efficiency in PCDTBT/PC70BM bulk heterojunction photovoltaic devices with embedded silver nanoparticle clusters. Adv. Energy Mater., 1 (2011) 766-770.

[10] F. X. Xie, W. C. H. Choy, C. C. D. Wang, W. E. I. Sha, D. D. S. Fung, Improving the efficiency of polymer solar cells by incorporating gold nanoparticles into all polymer layers Appl. Phys. Lett., 99 (2011) 153304.

[11] J. Yang, J. B. You, C. C. Chen, W. C. Hsu, H. R. Tan, X. W. Zhang, Z. R. Hong, Y. Yang, Plasmonic polymer tandem solar cell. ACS Nano, 5 (2011) 6210-6217.

[12] C. H. Kim, S. H. Cha, S. C. Kim, M. Song, J. Lee, W. S. Shin, S. J. Moon, J. H. Bahng, N. A. Kotov, S.-H. Jin, Silver nanowire embedded in P3HT:PCBM for high-efficiency hybrid photovoltaic device applications. ACS Nano, 5 (2011) 3319-3325.

[13] M. Heo, H. Cho, J. W. Jung, J. R. Jeong, S. Park, J. Y. Kim, High-performance organic optoelectronic devices enhanced by surface plasmon resonance. Adv. Mater., 23 (2011) 5689- 5693.

[14] D. H. Wang, D. Y. Kim, K. W. Choi, J. H. Seo, S. H. Im, J. H. Park, O. O. Park, A. J. Heeger, Enhancement of donor–acceptor polymer bulk heterojunction solar cell power conversion efficiencies by addition of Au nanoparticles. Angew. Chem. Int. Ed., 50 (2011) 5519-5523.

[15] N. Kalfagiannis, P.G. Karagiannidis, C. Pitsalidis, N.T. Panagiotopoulos, C. Gravalidis, S. Kassavetis, P. Patsalas, S. Logothetidis, Pasmonic silver nanoparticles for improved organic solar cells. Sol. Energ. Mater. Sol. Cells, 104 (2012) 165-174.

[16] C. C. D. Wang, W. C. H. Choy, C. Duan, D. D. S. Fung, W. E. I. Sha, F. X. Xie, F.Huang, Y. Cao, Optical and electrical effects of gold nanoparticles in the active layer of polymer solar cells. J. Mater. Chem., 22 (2012) 1206-1211.

[17] X. Li, W. Choy, L. Huo, F. Xie, W. Sha, B. Ding, X. Guo, Y. Li, J. Hou, J. You, Y. Yang, Dual plasmonic nanostructures for high performance inverted organic solar cells. Adv. Mater., 24 (2012) 3046-3052.

[18] M. C. Scharber, D. Wuhlbacher, M. Koppe, P. Denk, C. Waldauf, A. J. Heeger, C. L. Brabec, Design rules for donors in bulk-heterojunction solar cells-towards 10% energyconversion efficiency. Adv. Mater., 18 (2006) 789-794.

[19] B. Minnaert, M. Burgelman, Efficiency potential of organic bulk heterojunction solar cells. Prog. Photovoltaics, 15 (2007) 741-748.

[20] M. Koppe, H.J. Egelhaaf, G. Dennler, M.C. Scharber, C.J. Brabec, P. Schilinsky, C. N. Hoth, Near IR sensitization of organic bulk heterojunction solar cells: towards optimization of the spectral response of organic solar cells. Adv. Funct. Mater., 20 (2010) 338-346.

[21] C. E. Small, S. Chen, J. Subbiah, C. M. Amb, S-W. Tsang, T-H. Lai, J. R. Reynolds, F. So, High-efficiency inverted dithienogermole–thienopyrrolodione-based polymer solar cells Nat. Photon., 6 (2012) 115-120.

[22] N. Li, F. Machui, D. Waller, M. Koppe, C.J. Brabec, Determination of phase diagrams of binary and ternary organic semiconductor blends for organic photovoltaic devices. Sol. Energ. Mater. Sol. Cells, 95 (2011) 3465-3471.

[23] R. F. Bunshah, C. V. Deshpandey, Plasma assisted physical vapor deposition processes: A review. J. Vac. Sci. Technol., A 3 (1985) 553-560.

[24] J. Siegel, O. Lyutakov, V. Rybka, Z. Kolská, V. Švorčík, Properties of gold nanostructures sputtered on glass. Nanoscale Res. Lett., 6 (2011) 96.

[25] I. D. Mor, Z. Barkay, N. F. Granit, A. Vaskevich, I. Rubinstein, Ultrathin gold island films on silanized glass. Morphology and optical properties. Chem. Mater., 16 (2004) 3476.

[26] M. Sunderberg, O. Inganas, S. Stafstrom, G. Gustafsson, B. Sjogren, Optical absorption of poly(3-alkylthiophenes) at low temperatures. Solid State Commun., 71 (1989) 435-439.

Chapter 6: Effect of the active layer morphologies and device structures on their performances

6.1 Introduction

Extensive studies in photovoltaic (PV) technologies have been carried out in the past decade to achieve cost efficient high performance devices [1-4]. Although significant work on single bulk hetero-junction (BHJ) OSCs has doubled their power conversion efficiency from ~ 4% [5,6] to ~ 8-10 % for the latest devices,[7-10] competition with other mature PV technologies is still not reachable directly in the current market. Maximum PCE that could be achieved on the single BHJ OSCs may be limited to ~15% through optimisation of the blend of the active materials with an appropriate band gap, energy levels, and carrier mobility [11-15].

One of the key barriers in enhancing the PCE of OSCs except intrinsic properties of materials is their limited thin active layer in the devices leading to low light absorption. In recent years, introducing novel plasmonic nanostructures into the devices for enhancement of light absorption has emerged as an expanding area to increase the performance of OSC devices [16]. Many studies have been carried out to incorporate random and periodic nanostructures of metallic nanoparticles (NPs) into various layers of organic solar cells where some have demonstrated promising results in terms of enhancement of optical absorption, fill factor (FF), and current density in the devices without changing the thickness of the active layer [17-26]. Metals that support plasmonic resonances (PRs) modes and have resonances in the visible or near infrared region of the electromagnetic spectrum are used to constitute metal nanostructures in order to achieve strong plasmonic effects. Different noble metallic NPs and their positions with different concentrations, shapes and sizes have been reviewed [27-29].

Synthesis of plasmonic NPs is relatively simple; however, the control over their shapes, sizes and distributions in the devices presents a big challenge by various chemical or vacuum-based deposition methods. It is usually recognized that metallic NPs embedded inside the active layer cannot improve the device performance due to the loss mechanism including non-radiative decay and charge carrier recombination that can lead to a decrease of charge carriers [20].

Although deposition of noble metallic NPs on indium tin oxide electrodes or PEDOT:PSS hole transport layers has been widely studied and some good enhancement in the PCE and FF has been achieved,[21,29] the metallic NPs were relatively far from the active layer and showed the absorption enhancement either by light scattering or only weak light effects from plasmonic NPs. Compared with the incorporation of periodic nanostructures in the devices that leads to a narrow spectral enhancement, physical mechanism that received much attention is the randomly distributed NPs with varying shapes and sizes owing to that broadband light absorption enhancement can be realised [16].

This chapter presents further improved PV structures of the inverted OSCs where the thin film of Au NPs was sandwiched between the PEDOT:PSS and highly conducting PEDOT:PSS (hcPEDOT:PSS) layers. The Au NPs film was deposited by plasma assisted physical vapour deposition (PAPVD) in the OSC devices where Au NPs provided a significant plasmonic broadband light absorption enhancement to the active layer. The addition of the high boiling point substance of 1,8 diiodooctane (DD) was also used to improve the active layer, enabling to slow down the deposition drying rate and thus increasing the crystallinity of the organic blend active layer.

6.2 Device structures and experimental methods

The OSCs were fabricated on patterned ITO coated glass substrates (12–15 ohms/sq. from VisionTek Systems Ltd., UK). The OSC device structures as shown in Figure 6.1 are ITO/ZnO/P3HT:PCBM/PEDOT:PSS (plus embedded Au NPs)/Au top electrode (labelled as Device ID1), ITO/ZnO/P3HT:PCBM/PEDOT:PSS (plus embedded Au NPs)/Au NPs film/hcPEDOT:PSS (high conducting PEDOT:PSS)/Au top electrode (labelled as Device ID2) and ITO/ZnO/P3HT:PCBM with DD/PEDOT:PSS (plus embedded Au NPs)/Au NPs film/hcPEDOT:PSS/Au top electrode (labelled as Device ID3).

The embedded Au NPs in the PEDOT:PSS layer were obtained through penetration of Au NPs by the PAPVD simultaneously when either depositing the top Au electrode for ID1 or the thin Au NPs films between the PEDOT:PSS and hcPEDOT:PSS layers for ID2 and ID3, respectively. The ITO patterned glass substrates were ultrasonically cleaned in acetone, isopropyl alcohol and deionised water for 10 min, respectively. After drying with nitrogen, the substrates were spin-coated with a ~35 nm thick amorphous SG1 sol-gel derived ZnO layer as explained in Chapter 5. Then the samples were transferred into a nitrogen-filled glovebox. On top of the ZnO layer, a ~150 nm thick active layer with and without the additive of DD was spin-coated from the 1:1 CB3 chlorobenzene solution of P3HT:PCBM. The solution was stirred for more than 12 h at 70°C and then passed through 0.2 micron filter. After that the blend was divided into two equal parts with one part following the addition of 3.0 % DD. Equal volume of chlorobenzene was also added to free-DD part in order to maintain the same level of concentration. The active layers with and without DD were annealed at 80 °C and 140 °C for 10 min on a hot plate, respectively.

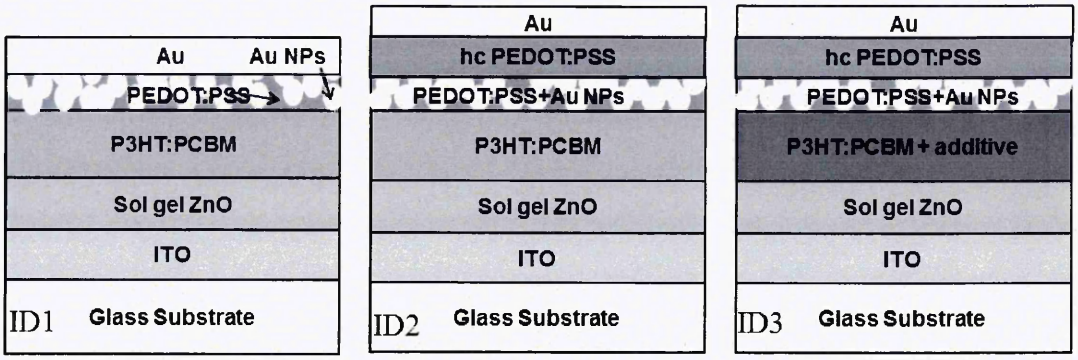

Figure 6.1 Schematic diagram of cross sections for inverted OSCs, (a) the processed reference structure for devices ID1 without the hcPEDOT:PSS layer, (b) the inferred real structure for ID2 devices where thin AU NPs film was sandwiched between two PEDOT:PSS layer, (c) the structure for ID3 devices where the active layer has 3.0 % DD as a high boiling point additive. (Note: not to scale).

Afterwards, the samples were removed out of the glove box, followed a PDS2 based ~25 nm thick PEDOT:PSS layer spin-coated on top of the active layer as the HTL. The samples were then transferred again into the nitrogen- filled glove box for heat treatment at 110 °C for 10 min. For Device ID1, ~80-nm-thick Au electrode was directly deposited onto the PEDOT:PSS layer by PAPVD at base pressure of $1x10^{-2}$ mbar [36]. Au NPs were embedded into the PEDOT:PSS layer through penetration in this process, providing plasmonic light absorption enhancement to the active layer. For Devices ID2 and ID3, ~5-nm-thick Au NPs thin films were deposited onto the PEDOT:PSS layer via the PAPVD at base pressure of $1x10^{-2}$ mbar and followed a ~40-nm-thick thin film of the hcPEDOT:PSS deposited by the spin coating method and then annealed outside at 110 °C for 10 min. Similarly, in this process Au NPs were at the same way encapsulated into the PEDOT:PSS layer through penetration. Finally, Au top electrode was deposited by the PAPVD at base pressure of $1x10^{-2}$ mbar and was then

annealed in air at 110 °C for 10 min. The thickness of the Au electrode layer is approximately at 80 nm. During this process, Au NPs may penetrate into the hcPEDOT:PSS layer; however, these Au NPs did not make their contributions via plasmon to light absorption enhancement of the active layer because they were far away from the active layer. The active area of PSCs was 4.0 mm^2 and the tested active area with mask was 3.2 mm^2.

Samples of the spin-coated P3HT:PCBM layer were prepared on pure glass slides without ITO thin films for characterisation of optical, morphological and structural properties, respectively. ID2 and ID3 samples after applying the 5-nm-thick Au NPs films were respectively produced, enabling to investigate their morphologies. For comparative studies of optical, morphological and structural properties, thin films of the active P3HT:PCBM layer with and without DD were also deposited on the pure glass slides. Dry powder samples of the P3HT and PCBM blends with and without DD was respectively obtained by removing the annealed thin films from pure glass substrates for FTIR analyses.

6.3 Results and discussion

6.3.1 Morphologies of the PEDOT:PSS, P3HT:PCBM and Au thin films

6.3.1.1 Surface morphologies of PEDOT:PSS and hcPEDOT:PSS layers

The surface morphologies of the PEDOT:PSS films were analysed using the tapping mode AFM. Figure 6.2 represents the surface morphologies of the PEDOT:PSS, Au NPs film on top of the PEDOT:PSS, and the hcPEDOT:PSS film deposited on top of the PEDOT:PSS/Au NPs thin film. Figure 6.2 (a) shows the surface morphology of the PEDOT:PSS thin film with an average roughness of nearly 5 nm. The morphology consists of uniformly interconnected structures of aggregates or clusters with island

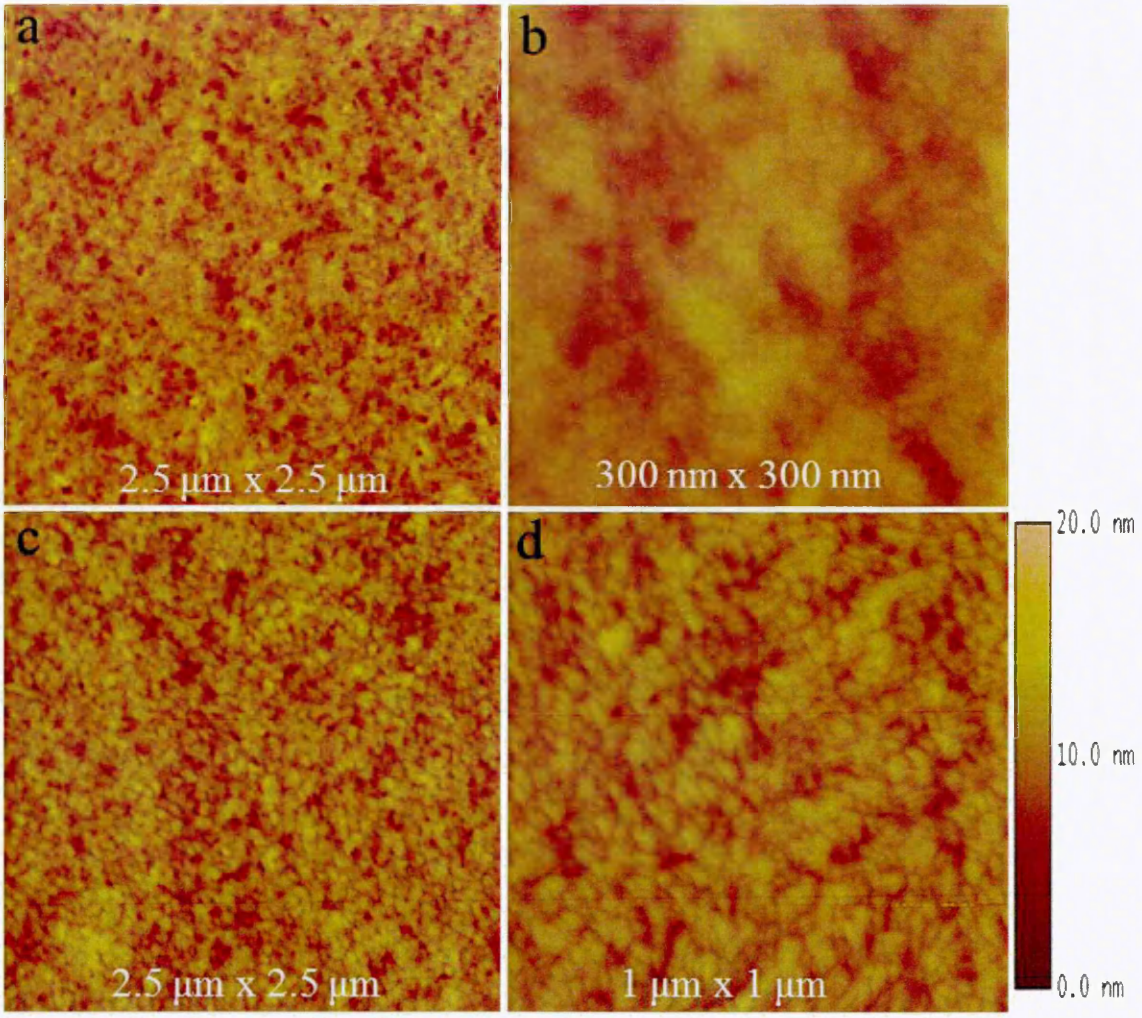

Figure 6.2 AFM morphological images of different thin films of : (a) PEDOT:PSS on glasses; (b) ~5 nm thick Au film on top of PEDOT:PSS film; (c) hcPEDOT:PSS film on top of PEDOT:PSS/Au NPs film; (d) magnified image of 6.2(c).

structures. The morphology of the ~5 nm Au NPs thin film on top of the PEDOT:PSS was presented in Figure 6.2 (b). The Au film was in its initial processing stage, presenting dispersed structures according to the surface pattern of the PEDOT:PSS film. In order to make a sandwiched structure of the Au NPs film, a hcPEDOT:PSS film was then deposited on top of the dispersed Au NPs thin film. Figure 6.2 (c) shows the morphology of the deposited film. The thin PEDOT:PSS film showed (Figure 6.2 a) the

nanosized interconnected structure while the hcPEDOT:PSS film exhibited a slightly coarser nanosized interconnected structure as more clearly observed in the magnified image of Figure 6.2(d).

6.3.1.2 Morphologies of the P3HT:PCBM and Au NPs thin films

Atomic force microscopy (AFM) was used to investigate the morphologies of the active layers. Figure 6.3 (a & b) shows the AFM tapping-mode height images of the P3HT:PCBM active layers produced with and without DD, respectively. A coarser morphology is observed for the active layer with DD in Figure 6.3 (b) compared to that of without DD as seen in Figure 6.3 (a). The coarser surface is related to the bigger-sized organic aggregates of more crystallinity of the P3HT:PCBM, which favours a stronger interaction between the active layer and the hole transport layer.

Low voltage scanning electron microscopy (LVSEM) was used to image the nanostructures of the P3HT:PCBM blend thin-film as shown in Figure 6.3 (c & d). A significant difference in morphologies has been observed. The morphology of the active layer without DD exhibits much less contrast, with contrast variations on different length scales, (Figure 6.3 c) compared to the active layer with DD that contains large contrast variations on the length scale of hundreds of nanometers. The latter reveals interconnected well-ordered aggregates that appear white in Figure 6.3 (d) in the P3HT:PCBM with DD. The high contrast could be an indication of a relatively pure or rich P3HT phase with high crystallinity, as any incorporation of PCBM would lead to a reduction in contrast.

Therefore the white aggregates may be beneficial to the dissociation of the generated excitons while their connection and the improved crystallinity may provide a well-formed carrier transport pathway. The latter would enable the enhanced efficiency of

the carrier collection following the dissociation of excitons at the interface of the P3HT:PCBM. The morphologies in Figure 6.3 (c & d) correspond to the results obtained by AFM in Figure 6.3 (a & b).

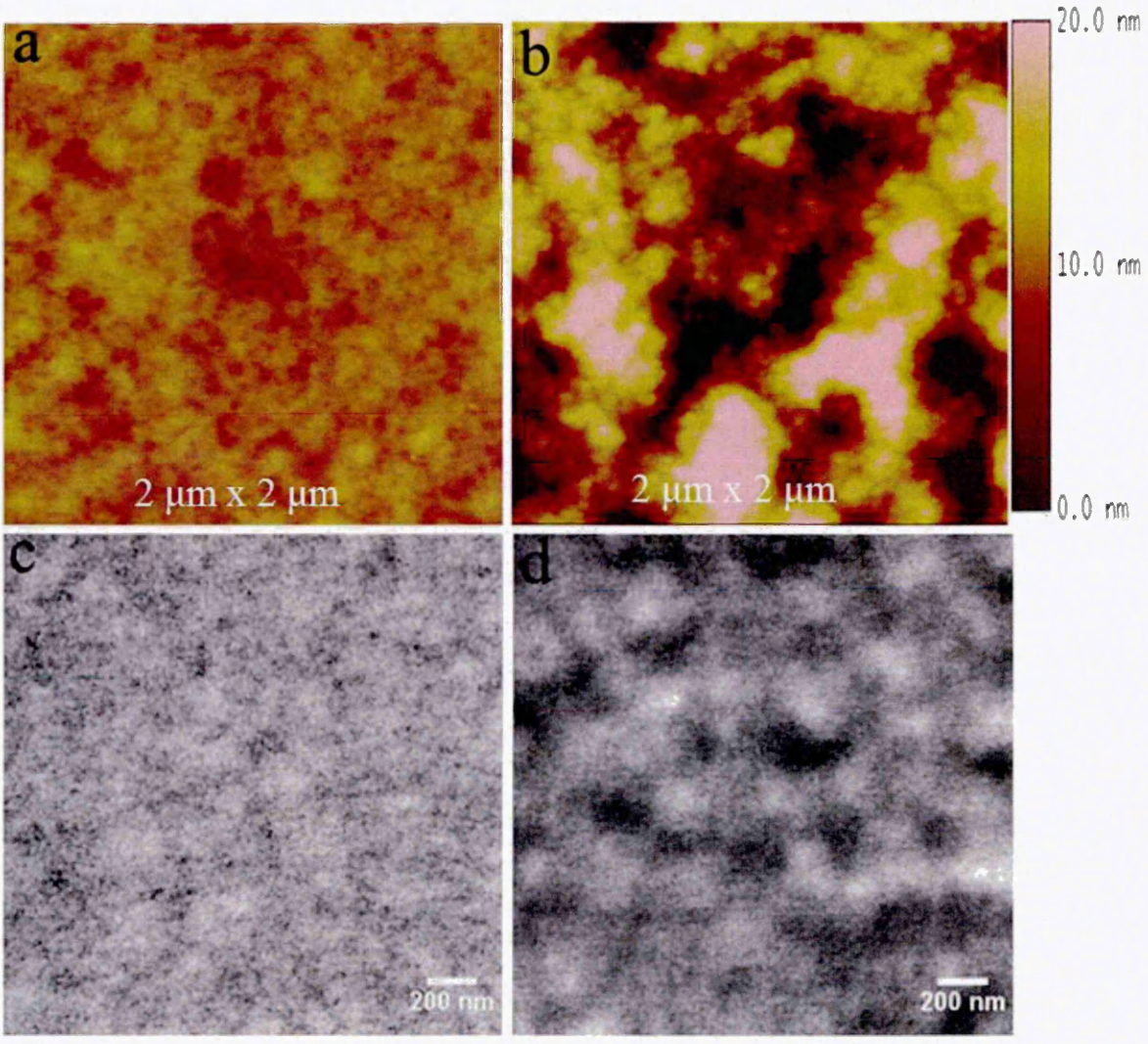

Figure 6.3 Morphological images of P3HT:PCBM thin films, (a) AFM morphological images of P3HT:PCBM without DD, (b) with DD, (c) LVSEM image of the P3HT:PCBM blend without DD, (b) with DD,

LVSEM was also used to investigate the morphology of the Au coated P3HT:PCBM sample (see Figure 6.4). Figure 6.4 reveals a well-defined morphology of the Au NPs. The Au NPs are present in circular oblong-shaped structures extending over a few nanometres. Morphologies observed in LVSEM can be further analysed by using Auto-correlation Functions (ACF) [30]. The ACF compares the image with itself when it is shifted by a certain distance. If the ACF-curve has a minimum, it means that it is unlikely to find structures with such a separation distance. A peak in the ACF curve means that it is very likely to find the same feature repeated at this distance. Figure 6.5 contains the ACFs for Au NPs and P3HT:PCBM active layers (with and without DD) which can be used to characterise their typical dimensions.

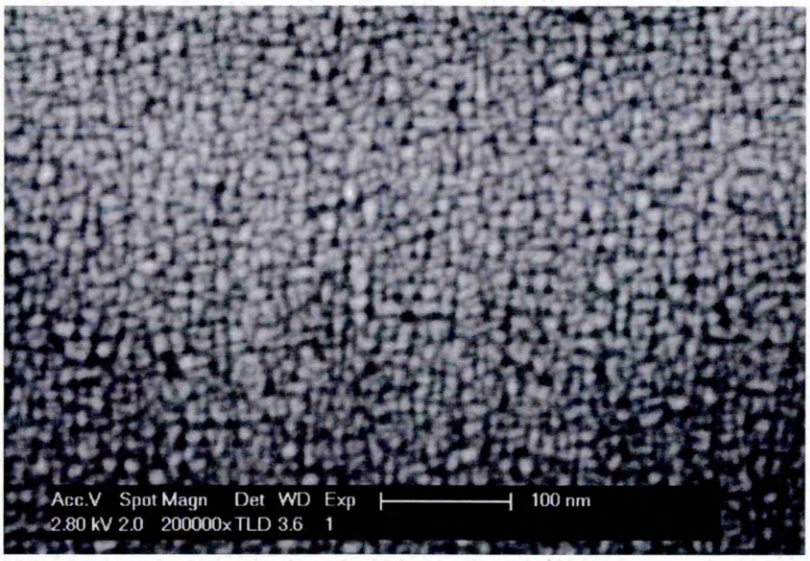

Figure 6.4 Low voltage scanning electron microscope images of the thin Au NPs.

For Au NPs a clear minimum is observed at 9 nm followed by a maximum at 17 nm. Thus, it can be inferred that the radius of the Au NPs is on average ~ 8 nm or less. The observed shape and size of Au NPs explain the enhanced broadband light absorption in

our OSCs [31-33]. Furthermore, the ACF curve derived from the Au-coated P3HT:PCBM in Figure 6.5 shows a maximum at the same location as that derived from the P3HT:PCBM (without DD) morphologies (with 17 nm at high magnification), which implies that Au NPs may be preferentially found on top of one of the phases. Figure 6.5 also contains ACFs from the low magnification images shown in Figure 6.3. It is clear by comparing the ACFs for the DD-free P3HT:PCBM with that for the DD-doped P3HT:PCBM that the latter is heavily dominated by a very clear minimum at 250 nm followed by a clear maximum at 460 nm indicating the typical size of 200 nm of the highly rich P3HT aggregates. The latter is also observed for the DD-free P3HT: PCBM but the peak is very weak (note the logarithmic scale) and only one of a number of peaks presents in the ACF, including one at 17 nm. From this analysis it appears that

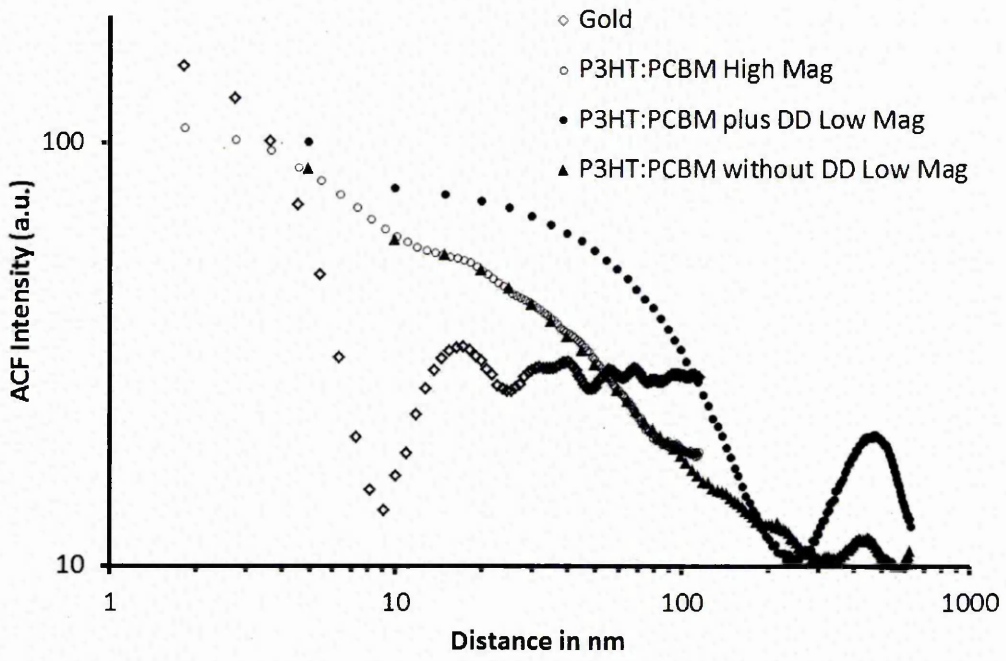

Figure 6.5 Auto-correlation-functions derived curves for the LVSEM image analyses.

the addition of DD favours the formation of a particular type of structure that is also present in the free-DD P3HT:PCBM but not dominating.

6.3.2 Properties of the P3HT:PCBM active layers with and without additives

6.3.2.1 Visible light absorption and structural properties

Figure 6.6 presents the light absorption spectra of the P3HT:PCBM film produced from the blend with and without the DD additive, respectively. The π-π^* absorption band of the active layer with DD shifts toward the red, distinguishing from three dominant features in absorption; i.e. one peak at 510 and two shoulders at 550 nm and 610 nm separately in comparison with that without the addition of DD. The vibronic shoulders of the active layer with DD near the wavelengths of 550 nm and 610 nm become wider and more clearly defined in the spectra, showing a strong interchain interaction. The red-shift in the absorption spectrum means a high degree of crystallinity of the P3HT:PCBM blend, indicating an enhanced interaction between the organic chains.

The X-ray diffraction (XRD) patterns were further performed to characterise the structures of the active layers. Figure 6.7 shows the XRD pattern of the P3HT:PCBM films. A much stronger peak at around ~5.45° is presented for the fabricated P3HT:PCBM when the DD was added in the blend. A slight shift of the peak position is also observed from ~ 5.28° of the active layer without DD to ~5.45° of the P3HT:PCBM with DD. The significantly increased peak intensity and the reduced full width at half maximum (FWHM) of the active layer with DD again confirm the highly oriented structures or crystallinity. The addition of the high boiling point DD additive in the blend leads to the much slow evaporation rate of solvents when fabricating the active layer, which enables that the organic had enough time to form more ordered structures.

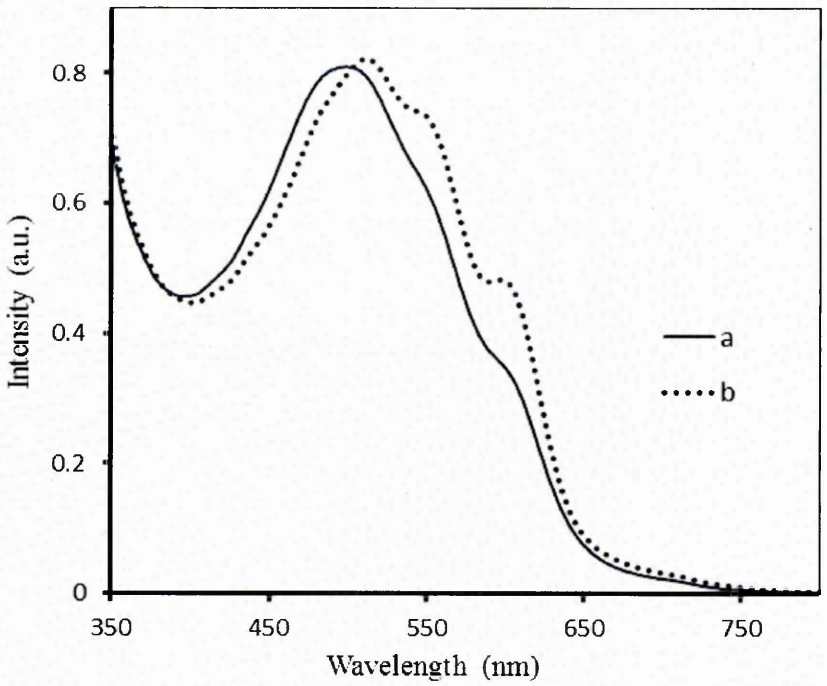

Figure 6.6 Optical absorption spectra of the ~150 nm thick P3HT:PCBM layer, (a) without DD, (b) with DD.

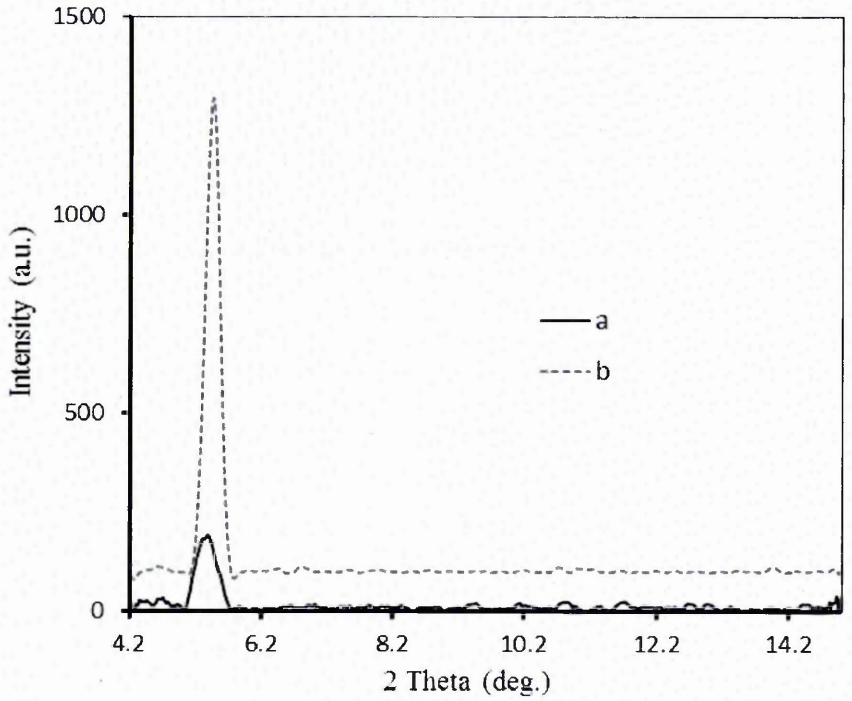

Figure 6.7 XRD patterns of the P3HT:PCBM layers, (a) without DD, (b) with DD.

6.3.2.2 ATR-FTIR analysis of the P3HT:PCBM active layers with and without additives

The FTIR spectra of the P3HT:PCBM film with and without the DD are separately presented in Figure 6.8. The characteristic bands of the P3HT:PCBM film are observed at 1510-1440 cm^{-1} (ring stretch), 1375 cm^{-1} (methyl deformation), and 820 cm^{-1} (aromatic out of plane vibrations) respectively while the C=O stretching vibration in the P3HT:PCBM film appears at 1735 cm^{-1}. The aromatic =C-H out of the plane vibrations at 820 cm^{-1} represents the characteristic of P3HT.

The two peaks in the band between 1510 and 1440 cm^{-1} are associated with the stretching vibration of the thiophene ring. The concerned two peaks at 1509 and 1448 cm^{-1} characterise the asymmetric C=C stretching and the symmetric stretching vibrations of the P3HT:PCBM because their relative ratio of the intensities can be used to probe the average conjugation of the P3HT in the P3HT:PCBM blend [34,35]. The reason is attributed to the preferential orientation of the organic chains or some variations in the conjugation length. Changes of the intensity and the ratio between these two peaks can be observed after the addition of DD into the P3HT:PCBM blend in Figure 6.9.

Another two fullerene peaks located at 1184 cm^{-1} and 1428 cm^{-1} are related to the PCBM. The intensities of these two characteristic peaks are improved after the addition of the DD, endorsing the enhanced mixing of PCBM with P3HT. Thus, FTIR results further exhibit the changes of the active layer by the addition of DD in the conjugated nature of the P3HT and the combination of P3HT and PCBM.

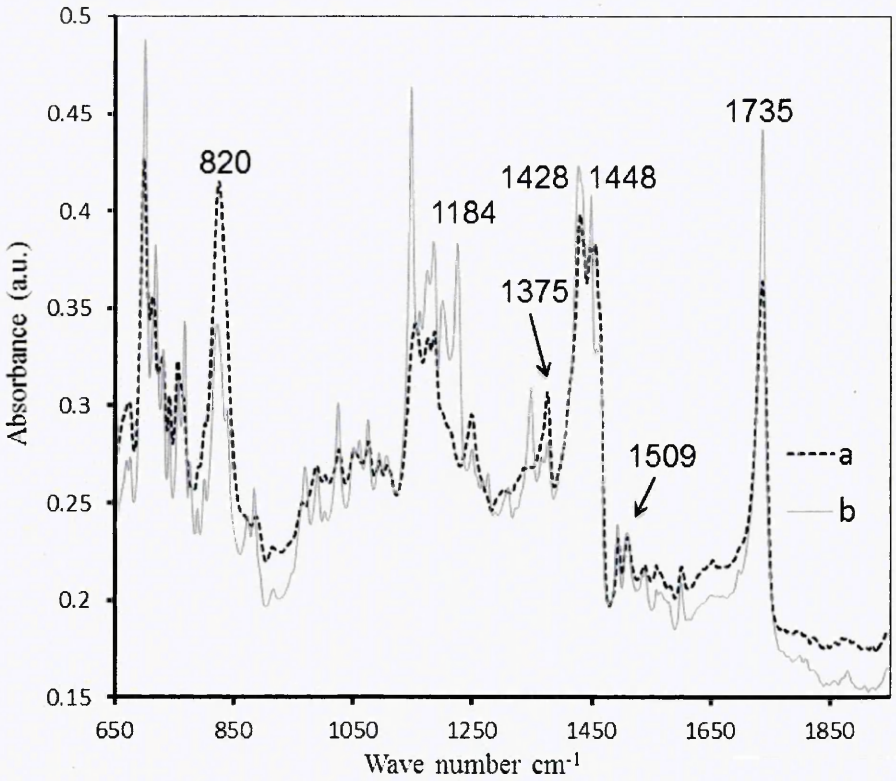

Figure 6.8 FTIR spectra of the P3HT:PCBM layers, (a) without DD, (b) with DD

6.3.3 Performance of OSC devices

6.3.3.1 Performance of OSC devices by extra hcPEDOT:PSS layer

In order to examine the influence of the extra hcPEDOT:PSS layer, Figure 6.9 illustrates the J-V characteristics of the devices ID1 and ID2. The open circuit voltages and current densities of both the devices are nearly same with a value of 0.62 V and ~11.80 mA/cm^2, respectively. The PCE has increased from a value of 4.0% for device ID1 to 4.5% for device ID2. Table 6.1 and 6.2 summarised the performance parameters of device ID1 and ID2. The results revealed that the extra hcPEDOT:PSS layer has no influence on V_{oc} and J_{sc} of the inverted OSC devices ID1 and ID2. The enhancement in PCE is due to the enhanced fill factor for device ID2 after the deposition of the extra

hcPEDOT:PSS layer and some contributions may also be related to the improved values of R_s and R_{sh}.

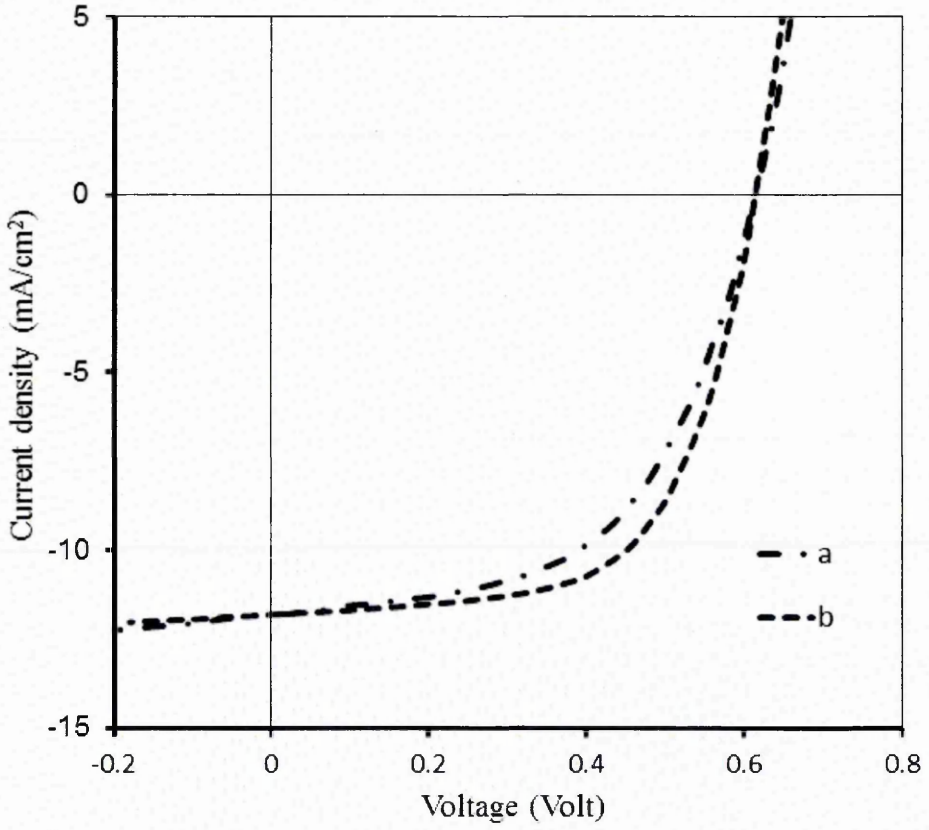

Figure 6.9 J-V characteristics of inverted OSC devices, (a) ID1, (b) ID2.

Table 6.1 Summary of photovoltaic parameters of OSC devices ID1

Device no.	V_{oc} (V)	J_{sc} (mA/cm^2)	FF (%)	PCE (%)	R_s (Ω-cm^2)	R_{sh} (Ω-cm^2)
No.1	0.62	11.76	54	3.94	14.28	406.00
No.2	0.62	11.96	54	3.99	13.46	353.66
No.3	0.62	11.80	55	**4.00**	14.35	415.76
No.4	0.62	12.10	53	3.85	16.07	313.86

Table 6.2 Summary of photovoltaic parameters of OSC devices ID2

Device no.	V_{oc} (V)	J_{sc} (mA/cm^2)	FF (%)	PCE (%)	R_s (Ω-cm^2)	R_{sh} (Ω-cm^2)
No.1	0.62	12.10	59	4.40	12.86	688.66
No.2	0.62	11.81	62	**4.51**	11.80	727.27
No.3	0.62	11.60	61	4.36	11.90	713.16
No.4	0.62	11.74	56	4.10	13.02	657.68

6.3.3.2 Performance of OSC devices with and without the additives to the P3HT:PCBM active layer

Performance of three types of OSCs labelled as ID1, ID2 and ID3 shown in Figure 6.1 were investigated, respectively. Figure 6.10 shows J-V curves of the ID1, ID2 and ID3 OSCs and their performance results are summarized in Table 6.3 and 6.4. Device ID1 had a generally inverted structure and obtained ~ 4% PCE. The same inverted OSCs as ID1 from previous chapter demonstrated that PCE were ~ 2.5 to 3 % if without any Au NPs plasmonic light absorption enhancement [36]. The thin Au NPs film by PAPVD presents broadband light absorption behaviour in the PEDOT:PSS layer as shown in previous chapter. Small-sized Au NPs produced by PAPVD can penetrate through the PEDOT:PSS layer to top of the active layer shown in Figure 6.1(a), which creates enhanced light absorption to the active layer due to plasmonic effects and leads to the increased PCE of ~ 4%. PCE of the OSC device ID2 further increased up to 4.51 % by forming a sandwiched PEDOT:PSS HTL structure in Figure 6.1 (b) where the very thin Au NPs film by the PAPVD was deposited between the general PEDOT:PSS and the high conducting PEDOT:PSS layer. This result confirmed that Au plasmonic light absorption enhancement can lead to an improved device performance in PCE.

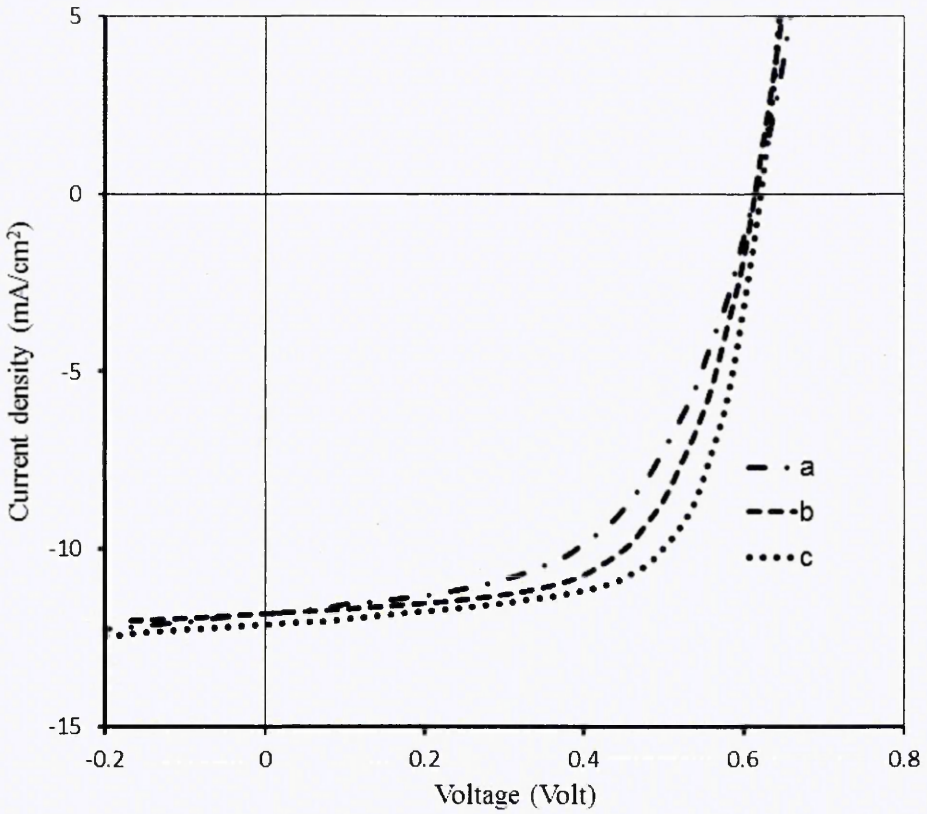

Figure 6.10 J–V characteristics under illumination of the inverted OSCs, (a) ID1 devices processed without the hcPEDOT:PSS layer, (b) ID2 devices where thin Au NPs film was sandwiched between two PEDOT:PSS layers, (c) ID3 devices where the active layer has 3.0 % DD as a high boiling point additive.

Table 6.3 Summary of photovoltaic parameters of OSC devices ID3

Device no.	V_{oc} (V)	J_{sc} (mA/cm^2)	FF (%)	PCE (%)	R_s (Ω-cm^2)	R_{sh} (Ω-cm^2)
No.1	0.62	12.12	67	**5.01**	09.13	889.00
No.2	0.62	12.25	65	4.95	09.80	857.88
No.3	0.62	12.74	61	4.80	11.16	796.38
No.4	0.62	11.96	66	4.90	9.16	888.66

Table 6.4 Summary of photovoltaic parameters of the best inverted OSC devices

Device	V_{oc} (V)	J_{sc} (mA/cm^2)	FF (%)	PCE (%)	R_s (Ω-cm^2)	R_{sh} (Ω-cm^2)
ID1	0.62	11.80	55	4.00	14.35	415.76
ID2	0.62	11.81	62	4.51	11.80	727.27
ID3	0.62	12.12	67	5.01	09.13	889.00

Surface plasmons produce large local electromagnetic fields near to Au NPs surfaces, which are proposed to increase light absorption in organic materials causing the overall improved efficiency [16]. Local surface plasmon resonance (LSPR) excitation from Au NPs not only enhances absorption of the photoactive conjugate organic, but also raises probability of excitons being dissociated into free charge carriers which leads to the reduced recombination loss [16,26]. If compared the device ID1 with ID2 in performance parameters shown in Table 6.1, the main cause for the increased PCE comes from the improved FF from 55% to 62%.

Series resistance (R_s) and shunt resistance (R_{sh}) of OSCs calculated from dark and illuminated I-V curves are also listed in Table 6.1. R_s exhibits a small decrease on average from 14.35 Ω.cm^2 of the device ID1 to 11.80 Ω.cm^2 of the device ID2 and R_{sh} shows a nearly double increase from 415.76 Ω.cm^2 of the device ID1 to 727.27 Ω.cm^2 of the device ID2. All these changes provide their contributions for the improvement of FF. The PCE of the inverted OSCs was further increased by adding a high boiling additive of DD in the blend of P3HT:PCBM as shown in Figure 6.1(c). The PCE of the inverted device ID3 has reached to 5.01% with the increased current of 12.12 mA/cm^2 and FF 67%. R_s and R_{sh} were also optimised as 9.13 Ω.cm^2 and 889.00 Ω.cm^2, respectively.

6.3.3.3 External quantum efficiency measurements

Results of external quantum efficiency (EQE) spectra were measured for the three types of OSCs, which further evidences the improvement of PCE. Figure 6.11 presents the obtained EQE of the inverted devices. EQE of the devices ID2 and ID3 is higher in the whole visible spectral range than that of the device ID1, which is in correspondence

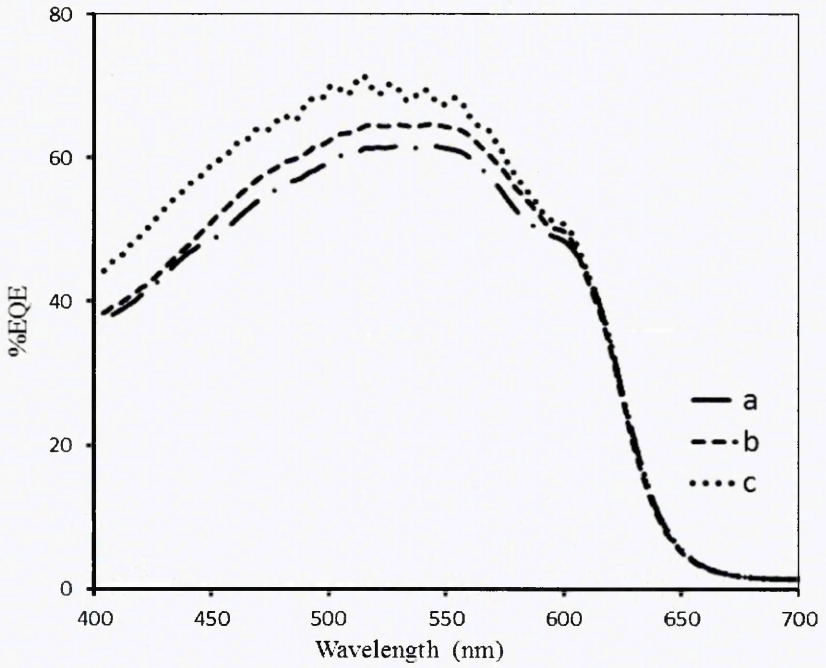

Figure 6.11 EQE measurement of the inverted OSCs, (a) ID1 devices processed without the hcPEDOT:PSS layer, (b) ID2 devices where thin Au NPs film was sandwiched between two PEDOT:PSS layers, (c) ID3 devices where the active layer has 3.0 % DD as an additive.

with their increased PCE as shown in Table 6.4. The EQE is defined as the ratio between the number of electrons flowing out of the device and the number of photons incident upon it, representing proportionally the efficiency of light absorption in the active layer. Previous chapter has demonstrated that the optical absorbance of the active

P3HT:PCBM layer was increased by depositing Au NPs in the PEDOT:PSS layer. Hence, the achieved high current density in the device ID3 is mainly owing to the combined effect of plasmonic near-field light absorption enhancement by Au NPs and the highly oriented structures of the active layer by the slow dry process due to the addition of DD.

6.4 Summary

(1) Surface morphologies of the PEDOT:PSS, PEDOT:PSS/Au NPs thin films, and PEDOT:PSS/Au NPs film /hcPEDOT:PSS films were investigated by the tapping mode AFM. The uniformly interconnected structure of the PEDOT:PSS was different from the hcPEDOT:PSS, which exhibited a slightly coarser nanosized interconnected structures. The morphology of the ~5 nm Au NPs thin film on top of the PEDOT:PSS film was also investigated with a dispersed structure that was affected by the formed pattern of the PEDOT:PSS film. As a comparative study, the morphologies of the P3HT:PCBM active layer were studied with and without the addition of DD using AFM. The coarser surface with bigger-sized organic aggregates leads to more crystallinity of the P3HT:PCBM active layer compared to that of without DD, which was also confirmed by LVSEM. LVSEM was further used to investigate the morphology of the Au coated P3HT:PCBM, which reveals a well-defined morphology of the Au NPs with circular oblong-shaped structures extending over a few nanometres. ACF was also used to analyse the LVSEM morphologies, which inferred that the radius of the Au NPs is on average ~ 8 nm or less and preferentially found on top of one of the phases. The ACF analysis of the P3HT:PCBM active layer with and without DD demonstrates that the addition of DD favours the formation of a particular type of structure that is also present (but not dominant) in the DD free P3HT:PCBM.

(2) Fabrication of the P3HT:PCBM active layer by the addition of DD which reduces its drying rate in the fabrication process led to a red shift of optical absorption. The vibronic shoulders at 550 nm and 610 nm in the spectra illustrated an enhanced interaction between the organic chains after the addition of DD. Furthermore, the enhanced XRD peak intensity at around 5.45^{o} and the reduced full width at half maximum (FWHM) of the active layer with DD again confirm the highly oriented structures. The FTIR spectra of the P3HT:PCBM film with and without the DD was also studied separately and the observed results further exhibited the changes in the conjugated nature of the P3HT and the combination of P3HT and PCBM by the addition of DD.

(3) Finally, the performances of three types of OSC devices (ID1, ID2 and ID3) were investigated, respectively. The device ID3 revealed the PCE of 5.01% compared to devices ID1 and ID2. The PCEs of ID1 and ID2 were ~4.0 and ~4.51%, respectively. The significantly improved PCE was due to the Au plasmonic effect which was created by sandwiching the thin PAPVD Au NPs film between two PEDOT:PSS HTL layers and also contribution from the addition of DD into the P3HT:PCBM active layer. The presence of Au NPs provide broadband light absorption enhancement, leading to the increased EQE. The modified P3HT:PCBM structure by the addition of DD can be beneficial to the dissociation of excitons and provide a well-formed pathway for carrier transportation. The obtained improvement in PCE was mainly assigned to the noticeable increase of the photocurrent and the fill factor. The changes in R_s and R_{sh} also provide their contributions in the overall enhancement in the performance.

6.5 References:

[1] C. J. Brabec, N. S. Sariciftci, J. C. Hummelen, Plastic Solar Cells, Adv. Funct. Mater., 11 (2001) 15-26.

[2] K. M. Coakley, M. D. McGehee, Conjugated polymer photovoltaic cells, Chem. Mater., 16 (2004) 4533-4542.

[3] S. K. Hau SK, H. L. Yip, A. K. Y. Jen, A review on the development of the inverted polymer solar cell architecture, Polym. Rev., 50 (2010) 474-510.

[4] F. Zhang, X. Xu, W. Tang, J. Zhang, Z. Zhuo, J. Wang, J. Wang, Z. Xu, Y. Wang, Recent development of the inverted configuration organic solar cells Sol. Energ. Mat. Sol. Cells., 95 (2011) 1785-1799.

[5] G. Li, V. Shrotriya, J. Huang, Y. Yao, T. Moriarty, K. Emery,Y. Yang, High-efficiency solution processable polymer photovoltaic cells by self-organization of polymer blends. Nat. Mater., 4 (2005) 864–868.

[6] W. L Ma, C. Y. Yang, X. Gong, K. Lee, A. J. Heeger, Thermally stable efficient polymer solar cells with nanoscale control of the inter-penetrating network morphology. Adv. Funct. Mater., 15 (2005) 1617–1622.

[7] Y. Y. Liang, Z. Xu, J. B. Xia, S. T. Tsai, Y. Wu, G. Li, C. Ray, L. P. Yu, For the Bright Future—Bulk Heterojunction Polymer Solar Cells with Power Conversion Efficiency of 7.4%, Adv. Mater., 22 (2010) 135-138.

[8] R. F. Service, Science, Outlook brightens for plastic solar cells, Science, 332 (6027) (2011) 293.

[9] C. E. Small, S. Chen, J. Subbiah, C. M. Amb, S. W. Tsang, T. H. Lai, J. R. Reynolds, F. So, High-efficiency inverted dithienogermole–thienopyrrolodione-based polymer solar cells, Nat. Photon., 6 (2012) 115-120.

[10] Z. C. He, C. M. Zhong, S. J. Su, M. Xu, H. B. Wu, Y. Cao, Enhanced power-conversion efficiency in polymer solar cells using an inverted device structure. Nat. Photon., 6 (2012) 591-595.

[11] B. Minnaert, M. Burgelman, Efficiency potential of organic bulk heterojunction solar cells, Prog. Photovoltaics, 15 (2007) 741-748.

[12] S. Y. Chou, W. Ding, Ultrathin, high-efficiency, broad-band, omni-acceptance, organic solar cells enhanced by plasmonic cavity with subwavelength hole array, Opt. Express, 21 (2013) A60-A76.

[13] J. H. Heo, S. H. Im, J. H. Noh, T. N. Mandal, C. S. Lim, J. A. Chang, Y. H. Lee, H. J. Kim, A. Sarkar, Md. K. Nazeeruddin, M. Grätzel, S. Sock, Efficient inorganic–organic hybrid heterojunction solar cells containing perovskite compound and polymeric hole conductors, Nat. Photon., 7 (2013) 486-491.

[14] M. C. Scharber, D. Wuhlbacher, M. Koppe, P. Denk, C. Waldauf, A. J. Heeger, C. J. Brabec, Design rules for donors in bulk-heterojunction solarcells - Towards 10% energy-conversion efficiency, Adv. Mater., 18 (2006)789-794.

[15] L. J. A. Koster, V. D. Mihailetchi, P. W. M. Blom, Ultimate efficiency of polymer-fullerene bulk heterojunction solar cells, Appl. Phys. Lett., 88 (2006) 093511/1-3.

[16] H. A. Atwater, A. Polman, Plasmonics for improved photovoltaic devices, Nat. Mater., 9 (2010) 205-213.

[17] X. Li, W. Choy, L. Huo, F. Xie, W. Sha, B. Ding, X. Guo, Y. Li, J. Hou, J. You, Y. Yang, Dual plasmonic nanostructures for high performance inverted organic solar cells. Adv. Mater., 24 (2012) 3046-3052.

[18] X. Xu, A. K. K. Kyaw, B. Peng, D. Zhao, T. K. S. Wong, Q. Xiong, X. W. Sun, A. J. Heeger, A plasmonically enhanced polymer solar cell with gold–silica core–shell nanorods, Org. Electron., 14 (2013) 2360-2368.

[19] C. M. Liu, C. M. Chen, Y.W. Su, S. M. Wang, K. H. Wie, The dual localized surface plasmonic effects of gold nanodots and gold nanoparticles enhance the performance of bulk heterojunction polymer solar cells, Org. Electron., 14 (2013) 2476-2483.

[20] M. Xue, L. Li, B. J. T. de Villers, H. Shen, J. Zhu, Z. Yu, A. Z. Stieg, Q. Pei, B. J. Schwartz, K. L. Wang, Charge-carrier dynamics in hybrid plasmonic organic solar cells with Ag nanoparticles, Appl. Phys. Lett., 98 (2011) 253302.

[21] X. Chen, L. Zuo, W. Fu, Q. Yan, C. Fan, H. Chen, Insight into the efficiency enhancement of polymer solar cells by incorporating gold nanoparticles, Sol. Energ. Mat. Sol. Cells, 111 (2013) 1-8.

[22] S. W. Baek, J. Noh, C. H. Lee, B. Kim, M. K. Seo, J. Y. Lee, Plasmonic forward scattering effect in organic solar cells: a powerful optical engineering method, Sci. Rep., 3 (2013) 1726.

[23] E. Stratakis, M. M. Stylianakis, E. Koudoumasa, E. Kymakis, Plasmonic organic photovoltaic devices with graphene based buffer layers for stability and efficiency enhancement, Nanoscale, 5 (2013) 4144-4150.

[24] N. Kalfagiannis, P. G. Karagiannidis, C. Pitsalidis, N. T. Panagiotopoulos, C. Gravalidis, S. Kassavetis, P. Patsalas, S. Logothetidis, Plasmonic silver nanoparticles for improved organic solar cells, Sol. Energ. Mat. Sol. Cells, 104 (2012) 165–174.

[25] Q. Gan, F. J. Bartoli, Z. H. Kafafi, Plasmonic-Enhanced Organic Photovoltaics: Breaking the 10% Efficiency Barrier, Adv. Mater., 25 (2013) 2385–2396.

[26] J. L.Wu, F. C. H. Chen, Y. S. Hsiao, F. C. Chien, P. Chen, C. H. Kuo, M. H. Huang, C. S. Hsu, Surface Plasmonic Effects of Metallic Nanoparticles on the Performance of Polymer Bulk Heterojunction Solar Cells, ACS Nano, 5(2) (2011) 959-967.

[27] D. Kozanoglu, D. H. Apaydin, A. Cirpan, E. N. Esenturk, Power conversion efficiency enhancement of organic solar cells by addition of gold nanostars, nanorods and nanospheres, Org. Electron., 14 (2013) 1720-1727.

[28] J. Pei, J. Tao, Y. Zhou, Q. Dong, Z. Liu, Z. Li, F. Chen, J. Zhang, W. Xu, W. Tian, Efficiency enhancement of polymer solar cells by incorporating a self-assembled layer of silver nanodisks, Sol. Energ. Mat. Sol. Cells, 95 (2011) 3281-3286.

[29] B. Gholamkhass, S. Holdcroft, Enhancing the durability of polymer solar cells using gold nano-dots, Sol. Energ. Mat. Sol. Cells., 95 (2011) 3106–3113.

[30] A. J. Pearson, S. A. Boden, D. M. Bagnall, D. G. Lidzey, C. Rodenburg, Imaging the bulk nanoscale morphology of organic solar cell blends using helium ion microscopy, Nano Lett., 11(2011) 4275–4281.

[31] J. Siegel, O. Lyutakov, V. Rybka, Z. Kolská, V. Švorčík, Properties of gold nanostructures sputtered on glass, Nanoscale Res. Lett., 6 (2011) 96.

[32] P. K. Jain, S. K. Lee, I. H. El-Sayed, M. A. El-Sayed, Calculated Absorption and scattering properties of gold nanoparticles of different size, shape, and composition: Applications in biological imaging and biomedicine J. Phys. Chem. B, 110 (2006) 7238- 7248.

[33] C. J. Murphy, C. J. Orendorff, Alignment of Gold Nanorods in Polymer Composites and on Polymer Surfaces, Adv. Mater., 17 (2005) 2173-2177.

[34] Y. Furukawa, M. Akimoto, I. Harada, Vibrational key bands and electrical conductivity of polythiophene, Synth. Met., 18 (1987) 151-156.

[35] M. Trznadel, A. Pron, M. Zagorska, R. Chrzaszcz, J. Pielichowski, Effect of molecular weight on spectroscopic and spectro electrochemical properties of regioregular poly(3-hexylthiophene), Macromolecules, 31 (1998) 5051-5058.

[36] V. Kumar, H. Wang, Plasmonic Au nanoparticles for enhanced broadband light absorption in inverted organic photovoltaic devices by plasma assisted physical vapour deposition, Org. Electron., 14 (2013) 560–568.

7.1 Introduction

Among many PV technologies, organic semiconducting organics are potentially appropriate materials for achieving the low-cost production of large area PV cells because they are solution processable and can be deposited by various conventional coating methods including spin-coating, doctor-blading, spray-coating, slot-die coating, and ink-jet printing [1-5]. Various technologies of manufacturing large area OSC devices by the roll-to-roll (R2R) processing technique have been reviewed recently by F.C. Krebs' group [6]. The advantages of high mechanical flexibility of organics for the R2R processing technique have assisted its fast progress towards fabricating large area OSC devices on flexible substrates [7-13]. As discussed in Chapter 2 (Section 2.4), compared to the conventional configuration, OSC devices with the inverted structures have gained more and more academic and industrial attention owing to that the inverted configuration has an opposite charge collection mechanism that can allow the use of high work function metal as the substrate and highly stable transparent materials as hole collecting electrode. However, currently most of the reported inverted OSC devices have been fabricated on ITO coated glasses or transparent plastics. Glasses are very rigid and not compatible with the roll-to-roll processing. Plastic substrates are highly flexible; nevertheless, the resource of indium is scarce on earth and sheet resistance of ITO films obtained on flexible plastic substrates via the deposition method under the vacuum condition is relatively high, which decreases short circuit current and fill factor of the OSC devices [14].

The metal substrate is a potential alternative of producing flexible OSC devices via the inverted structures. Compared to the plastics, metal has the advantages of cost-effective,

excellent mechanical flexibility and thermal stability in the industrial fabrication processes, [15] delivering good ambient interfacial device stability and also providing an opportunity to use non-vacuum solution-processed top electrode which can further reduce the fabrication cost. Furthermore, metal has high conductivity and good dimensional stability during the processing at elevated temperature.

In this chapter, we investigated top illuminated inverted OSC devices on metal substrates namely: polished stainless steel 304 (SS), titanium coated steel (Ti-S), chromium coated aluminium (Cr-Al), polished aluminium (Al). Electrons in the OSC devices were collected by the bottom metal electrode and holes transported through the transparent PEDOT:PSS to the hcPEDOT:PSS top electrode. Metal stored in air can naturally form a passive oxide layer which has a significant effect on the performance of the inverted OSC devices. Good performance OSC devices were achieved on both the SS and Cr-Al substrates while no effective device was produced on the Al substrate. We then used the electrical impedance spectroscopy (EIS) to investigate the electrical properties of the fabricated OSC devices on various substrates. The fitting results disclosed the reasons why different metal substrates can provide significantly different performance in PCE for the inverted OSC devices.

7.2 Device structures and experimental method

The top illuminated inverted OSCs were fabricated on different metal substrates. The cross sectional view of the studied device structures (i.e. Metal substrate /ZnO/P3HT:PCBM/PEDOT:PSS/hcPEDOT:PSS) is schematically shown in Figure 7.1 (a) and photos of a pair of fabricated real devices on five different substrates are simultaneously presented in Figure 7.1 (b). All the substrates were cut in a size of 2 x 1.5 cm^2 and ultrasonically cleaned in acetone, isopropyl alcohol, and then deionised

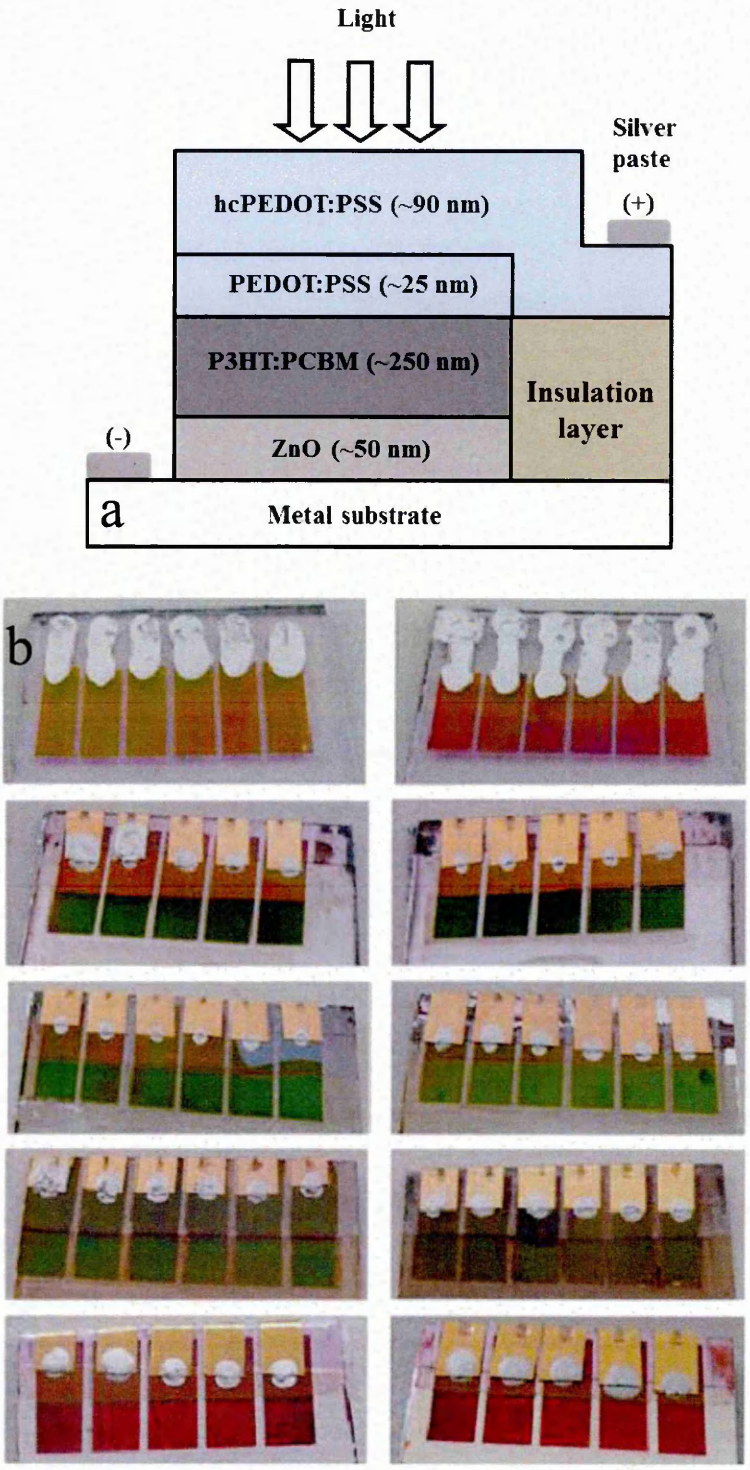

Figure 7.1 (a) Schematic diagram of cross section for top illuminated inverted OSC devices on metal substrates, (b) photos of a pair of real devices on ITO-coated glasses, SS, Cr-Al, Ti-S, and pure Al, from top to bottom. (Note: not to scale).

water for 10 min, respectively. After drying with nitrogen, the substrates were spin-coated with a ~ 50 nm thick amorphous ZnO layer by SG1 sol-gel method and then annealed on a hot plate at 150° C for 15 min.

The samples were transferred into a nitrogen-filled glove box. On top of the ZnO layer, a ~ 250 nm thick active layer was spin coated from CB4 active layer blend and then was annealed at 140 °C for 10 min on a hot plate. More detail about the preparation of ZnO sol and the active layer we have already discussed in chapter 4. Afterwards, the samples were removed out of the glovebox, followed a ~ 25 nm thick PDS2 (PEDOT: PSS) layer spin-coated on top of the active layer and was annealed at 120 °C for 5 min. To complete the device stack ~ 90 nm thick hcPEDOT:PSS layer with 6% dimethyl sulfoxide (DMSO) was spin coated on top of the PEDOT:PSS layer which will work as a hole collecting electrode. Finally, the complete device annealed under the ambient air condition at 120 °C for 10 min. The tested active area of the OSC devices was 7.0 mm^2.

7.3 Flexible metal substrates

Selection of electron contact metal substrates for top illuminated inverted OSCs is a challenge, as the work function of the electron contact must be close to the LUMO level of the acceptor (3.7-4.3 eV) [25,26]. To achieve this requirement, the electron contact must be low work function materials which comply with the following points regarding the mechanical, optical, electrical and electronic properties:

- The work function must be in the range of the electron acceptor LUMO level.
- The material must be economic and should be resistant to corrosion.
- The top surface should be mirror finished and have good wetting properties.
- The electrical conductivity must be very high for an efficient charge transport.

These requirements can be fulfilled by the use of alloys or a combination of different layers. Thin metal substrates provide the excellent barrier to water and oxygen, which is one of the most critical properties affecting the lifetime of organic solar cells [27,28]. Additionally, the substrates like stainless steel have superior chemical resistance to most of the chemicals used during OSC device fabrication. The top surface can be optimised by polishing with excellent dimensional stability at the elevated temperature. The conductivity of metal substrates can be considered as another advantage for an efficient charge transport which made them very durable for applications. To find a suitable metal substrate for the electron contact, we studied different metals as substrate materials. We used 0.5 mm thick polished stainless steel (grade 304) wafers with an average roughness of less than 5.0 nm, brought from Valley Design Corporation. 520 nm thick titanium coated steels were received from Sidrabe Inc. Polished aluminium alloys were supplied by Backer Industrial Coating LTD. 100 nm thick chromium thin films on the polished Al were deposited in our lab by plasma assisted physical vapour deposition (PAPVD). ITO coated glass substrates (12-15 ohms/sq.) were purchased from VisionTek Systems LTD to fabricate the reference device.

7.4 Results and discussion

7.4.1 Surface morphologies of metal substrates

The surface morphologies were investigated in order to identify whether they have an effect on the performance of the OSC devices on metals. Figure 7.2 showed the SEM surface morphologies of various metal substrates. Figure 7.2 (a) presented a very smooth surface of the SS substrates with average roughness of less than 5 nm and no clear features or crystalline structures were observed. Figure 7.2 (b) illustrated the smooth surface morphology of the Cr-Al substrates. A regularly ordered crystalline

structure was observed in the inserted high-magnification image in Figure 7.2 (b). Figure 7.2 (c) illustrated the morphology of the Ti-S substrate, showing a structure with larger sized crystallities and grater surface roughness than that of the Cr-Al substrates. The morphology of the polished Al was shown in Figure 7.2 (d), revealing a smooth and fine crystalline structure with the defect-free surface in the submicron range.

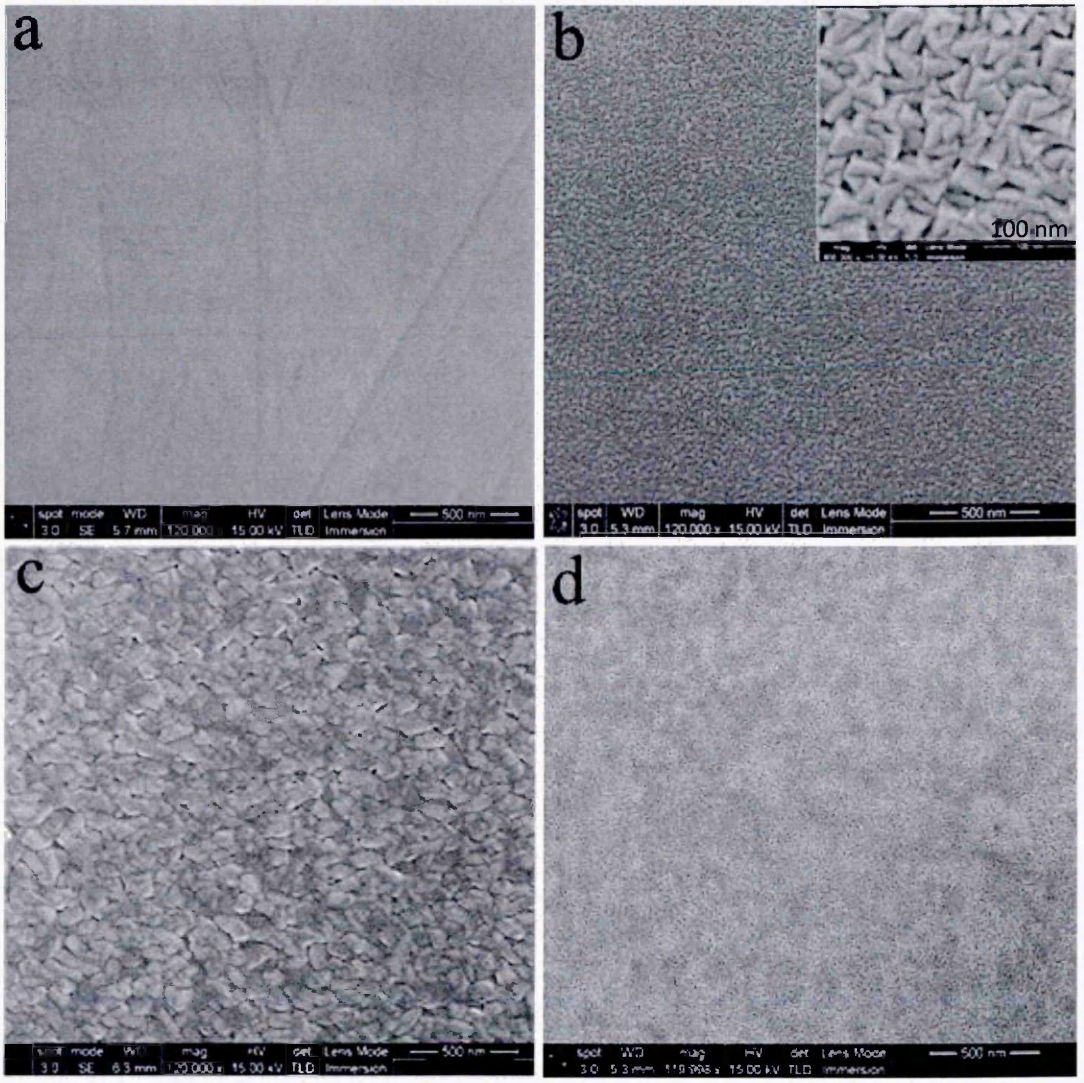

Figure 7.2 SEM morphological images of metal substrates, (a) the polished stainless steel, (b) the chromium coated aluminium (the inset shows the magnified image), (c) the titanium coated steel, (d) the polished aluminium.

7.4.2 Optical properties of the hcPEDOT:PSS

Since incident light reaches to the active layer through the top transparent organic electrode in top illuminated inverted OSC devices, the transmittance spectrum of the PEDOT:PSS and hcPEDOT:PSS thin films on glasses were investigated shown in Figure 7.3. The 25 nm thick PEDOT: PSS thin film on glasses (Figure 7.3 a) is highly transparent with ~96% transmittance over the whole spectral range. The hcPEDOT:PSS layer on top of the normal PEDOT:PSS film that was deposited using the spin coating method at 2000 rpm, presented a thickness of around 45 nm as shown in Figure 7.4,

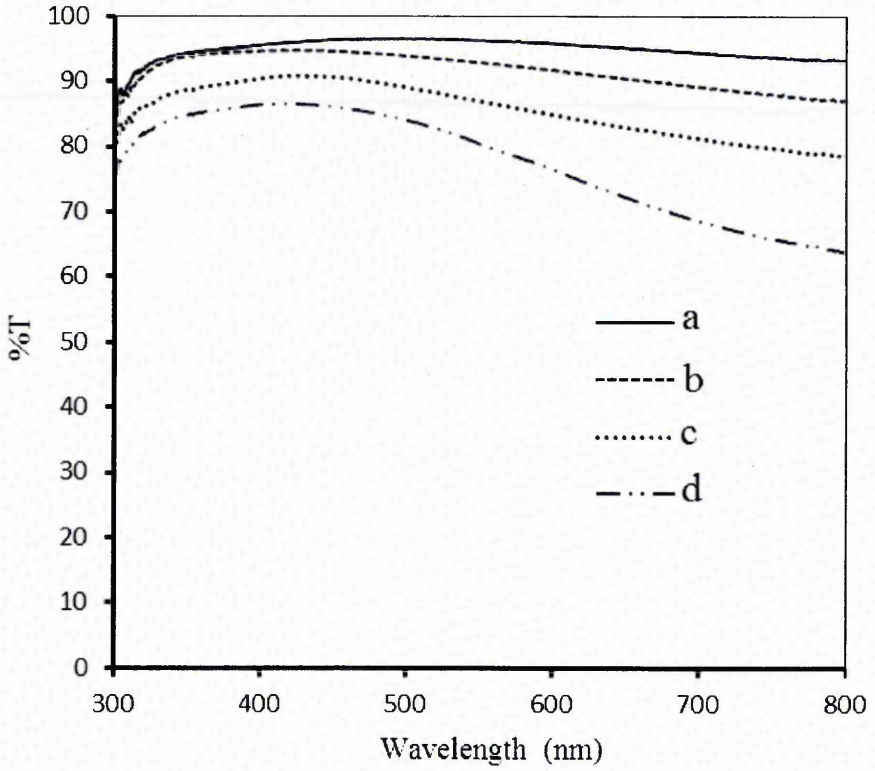

Figure 7.3 Transmittance spectra of the PEDOT:PSS and hcPEDOT:PSS films on glasses, (a) PEDOT:PSS film, (b) PEDOT:PSS plus one layer hcPEDOT:PSS film, (c) PEDOT:PSS plus bi-layer hcPEDOT:PSS film, (d) PEDOT:PSS plus tri-layer hcPEDOT:PSS film.

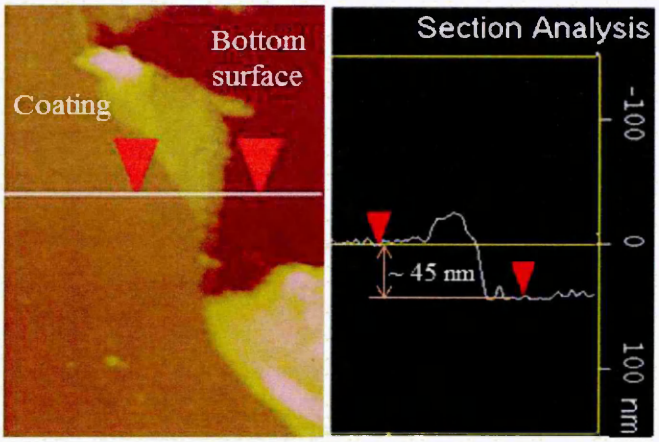

Figure 7.4 Thickness of the one-layer hcPEDOT:PSS film on glasses

where left red triangle belong to PEDOT:PSS coating and right red triangle belongs to non-coated bottom surface. The thicknesses of double or triple-coatings of the hcPEDOT:PSS were estimated to be ~90 nm and ~135 nm, respectively. The increased thickness of the hcPEDOT:PSS film reduced the transmittance of the film as shown in Figure 7.3 (b-d). The 45 nm thick hcPEDOT:PSS film shows a transmittance of more than 90% in the full spectral range. The transmittance of double layer ~90 nm thick hcPEDOT:PSS is ~87% at 550 nm and the more than 83% in the spectral range from 350 to 650 nm. The triple layer ~135 nm thick hcPEDOT:PSS shows low transmittance of ~80% at 550 nm whereas from 400 to 500 nm the transmittance is more 85%.

The transmittance spectrum of the hcPEDOT:PSS plus the PEDOT:PSS thin films on glasses are presented in Figure 7.5. The transmittance spectrum of the ITO film is also shown in Figure 7.5 as the baseline for comparison. The double-layered 90 nm thick hcPEDOT:PSS plus the 25 nm thick PEDOT:PSS thin film illustrated the transmittance greater than 80% over the full spectral range.

In detail, the double-layer organic film revealed higher transmittance (as shown in Figure 7.5 c) in the range of 350-450 nm and lower transmittance in the range of 450-650 nm than that of the ~100 nm thick ITO thin film (as shown Figure 7.5 b). The overall transmittance in the range of 400 to 650 nm is above the average of 84% that is close to that of the ITO thin film. The absorption spectrum of the active P3HT:PCBM layer was also plotted in Figure 7.5 (d), showing its well-known absorption band in the spectral range of 400–650 nm [29].

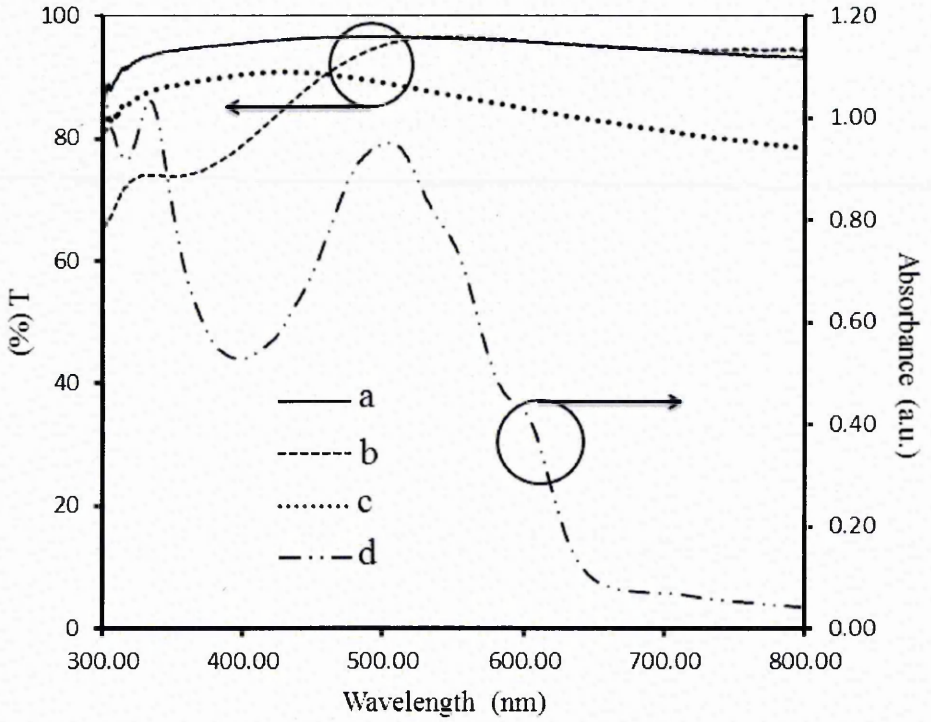

Figure 7.5 (a) Transmittance spectra of the PEDOT:PSS films on glasses, (b) Transmittance spectra of ~100 nm thick ITO film on glasses, (c) Transmittance spectra of double-layer of the 90 nm thick hcPEDOT:PSS plus the 25 nm thick PEDOT:PSS thin films, (d) Absorption spectra of P3HT:PCBM film on glasses

7.4.3 Performance of the inverted OSC devices by hcPEDOT:PSS top anode

Device performances of top illuminated inverted OSCs fabricated on the Cr-Al substrates with different thicknesses of the hcPEDOT:PSS layer were studied as shown in Figure 7.6. The top hole collecting electrode of the hcPEDOT:PSS had different thicknesses of ~45nm, ~90 nm and ~135 nm respectively. Table 7.1 summarized the performances of the fabricated devices on Cr-Al substrates. The OSC device with the ~90 nm thick top anode presented the highest PCE amongst three types of OSC devices. The FF of the OSC device with the ~135 nm top anode is higher than that of the OSC device with the ~90 nm top anode while the short circuit current of the ~135 nm top anode device is lower than that of ~90 nm top anode device. This was attributed to the low transmittance of the top anode for the ~135 nm top anode device as shown in Figure 7.3 (d). Hence, the ~90 nm thick hcPEDOT:PSS top thin film will be chosen as the hole collecting electrode for all OSC devices on other different metal substrates. The PCE results confirm that the hcPEDOT:PSS thin film can be an alternative for replacement of the transparent ITO thin films as the top electrode in the inverted OSC devices.

Table 7.1 Summary of photovoltaic parameters of the inverted OSC devices

hcPEDOT:PSS thickness (nm)	V_{oc} (V)	J_{sc} (mA/cm^2)	FF (%)	PCE (%)
45	0.60	7.91	41.50	1.97
90	0.62	10.62	40.40	2.66
135	0.62	9.09	44.53	2.51

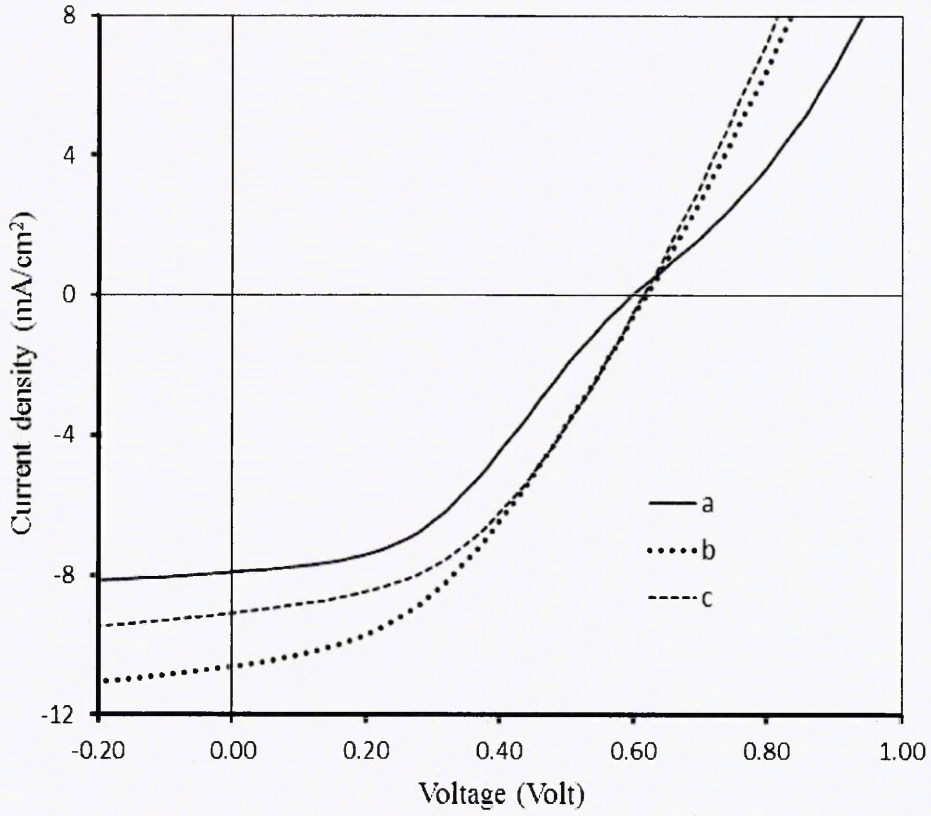

Figure 7.6 J-V characteristics of the top illuminated inverted OSC devices on Cr-Al metal substrates with hcPEDOT:PSS top anode, (a) with ~45 nm thick top anode, (b) with ~90 nm top anode, (c) with ~135 nm top anode.

7.4.4 Surface morphologies of ETLs, active layers, HTLs and hcPEDOT:PSS electrodes on metal substrates

7.4.4.1 Morphologies of the ZnO layer

The SEM images are shown in Figure 7.7 for the typical surface morphologies of the sol-gel (SG1) derived ZnO electron transport layer on different metal substrates using spin coating method. All the samples were prepared following the same procedure as that in fabrication of the OSC device. The morphologies were homogeneous and smooth on all the substrates except the Ti-S substrates. The morphology of the ZnO film on the

Ti-S substrates (Figure 7.7 c) reveals a coarser structure because of the effect of the surface morphology by the Ti-S substrate as shown in Figure 7.2 (c).

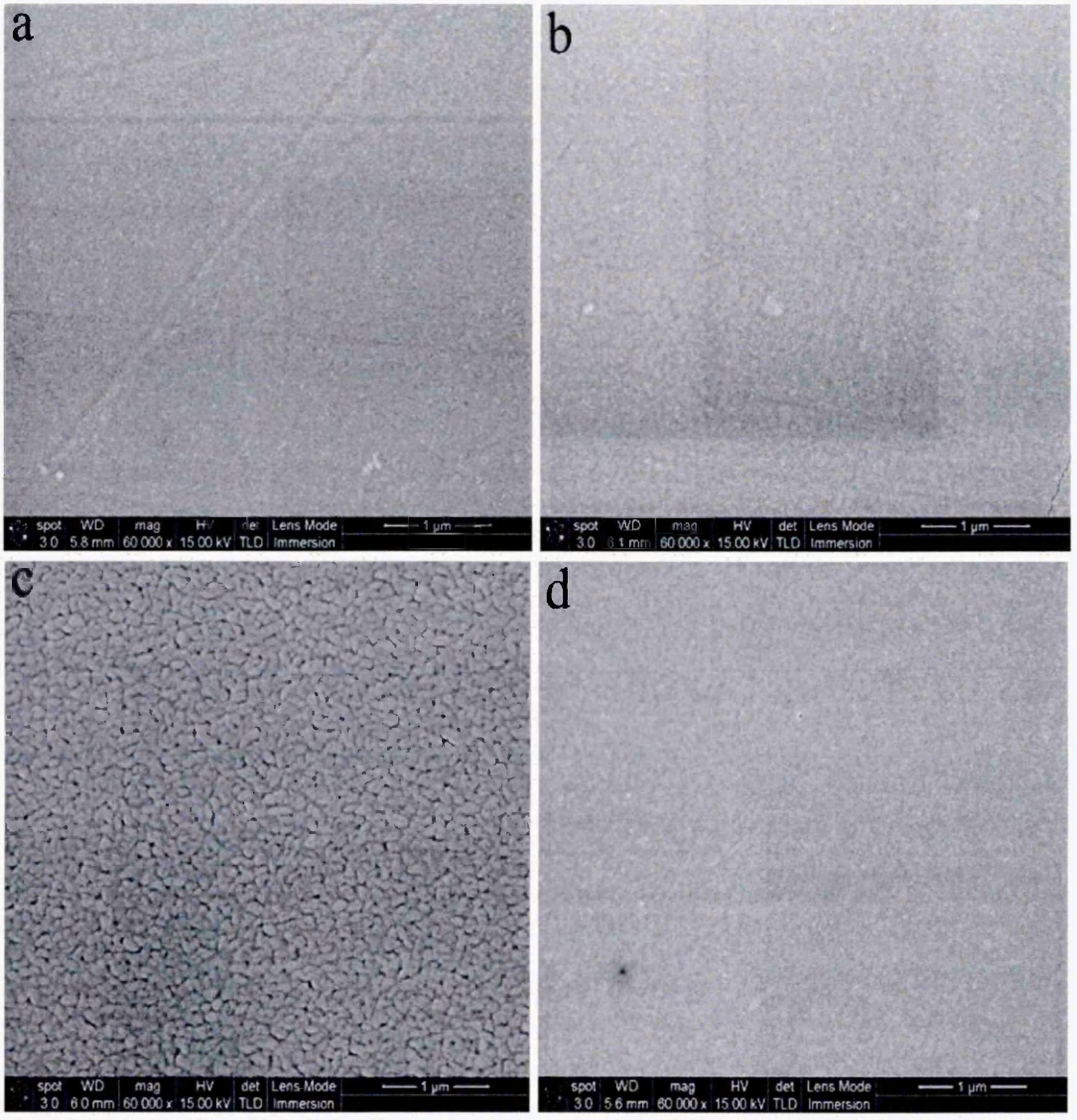

Figure 7.7 SEM morphological images of ZnO thin film on different metal substrates, (a) on polished stainless steel, (b) on chromium coated aluminium, (c) on titanium coated steel, (d) on polished aluminium.

7.4.4.2 Morphologies of the active layer

After deposition of zinc oxide thin films by the sol-gel method on the metal substrates, the active P3HT-PCBM layer was then spin-coated on top of the annealed ZnO layer. Significantly different surface topographies of the P3HT-PCBM layer were revealed using AFM as shown in Figure 7.8 with a 1x1 μm^2 scale range. The AFM topography of the P3HT-PCBM layer on the ITO coated glass was also presented in Figure 7.8 (a), showing two contrast phases with an average roughness of 0.76 nm and maximum at 7.30 nm. The appearance of two colour contrasts in the AFM image was due to the varied material interaction with the AFM tip. There were no regular nano-sized particulates for the P3HT-PCBM layer on glasses. However, the surface of the P3HT-PCBM thin film on the SS substrate illustrated a quite different morphology from that of the active layer on glasses. Except two contrast phases, nano-sized elongate particulates with an orientation like organic domain structures were observed as shown in Figure 7.8 (b), presenting an average roughness of 0.84 nm and maximum at 7.43 nm. The elongate particle has a width of ~ 40 nm.

The AFM surface topography of the P3HT:PCBM thin film on the Cr-Al substrate was also presented in Figure 7.8 (c). It did not reveal a regular morphology formed by the oriented nano-sized particulates compared to the AFM topography of the active layer on the SS substrate. It is much closer to the morphology of the P3HT:PCBM thin film on glasses as shown in Figure 7.8 (a) except possessing larger sized nano clusters with an average ~ 50 nm in diameter and average roughness of 1.03 nm with maximum at 10.37 nm.Figure 7.8 (d) presented the AFM morphology of the P3HT:PCBM thin film on the Ti-S substrate, illustrating the similar organic domain structure as that of the active layer on the SS substrate. Nevertheless, nano-sized elongate particles were much smaller with an average roughness of 0.77 nm and maximum at 8.07 nm.

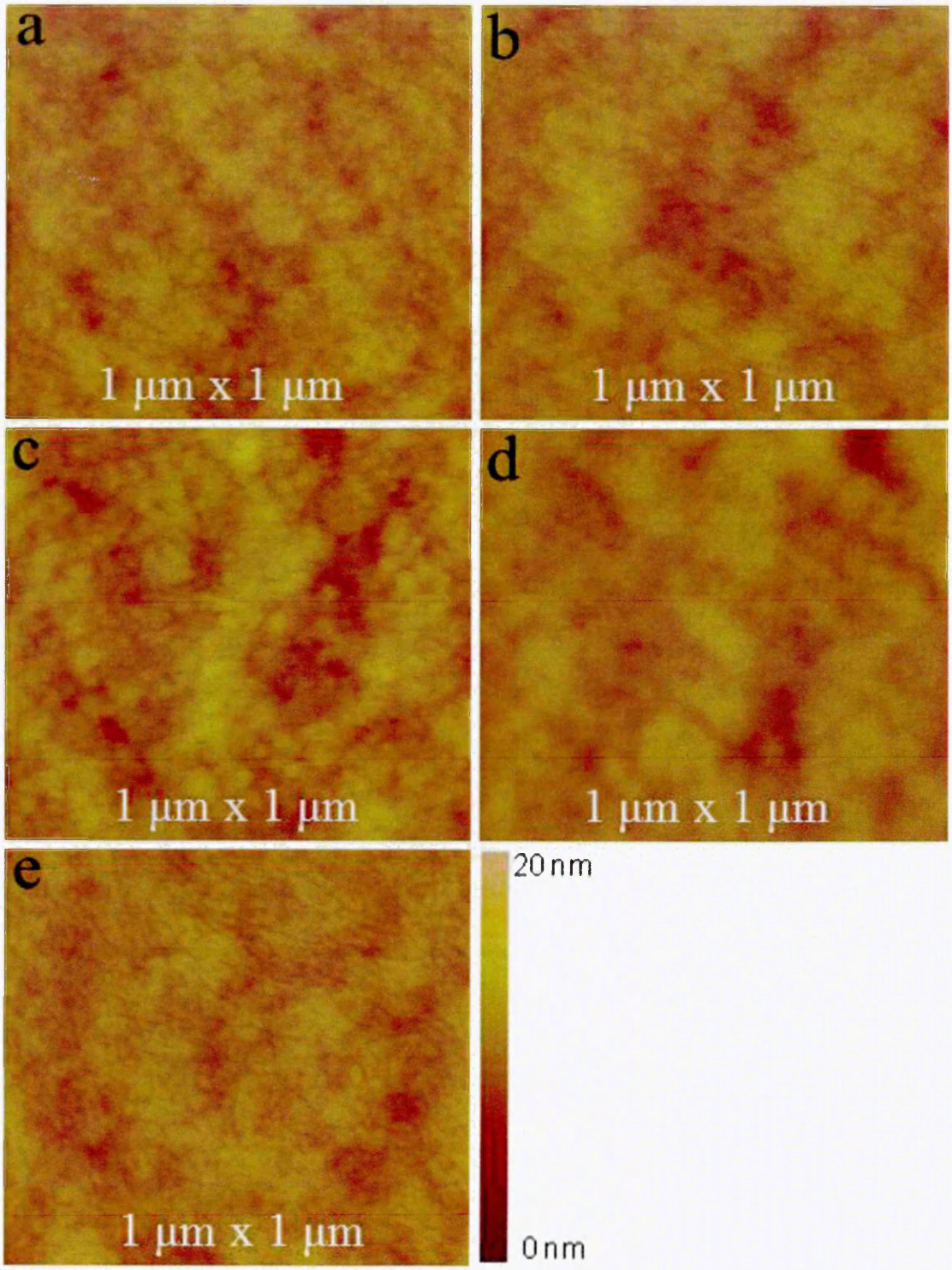

Figure 7.8 1x1 μm^2 scale tapping mode AFM topographic images of the P3HT:PCBM blend deposited on the sol–gel ZnO coated (a) ITO glass substrate, (b) polished SS substrate, (c) Cr-Al substrate, (d) Ti-S substrate, (e) polished Al substrate.

Furthermore, organic domain structures with the oriented nano-sized elongate particulates was more clearly obtained for the P3HT:PCBM thin film on the Al substrate as shown in Figure 7.8 (e). Average roughness of the thin film is 0.75 nm with maximum at 6.44 nm. These results demonstrated that different metal substrates can significantly affect the morphologies of the active P3HT:PCBM layer that would influence the performance of the OSC devices on metals. In fact, this effect does not play a key part on determining whether the OSC structures can effectively provide the solar energy conversion that will be discussed in Section 7.4.4.

7.4.4.3 Morphologies of the PEDOT:PSS

The surface of the PEDOT:PSS and hcPEDOT:PSS film on top of the active layer were also observed by the AFM. Their differences in the morphology were presented in Figure 7.9. The thin PEDOT:PSS film presented an uniform fine nanosized interconnected structure with an average roughness of 1.05 nm and maximum at 12.50

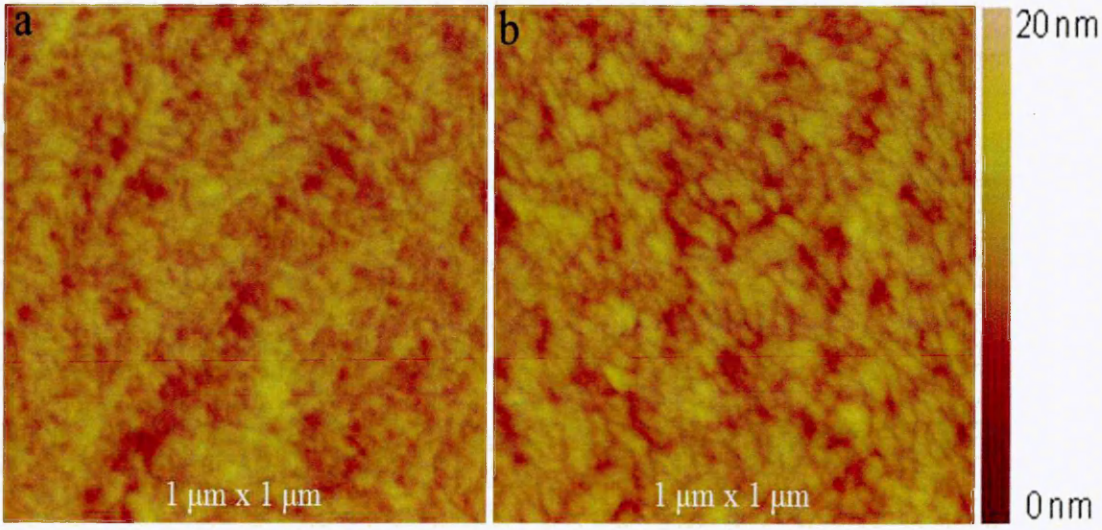

Figure 7.9 1x1 μm^2 scale tapping mode AFM topographic images of (a) the PEDOT:PSS on top of the P3HT:PCBM thin film, (b) the hcPEDOT:PSS on top of the PEDOT:PSS thin film.

nm as shown in Figure 7.9 (a) while the hcPEDOT:PSS film exhibited an coarser nanosized interconnected structure with an average roughness of 1.18 nm and maximum at 14.21 nm as shown in Figure 7.9 (b).

7.4.5 Performance of the inverted OSC devices on metal substrates

Top illuminated inverted OSC structures on five different substrates (ITO/glass, SS, Cr-Al, Ti-S, and polished Al) were fabricated to explore their device performances. Five or six devices for each substrate were produced separately. Performance of all OSC devices by J-V characterisation is listed in Table 7.2 to 7.6. The results for the best device in each group were illustrated by J-V characterisation as shown in Figure 7.10 while J-V characteristic of the OSC device on the Al substrate was inserted on the top left.

The top illuminated device based on the ITO coated glass substrate exhibited maximum PCE of 2.02% with short circuit current density (Jsc) at 7.83 mA/cm^2 and fill factor (FF) at 43%. Highest PCE amongst the investigated OSC devices on the polished SS and the Cr-Al substrates was revealed, respectively reaching 3.11% with Jsc at 10.31 mA/cm^2 and FF at 49% for the SS and 3.10% with Jsc at 10.74 mA/cm^2 and FF at 47% for the Cr-Al; However, the OSC devices on the Ti-S substrate presented a very low FF at 27%, leading to low PCE of 1.48% with Jsc at 8.95 mA/cm^2. No PCE of the OSC devices fabricated on the polished Al substrate was achieved, showing a negligible Jsc at 2.55×10^{-4} mA/cm^2 although an open circuit voltage of 0.58 V was obtained.

All parameters of the best OSC devices for each group were listed in Table 7.7. There were also some small changes of open circuit voltage (Voc) for the OSC devices fabricated on the different substrates in Table 7.7, which could be assigned to the effect of work function of the substrates used for OSC devices. The PCE results exhibited that

the performance of the OSC devices on different metals could mainly be due to the passive layer (oxidation layer) formed on the top surface of metals.

Table 7.2 Summary of photovoltaic parameters of the inverted OSC devices on ITO-glass substrates

Glass/ITO substrate (as ref.)	V_{oc} (Volt)	J_{sc} (mA/cm^2)	FF (%)	PCE (%)
No.1	0.60	7.89	42	1.97
No.2	0.60	7.83	43	2.02
No.3	0.60	8.42	39	1.98
No.4	0.60	7.86	41	1.92
No.5	0.60	7.25	38	1.63

Table 7.3 Summary of photovoltaic parameters of the inverted OSC devices on SS substrates

Polished SS substrate	V_{oc} (Volt)	J_{sc} (mA/cm^2)	FF (%)	PCE (%)
No.1	0.62	10.99	42	2.86
No.2	0.62	10.69	45	2.98
No.3	0.62	10.31	49	3.11
No.4	0.62	9.92	47	2.90
No.5	0.62	10.25	46	2.90
No.6	0.62	10.93	45	3.06

Table 7.4 Summary of photovoltaic parameters of the inverted OSC devices on Cr-Al substrates

Cr-Al substrate	V_{oc} (Volt)	J_{sc} (mA/cm^2)	FF (%)	PCE (%)
No.1	0.62	10.62	40	2.66
No.2	0.62	10.96	44	3.00
No.3	0.62	10.75	47	3.10
No.4	0.62	10.44	46	2.99
No.5	0.62	10.92	45	3.03
No.6	0.62	11.01	43	2.94

Table 7.5 Summary of photovoltaic parameters of the inverted OSC devices on Ti-S substrates

Ti-S substrate	V_{oc} (Volt)	J_{sc} (mA/cm^2)	FF (%)	PCE (%)
No.1	0.62	8.36	24	1.22
No.2	0.62	8.95	27	1.48
No.3	0.62	7.77	28	1.37
No.4	0.62	9.50	25	1.49
No.5	0.62	6.99	24	1.03

Table 7.6 Summary of photovoltaic parameters of the inverted OSC devices on polished Al substrates

Polished Al substrate	V_{oc} (Volt)	J_{sc} (mA/cm^2)	FF (%)	PCE (%)
No.1	0.58	9.20 x10-4	-	-
No.2	0.58	4.04 x10-4	-	-
No.3	0.58	4.50 x10-4	-	-
No.4	0.58	4.12 x10-4	-	-
No.5	0.58	2.55 x10-4	-	-

Table 7.7 Summary of the photovoltaic parameters of the inverted OSC devices on the metal substrates

Substrates	V_{oc} (Volt)	J_{sc} (mA/cm^2)	FF (%)	PCE (%)
Glass/ITO (as ref.)	0.60	7.83	43	2.02
Polished SS	0.62	10.31	49	3.11
Cr-Al	0.62	10.74	47	3.10
Ti-S	0.62	8.95	27	1.48
Polished Al	0.58	$2.55x\ 10^{-4}$	-	-

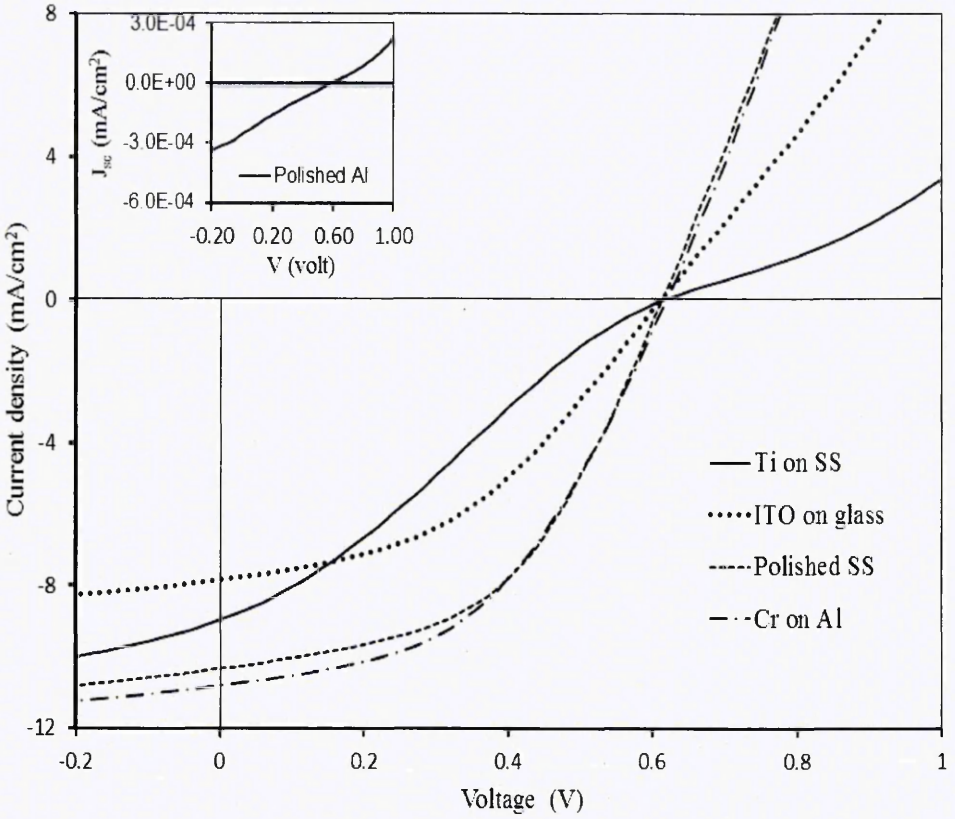

Figure 7.10 J–V curves of the top illuminated inverted best OSC devices on different metal substrates under the condition of 100 mW/cm^2 AM 1.5G spectra

It is well-known that there is always a thin chromium oxide film at several nano-meters thick on the very top surface of the SS which protects the SS from oxidation. This explained why the OSC devices on the SS and Cr-Al substrates obtained the same value of PCE, meaning that the thin Cr_xO_y is favourable for the transport of generated electrons by the active P3HT:PCBM layer to the metal electrode. In contrast, the thin oxide layer (Al_xO_y) on the surface of the Al substrate presented as an insulating layer with high contact resistance for the electron transport while the thin TiO_x on the Ti-S substrate can provide the capability as a semiconducting layer for conducting electrons. Some details will be further discussed in Section 7.4.6.

7.4.6 Device properties by the electrical impedance spectroscopy

The performance parameters of the OSC devices on different metals and their morphologies of the active layers revealed that the variation in PCE was mainly related to the interfacial resistance between the P3HT:PCBM layer and the corresponding metal electrode. Thin oxide layer formed on very top of metals has an effect on PCE of the inverted OSC devices. It has been reported that the interface between the P3HT:PCBM active layer and the ETL (ZnO) layer does not play an important influence on the electrical properties, which behaves as an ohmic contact [30].

Hence, the main contribution to block the transport of electrons came from the interfacial resistance between the ZnO thin film and the metal electrode due to a passive layer formed on the very top surface of the corresponding metal substrate. In order to further disclose the interfacial resistance that affected the performance of the OSC devices, AC impedance spectroscopy were measured for the best OSC devices fabricated on different metals respectively.

The Nyquist plots of different OSC devices were shown in Figure 7.11(a) and (b), revealing the variation in the value of impedance by the shape and sizes of semicircles. The main feature in the Nyquist plot is a combination of two semicircles that were more or less depressed for the OSC devices on the different metal substrates, a large one at low frequencies (right part of the curves) and a very small one at high frequencies (left part and inserted on left top in Figure 7.11 for the magnified curves). The change of semicircle shapes was clearly observed with the different metal substrates. The low frequency semicircle in the right part became larger and the high frequency one in the left part changed their depressed shapes and turned into larger with the changing substrates of SS, Cr-Al, Ti-S and Al. The overall impedance varied in the range of 16 to 250 $k\Omega\text{-}cm^2$.

Since the shape of the impedance curves presented two semicircles in the Nyquist plots, different equivalent electrical circuits including the basic RC series model, the Garcia-Belmonte [31] series model and the Mani parallel [32] model for two semicircles curves were considered for the use to fit the impedance curves by using ZSimp 3.10 software. The basic RC series model was shown in Figure 7.12 (a), where each RC parallel element is attributed to a semicircle. If the capacitance C behaves as an ideal capacitor, the impedance is presented as

$$Z_C = 1/ i\omega C \qquad (7.1)$$

However, when using an ideal capacitor in the basic RC series model, it didn't fit our impedance curves very well. The reason is that the blocking interfacial layer in the OSC devices was not perfectly homogeneous and it can be affected by defects (e.g. porosities) generated from the fabricating processes. In this circumstance, a constant phase element CPE is usually adopted to replace the ideal capacitor in the model circuit, leading to the depressed semi-circle in the Nyquist plots. A constant phase element CPE is then written as

$$Z_{CPE} = 1/ CPE (i\omega) n \qquad (7.2)$$

When n equals to 1, CPE becomes C and the equation (7.2) will be the same as the equation (7.1).

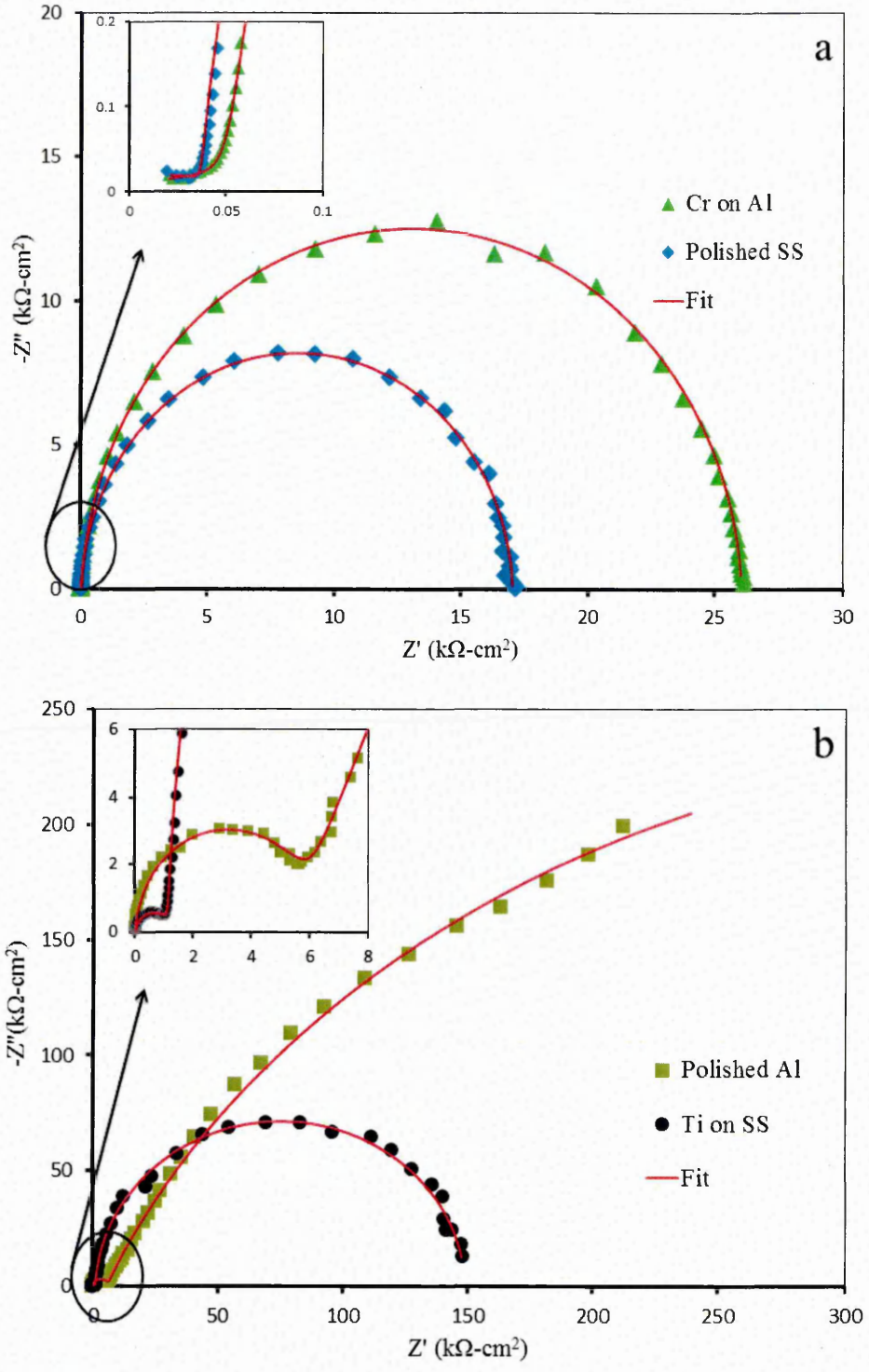

Figure 7.11 Electrical impedance the Nyquist plots of the inverted best OSC devices, (a) the Cr-Al and SS based devices, (b) the Al and Ti-S based devices. Solid lines indicate the fitting curves.

The fitting results demonstrated that only this modified basic RC series model as shown in Figure 7.12 (b) can give the perfect fitting for the devices on the SS, Cr-Al, and Ti-S substrates except fitting the impedance curve for the OSC devices on the Al substrates. The fitting results were shown as the solid line in Figure 7.11 (a) and (b) for the OSC devices on the SS, Cr-Al, and Ti-S substrates, respectively. As observed in Figure 7.11 (b), the Nyquist plot for the device on Al presented a depressed small circle and an unfinished large circle, meaning towards potentially infinite impedance. This feature can be related to systems where carrier transport is limited by diffusion-recombination. Hence, when Warburg impedance (Z_w) was introduced into the equivalent electrical circuit as shown in Figure 7.12(c), the perfect fitting for the device on Al susbstrates was achieved as shown the solid line in Figure 7.12 (b).

In the equivalent circuits, R_s represents series resistance that arose due to connection leads, metallic contact, etc. R_1 corresponds to resistance between the metal and the P3HT:PCBM and R_2 is assigned to resistance between the P3HT:PCBM and the hcPEDOT:PSS layer. As mentioned above, the interface between the P3HT:PCBM active layer and the ETL (ZnO) layer behaves as an ohmic contact, hence the variation in R_1 was mainly related to the interfacial layer between the ETL and the metal; i.e. the metal oxide layer. Table 7.8 list the resistance from the fitting results. In Table 7.8, R_s varies in the range of 13 to ~17 Ω for all the devices. R_1 and R_2 were obtained at 36 Ω-cm^2 and 17 kΩ-cm^2 for the devices on the SS substrates while they were 54 Ω-cm^2 and 25 kΩ-cm^2 for Cr-Al substrates, respectively. These results clearly evidenced that there existed only small resistance between the metal and P3HT: PCBM layer for the OSC devices on the SS and Cr-Al substrates, demonstrating why high performance in PCE on these devices was achieved.

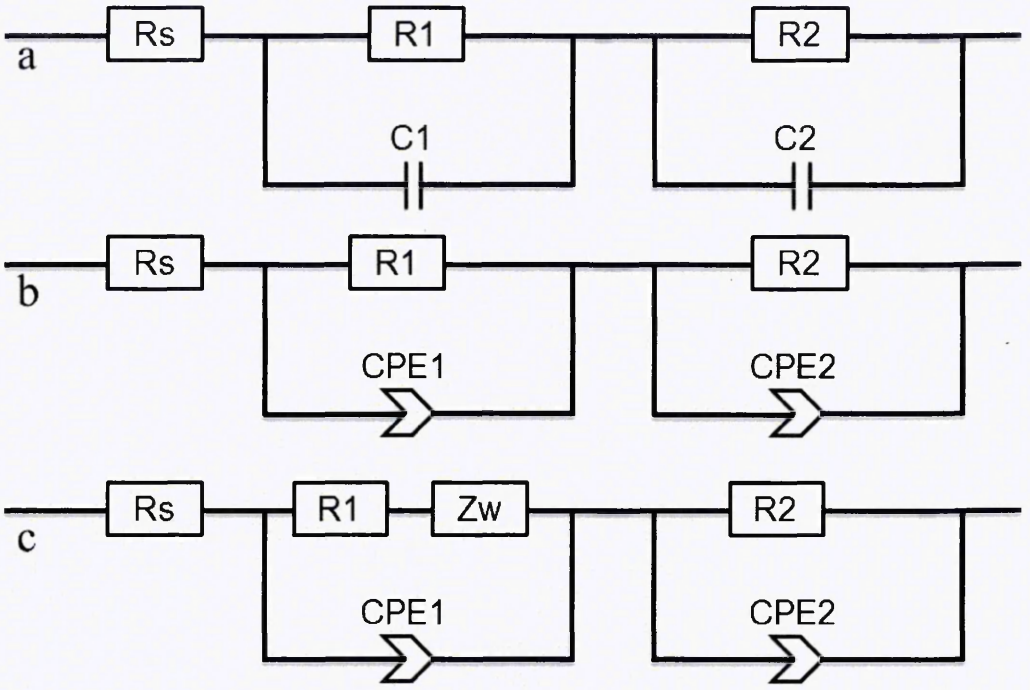

Figure 7.12 (a) The basic RC circuit, (b) the RCPE based equivalent circuit used to fit the impedance curves of the SS, Cr-Al, and Ti-S based devices, (c) the RCPE based equivalent circuit with the introduced Warburg impedance used to fit the impedance curves of the Al based device.

Table 7.8 Resistance of the devices from the EIS fitting results

Devices	R_s (Ω)	R_1 ($k\Omega$-cm^2)	R_2 ($k\Omega$-cm^2)
Polished SS	13.00	0.036	17.00
Cr-Al	15.23	0.054	25.00
Ti-S	16.70	147.90	11.00
Polished Al	14.03	3829.00	5.80

R_2 changed in the same range of values from 17 to 25 kΩ-cm^2, which can be attributed to slightly changing surface morphologies and phase contrast of the P3HT:PCBM blend as previously discussed in section 7.4.3. R_1 obtained from the fitting results for the devices on the Ti-S and Al substrates were respectively 147.9 kΩ-cm^2 and 3829 kΩ-cm^2, revealing significantly high resistance between the metal and P3HT:PCBM layer. This was the reason why low FF and PCE for the devices on the Ti-S substrates were obtained and no PCE was realised besides an open circuit voltage for the devices on Al substrates. R_2 for the devices on the Ti-S and Al substrates was separately, 11.0 kΩ-cm^2 and 5.8 kΩ-cm^2. Again, this difference in R_2 was affected by the morphologies of the P3HT:PCM blend. Overall, the fitting results from the Nyquist plots illustrated that the passive layer on metals played an important part on the inverted OSC devices for achieving high PCE. Metals with the Cr_xO_y layer are mostly suitable substrates for the inverted OSC devices amongst investigated metals and high PCE of 3.11% was obtained.

7.5 Summary

(1) Surface morphologies of metal substrates were investigated for the fabrication of completely solution-processed inverted OSC devices. The results showed that the variable roughness of the metal surfaces under the submicron range did not play a main role on the performance of the OSC devices. In the top illuminated inverted OSC devices light reaches to the active layer through the top transparent organic electrode. Therefore the transmittance spectrum of the various thicknesses of hcPEDOT:PSS thin films on glasses were investigated. The optimised double-layered 90 nm thick hcPEDOT:PSS plus the 25 nm thick PEDOT:PSS thin film illustrated the transmittance greater than 80% over the full spectral range. The PCS device using ~90 nm thick

hcPEDOT:PSS top anode performed better than that of the devices using the ~45 nm and ~135 nm thick top anode, respectively. Hence, the ~90 nm thick hcPEDOT:PSS top thin film was chosen as the hole collecting electrode for all OSC devices on other different metal substrates.

(2) The different surface morphologies of the metal substrates and the active layers on top of SG1 derived ETL did not present a large difference on the performance of the OSC devices. Highest PCE of 3.11% was obtained on the SS substrate. Similar performance of the OSC devices on the Cr-Al substrate was also achieved. We inferred that this result was due to low resistance caused by the Cr_xO_y layer between the ETL layer and the SS or Cr-Al substrates. Compared with the SS and Cr-Al substrate, the performance of the OSC device on Ti-S and Al substrates was poor. Therefore, the passive layer (oxides) on the very top surface of Ti-S and Al substrates was taken as the key factor that influenced PCE of the OSC devices by blocking the transport of electrons.

(3) The OSC devices on different metal substrates were investigated by EIS technique to revealed the interfacial resistance between the P3HT:PCBM layer and the corresponding metal electrodes. High resistance of the interface derived from the EIS curves between the P3HT:PCBM layer and the metal substrates led to very low FF and PCE for the devices on Ti-S and no PCE for the devices on the Al, respectively. The PCE results exhibited that the performance of the OSC devices on different metals could mainly be due to the passive layer (oxidation layer) formed on the top surface of metals.

7.6 References:

[1] Q. Dong, Y. Zhou, J. Pei, Z. Liu, Y. Li, S. Yao, J. Zhang, W. Tian, All-spin-coating vacuum-free processed semi-transparent inverted polymer solar cells with PEDOT:PSS anode and PAH-D interfacial layer, Org. Electron., 11 (2010) 1327-1331.

[2] P. Schilinsky, C. Waldauf, C.J. Brabec, Performance analysis of printed bulk heterojunction solar cells, Adv. Funct. Mater., 16 (2006) 1669-1672.

[3] S. I. Na, B. K. Yu, S. S. Kim, D. Vak, T. S. Kim, J. S. Yeo, D. Y. Kim, Fully spray-coated ITO-free organic solar cells for low-cost power generation, Sol. Energy Mater. Sol. Cells, 94 (2010) 1333-1337.

[4] F. C. Krebs, All solution roll-to-roll processed polymer solar cells free from indium-tinoxide and vacuum coating steps, Org. Electron., 10 (2009) 761–768.

[5] C. N. Hoth, S. A. Choulis, P. Schilinsky, C. J. Brabec, High photovoltaic performance of inkjet printed polymer:fullerene blends, Adv. Mater., 19 (2007) 3973-3978.

[6] R. R. Søndergaard, M. H¨osel, F. C. Krebs, Roll-to-Roll fabrication of large area functional organic materials, J. Polym. Sci., Part B: Polym. Phys., 51 (2013) 16–34.

[7] F. C. Krebs, T. Tromholt, M. Jørgensen, Upscaling of polymer solar cell fabrication using full roll-to-roll processing, Nanoscale, 2 (2010) 873-886.

[8] G. Dennler, M. C. Scharber, C. J. Brabec, Polymer-fullerene bulk-heterojunction solar cells. Adv. Mater., 21 (2009)1323-1338.

[9] F. C. Krebs, S.A. Gevorgyan, J. Alstrup, A roll-to-roll process to flexible polymer solar cells: model studies, manufacture and operational stability studies, J. Mater. Chem., 19 (2009) 5442-5451.

[10] F. C. Krebs, Roll-to-roll fabrication of monolithic large-area polymer solar cells free from indium-tin-oxide, Sol. Energy Mater. Sol. Cells, 93 (2009) 1636–1641.

[11] F. C. Krebs & N. Kion, Using Light-Induced Thermocleavage in a Roll-to-Roll Process for Polymer Solar Cells, ACS Appl. Mater. Interfaces, 2 (2010) 877-887.

[12] J. S. Yu, I. Kim, J. S. Kim, J. Jo, T. T. Larsen-Olsen, R. R. Søndergaard, M. H¨osel, D. Angmo, M. Jørgensen, F. C. Krebs, Silver front electrode grids for ITO-free all printed polymer solar cells with embedded and raised topographies, prepared by thermal imprint, flexographic and inkjet roll-to-roll processes, Nanoscale, 4 (2012) 6032–6040.

[13] M. Manceau, D. Angmo, M. Jørgensen, F. C. Krebs, ITO-free flexible polymer solar cells: From small model devices to roll-to-roll processed large modules, Org. Electron., 12 (2011) 566–574.

[14] R. N. Chauhan, C. Singh, R. S. Anand, J. Kumar, Effect of sheet resistance and morphology of ITO thin films on polymer solar cell characteristics, Int. J. Photoenergy, 2012 (2012), Article ID 879261.

[15] F. C. Chen, J. L. Wu, C. L. Lee, W. C. Huang, H. M. P. Chen, W. C. Chen, Flexible polymer photovoltaic devices prepared with inverted structures on metal foils, IEEE Electron Device Lett., 30 (2009) 727-729.

[16] Y. Galagan, D. J. D. Moet, D. C. Hermes, P. W. M. Blom, R. Andriessen, Large area ITO free organic solar cells on steel substrate, Organ. Electron., 13 (2012) 3310-3314.

[17] Y. M. Chang, C. P. Chen, J. M. Ding, C. Y. Leu, M. J. Lee, R. D. Chen, Top-illuminated organic solar cells fabricated by vacuum-free and all-solution processes, Sol. Energy Mater. Sol. Cells, 109 (2013) 91-96.

[18] B. Zimmermann, U. Wurfel, M. Niggemann, Long term stability of efficient inverted P3HT:PCBM solar cell, Sol. Energy Mater. Sol. Cells, 93 (2009) 491-496.

[19] T. S. Kim, S. I. Na, S. H. Oh, R. Kang, B. K. Yu, J. S. Yeo, J. Lee, D. Y. Kim, All-solution processed ITO-free polymer solar cells fabricated on copper sheets, Sol. Energy Mater. Sol. Cells, 98 (2012) 168-171.

[20] D. Angmo, M. H¨osel, F. C. Krebs, All solution processing of ITO-free organic solar cell modules directly on barrier foil, Sol. Energy Mater. Sol. Cells, 107 (2012) 329-336.

[21] C. H. Hsieh, Y. J. Cheng, P. J. Li, C. H. Chen, M. Dubosc, R. M. Liang, C. S. Hsu, Highly efficient and stable inverted polymer solar cells integrated with a cross-linked fullerene material as an interlayer, J. Am. Chem. Soc., 132 (2010) 4887-4893.

[22] J. H. Chang, Y. H. Chen, H. W. Lin, Y. T. Lin, H. F. Meng, E. C. Chen, Highly efficient inverted rapid-drying blade-coated organic solar cells, Org. Electron., 13 (2012) 705-709.

[23] Y. Zhou, H. Cheun, S. Choi, C. F. Hernandez, B. Kippelen, Optimization of a polymer top electrode for inverted semi-transparent organic solar cells, Org. Electron., 12 (2011) 827-831.

[24] B. Zimmermann, M. Glatthaar, M. Niggemann, K. M. Riede, A. Ziegler, T. Gombert, Organic solar cells with inverted layer sequence incorporating optical spacers-simulation and experiment, SPIE-Organic Optoelectronics and Photonics, 6197 (2006).

[25] V. D. Mihailetchi, P. W. M. Blom, J. C. Hummelen, and M. T. Rispens. Cathode dependence of the open-circuit voltage of polymer: fullerene bulk heterojunction solar cells, J. Appl. Phys., 94(2003) 6849- 6854.

[26] D. Chirvase, Z. Chiguvare, M. Knipper, J. Parisi, V. Dyakonov, and J. C. Hummelen, Electrical and optical design and characterisation of regioregular poly (3-hexylthiophene-2,5diyl)/fullerene-based heterojunction polymer solar cells, Synth. Met., 138 (2003) 299-304.

[27] J. Jensen, M. Mikkelsen, F. C. Krebs, Flexible substrates as basis for photocatalytic reduction of carbon dioxide, Sol. Energy Mater. Sol. Cells, 95 (2011) 2949–2958.

[28] T. Chuang, M. Troccoli, P. Kuo, A. Jamshidi-Roudbari, M. K. Hatalis, I. Biaggio, A. T. Voutsas, Top-emitting 230 dots/in. active-matrix polymer light-emitting diode displays on flexible metal foil substrates, Appl. Phys. Lett., 90 (2007) 151114.

[29] K. Inoue, R. Ulbricht, P.C. Madakasira, W.M. Sampson, S. Lee, J. Gutierrez, J. Ferraris, A. A. Zakhidov, Temperature and time dependence of heat treatment of RR–P3HT/PCBM solar cells, Synth. Met., 154 (2005) 41-44.

[30] G. Perrier, R. D. Bettignies, S. Berson, N. Lemaˆıtre, S. Guillerez, Impedance spectrometry of optimized standard and inverted P3HT–PCBM organic solar cells, Sol. Energy Mater. Sol. Cells, 101 (2012) 210-216.

[31] G. Garcia-Belmonte, A. Munar, E. M. Barea, J. Bisquert, I. Ugarte, R. Pacios, Charge carrier mobility and lifetime of organic bulk heterojunctions analyzed by impedance spectroscopy, Org. Electron., 9 (2008) 847-851.

[32] A. Mani, C. Huisman, A. Goossens, J. Schoonman, Mott–Schottky analysis and impedance spectroscopy of TiO2/6T and ZnO/6T devices, J. Phys. Chem., B112 (2008) 10086-10091.

8.1 Conclusions

After the development of bulk heterojunction concept by Tang et al. in 1986, the PCE of organic solar cells have increased several orders of magnitude. Compared to the conventional device structure, the inverted device structures is a promising alternative way for fabrication of organic based solar cells. This type of device structure has recently gained considerable attention due to its advantages of device stability and potentially low-cost processing route. In this context, the major outcomes of the present thesis can be enlisted as follows:

(1) In the inverted device structure, the electron transport layer was investigated by various deposition methods including the ZnO nanoparticles-dispersion and sol-gel derived ZnO films. For the nanoparticles route, zinc oxide NPs of ZNP5 were dispersed in a combination of methanol and dichloromethane (10:0.7) using the ball mill method. The deposited film was porous, limiting its use as an electron transport layer. For a comparative study, ZnO commercial dispersion of ZNP10 was also used to deposite the ZnO film on the substrates, which formed a moderately dense structure. The OSC device with the ZNP10 derived ETL performed better with a PCE of 1.85% as compared to that of the ZNP5 created ETLs with 0.37%. With regard to the sol-gel route, the ZnO sol was made by dissolving zinc acetate dehydrate in a combination of 2-methoxyethanol and then ethanolamine. The performance of OSC devices using the sol-gel based ZnO ETL of SG1 was closely the same as that of the ZNP10 nanoparticcle-derived ZnO ETL; i.e. 1.85% and 1.80%, respectively.

(2) The P3HT:PCBM active layer deposited on top of the ZnO layer was studied for optimisation. It was found that the CB3 (35mg/ml) in chlorobenzene with a weight ratio of 1:1 presented good properties as the active layer of our photovolataic devices. The AFM morphological characteristic revealed a nano-scale phase separation between the donor and acceptor materials. Optimisation of the P3HT:PCBM active layer was also studied by doping high-boiling point solvents in the blend in order to reduce its drying rate in the fabrication process, which led to high crystallinity of the active layer in morphologies, contributing to the improvement of the device performance.

(3) Poor wettability of the aqueous PEDOT:PSS solution on the hydrophobic P3HT:PCBM active layer was improved by adding the surfactant triton X-100 into the solution. The contact angle of the PEDOT:PSS droplets has reduced from 74.8 ± 4.0^{o} to 39.0 ± 3.0^{o}.

(4) The inverted OSC device on the ITO coated glass with big-sized Au nanoparticles formed anode (without plasmonic effects) revealed a PCE of 2.30%. As the active layer of OSC devices typically is very thin, leading to poor light absorption. Therefore, for an efficient light-trapping purpose, we used a low vacuum PAPVD method to deposit the fine Au nanoparticles thin film onto the PEDOT:PSS layer in inverted P3HT:PCBM OSC devices. The Au NPs incorporated into the PEDOT:PSS layer and reached to the active P3HT:PCBM layer. Two types of the Au NPs deposited on top of PEDOT:PSS layer were compared one with a diameter of nearly 50 nm in size and another with a diameter of ~15 nm, respectively. The obtained PCE of the fabricated devices with ~50 nm Au nano particles was in average 2.07 % with short circuit current density (J_{sc}) of 6.60 mA/cm^2. However, the short circuit current density of the devices with ~15 nm Au

nano particles has reached in average 12.38 mA/cm^2 with maximum at 13.40 mA/cm^2. The obtained PCE on average was 3.92 % with maximum at 4.05%. An approximately 50 to 90% improvement in short-circuit current density and in power convention efficiency has been achieved compared with those OSC devices without the plasmonic light absorption enhancement.

(5) No enhanced light absorption was obtained when the PAPVD Au NPs film was directly applied on the active layer.

(6) We also demonstrated a further enhancement in the efficiency and fill factor of the inverted OSC devices by sandwiching a thin film of Au nano particles between two PEDOT:PSS layers. The Au NPs film was deposited by PAPVD on top of the first low conductive PEDOT:PSS layer and followed a high conductive PEDOT:PSS layer, which provided a significantly plasmonic broadband light absorption enhancement to the active layer. High efficient inverted organic solar cells were obtained with a PCE up to 5.01 %. Broadband light absorption enhancement was achieved due to Au NPs that presented the circular oblong-shaped structures.

(7) Metal substrates with excellent mechanical flexibility and thermal stability are also a potential alternative for producing top illuminated inverted OSC devices High conductivity and good dimensional stability during the processing at elevated temperature is their advantages for the use of metal substrates.

We investigated some typical metals and produced the top illuminated inverted OSC devices on these substrates namely: polished stainless steel (SS), titanium coated steel (Ti-S), chromium coated aluminium (Cr-Al), and polished aluminium (Al). The inverted

OSC devices on different metal substrates were fabricated where the hcPEDOT:PSS was used as a semi-transparent top electrode for hole collection. The inverted OSC devices fabricated on different morphologies of SS and Cr-Al metals did not present a large difference in terms of PCE. High PCE of 3.11% was obtained on the SS substrate while the PCE of the reference devices on the ITO coated glass was ~2.0%. Similar performance of the OSC devices on the Cr-Al substrate was also achieved with a PCE of 3.10%. Our studies showed that the results was due to low resistance caused by the chromium oxide layer between the ETL layer and the SS or Cr-Al substrates and concluded that the variable roughness of the metal surfaces under the submicron range did not play a main role on the performance of the OSC devices. Compared with the SS and Cr-Al substrate, the passive layer (oxides) on the very top surface of Ti-S and Al substrates was taken as the key factor that influenced PCE of the OSC devices by blocking the transport of electrons. The PCE of the inverted OSC devices on Ti-S substrate was 1.48% while no PCE was observed on polished Al substrates.

(8) EIS was used to characterise the interfaces between the P3HT:PCBM active llayer and metal substrates. High resistance of the interface derived from the EIS curves between the P3HT:PCBM layer and the metal substrates led to very low FF and PCE for the devices on Ti-S and no PCE for the devices on the Al, respectively.

In conclusion, this thesis presents findings of novel inverted structure where application of plasmonic metal nano particles provides an optional route for achieving high performance OSC devices. For the OSC devices on metal substrates, interfaces between the active layer and metal substrates play an important role due to the naturally formed oxide layer on top of metal substrates.

8.2 Future Scope

(1) Present work deal with nanoparticle based or sol gel based ZnO thin films for electron transportation. Recently, it is observed that sol gel based zinc oxide nanowire (ZnO-NW) structures have better device efficiency. Therefore, it would be interesting to extend this work with the ZnO-NW electron transport layer and to further improve the charge collection efficiency and the overall efficiency of the discussed inverted structure devices. The morphology of ZnO NWs need to be long enough with small spacing between the wires. The longer NW can provide the larger interface for charge collection and continuous pathways for charge transport and the small spacing close to the diffusion length may enhance the exciton dissociation rate. Another interesting subject for exploration could be the use of a low band gap and high mobility organic material for the active layer to enhance the range of the light absorption band.

(2) The use of plasmonic NPs with various sizes and shapes and hence different LSPR bands can be placed into different layers (e.g. ETLs and HTLs) and/or the interfaces of the OSC devices can provide simultaneous benefits for light absorption enhancement and has the potential to further enhance the power conversion efficiency

(3) Another direction is to further develop the technologies for fabrication of large-area top illuminated inverted OSC devices on flexible metal substrates. For this type of devices, the key issue is to look for moisture and chemical resistant materials for fabricating the low cost and long term stable photovoltaic devices. Experiments on these directions are currently underway and work will continue after this thesis.

- Bachelor of Science in Physics, Chemistry and Mathematics. (2001-2004) from C.C.S. University, Meerut, India- Marks scored- 66.8 %.
- Master of Science in Physics (Specialization in Electronics) (2005-2007) from C.C.S. University, Meerut, India- Marks scored- 71.6 %.
- Master of Technology in Energy Studies (Specialization in CdS/CdTe thin film solar cells) (2008-2010) from Indian Institute of Technology, Delhi India- CGPA - 8.60/10
- Joined Material Engineering Research Institute, Sheffield Hallam University, Sheffield, UK as a PhD student in January 2011.